NORTHWESTERN UNIVERSITY

Advances in Optical Coherence Tomography for Retinal Oximetry and Angiography

A DISSERTATION

SUBMITTED TO THE GRADUATE SCHOOL
IN PARTIAL FULFILLMENT OF THE REQUIREMENTS

for the degree

DOCTOR OF PHILOSOPHY

Field of Biomedical Engineering

By

Brian Soetikno

EVANSTON, ILLINOIS

December 2018

Abstract

Advances in Optical Coherence Tomography for Retinal Oximetry and Angiography

Brian Soetikno

Optical coherence tomography (OCT) is a high-resolution, non-contact, three-dimensional imaging technique, which has revolutionized the diagnosis and treatment of retinal diseases. Visible-light OCT (vis-OCT) extends OCT by enabling retinal oximetry – the measurement of oxygen saturation of hemoglobin from within individual retinal blood vessels. Three advances in the vis-OCT technique are presented: an improved vis-OCT oximetry method based on circumpapillary scan and graph-search segmentation; the calibration, simulation, and correction of spectroscopic sensitivity rolloff for vis-OCT oximetry; and the measurement of the inner retinal oxygen metabolism in the 50/10 oxygen-induced retinopathy model, an animal model for human retinopathy of prematurity. Optical coherence tomography angiography (OCTA) is another functional extension of OCT, which provides three-dimensional, non-invasive, capillary-level mapping of vascular perfusion. Two studies of OCTA in animal models are described: the monitoring of retinal vascular occlusions produced by imaging-guided laser photocoagulation; and the monitoring of laser-induced choroidal neovascularization, a model of wet age-related macular degeneration. Whether by providing insight into disease mechanisms or by directly imaging functional biomarkers in the human retina, vis-OCT oximetry and OCTA will be instrumental in preventing blindness for those suffering from vision-threatening disease.

Acknowledgements

Thank you to my Ph.D. advisor Prof. Hao F. Zhang, who placed his trust in me from the very beginning. His mentorship and guidance throughout my Ph.D. training have undoubtedly helped me mature as a scientist. My conversations with Dr. Zhang have spanned all topics, from medical training to scientific questions to major life decisions. In all cases, I have always received and learned more than I asked for. I appreciate his support and patience when dealing with the challenging moments in research.

Thank you to my co-advisor Prof. Amani Fawzi. As a clinician-scientist, Dr. Fawzi has shown me the challenges and rewards of simultaneously balancing duties as a physician and scientist. Our discussions have always taught me something scientifically valuable and have challenged me to think more rigorously. Much of my interest in ophthalmology has been fueled by working with Dr. Fawzi.

Thank you to my committee members Prof. Linsenmeier and Prof. Sun. With his longstanding experience in retinal physiology, Dr. Linsenmeier has always provided a careful attention to detail for the physiological aspects of my work, particularly with regards to animal models of retinal disease and retinal oximetry. With his expertise in optics, material science, and research, Prof. Sun has also been instrumental in giving me feedback along the way.

Thank you to the members of the Zhang and Fawzi labs whom I have acquired skills, knowledge, and experience from. I thank Dr. Ji Yi for laying the foundation of visible light OCT; Dr. Wenzhong Liu for first introducing me to OCT; Dr. Siyu Chen for taking his time to have many fruitful discussions about retinal oximetry with me; Dr. Xiao Shu for his patience with my countless questions and for teaching me optical alignment; Peter Nesper for his hard work on many

manuscripts together; Dr. Ronil Shah for the hard work performing choroidal neovascularization experiments in M2 year; Lisa Beckmann for her patience with me during many long and demanding imaging experiments; Dr. Roman Kuranov for his help and experience in OCT knowledge; and Dr. Yuanbo Wang for his help building the graphical user interface for processing vis-OCT oximetry data.

Obtaining a Ph.D. was a dream that I first internalized in my sophomore year of college, while working with my two undergraduate mentors: Dr. Lihong Wang and Dr. Jin-Moo Lee. I thank Dr. Wang for inspiring me to take on the challenge of pursuing a Ph.D. and for allowing me to have an active role in his lab. Thank you to Dr. Lee for inspiring me to take on the additional challenge of applying for M.D./Ph.D. programs and for teaching me about stroke neurology. I also thank Dr. Song Hu for giving me one-on-one attention and scientific training during my undergraduate years.

I thank my grandparents, who sacrificed much of their lives working hard so that I can now pursue my dreams. I thank my parents, who inspire me to work tirelessly towards my goals. I thank my brother, who has provided much emotional support along the way. I thank my friends, who have made this work worth the effort. Finally, I thank my love, who gave me unwavering support throughout this entire process.

List of Abbreviations

2-D	Two-dimensional
3D	Three-dimensional
AGPF	Axial global phase fluctuations
AMD	Age-related macular degeneration
AO	Adaptive optics
APD	Avalanche photodetector
ARVO	Association for Research in Vision and Ophthalmology
BRAO	Branch retinal artery occlusion
BRVO	Branch retinal vein occlusion
CNV	Choroidal neovascularization
CRAO	Central retinal artery occlusion
CRVO	Central retinal vein occlusion
DeHb	Deoxygenated hemoglobin
DR	Diabetic retinopathy
FA	Fluorescein angiography
FD-OCT	Fourier-domain optical coherence tomography
FFT	Fast Fourier Transform
FOV	Field of view
FWHM	Full-width at half maximum
GPU	Graphical processing unit
GVD	Group velocity dispersion
HbO_2	Oxygenated hemoglobin
ICG	Indocyanine green angiography
IPL	Inner plexiform layer
$irDO_2$	Inner retinal delivery rate of oxygen
$irMRO_2$	Inner retinal metabolic rate of oxygen
LGL	Lens-Grating-Lens configuration
MAP	Maximum amplitude projection
ME	Mean error
MRI	Magnetic resonance imaging
MRO_2	Metabolic rate of oxygen
NA	Numerical aperture
NIR	Near infrared
NUFFT	Non-uniform Fast Fourier Transform
OCT	Optical coherence tomography
OCTA	Optical coherence tomography angiography

OEF	Oxygen extraction fraction
OIR	Oxygen-induced retinopathy
OMAG	Optical microangiography
ONH	Optic nerve head
ONL	Outer nuclear layer
OPL	Outer plexiform layer
OST	Optical section thickness
PAOM	Photoacoustic ophthalmoscopy
PMT	Photomultiplier tube
pO_2	Partial pressure of oxygen
PR	Photoreceptor
PSF	Point spread function
RAO	Retinal artery occlusion
RB	Rose Bengal
RIN	Relative intensity noise
RMSE	Root mean squared error
ROP	Retinopathy of prematurity
RPE	Retinal pigment epithelium
RVO	Retinal vein occlusion
SD	Standard deviation
SD-OCT	Spectral-domain optical coherence tomography
SHWS	Shack-Hartmann Wavefront Sensor
SLED	Superluminescent light emitting diode
SLO	Scanning laser ophthalmoscopy
SNR	Signal-to-noise ratio
sO_2	Oxygen saturation of hemoglobin
SR	Sensitivity rolloff
SSADA	Split-spectrum amplitude decorrelation algorithm
SSR	Spectroscopic sensitivity rolloff
STFT	Short-time Fourier Transform
TD-OCT	Time-domain optical coherence tomography
VEGF	Vascular endothelial growth factor
Vis-OCT	Visible-light Optical coherence tomography
vis-OCTA	Visible-light optical coherence tomography angiography

Table of Contents

List of Figures

List of Tables

Chapter 1

Introduction

1.1 BACKGROUND AND MOTIVATION

Retinal diseases impair vision and cause blindness, drastically affecting a person's quality of life. The diagnosis of retinal disease relies on the natural optics of the eye, which enable the retina to be visualized from the outside. Many technologies have been invented for ophthalmic imaging, utilizing both light and sound interactions with tissue. By far, the most important retinal imaging technology over the last twenty-five years is optical coherence tomography (OCT) (1), a technique which provides micron-resolution, non-contact, cross-sectional tissue imaging.

Advancements in OCT technology have primarily focused on perfecting structural imaging of the retina. The increase in performance for OCT structural imaging has been impressive. Faster OCT systems – based on swept source light sources – have reached megahertz A-line rates (2). In addition, wide-field-of-view three-dimensional retinal imaging and simultaneous anterior and posterior segment imaging have also been demonstrated (3, 4). However, the ability to infer functional activity of the retina remains highly desirable. This dissertation concentrates on two emerging functional OCT technologies: visible-light OCT retinal oximetry and OCT angiography.

1.1.1 Visible-light OCT

The retina is one of the most metabolically active tissues in the human body, making it particularly susceptible to hypoxia (5). In many ischemic retinal diseases, aberrant oxygen metabolism is hypothesized to play a pivotal role in disease pathophysiology. Vis-OCT aims to directly probe changes in the oxygen metabolism to provide a biomarker of tissue hypoxia. First demonstrated by Yi et al. in 2013 (6), retinal oximetry with vis-OCT measures the oxygen saturation of hemoglobin (sO_2) from within individual retinal blood vessels. Retinal sO_2 measurements using vis-OCT have been demonstrated and validated in rodents (7, 8). In addition, the retinal oximetry capabilities have been combined with Doppler OCT to measure blood flow. When examined together, sO_2 and blood flow can be used to estimate the retinal metabolic rate of oxygen (MRO_2). For example, vis-OCT was used to study the MRO_2 during progressive systemic hypoxia challenges, where the inhaled oxygen content was progressively decreased (7). In another study, vis-OCT was applied to measure the MRO_2 in an animal model of diabetic retinopathy (9).

1.1.2 Challenges for visible-light OCT

The calculation of sO_2 with vis-OCT requires reliable estimation of the true spectrum of backscattered light. The spectrum can come from either hemoglobin in the blood or a reflector beneath the blood vessel, such as the posterior vessel wall. Unfortunately, subject motion and image noise make averaging at the same depth position challenging, and lead to inaccurate sO_2 estimation. An automated technique that enables averaging of the backscattered light spectrum at the same depth location is highly desired to obtain accurate sO2 measurements.

In addition, the detection of backscattered light spectrum is inferred from signals detected by a spectrometer. The spectrometer detects an interference pattern whose amplitude information encodes the spectral content of the sample. However, due to the spectrometer’s frequency response, the spectrometer itself can impose spectral modifications on the interference pattern. These spectral transfer functions have previously not been studied and compensated for in OCT oximetry measurements, which decreases the accuracy of the collected spectra.

Retinopathy of prematurity (ROP) represents a major cause of childhood vision loss worldwide (10). The 50/10 oxygen-induced retinopathy (OIR) model in rats presents findings similar to human ROP (11), but the MRO_2 of the inner retina has not been previously explored. A study with vis-OCT to measure the oxygenation would provide an improved understanding of the pathophysiology of OIR model.

1.1.3 Optical coherence tomography angiography

Optical coherence tomography angiography (OCTA) provides label-free, three-dimensional (3D) imaging of the retinal and choroidal vasculature (12). While conventional OCT excels at capturing static 3D structural information within the retina, the image contrast from blood vessel walls alone is insufficient to provide meaningful angiograms. On the other hand, OCTA exploits the motion of blood cells within the retinal vessels to generate exquisite image contrast of blood vessels. Within the past decade, hardware advances in spectral-domain OCT technology have enabled more rapid acquisitions so that complex OCTA scanning protocols can be performed within a few seconds (13).

1.1.4 Challenges for OCTA

Retinal vascular occlusive diseases represent a major form of vision loss worldwide (14). Rodent models of retinal vascular occlusion have traditionally relied upon a slit-lamp biomicroscope to visualize the fundus and subsequently to deliver high-power laser shots to a target vessel for occlusion (15). OCTA would be a perfect technology to monitor the vascular changes and longitudinal morphological response in these animal models, especially with therapeutic intervention. A device, which could consistently create and monitor retinal vascular occlusions, would be highly desirable for better understanding the pathophysiology of these diseases.

Age-related macular degeneration (AMD) is the leading cause of blindness in individuals greater than 50 years old (16). In the wet form of AMD, abnormal blood vessels from the choroidal circulation, term choroidal neovascularization (CNV), grow underneath the retina. These abnormal vessels may leak fluid, which damages the retinal photoreceptors. One animal model for wet AMD is the laser-induced CNV model (17). This model has not been previously studied with OCTA. OCTA would reveal key insights into the pathogenesis of the animal model, providing insight into the disease mechanisms.

1.2 SCOPE OF THE DISSERTATION

The objective of this dissertation is two-fold. The first objective is to provide the necessary background and reference knowledge for understanding ophthalmic imaging, with specific emphasis on OCT. The second objective is to address the challenges for both vis-OCT and OCTA. For vis-OCT, this dissertation includes technological development studies to improve the vis-OCT oximetry method as well as an animal study to investigate the metabolic rate of oxygen in the 50/10 oxygen-induced retinopathy model. For OCTA, this dissertation includes technological development to develop an improved device for creating an animal model of retinal vascular occlusions as well as an animal study to investigate longitudinal changes in the laser-induced CNV model for wet AMD.

1.3 DISSERTATION OUTLINE

Chapter 2 presents an overview of each of the major retinal imaging modalities. This includes discussion of fundus photography, scanning laser ophthalmoscopy (SLO), OCT, photoacoustic ophthalmoscopy (PAOM), and adaptive optics (AO) imaging. The key principles and theory behind each technique are presented.

Chapter 3 delves deeper into OCT theory and signal processing. Here the key equations of OCT are reviewed. Modern OCT image formation theory is explained. A signal processing algorithm for reconstruction OCT images is explained.

Chapter 4 presents an algorithm to reliably extract the backscattered light's spectrum, using a combined cross-correlation and graph-search based segmentation approach. Using measurements from 100 B-scans as a gold standard, we demonstrated that our method achieved highly accurate measures of sO_2 with minimal bias. In addition, we also investigated how the number of repeated measurements affects the accuracy of sO_2 measurement.

Chapter 5 outlines a method to carefully to carefully calibrate a spectrometer for spectroscopic OCT. We characterize the wavelength distribution of a spectrometer. Using simulations, we calculated the theoretical transfer function of a customized visible light spectrometer. We then demonstrate the correction of the spectroscopic sensitivity rolloff to retrieve more accurate spectroscopy using OCT.

Chapter 6 presents metabolic rate of oxygen measurements of vis-OCT in the 50/10 OIR of prematurity model. We found significant decreases in both the inner retinal oxygen delivery ($irDO_2$) and the metabolic rate of oxygen ($irMRO_2$) in the OIR model compared to controls. Using fluorescence immunostaining, we examined the retinal vascular density post-mortem and determined that a significant decrease in retinal vascular density exists in the OIR group. Moreover, from histological stains, we also observed a significant reduction in retinal thickness in the OIR group.

Chapter 7 discusses the development of a multi-purpose imaging system, which can produce, image, and monitor retinal vascular occlusions in rodents. The system combines a near-infrared OCT system, for cross-sectional structural imaging and OCTA, with a fluorescence SLO, for Rose Bengal monitoring and high-power laser delivery to a target vessel.

Chapter 8 demonstrates visible-light OCTA (vis-OCTA) as a reliable method for the detection of CNV development and determining the size of the lesion in rodents. We imaged at different time points after laser injury to monitor CNV development and measure CNV lesion size and determined the earliest time point at which evidence of CNV could be detected. Measurements obtained from vis-OCTA angiograms were compared to histopathologic measurements from isolectin-stained choroidal flatmounts.

Chapter 9 summarizes this dissertation and presents areas for future work.

Chapter 2

Imaging the Living Eye

2.1 INTRODUCTION

Since the dawn of photography in the 1800s, scientists and physicians have pursued techniques to capture images from inside the living eye. Capturing the fundus, or the interior surface of the retina, proved to be challenging. Indeed, early fundus photographs suffered from motion artifacts, overlapping corneal reflections, and long exposure times (18). Since these early explorations, however, significant advances in eye imaging have emerged, owing to new innovative modalities including the fundus camera, scanning laser ophthalmoscope (SLO), and optical coherence tomography (OCT). Of note, OCT has enabled three-dimensional imaging of the living retina, providing images which approach the quality of *ex vivo* histology. More recently, techniques such as photoacoustic ophthalmoscopy (PAOM) and adaptive optics (AO) have made additional impact in living eye imaging by making advances in absorption imaging contrast and aberration correction, respectively. Each of these technologies has provided new avenues towards understanding how we see.

The study of the eye's physiological processes in health and disease rely upon the aforementioned techniques to answer scientific questions. Studies have combined animal models of human ocular diseases with advanced imaging tools to improve our understanding of disease pathogenesis and to develop new therapies. Ophthalmic imaging has also helped reveal the mechanisms of neural circuitry, since the eye is developmentally an extension of the brain (19). Ultimately, most of these techniques have made their way into routine clinical practice. Thus, the understanding of these innovative eye imaging technologies is important to a wide variety of researchers and clinicians. This chapter will introduce the ocular anatomy and then follow with discussion of the most important imaging technologies. The operating principles underlying each technology will be outlined, and their applications to ophthalmic research will be illustrated.

2.2 OCULAR ANATOMY

An understanding of the ocular anatomy is required to grasp the principles of ophthalmic imaging. The refractive elements of the eye focus parallel rays of light to the light-sensitive posterior layers of the eye, and, therefore, the optical system of the eye must be considered when designing an imaging system. Figure 2-1(A) illustrates the human eye, which can be divided into anterior and posterior segments. The anterior segment contains the curved surfaces of the cornea and lens, which focus light onto the retina. In addition, the iris dilates and constricts, controlling the amount of light reaching the retina. The posterior segment consists of the vitreous, retina, choroid, and optic nerve head. Most of the ophthalmic imaging modalities focus on capturing the posterior segment and, more specifically, the retina.

A significant part current ophthalmic research is performed in rodents due, in part, to their simple handling and housing, and their similarities in development, morphology, and function to the human eye. In addition, genetic manipulations in mice are simpler compared to other mammals (20, 21). These genetic manipulations have enabled the creation of animal models of human disease, the investigation of disease mechanisms, and the study of therapeutic targets. As shown in Figure 2-1(B), the anatomy of the human eye and the mouse eye are similar, but have some important distinctions (22). In particular, the rodent eye lacks a fovea and macula, an area responsible for sharp vision in humans that mainly consists of cone photoreceptors. Thus, rod photoreceptors predominate the rodent retina. Notably, the rodent lens takes up a significant portion of the ocular volume (23). Because the focal length of the rodent eye is relatively smaller than humans, the numerical aperture in mice (NA~0.5) is larger than in humans (NA~0.18) (24). This chapter will focus on ophthalmic imaging in rodents, but many of the principles can be transferred to humans.

As shown in Figure 2-1(C), the retina is composed of 8 distinct layers, which can be grouped into the outer and inner retina. The outer retina is composed of photoreceptors and the retinal pigment epithelium (RPE). Photoreceptors are further divided into rod and cone photoreceptors, which are responsible for low-light vision and color perception, respectively. The RPE layer contains various pigments, including melanin, which aid in absorbing focused light energy. In addition, the RPE also transports nutrients between the photoreceptors and the choriocapillaris, participates in the visual cycle, removes shed photoreceptor membranes by phagocytosis, and secretes a variety of growth factors (25). The inner retina is composed of four classes of neurons: ganglion cells, amacrine cells, horizontal cells, and bipolar cells. The combination and connections of these cells form small neuronal networks, which amplify, process and filter information from the photoreceptors (26). Eventually, the ganglion cells collect the information and send it to the visual cortex of the brain via their axons, which together form the optic nerve.

The retina possesses an intricate circulatory system, which provides the nutrients necessary to meet the high metabolic demand of the tissue (27, 28). Unlike any other tissue in the body, the retina possesses two circulations: the anterior, termed the retinal circulation, and the posterior, termed the choroidal circulation. Each is distinct by anatomy and by autoregulatory control. The retinal circulation is divided into a trilaminar network (29). Arterioles enter at the optic nerve head and spread outward at the level of the nerve fiber layer and the ganglion cell layer (Figure 2-1(C)). Branches dive deeper into the retina and form an intermediate capillary plexus at the boundary between the inner nuclear layer and the inner plexiform layer. A dense deep capillary plexus is also formed at the boundary of the outer nuclear layer and the outer plexiform layer. The capillaries vertically ascend and drain to large veins, which exit at the optic nerve head. The choroidal circulation consists of large vessels, which ultimately branch to form the choriocapillaris, a dense mesh of capillaries beneath the RPE layer. The retinal circulation is autoregulated, while the choroidal circulation is not. Thus, the flow rate of the retinal circulation is controlled and varies depending on the metabolic demands of the. On the other hand, the flow rate of the choroidal circulation remains mostly constant with one of the highest flow rates in the body (30).

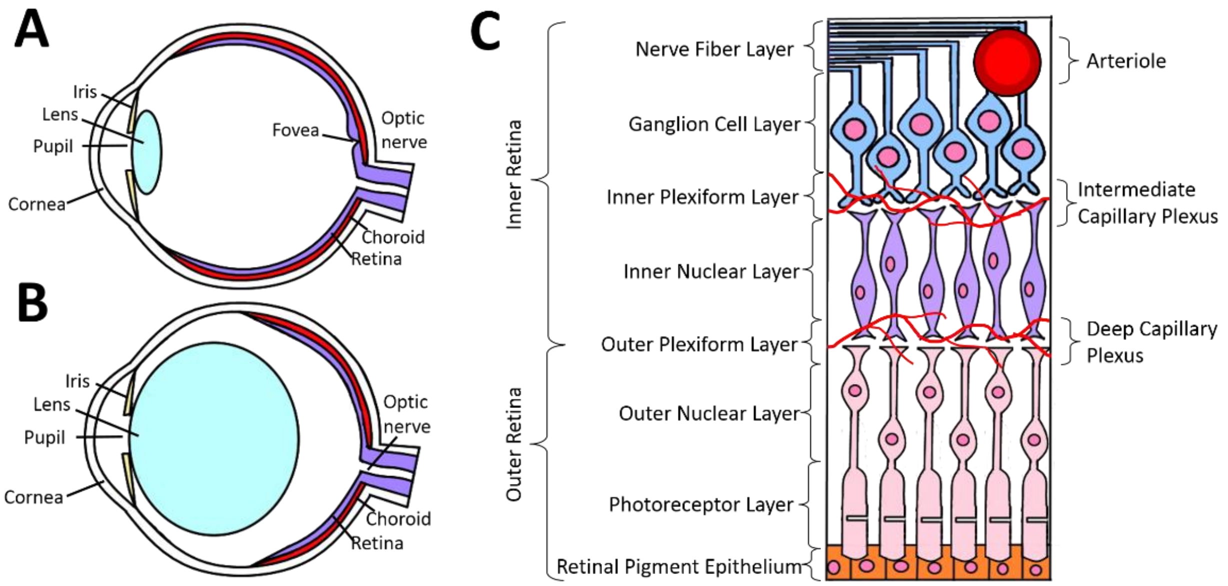

Figure 2-1: Schematic of human eye, mouse eye, and retina. (a) A schematic of a human eye and (b) a schematic of a mouse eye. (c) A cross sectional depiction of the layers of the retina. The intermediate and deep capillary plexi are shown in this depiction.

2.3 FUNDUS CAMERA

The fundus camera magnifies and photographs the retinal fundus, providing two-dimensional structural and anatomical information. Images can be used to observe the progression of retinal diseases, especially those that involve the retinal vasculature or retinal lesions. With monochromatic filters, the fundus camera can also enhance the contrast of the hemoglobin in the vasculature or other pigmented material in the retina, such as drusen in age-related macular degeneration. Using wavelength filters designed to pass specific fluorescence emission, fluorescent dyes can also be imaged, which is primarily used for fluorescein angiography, a method to map the retinal vasculature after intravenous injection of fluorescein dye. Fundus cameras can be integrated with other imaging techniques, such as photoacoustic ophthalmoscopy (31) or optical coherence tomography (32). Multi-wavelength and hyperspectral fundus cameras, which can obtain spectroscopic measurements of hemoglobin absorption inside the vasculature, may potentially be useful in quantifying the oxygen saturation in the retinal blood vessels (33, 34).

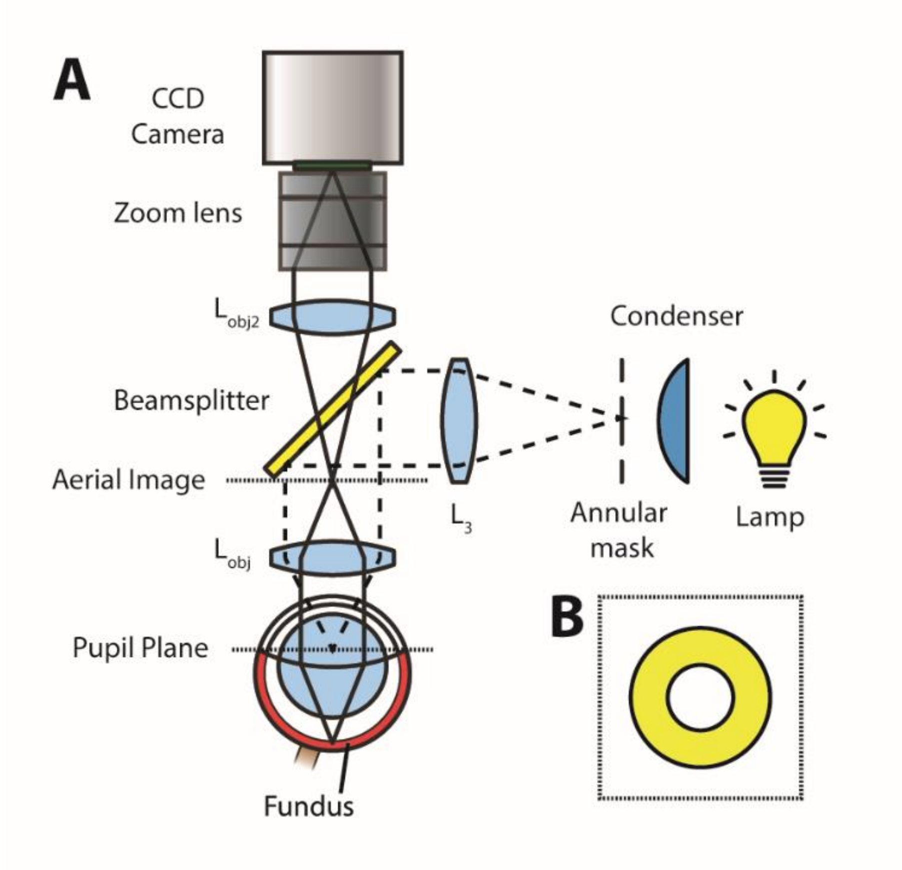

Figure 2-2: Principles of fundus photography. (A) Schematic of a fundus camera. CCD: charge-coupled device camera. Solid lines: fundus photography observation light path. Dashed lines: illumination light path. (B) Illustration of the Gullstrand principle. An annulus illumination is projected at the pupil plane.

Figure 2-2(A) illustrates principles of a custom-built fundus camera. There are two light paths to consider: the observation light path (solid lines) and the illumination light path (dashed lines). The observation light path is similar to that of an indirect ophthalmoscope, where a lens is placed in front of the eye focuses parallel rays exiting the eye to form an aerial image. As shown, the first objective lens (L_{obj}), in conjunction with the subject's own cornea and lens, forms an aerial image of the fundus. The aerial image is then imaged through a 50/50 beamsplitter to a camera's CCD sensor by the combination of a second objective lens (L_{obj2}) and a zoom lens.

The illumination light path takes advantage of the Gullstrand principle, which was first introduced in 1910 by Alvar Gullstrand (35). Gullstrand realized that to eliminate the strong corneal reflections in ophthalmoscopy, the illumination and observation light paths should be separated at the pupil plane. To implement the Gullstrand principle, the light source illuminates an annular mask. The light annulus is then projected to the subject's outer pupil plane by L_{obj} and L3. The outer rim of the annulus serves as the illumination light, while the center dark portion of the annulus allows observation light to pass through (Figure 2-2(B)). Fundus cameras typically use a non-coherent, incandescent source (e.g. halogen or xenon lamp). In this design, a beamsplitter was used so that the illumination and observation light paths were concentric. Alternative designs have incorporated a mirror with a pinhole to achieve a similar effect (36). At the pupil plane, the inner diameter of the annulus must be small enough so that enough light enters the eye. If the subject's pupil cuts off the annular illumination, the retina will be non-uniformly illuminated.

Mouse and rat eyes possess much higher chromatic aberration than human eyes (24, 37, 38), ranging from 6 to 10 diopters in the visible spectral range. Additionally, eyes from albino rodent strains have more severe chromatic aberration than those from pigmented animals. Without correction for the chromatic aberration, broadband fundus photographs in rodents possess low lateral resolution and blur. By narrowing the illumination bandwidth, the lateral resolution can be optimized. Using a combination of numerical simulation and experimental studies, Li et al. demonstrated the highest resolution images can be taken when the light source bandwidth was between 10 nm and 20 nm (39).

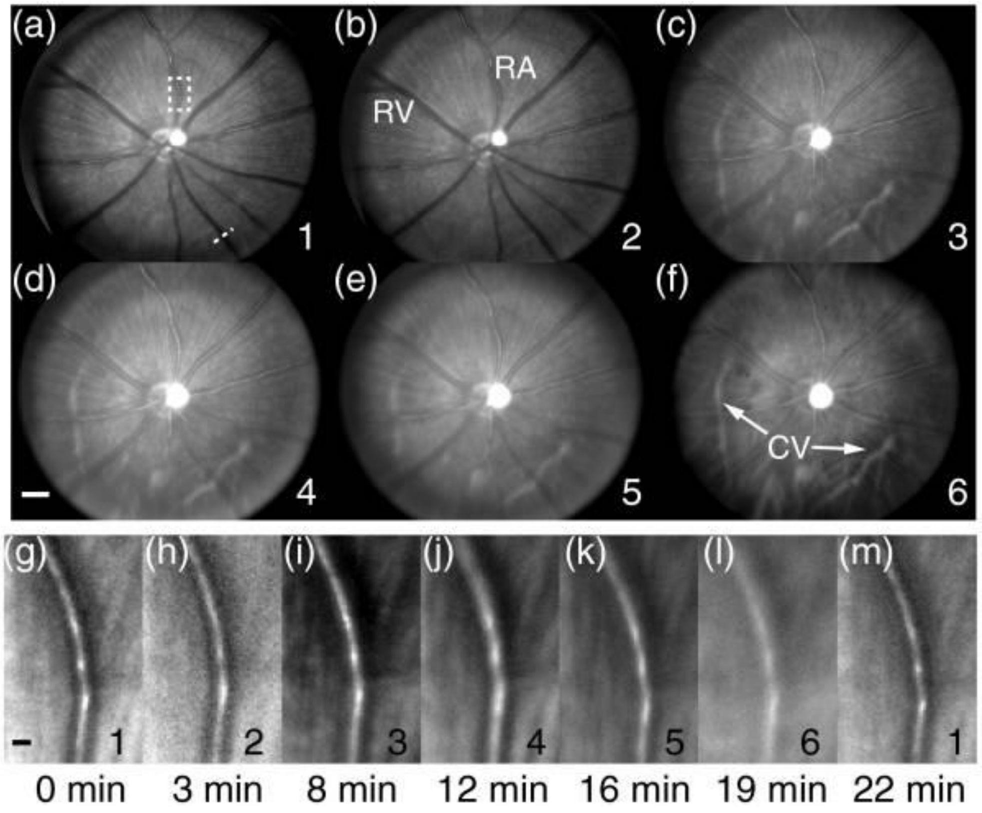

Figure 2-3: Fundus photographs from a pigmented adult rat. The chromatic aberration in the rodent is large. Each photograph shows the same animal, but with different illumination bandwidth. (A-F) As the bandwidth increasesthe resolution degreases. Scale bar: 500 μm (G-I) Magnified view of the white dashed box in A-F, illustrating the change in resolution with increasing illumination bandwidth. Filters were changed at the times indicated below each image. 1-6 indicates different filters that were used. (M) The filter for 1 was replaced and the image quality was similar to G, indicating that the effects of eye quality were minimal. Scale bar: 50 μm. Adapted from ref. (39).

Figure 2-3 shows fundus camera images for six different wavelength bandwidths. The filter bandwidths were 1: 19 nm, 2: 30 nm, 3: 89 nm, 4: 143 nm, 5: 162 nm, 6: 270 nm, respectively (Figure 2-3(A-F)). The image resolution degrades with increasing bandwidth, which can be best observed in the magnified views of a blood vessel in Figure 2-3(G-M). The best resolution achieved was ~10 μm for the 19 nm bandwidth illumination, which is consistent with the expected fundus camera performance given the large chromatic aberration in the rodent eye.

Other solutions for performing fundus photography have been suggested. Paques et al. developed a low-cost, direct-contact solution by combining an illuminating endoscope with a digital camera (40). The eye is still illuminated with annular or crescent illumination to minimize reflections. Standard laboratory microscopes can also be used to visualize the fundus by using an additional objective lens, or by applanation of the cornea with a contact lens or microscope cover-slip (41, 42). Finally, a handheld smartphone's flash light and camera for illumination and observation, with the help of a standard indirect ophthalmoscope lens, was also successfully demonstrated (43).

2.4 CONFOCAL SCANNING LASER OPHTHALMOSCOPE

The scanning laser ophthalmoscope (SLO) was first described in 1980 by Webb et al. (44). Since then, the original SLO design has improved to utilize a confocal design, where the focus at the retina and the focus at the detector are conjugate (45). Similar to a standard confocal microscope, a pinhole, positioned at a plane conjugate to the retina (usually in front of the detector), rejects off-axis scattered light, which increases the image contrast, improves the point spread function, and allows for depth-sectioning. Here we discuss the *confocal* SLO (cSLO) as it predominates most research and SLO technology today. Contrast in cSLO can be derived from retinal reflectance, autofluorescence, and fluorescence from exogenous dyes. In genetically modified animal models, fluorescent proteins in specific retinal cells can also be imaged (46). In rodents, the high numerical aperture (NA) of the eye (NA~0.5) allows changing of the image z-plane. By consecutively taking z-slices at retinal depth positions, a three-dimensional image can be created.

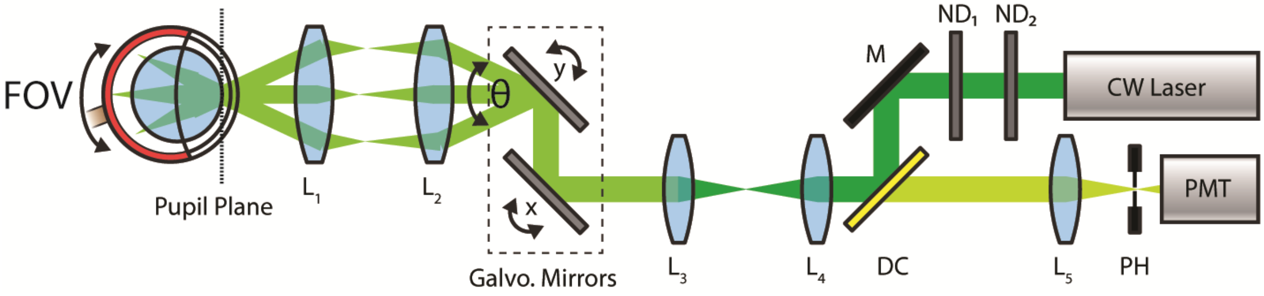

Figure 2-4: Confocal fluorescence scanning laser ophthalmoscope. A pinhole (PH) in front of the detector is used to reject off-axis scattered light. The magnification of the Keplerian telescope made by L1 and L2 and the maximum scanning angle of the galvanometer mirrors determines the field of view (FOV). CW: continuous wave. ND: neutral density filters. DC: dichroic mirror. PMT: photomultiplier tube. Adapted from ref. (47).

Figure 2-4 shows a schematic of a cSLO, which is designed for fluorescent imaging of Rose Bengal dye injected in the vasculature (47). In contrast to the fundus camera, a coherent light source is typically used. In this design, a 532 nm continuous-wave laser is used for illumination. The beam is reflected off a hot dichroic mirror (DC; cutoff wavelength: 560 nm) and then resized by a telescope (L_3 and L_4). Two galvanometer mirrors direct the beam and are placed perpendicularly to steer the beam along orthogonal axes. Change in the mirror angles translates to movement of the beam across the retina. After the mirrors, a Keplerian telescope (L_1 and L_2) images the mirror plane to the pupil plane of the rodent's eye, making planes conjugate and creating a stationary entrance point at the pupil plane. The cornea and lens of the eye act as an objective lens, which focuses the illumination light onto the retina.

Unlike the fundus camera, the cSLO has the advantage that it does not require geometric pupil separation of the illumination and detection light to avoid crosstalk. In fact, the cSLO's illumination and detection light paths are interchanged with those of the fundus camera. The central portion of the pupil is used for illumination, while the entire pupil is used to collect light for detection. The same Keplerian telescope both delivers and collects light from the eye. The collected light is passed through a dichroic mirror (DC), where it is focused by a lens (L_5) through a pinhole (PH). At each scan position of the gavlo-mirrors, the signal is recorded by a photodetector, such as a photomultiplier tube (PMT) or avalanche photodetector (APD, not shown in Figure 2-4), resulting in a two-dimensional image.

The field of view in angular units is determined by two parameters: the maximum scanning angle of the mirrors, θ, and the magnification of the telescope, M (48). This can be written as:

$$FOV = \theta\, M \tag{2-1}$$

This FOV, in angular units, can be approximately converted to metric units if the eyeball length is known. For example, approximate mouse eye and rat eyeball lengths are 3.3 mm and 6.4 mm, respectively (49, 50).

The lateral and axial resolution of the cSLO can be approximated by examining the point spread function (PSF) (51, 52):

$$PSF_{cSLO} = PSF_{in} \times \left(PSF_{out} \otimes PSF_{pinhole}\right) \tag{2-2}$$

PSF_{in} and PSF_{out} denote the PSFs in and out of the eye, which are determined by the cornea and lens. The $PSF_{pinhole}$ is convolved with the PSF_{out}. If the pinhole is adequately small (<0.25 airy unit), the PSF_{cSLO} approaches the square of the PSF of the eye; therefore, smaller lateral and axial resolutions can be potentially be reached. However, in cases when the pinhole is large (> 1 airy unit), its diffraction effects can be ignored, and in this scenario, the lateral and axial resolutions are approximated by:

$$FWHM_{lateral} = \frac{0.51\, \lambda_{exc}}{NA} \tag{2-3}$$

$$FWHM_{axial} = \frac{1.67\,\lambda_{exc}}{NA^2} \tag{2-4}$$

where λ_{exc} is the excitation wavelength (53, 54). The illumination numerical aperture can be calculated as:

$$NA = n\,sin\left(arctan\left(\frac{d}{2f}\right)\right) \approx \frac{nd}{2f} \tag{2-5}$$

where n is the refractive index, d is the beam diameter, and f is the focal length of the eye (55, 56). Increasing the magnification of the Keplerian telescope will result in increasing the FOV, but will also decrease d, which will in turn decrease the lateral resolution and depth of focus. Therefore, a tradeoff generally exists between FOV, lateral resolution, and depth of focus. These equations mainly serve as rough approximations, as the natural aberrations of the eye will prevent achievement of diffraction-limited resolution. Adaptive optics technology, discussed in the last section of this chapter, can help counter the eye's aberrations. A variant of fluorescence cSLO, called oblique-scanning cSLO, can overcome the tradeoffs between FOV and lateral resolution by breaking the coaxial alignment of excitation and emission detection (57, 58).

The pinhole of the cSLO reduces stray light, which results in contrast improvement. In addition, the pinhole also enables optical sectioning. When the pinhole is large, the depth discrimination is primarily determined by the emission-side diffraction pattern and the geometric optics effects of the pinhole (54). An important measure of the sectioning capability is the optical section thickness (OST), which is the full-width at half maximum (FWHM) of the detection PSF:

$$OST = \sqrt{\left(\frac{0.88 \times \lambda_{em}}{n - \sqrt{n^2 - CollectionNA^2}}\right)^2 + \left(\frac{\sqrt{2} \times n \times PH}{Collection\ NA}\right)^2} \tag{2-6}$$

As the pinhole diameter decreases, the OST decreases linearly, which improves depth discrimination.

SLO’s can be designed with different illumination light sources and collection filters, enabling high-contrast imaging of fluorescent dyes in the living eye. Common dyes used in ophthalmic research include fluorescein, indocyanine green, Rose Bengal, and acridine orange. These dyes are often administered via tail injection or intraperitoneal injection. Fluorescein (excitation peak: 494 nm, emission peak: 512 nm) is primarily used for fluorescein angiography (FA) and labeling the vasculature. In rodents, shifting of the confocal plane allows for the observation of the three distinct capillary plexi (59). In certain disease models, such as choroidal neovascularization in age-related macular degeneration (AMD), the vasculature is immature, and fluorescein leaks from the vasculature. This phenomena can also be observed with FA (55). The dye Rose Bengal (excitation peak: 560 nm, emission peak: 570 nm) is a fluorescein derivative, which generates singlet oxygen radicals upon high-intensity laser excitation. The singlet oxygen radicals activate the clotting cascade. The clotting process can be used to model retinal occlusive diseases in rodents, such as branch retinal vein occlusion (47, 60-63). Acridine orange (excitation peak: 500 nm, emission peak: 526 nm) can label the nuclear DNA of leukocytes within the bloodstream (64-66). Acridine orange fluorography can be used to assess the level of inflammatory response in models of diabetic retinopathy (DR) (67, 68).

2.5 OPTICAL COHERENCE TOMOGRAPHY

Optical coherence tomography (OCT) is one of the most successful imaging technologies of the past two decades. Introduced by Huang et al. in 1991 (69), OCT enables cross-sectional imaging of the retina. Here we will briefly review some of the fundamental concepts of OCT, before discussing more recent technologies such as OCT angiography and visible-light OCT.

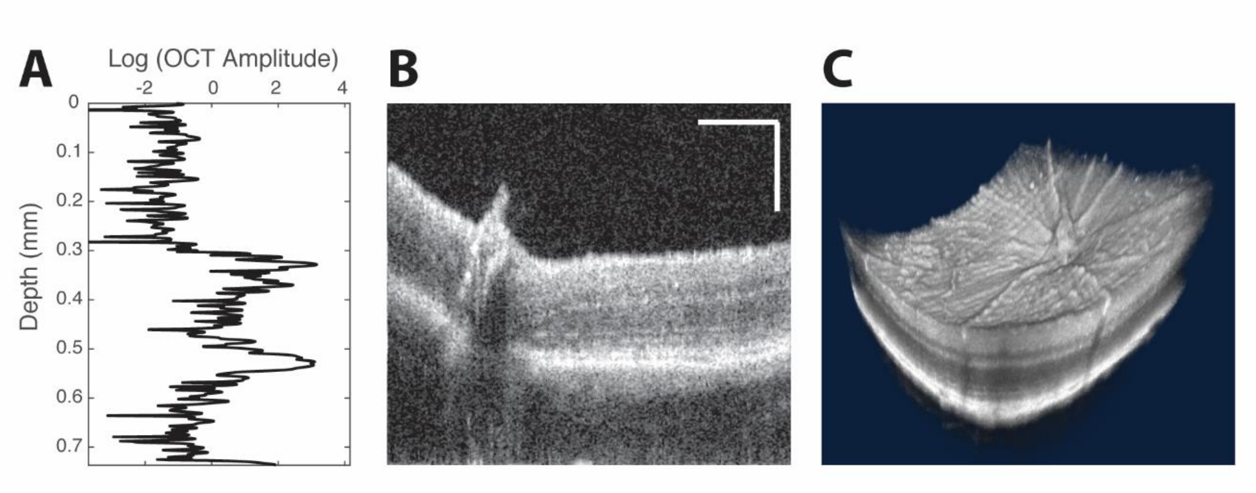

Figure 2-5 Optical coherence tomography of the wildtype C57BL/6 mouse. (A) One-dimensional OCT A-line (B) Cross-Sectional B-scan through the murine optic nerve head. Horizontal Scalebar: 500 µm. Vertical scale bar: 200 µm. (C) OCT volume rendering of the murine retina.

The objective of OCT is to recover the time-of-flight of backscattered light echoes from tissue. An OCT A-line is a one-dimensional depth-resolved OCT image (Figure 2-5(A)). By raster scanning the illumination across a sample, a set of A-lines can be acquired to form a two-dimensional cross-section, called a B-scan (Figure 2-5(B)). Multiple B-scans form a three-dimensional OCT volume data (Figure 2-5(C)). Early work with femtosecond optics and ultrahigh speed photography showed that light echoes could be timed, in exact analogy to ultrasound imaging. However, the poor scalability of these systems led to an alternative technique to measure light echoes (70).

Instead of timing echoes directly, OCT uses the temporal coherence properties of light. Temporal coherence refers to the ability of light to interfere with a time-delayed copy of itself. Delayed light beams are said to be *temporally* coherent, when their combined detection results in a high contrast constructive or destructive interference pattern. Ideally, a perfectly sinusoidal light field will have perfect temporal coherence, meaning it will always be able to interfere with a time-delayed version of itself. In reality, however, light fields fluctuate randomly in time, and therefore, interference will depend on the statistical temporal similarity of interfering light beams. One measure of the statistical temporal similarity is the coherence length. Light beams which have temporal delay within the coherence length are statistically correlated enough to interfere. Importantly, the coherence length is inversely proportional to the bandwidth of the light source, $\Delta\lambda$. Thus, a monochromatic light source, such as a HeNe laser, has a long coherence length on the order of ~1 m. However, a broad bandwidth light source, such as a white light source, has a coherence length on the order of ~1 μm.

OCT is based on the Michelson interferometer, a device which measures the temporal interference between two light beams emitted from the same source. Light from a broadband light source is directed to a 50/50 beam splitter, sending the light into two arms. One arm contains the sample, while the other contains a reference mirror. The splitter directs the back-reflected light from the sample and reference arms to a detector. The detector signal can be expressed as:

$$I(\tau) = \langle I_S(t) \rangle + \langle I_R(t) \rangle + 2Re[\Gamma_{SR}(\tau)] \qquad (2\text{-}7)$$

where $I_S(t)$ and $I_R(t)$ denote the collected light intensity (amplitude-squared of the electric field) from the sample and reference arm, respectively; $\langle \quad \rangle$ denotes time averaging; and τ denotes the time delay between the two arms. The first-order cross-correlation function $\Gamma_{SR}(\tau)$ represents the interference term and can be written as

$$\Gamma_{SR}(\tau) = \langle E_S(t) E_R^*(t+\tau) \rangle = \Gamma_{source}(\tau) \circledast h(\tau) \qquad (2\text{-}8)$$

where $E_S(t)$ and $E_R(t)$ are the sample and reference arm electric field amplitudes and the superscript * denotes the complex conjugate. $\Gamma_{source}(\tau)$ is the source coherence function, $h(\tau)$ is the reflectivity function of the sample, and $\circledast$ denotes convolution. $\Gamma_{\mathrm{SR}}(\tau)$ is the OCT A-line itself. If the difference in path length between the two arms is within the coherence length of the source, an interference signal will be observed at the detector. In other words, the short coherence length acts as a coherence gate; reflections within the coherence length are accepted and reflections outside are rejected. This forms the basis of depth-resolved imaging with OCT.

In the original OCT design, the reference mirror was moved back and forth to generate an OCT A-line, which is known as time-domain OCT (TD-OCT). TD-OCT varies τ such that $\Gamma_{\mathrm{SR}}(\tau)$ (the OCT A-line) can be reconstructed. Unfortunately, TD-OCT suffers from slow imaging speeds and low sensitivity. An alternative way to obtain the OCT A-line, termed Fourier-domain OCT (FD-OCT), measures a spectral interferogram to improve imaging speeds and increase sensitivity (71). When the Fourier transform of Eq. 7 is taken, the spectral density function is obtained (72):

$$S(\omega,\tau) = \langle S_S(\omega)\rangle + \langle S_R(\omega)\rangle + 2Re[W_{SR}(\omega)]\, cos\, 2\pi\omega\tau \qquad (2\text{-}9)$$

$\mathrm{W_{SR}}(\omega)$ is the cross spectral density given by:

$$W_{SR}(\omega) = S_{Source}(\omega)H(\omega) \qquad (2\text{-}10)$$

$\mathrm{S}(\omega,\tau)$ can be measured by using a spectrometer or a swept-source laser. Note that while $\omega \leftrightarrow t$ are a FT pair, they can also be converted to $k \leftrightarrow z$ by multiplying by the phase velocity of light c/n. Spectral domain OCT (SD-OCT) measures $\mathrm{S}(\omega,\tau)$ by incorporating a diffractive element in the detection arm. The diffracted light is then focused, and the spectrum is recorded with a line camera, consisting of an array of a small individual detectors. In this technique, $\mathrm{S}(\omega,\tau)$ is obtained in a single shot, i.e. all wavelengths are acquired simultaneously. In swept-source OCT

(SS-OCT), a swept-source laser sweeps ω over time, and a single-element photodetector in the detection arm collects $S(\omega, \tau)$. The sweep rate of the laser can be fast, resulting in MHz speeds of A-line collection. In both cases, taking the inverse Fourier transform of $S(\omega, \tau)$ allows reconstruction of $\Gamma_{SR}(\tau)$, and the reference arm is stationary during imaging.

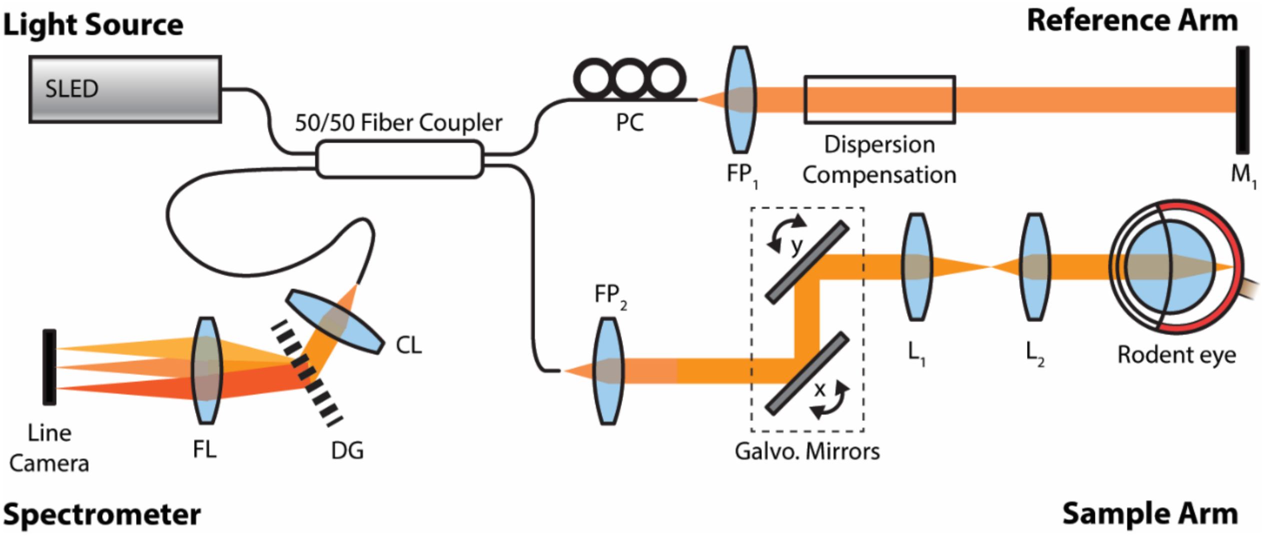

Figure 2-6 Spectral-domain OCT system. SLED: superluminescent light emitting diode. M: mirror. L: lens. PC: polarization controller. FP: fiber port. CL: collimating lens. FL: focusing lens. DG: diffraction grating.

Figure 2-6 shows an example of a near-infrared, fiber-based SD-OCT system (47). The light source in the SD-OCT system is a superluminescent light emitting diode (SLED) with a center wavelength of 840 nm and a bandwidth of 95 nm (full width at half maximum). A 50/50 fiber coupler collects the light from the SLED and splits it into the sample and reference arms. The sample arm is steered by two galvanometer mirrors in the same fashion described in the SLO section. The x-y scanning galvanometer mirrors deflect the sample arm beam, while a Keplerian telescope creates a point conjugate from the scanning mirrors to the rodent's pupil plane. The reference arm beam is back-reflected by a silver mirror (M_1). Several BK7 glass plates re used for dispersion compensation. The back-reflected sample beam recombines and interferes with the backscattered light from the sample. A custom-built spectrometer consisting of a collimating lens, transmission diffraction grating, focusing lens, and line CCD camera detects the spectral interferogram.

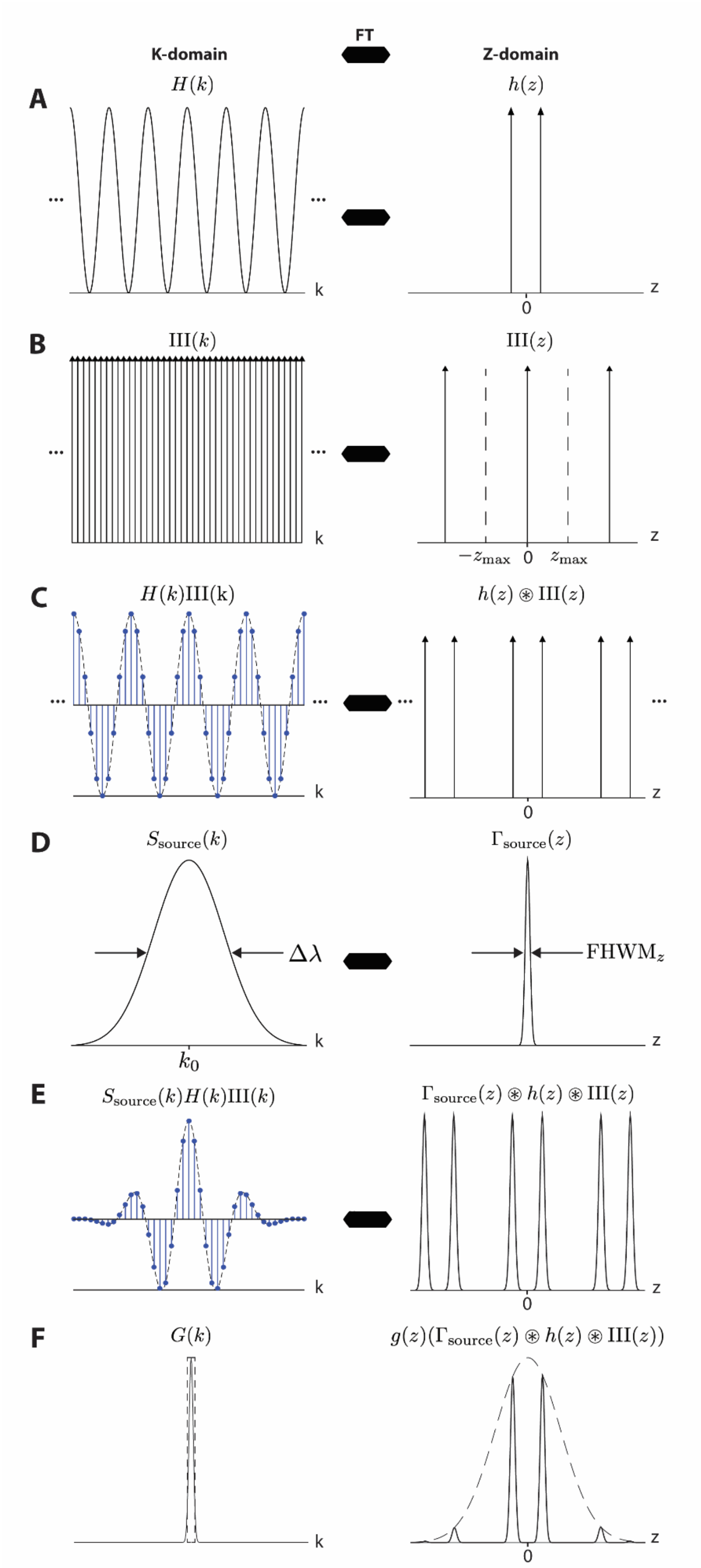
FT
K-domain
Z-domain
A
$H(k)$
$h(z)$
k
z
0
B
$\mathrm{III}(k)$
$\mathrm{III}(z)$
k
z
$-z_{\max}$
0
$z_{\max}$
C
$H(k)\mathrm{III}(\mathrm{k})$
$h(z) \circledast \mathrm{III}(z)$
k
z
0
D
$S_{\mathrm{source}}(k)$
$\Gamma_{\mathrm{source}}(z)$
$\Delta\lambda$
FHWM_z
k_0
k
z
E
$S_{\mathrm{source}}(k)H(k)\mathrm{III}(k)$
$\Gamma_{\mathrm{source}}(z) \circledast h(z) \circledast \mathrm{III}(z)$
k
z
0
F
$G(k)$
$g(z)(\Gamma_{\mathrm{source}}(z) \circledast h(z) \circledast \mathrm{III}(z))$
k
z
0

Figure 2-7 Image formation in FD-OCT. (A) Frequency encoding. (B-C) Sampling of the interferogram. (D-E) Axial resolution. (F) Sensitivity Rolloff. $\circledast$ denotes the convolution operator.

A complete mathematical framework for the image formation process of FD-OCT is beyond the scope of this chapter (73-75); however, the major principles can be grasped with knowledge of Fourier Transform (FT) theory. Figure 2-7 depicts several important concepts related to the FD-OCT image formation process.

1. **Frequency encoding (Figure 2-7(A)).** From Equation (2-9), the spectral interferogram includes a sinusoidal term, which depends on both τ and ω. In FD-OCT, a spectral interferogram is acquired as a function of ω (or k, if the coordinates are changed from optical frequency to wavenumber). Figure 2-7(A) depicts the sinusoidal interferogram in k-space. Taking the FT of the sinusoid gives the sample reflectivity function: two delta functions positioned a distance away from zero. The frequency of the interferogram with respect to k, which depends on the depth of the sample, determines the position of the delta functions away from the zero-depth position. In other words, the k-frequency of the spectral interferogram encodes z, the depth information. Usually the amplitude and the frequency of the interferogram is recorded but not its absolute phase, leading to FT being symmetric around the zero-depth position (Hermitian symmetry).
2. **Sampling interval in k-space determines the maximum imaging depth (Figure 2-7(B-C)).** Although the spectral interferogram is ideally continuous, in practice, it is sampled in k-space. In SD-OCT, the individual pixels of the spectrometer's line camera sample the spatially distributed spectral interferogram. In SS-OCT, the evenly spaced wavenumbers are recorded and act as the sampling function. The sampling process is modeled by multiplying the spectral interferogram with a Dirac comb function, $III(k)$ (76), shown in Figure 2-7(B). Because of the finite sampling,

aliasing occurs in the z-domain. The sampling step size in k-space, δk, determines the Nyquist limit for in z-space. The maximum imaging depth corresponds to half of the Nyquist value:

$$z_{max} = \frac{\pi}{2\delta k} \tag{2-11}$$

Aliasing also means that images are repeated in z-space, as shown in Figure 2-7(C).

3. **Coherence length of the light source primarily determines the axial resolution Figure 2-7(D-E)).**

   In OCT, the bandwidth of the low-coherence light source is the dominant factor that determines the axial resolution. The spectral interferogram is modulated by the power spectral density of the light source, which is depicted as a Gaussian density function in Figure 2-7(D). The full width at half maximum (FWHM) in z-space is typically assumed as the axial resolution, which is given by the following equation.

   $$FWHM_z = \frac{2ln2}{\pi n}\frac{\lambda_0^2}{\Delta\lambda} \tag{2-12}$$

   Where λ_0 is the center wavelength of the light source, $\Delta\lambda$ is the FWHM of the light source power spectrum, and n is the refractive index of the sample. Figure 2-7(E) shows the sampled spectral interferogram, modulated by the Gaussian power spectral density, and its respective Fourier transform.

4. **Sensitivity Roll-off is determined by the spectral resolution (Figure 2-7(F)).** In FD-OCT, portions of the cross spectral density are integrated in k-space. In spectrometer-based systems, this is due to the square or rectangular pixel shape. In addition, the spectrometer has a limited spectral resolution due to the optical aberrations of the internal lens elements (76). In most cases, the size of the PSF on the line-camera is larger than the individual pixel dimensions. In swept-source

systems, the instantaneous linewidth of the source determines the range of k integrated at each wavelength. In either scenario, this results in the cross spectral density being convolved with an integration function, $G(k)$. In z-space, this leads to multiplication with a sensitivity roll-off function $g(z)$. $g(z)$ usually has both sinc and Gaussian behavior. Therefore, OCT signals further from the zero delay have lower OCT amplitude than those closer to the zero delay.

2.5.1 OCT angiography

OCT angiography (OCTA) extends OCT imaging by providing label-free, high-contrast three-dimensional imaging of the retinal vasculature (13, 77). The arrival of FD-OCT led to increases in OCT imaging speed, which made OCTA possible. In 2006, Makita et al. demonstrated volumetric OCTA by utilizing the Doppler phase shift (78). Since then, multiple algorithms have been studied and developed to perform OCTA. The algorithms can be generally divided based on the components of the OCT signal that are used, which include changes in Doppler shift, OCT amplitude, OCT phase, or a combination thereof (13, 79). Spectral, temporal, or depth-dependent filtering is often incorporated to reduce dependence of the OCTA signal on subject motion. For example, the split-spectrum amplitude decorrelation algorithm (SSADA) uses spectral splitting to generate multiple OCT volumes with reduced axial resolution, and the average of those volumes is calculated (80). By reducing the axial resolution, subject motion has less impact on the SSADA signal and image contrast may be improved (81). In comparison, the optical microangiography algorithm (OMAG) uses the full complex OCT signal, instead of just the amplitude alone, and B-scans are averaged temporally (82).

Regardless of the algorithm used, a common acquisition protocol exists between OCTA techniques. As depicted in Figure 2-8(A), OCTA uses repeated B-scans co-localized on the retina.

The raster scanning pattern of OCT (solid lines) and OCTA (dashed lines) are drawn at low density for illustration. The number of B-scans can vary between techniques, but at least two are needed to achieve OCTA contrast. In this illustration, five OCT B-scans were repeated at the same location as depicted by the array of B-scans over time in Figure 2-8(B). In ultra-fast OCT systems where the A-line acquisition rate exceeds MHz speeds, OCT volumes can also be repeated at the same location to achieve angiography contrast (83). By applying an OCTA algorithm to these B-scans, OCT signal changes due to blood cell movement can be highlighted, while eliminating signals from static tissue (Figure 2-8(C)). The final 3-D OCTA volume can be displayed as a depth colored *en face* OCTA, as shown in Figure 2-8(D).

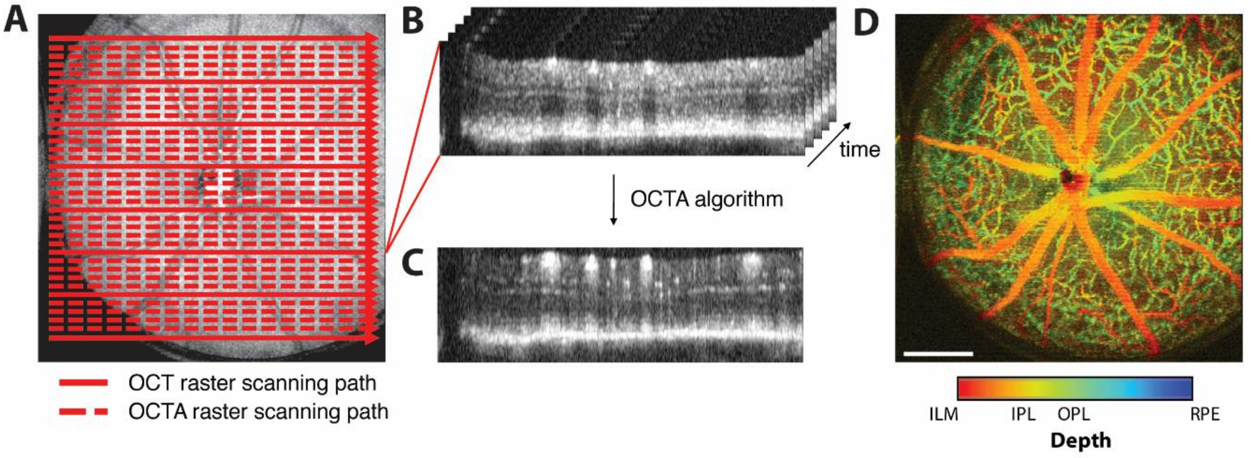

Figure 2-8: OCTA scanning protocol and image formation. (A) *En face* OCT of a mouse retinal fundus. OCT and OCTA raster scanning paths are depicted by the solid and dashed arrows, respectively. (B) OCT B-scans acquired from the OCTA raster scanning path. (C) After processing by an OCTA algorithm, an OCTA B-scan is created. (D) Depth-colored *en face* OCTA. Scale bar: 500 μm.

Here we describe a complex OCT, difference-based algorithm, which utilizes spectral-splitting and time averaging (84). The collected OCT spectral interferogram for each A-line undergoes the typical OCT signal processing steps, including removal of the DC component, interpolation from lambda to k-space, and numerical dispersion compensation. The OCT signal is then spectrally split into several sub-bands, using a short-time Fourier transform (STFT):

$$A(x,z,t,k_c) = STFT\big(S(k), w_k(k_c, \delta k)\big) \tag{2-13}$$

where $S(k)$ is the full spectral interferogram; w_k is the window function; and $k_c, \delta k$ are the center wavenumber and the bandwidth of the window function, respectively. Gaussian functions were used as the window function in this algorithm.

To compensate for axial motion between the consecutive B-scans, axial global phase fluctuations (AGPF) were computed by finding the peak position of the 2D cross-correlation between the first B-scan at time t_1 and a subsequent co-localized B-scan at time t_n:

$$AGPF(z,k_c) = -\underset{z}{argmax} \int A(x,z,t_1,k_c)A^*(x,z,t_n,k_c)dz \tag{2-14}$$

The AGPFs were then compensated for by multiplying the A-line signal with an exponential phase term.

$$A'(x,z,t,k_c) = A(x,z,t,k_c)\, exp[iAGPF(z,k_c)] \tag{2-15}$$

To compute the angiogram AG, the amplitude of the complex difference, between the first and consecutive B-scans, is averaged over time. In addition, averaging is also performed across the split sub-bands.

$$AG(x,z) = \frac{1}{N-1}\frac{1}{C}\sum_{c=1}^{C}\sum_{n=2}^{N}|A'(x,z,t_n,k_c) - A(x,z,t_1,k_c)| \tag{2-16}$$

N is the total number of B-scans, and n is the B-scan number. C is the total number of spectral sub-bands used.

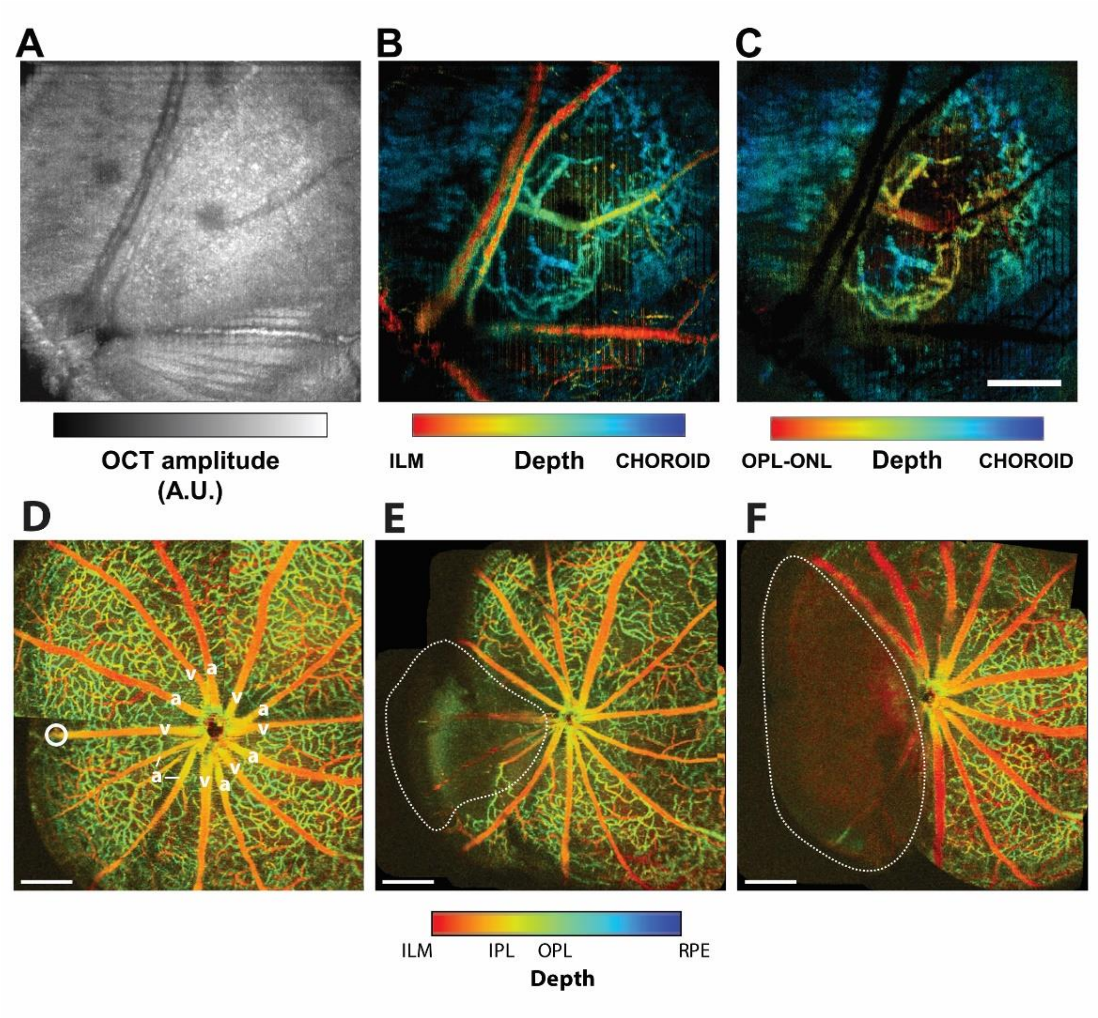

Figure 2-9: OCTA in animal models of age-related macular degeneration and retinal vein occlusion. (A) En face vis-OCT of the area encompassing a CNV lesion. The CNV lesion is not visible on standard OCT. Arbitrary Units (A.U). (B) En face vis-OCTA of the same area, revealing the CNV lesion. Image color-coded by depth. (C) Final postprocessed outer retina en face angiogram, color-coded by depth. Scale bar: 200 µm (D) Montage of 9 OCTA images before vein occlusion. a and v denote arteries and veins respectively. White circle denotes the targeted site of occlusion on the 9 o' clock vein. (D) Montage after vein occlusion. (E) Montage on day 1 after the vein occlusion. White dotted regions in B and C denote areas of capillary non-perfusion. Scale bars: 500 µm. Adapted from refs. (47, 85).

Figure 2-9 shows some of the applications of this OCTA algorithm towards studying rodent models of retinal disease. Choroidal neovascularization (CNV) is a hallmark of wet age-related macular degeneration. Abnormal vessels from the choroid grow into the retina from beneath the

RPE layer. To investigate CNV in rodents, a laser-induced model has been described (86, 87). In this study, a visible-light OCT system was used. Figure 2-9(A) shows the en face projection of the OCT volume near the CNV lesion. OCTA of the same area shows abnormal vasculature (green) above the choroid (blue) (Figure 2-9(B)). By removing the inner retinal vasculature (red) from the OCTA volume, the CNV lesion can be separated for further analysis Figure 2-9(C). OCTA can also be integrated with fluorescein angiography to compare the differences between the two techniques when studying this animal model. OCTA and FA matched well; however, OCTA cannot assess dye leakage from the vasculature (55).

Branch retinal vein occlusions (BRVO) is an ischemic disease of the retina, which results from decreased blood flow in one or more major retinal veins. Figure 2-9(D-F) show OCTAs of a BRVO model created by imaging-guided photocoagulation (47). Figure 2-9(D) shows an *en face* OCTA of the vasculature before occlusion. The major arteries and veins are labeled as an *a* and *v*, respectively. The vein branch indicated by the white circle was occluded. The OCTA after occlusion (Figure 2-9(E)) shows capillary non-perfusion in the area (white dashed area) surrounding the occlusion site. This area increased on day 1 as detected by the OCTA shown in Figure 2-9(F).

2.5.2 Visible-light OCT

2.5.2.1 Retinal oximetry

Visible-light OCT (vis-OCT) is a functional extension of OCT technology, where a light source with a visible spectrum is used instead of near-infrared (NIR). By using shorter wavelengths, vis-OCT typically provides a higher axial resolution than most near-infrared counterparts (88). Additionally, visible-light spectroscopic OCT can be used to measure oxygenation within the retinal vasculature (89). Many retinal diseases involve disorders in oxygenation, and vis-OCT is especially attractive for providing quantitative measurements of oxygen metabolism. One major goal of vis-OCT is to quantify the amount of hypoxia using a combination of spectroscopic imaging and Doppler OCT. In this section, we will describe the process of extracting the oxygen saturation of hemoglobin (sO_2) from within blood, using vis-OCT. In addition, we will discuss combining these measurements with Doppler OCT to derive the metabolic rate of oxygen in the retinal circulation.

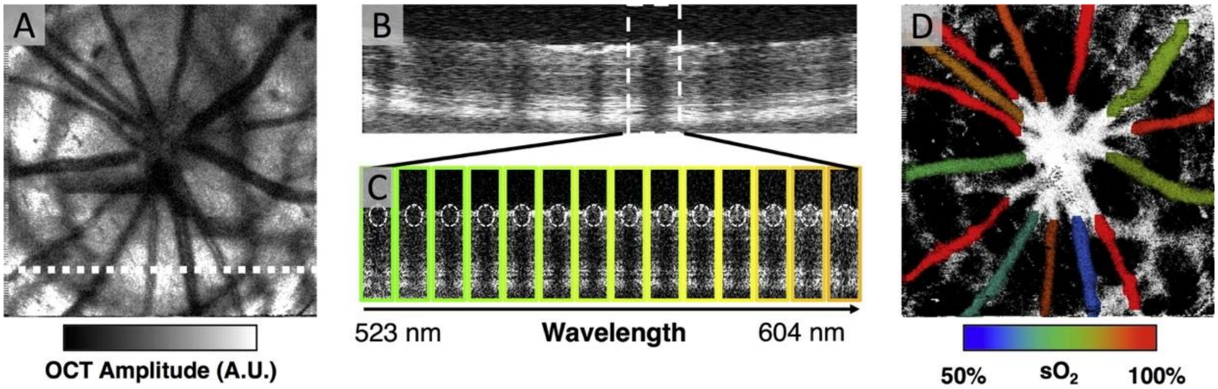

Figure 2-10: Retinal oximetry with vis-OCT. (A) En face OCT of a rat retinal fundus. (B) OCT B-scan at the location of the white dashed line in (A). (C) Short-time Fourier Transforms split the OCT image into 14 spectral bands, which are used for sO2 fitting. (D) sO2 measurements in the major retinal arteries and veins. Adapted from ref. (90).

Figure 2-10 depicts the process of retinal oximetry with vis-OCT. A 3-D vis-OCT image of a healthy rat fundus was acquired and reconstructed (Figure 2-10(A)). The supercontinuum light source spectrum was centered at 585 nm and had a bandwidth of 85 nm (SuperK, NKT Photonics). Further details of this system can be found in previous studies (91). The full-spectrum vis-OCT B-scan in Figure 2-10(B), corresponding to the white dashed line on Figure 2-10(A), shows several blood vessel cross-sections. For each A-line within every vessel, the spectral interferogram was split into 14 Gaussian bands with the STFT. The bandwidth of each band was ~0.32 μm^{-1} (FWHM) corresponding to an axial resolution of ~8.9 μm in air. Figure 2-10(C) shows the split-spectrum images for a selected vessel in the white dashed box of Figure 2-10(B). For each of the wavelength bands, the OCT signal intensity, $I(\lambda)$, at the bottom of each of the circles labeled in Figure 2-10(C), was measured.

The Beer-Lambert law was used to model light attenuation after passing through the blood vessel. The model can be written as:

$$I(\lambda) = I_0 R_0 r\, exp\left(-2nd\left(\mu_{HbO_2}(\lambda) sO_2 + \mu_{Hb}(\lambda)(1 - sO_2)\right)\right) \tag{2-17}$$

where I_0 is the incident light intensity; R_0 is the reference arm reflectance; r is the reflectivity of the vessel wall; n is the refractive index; d is the thickness of the blood vessel; μ_{HbO_2} and μ_{Hb} are the attenuation coefficients of oxygenated and deoxygenated hemoglobin, respectively (92). The factor of 2 in the exponential is due to round-trip attenuation. The reflectance of the vessel wall can be modeled as a power law with a first-order Born approximation, as $r(\lambda) = A\lambda^{-\alpha}$.

Taking the logarithm of Eq. 17 converts it into a linear equation.

$$ln\left(\frac{I(\lambda)}{I_0(\lambda)}\right) = -2nd\left(sO_2 \mu_{HbO_2}(\lambda) + (1 - sO_2)\mu_{Hb}(\lambda)\right) - \alpha\, ln(\lambda) + ln\, AR_0 \tag{2-18}$$

With the measured $I(\lambda)$, at the bottom of the vessel wall, and experimental values of μ_{HbO_2} and μ_{Hb} spectra (93), a least-squares fitting can be performed to derive sO_2. Figure 2-10(D) shows the measured sO_2 for the major retinal arteries and veins color-coded on the *en face* OCT.

2.5.2.2 Doppler vis-OCT

In addition to retinal oximetry, vis-OCT can also measure the volumetric blood flow rate, using established Doppler OCT methods (94, 95). To measure the volumetric blood flow rate (in μL/min), the blood vessel diameter (in μm) and blood flow velocity (in mm/s) must be measured. The vessel diameter can be measured by calculating the distance between the vessel walls on OCT B-scans, while the blood flow velocity is measured analyzing the phase of the OCT signal. When the time difference between successive OCT A-lines is small, blood flow imparts a linear phase shift on the OCT signal (96). This phase difference between two successive A-lines can be calculated from the phase of the complex OCT signal after FT of the real-valued spectral interferogram. The phase difference gives information about sub-resolution offsets within the coherence gate (97). The phase offset between two temporally delayed A-scans can be expressed as:

$$\Delta\phi' = \tan^{-1}\left(\frac{\mathrm{Im}(\mathrm{I}_{t_2})}{\mathrm{Re}(\mathrm{I}_{t_2})}\right) - \tan^{-1}\left(\frac{\mathrm{Im}(\mathrm{I}_{t_1})}{\mathrm{Re}(\mathrm{I}_{t_1})}\right) \tag{2-19}$$

Where t_1 and t_2 are the time points separated by $\Delta T = t_2 - t_1$. In many situations, averaging of $\Delta\phi'$ is performed to improve the signal to noise ratio; however, because phase is extracted from the complex OCT signal, averaging should be performed in the complex plane. The phase difference average is then:

$$\Delta\phi = tan^{-1}\left(\frac{Im(\sum_{m=1}^{M} exp(i\Delta\phi_m'))}{Re(\sum_{m=1}^{M} exp(i\Delta\phi_m'))}\right) \tag{2-20}$$

where M is the total number of measurements used for averaging. Averaging phase differences without complex plane statistics may underestimate the true phase difference and, thereby, the blood flow velocity (98).

Animal movement is inevitable for *in vivo* flow measurements. Movement along the direction of the probing beam imparts a bulk phase shift, $\Delta\phi_{bulk}$, on top of the phase shift from blood flow, $\Delta\phi_{flow}$. Therefore, the total measured phase difference is:

$$\Delta\phi = \Delta\phi_{bulk} + \Delta\phi_{flow} \tag{2-21}$$

The bulk phase shift can be determined by trying to estimate the phase difference for the tissue outside the blood vessel**.** For example, average-shifted histograms to determine the mode of the phase shifts in a given A-line (78). After determining $\Delta\phi_{bulk}$, it can be subtracted from $\Delta\phi$ to obtain $\Delta\phi_{flow}$. $\Delta\phi_{flow}$ is then proportional to the flow speed (99).

Since $\Delta\phi$ is only sensitive to motion along the direction parallel to the sample beam, the measured velocity must be corrected for the Doppler angle, θ: the angle between the probing beam and the blood vessel direction. The dual-circle Doppler OCT is one of the ways to obtain the Doppler angle and calculate the actual volumetric flow rate (94, 95). In the dual-circle method, two circular scans of different diameters are acquired around the optic nerve head. In the original method, the coordinates of the blood vessel in the two circular scans are used to compute θ. However, this method relies on prior knowledge of the eyeball's axial length, which is unknown and varies between subjects. Liu et al. proposed an alternative calculation of θ from dual-circle scans, which is independent of the eyeball's axial length. The calculated phase differences for a vessel from the two circular scans are used to compute θ (100). Once θ is determined, the blood flow speed can be calculated with $\Delta\phi_{flow}$ using:

$$v = \frac{f_s \lambda_0 \Delta\phi_{flow}}{4\pi n \cos\theta} = v_{max} \frac{\Delta\phi_{flow}}{\pi} \tag{2-22}$$

where f_s is the A-line scanning frequency; λ_0 is the center wavelength of the light source; and n is the refractive index of the sample (94). Note that $\Delta\phi_{flow}$ is limited to values between $[-\pi, \pi]$, and the maximum speed, v_{max}, is $v_{max} = \frac{f_s \lambda_0}{4n\cos\theta}$. To obtain velocity values greater than v_{max}, $\Delta\phi_{flow}$ must be phase-unwrapped to extend its range to $[-2\pi, 2\pi]$ (101).

Figure 2-11 shows flow measurements with dual-circle Doppler vis-OCT. Figure 2-11(A) shows an *en face* vis-OCT image of a healthy rat retina (100). The white dashed circles illustrate the paths of the inner and outer circular scans. Each circular scan must have high scanning density, such that the scanning step size is smaller than the beam diameter on the retina. The high scanning density maintains the assumption that adjacent A-lines are acquired at the same location. In this example, the 4096 A-lines per circular scan were collected. Figure 2-11(B) shows the average phase difference B-scan, from the inner circular scan, after bulk-motion correction. The red and blue arrows indicate an artery and vein, respectively. The phase-differences were averaged over multiple points in the cardiac cycle. Figure 2-11(C) shows the average phase value with each cumulative circular B-scan for the phase measurements from the small and large circular scans. Figure 2-11(D) shows the measured Doppler angles for each of the ten blood vessels. Figure 2-11(E) shows the recorded electrocardiogram, which was compared to pulsatile velocity profiles measured by phase-resolved vis-OCT and shown in Figure 2-11(F-G). The vis-OCT pulsatile profiles correlate well with the cardiac cycle measured by the electrocardiogram. To estimate blood flow from velocity, the velocity was multiplied by the cross-sectional area of the vessel, with the assumption that the flow was parabolic. The cross-sectional area was approximated as a circle, where the diameter was measured from the OCT B-scan. Figure 2-11(H) shows the repeatability of flow measurements over several days of imaging.

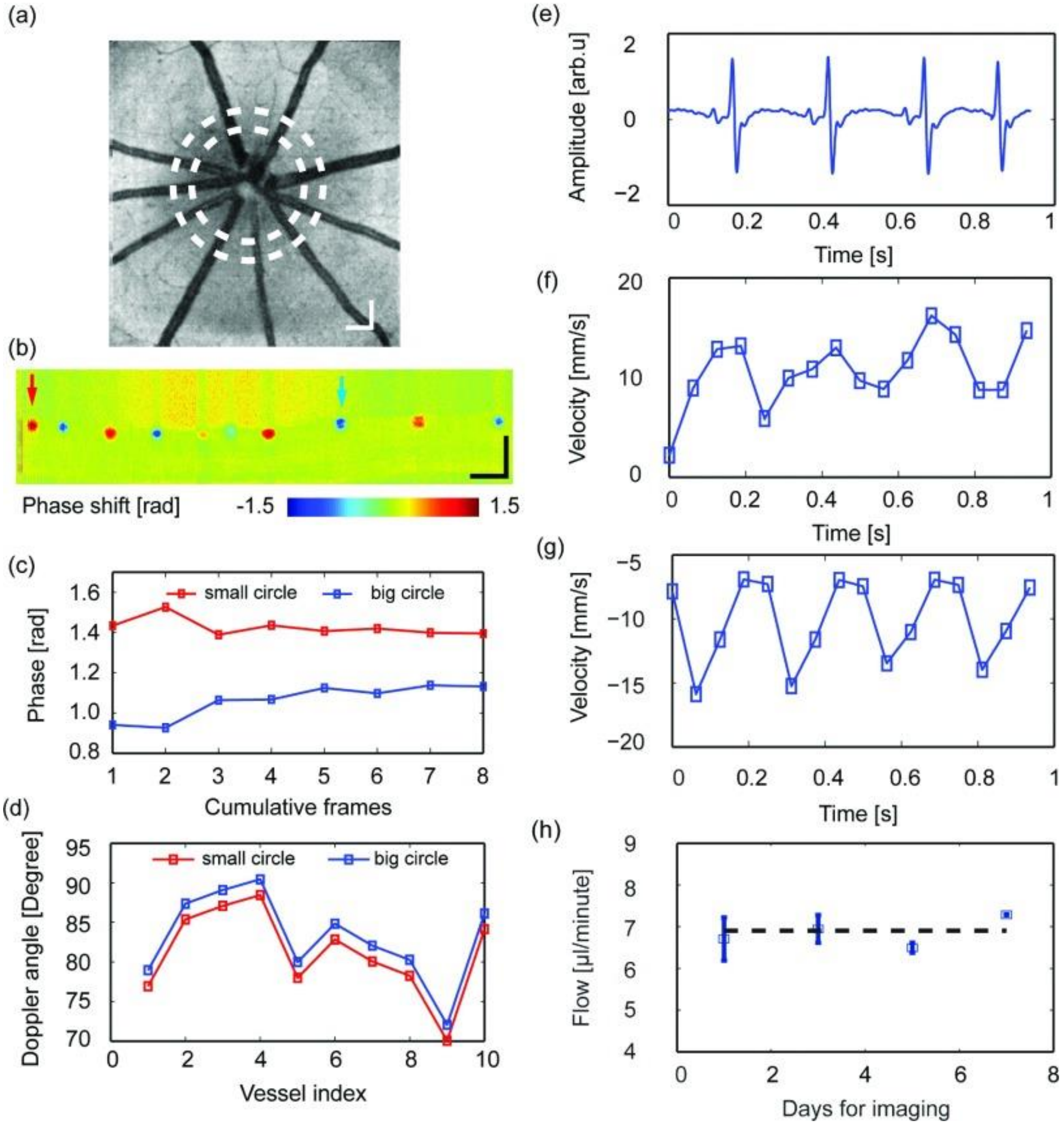

Figure 2-11 Doppler vis-OCT for retinal blood flow measurements in rat. (A) En face vis-OCT of the rat eye. The two dashed circles indicate where the dual-ring scans were performed. (B) The phase image from the inner-circle scan. (C) Phase stability across a different number of cumulative frames for a sample vessel, indicated by the left arrow in panel (b). (D) Estimated Doppler angles for all the vessels from both small and large scanning locations. (E) Recorded rat electrocardiogram during imaging. (F) Measured pulsatile flow from one retinal artery, highlighted by the left arrow in panel (B). (G) Measured pulsatile flow from one retinal vein, highlighted by the right arrow in panel (B). (H) Repeatability of flow imaging for the same rodent subject over seven days. Scale bar: 200 µm. Adapted from ref. (100).

2.5.2.3 Calculating the inner retinal metabolic rate of oxygen

The inner retinal metabolic rate of oxygen (irMRO$_2$) and delivery rate of oxygen (irDO$_2$) are two functional markers, which provide absolute measurements of oxygen consumption and oxygen delivery in the inner retina, respectively. According to the Fick principle, which is based on mass balance, the irMRO$_2$ is equal to the product of the arterial-venous sO$_2$ difference and the volumetric blood flow rate. irMRO$_2$ measurements assume that the difference in oxygen mass, between the arterial and venous circulations, is the oxygen consumed by the tissue. Although this is true in normal tissue circulations, the retina has contributions from both the retinal and choroidal circulation. Because choroidal circulation is difficult to assess, the true metabolic rate of the entire retina is difficult to measure *in vivo*. Nevertheless, the irMRO$_2$ can still provide useful information about retinal function

The inner retinal oxygen delivery, irDO$_2$, in nl min^{-1} can be expressed as:

$$irDO_2 = \varepsilon \times C_{Hb} \times F_{Total} \times \overline{s_a O_2} \tag{2-23}$$

Here ε is the oxygen binding capacity of hemoglobin (1.36 ml O$_2$/g of Hb) (102); C_{Hb} is the total hemoglobin concentration (150 g of Hb/L of blood); and $\overline{s_a O_2}$ is the average arterial oxygenation. F$_{\text{Total}}$ (in ml/min) is the total blood flow entering and leaving the inner retinal circulation, measured with Doppler OCT. If blood flow is measured for all the blood vessels entering and leaving the ONH, the total flow rate can be calculated as the sum of flow rates from all the vessels. However, in practice, measurements may be incomplete. In this situation, the total blood flow can be approximated by using an average value for the arterial and venous blood flows:

$$F_{Total} = \frac{N}{2} \frac{(\overline{F_a} + \overline{F_v})}{2} \tag{2-24}$$

$\overline{F_a}$ and $\overline{F_v}$ are the average arterial and venous measured blood flows, respectively, and N indicates the total number of vessels. The irMRO$_2$ can be calculated with an equation similar to Equation (23):

$$irMRO_2 = \varepsilon \times C_{Hb} \times F_{Total} \times (\overline{s_aO_2} - \overline{s_vO_2}) \qquad (2\text{-}25)$$

Where $\overline{s_aO_2}$ and $\overline{s_vO_2}$ are the average arterial and venous sO$_2$ percentage values, respectively

Another measure of oxygen consumption is the oxygen extraction fraction (OEF):

$$OEF = \frac{\overline{s_aO_2} - \overline{s_vO_2}}{\overline{s_aO_2}} \qquad (2\text{-}26)$$

The OEF is a *relative* marker of oxygen consumption by the retina because it does not include a blood flow term. Therefore, OEF can be difficult to interpret in circumstances, when blood flow is also changing. Nevertheless, it is a commonly used measurement in metabolic imaging.

2.5.2.4 Validation of metabolic imaging with vis-OCT

The gold-standard for oxygenation measurements in the retina is electrode-based oxygen measurements. However, these measurements are difficult to perform experimentally, and a study comparing vis-OCT to this gold-standard has not yet been performed. However, the accuracy of vis-OCT for retinal oximetry has been studied *in silico*, *in vitro*, and *in vivo* studies.

1. ***In silico* verification:** Chen et al. modeled visible light propagation through a retinal blood vessel using Monte-Carlo simulations. The parameters used to simulate the vis-OCT measurements matched the current state-of-art systems. The major finding was that OCT in the visible range can accurately quantify retinal oxygenation, while near-infrared OCT failed to do so in practice due to scattering dominating absorption (103).

2. ***In vitro* verification:** Yi et al. and Chen et al. have used vis-OCT to quantify the sO_2 of bovine blood at different oxygen saturations values in capillary tubes. Measurements agreed well with those from a blood-gas analyzer (7, 91).
3. ***In vivo* verification**: Pulse oximetry measurements from the peripheral arteries in rats have also been compared with vis-OCT sO_2 readings (7, 91). The level of inhaled oxygen was modulated to change the arterial oxygenation. Vis-OCT measured sO_2 from the retinal arteries correlated well with measurements made from the peripheral arteries.

Animal studies with vis-OCT

Vis-OCT has been used to study diabetic retinopathy (DR) in animal models. With respect to early stage diabetes, vis-OCT has been used to quantify the $irMRO_2$ in the $Akita^+/TSP^{-/-}$ mouse. The $Akita^+$ mouse develops Type 1 diabetes and early signs of mild diabetic retinopathy (104). Liu et al. found that the inner retinal metabolic rate increased from weeks 6 to week 13, while microvascular pericyte numbers did not change (105). This suggested that functional measurements with vis-OCT could provide an early biomarker of DR before major vascular changes are detectable.

Vis-OCT has also been used to study an animal model of late stage DR. The oxygen-induced retinopathy (OIR) model in rats was originally developed as a model of retinopathy of prematurity, but has also been partially accepted as a model of late stage DR due to the findings of retinal avascularity and proliferative neovascularization. Soetikno et al. used vis-OCT to measure $irMRO_2$ on postnatal day 18 (106). The $irDO_2$ and $irMRO_2$ were significantly decreased in rats with OIR compared to healthy controls, which correlated with decreased retinal thickness in the OIR rats compared to controls. It is hypothesized that the decrease in retinal thickness may contribute to the observed decreased in retinal metabolic demand.

2.6 PHOTOACOUSTIC OPHTHALMOSCOPY

Photoacoustic ophthalmoscopy (PAOM) relies on the photoacoustic effect to produce 3-D images of optical absorbers in the eye (107-109). PAOM is based upon photoacoustic microscopy (PAM) (110-113), with the objective lens replaced by the natural refractive surfaces of the eye. In PAM, nanosecond-range, pulsed light illuminates the sample. When the pulses reach an absorber, such as hemoglobin within a blood vessel, a temporary temperature rise is generated (114). Part of that energy is converted into mechanical energy, which manifests as spherical, broadband ultrasonic waves, known as photoacoustic waves. The photoacoustic waves are detected by placing an ultrasonic needle transducer on the surface of the eye (Figure 2-12(A)). The time-gated arrival of the waves gives the depth information of the absorber. The axial resolution of the PAOM is primarily determined by the bandwidth of the ultrasonic detector; the larger the detection bandwidth, the higher the axial resolution. Scanning the illumination beam allows for volumetric imaging.

Unlike OCT which is sensitive to optical scattering and absorption, PAOM is primarily sensitive to optical absorption, as the initial pressure rise is directly proportional to the absorption coefficient of the absorber. In the eye, optical absorbers include hemoglobin in blood vessels and melanin in RPE cells. Hemoglobin imaging allows for visualization of vasculature, and applications include imaging of the retinal fundus vessels, corneal neovascularization, as well as vessels of the iris (109, 115, 116). With multi-wavelength PAOM, absorption spectroscopy of hemoglobin can be performed, and the sO_2 of major retinal blood vessels can be calculated (113, 115). When combined with Doppler OCT for blood flow, PAOM can be used to measure the $irMRO_2$ (115). Melanin imaging with PAOM may provide a non-invasive screening tool to evaluate the health of the RPE, which has been implicated in several retinal diseases including AMD (117, 118).

Figure 2-12(B) shows an example PAOM image, acquired from an adult Sprague-Dawley rat The light source was a tunable dye laser, pumped by a pulsed laser, at wavelengths of 578 nm, 580 nm, and 588 nm. The lateral and axial resolutions were 20 μm and 23 μm, respectively. The ultrasonic bandwidth was 30 MHz (108, 115). By fitting the photoacoustic signals to the oxygenated and deoxygenated hemoglobin absorption values at 578 nm, 580 nm, and 588 nm, the sO_2 was calculated for each vessel. Figure 2-12(C) shows the sO_2 measurements for the vessels labeled in Figure 2-12(B).

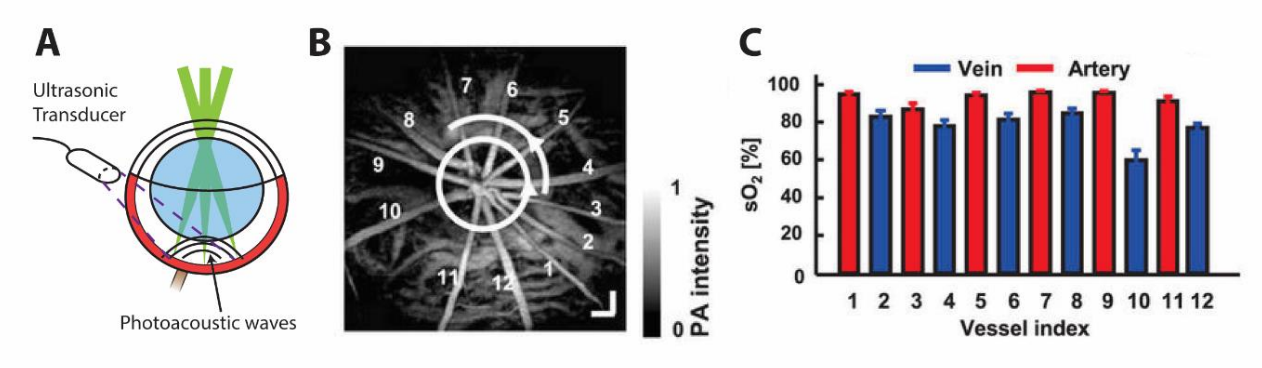

Figure 2-12 Photoacoustic ophthalmoscope (PAOM). (A) The basic schematic of PAOM showing the incoming laser beam scanned across the retina as well as the resulting photoacoustic waves and ultrasonic transducer. (B) An example image of the rat retina taken by PAOM. (C) Oxygen saturation values calculated from the image in (b). Adapted from ref. (115) .

PAOM is uniquely sensitive to optical absorption. However, current systems possess relatively low axial resolution, especially when compared with OCT. High bandwidth detectors using microring resonators have been demonstrated, which can provide higher axial resolution (119, 120). Unfortunately, PAOM requires direct-contact onto the surface of the eye, which can be cumbersome when working with the sensitive tissues of the eye. PAOM has not yet demonstrated the capability of measuring blood flow, and therefore, PAOM must be coupled with OCT or ultrasound to measure the metabolic rate (107, 115, 121, 122).

2.7 ADAPTIVE OPTICS

Adaptive optics (AO) improves the lateral resolution of scanning-based ophthalmic imaging technologies by correcting for the natural aberrations of the eye. Irregularities in the lens and cornea cause high-order aberrations, which distort the regular structure of laser beam wavefronts entering the eye. Ultimately, this distortion of the normal diffraction pattern of the near Gaussian beam leads to a larger and distorted spot shape on the retina and even larger aberrations at the signal collection. These aberrations prevent retinal imaging devices from reaching the diffraction limit performance and reduce overall SNR and quality of the images (123). For example, the diffraction-limited lateral resolution of an OCT system with center wavelength 840 nm in a fully dilated mouse eye with NA~0.5 is ~0.6 μm, but the actual lateral resolution without aberration correction is ~15 μm. To correct for the eye's aberrations, AO systems use technology originally developed by astronomers to image objects in space, such as stars and planets, where the real image of the object is corrupted after passing through the earth's scattering atmosphere.

To apply AO correction, a sensor must first measure the wavefront aberrations introduced by the eye. Then, a deformable mirror pre-distorts the wavefront to compensate for the aberrations of the eye. Predistortion of the wavefront of the illumination light allows achievement of a regular, focused Gaussian beam wavefront at the retina. Ultimately, near diffraction-limited performance of the imaging system can be obtained in an arbitrary eye.

The Shack-Hartmann Wavefront Sensor (SHWS) is the most commonly used wavefront sensor in AO retinal imaging (124). The diagram in Figure 2-13(A) depicts the principle of the

SHWS. A collimated light source is reflected by a beam splitter and then focused by the anterior eye's refractive system to a point on the retina. The wavefront of reflected light out of the eye is distorted by the eye's natural aberrations. The distorted wavefront passes through the beam splitter and onto a lenslet array, composes of hundreds of lenses. These lenslets focus the light onto a 2D detector, which creates a spot diagram. Without aberrations, the spot diagram is evenly spaced, bright, and in focus. With aberrations, the points will be off-centered and blurred. The spot diagram is used to calculate an approximation of the wavefront.

Once the aberrations are sensed, pre-distortions can be introduced to the illumination of the eye by a deformable mirror. The deformable mirror is composed of many small mirrors, which can be individually and electronically controlled. The distortion of the illumination is equal to – but has opposite wavefront to – the sensed aberrations. With this technique, near diffraction-limited resolution can be achieved.

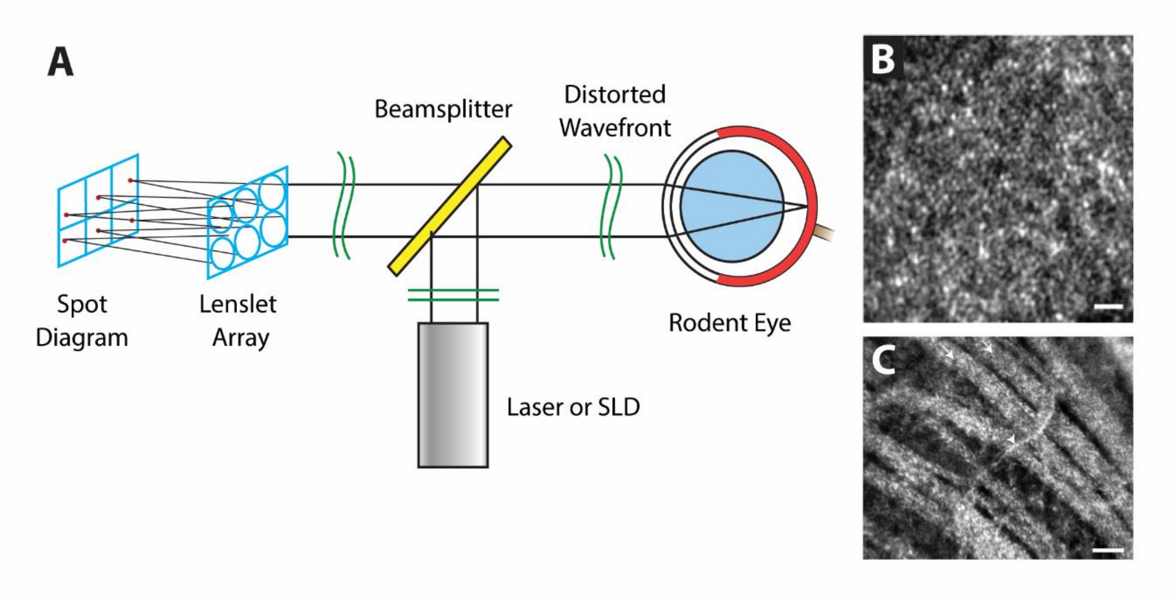

Figure 2-13 Shack-Hartmann Wavefront Sensor (SHWS). (A) The basic schematic of a Shack-Hartmann Wavefront Sensor. Light from a laser or superluminescent diode is reflected at a beamsplitter and focused onto the back of the eye. The returning distorted

wavefront with information about the back of the eye is transmitted through the beamsplitter and passes through an array of small lenses that focus the light onto a spot diagram. This spot diagram is used to shape the deformable mirror of the AO system so that the distorted wavefront is matched in an exactly opposite way to the distortion to compensate for those imperfections in the lens and cornea of the eye. (B) Images of the photoreceptors and (C) nerve fiber layer taken from an AOSLO system. Reprinted with permission from Ref. (4).

AO techniques can be combined with ophthalmic imaging systems to improve lateral resolution, including fundus, SLO, and OCT imaging (124, 125). AO enhanced imaging devices have been used to study photoreceptors, the nerve fiber layer (NFL), and the retinal pigment epithelium (RPE). As shown in Figure 2-13(B), AOSLO can image mosaics of distinct photoreceptors. The clearest images of photoreceptors have been obtained from confocal AOSLO systems (124). AO is the first, and thus far the only, technology which has been able to image the entire mosaic of photoreceptors in the living eye (124). AO coupled imaging of photoreceptors may be eventually be used to analyze the health of photoreceptors. Figure 2-13(C) shows a detailed image of the nerve fiber layer taken in an adult mouse. Individual nerve fiber bundles are visible, as indicated by the arrow. Additionally, small capillaries (arrowhead) are also visible in this region. The nerve fiber layer is made up almost entirely of the axons of retinal ganglion cells (RGC). RGC loss has been shown to be an important indicator of glaucoma. Future studies using AO powered optical imaging may be useful in learning more about RGC loss as well as in glaucoma diagnosis.

2.8 SUMMARY

In conclusion, this chapter has introduced the major ophthalmic imaging techniques used in biomedical research and clinical practice. While the fundus camera, cSLO, and OCT have become well established tools in vision science and ophthalmology, newer technologies, such as OCTA, vis-OCT, PAOM, and AO, are still ongoing research efforts and finding clinical utility. Some imaging technologies were not discussed, including ultrasound imaging and other functional variants of OCT (126), including polarization-sensitive OCT (127). For many of the discussed techniques, ideas were borrowed from microscopy, chemistry, physics, and astronomy. Therefore, by continuing to look at these fields for new ideas, we may realize yet undiscovered ophthalmic technologies, bringing with them further understanding of the eye and its function in health and disease. Ultimately, new ophthalmic imaging technologies provide powerful tools for diagnostics and carve the way for improved therapeutic strategies.

Chapter 3

Optical Coherence Tomography Image Formation and Signal Processing

3.1 INTRODUCTION

In this chapter, we will delve into the fundamentals of OCT image formation, starting with the Michelson interferometer. We will then discuss the more general case of low-coherence interferometry, which forms the basis of OCT. A multiple reflector single scattering model will then be used to explain image formation in Fourier-domain OCT. The basic calibration of spectrometers will be discussed. Finally, a practical signal processing algorithm for performing OCT image reconstruction will be discussed in detail.

3.2 MICHELSON INTERFEROMETRY

The Michelson interferometer is a simple device with wide-ranging and powerful applications in physical experiments. Perhaps most famously, Michelson and Morley in 1887 used the interferometer to disprove that light traveled through a luminiferous aether (128). This eventually led to the special theory of relativity, where one of its postulates states the speed of light in a vacuum is the same for all observers. More recently, large constructions (4 km) of a MI at the Laser Interferometer Gravitational-Wave Observatory (LIGO) were used to make the first observations of gravitational waves in 2015 (129). In addition to its applications in astronomy and physics, the MI forms the basis of OCT.

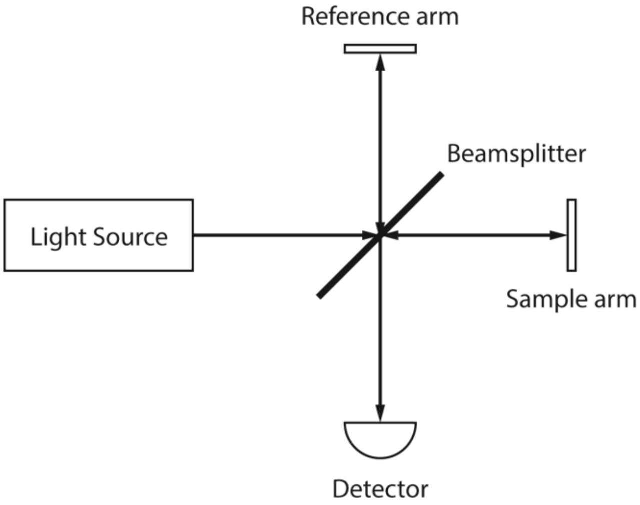

Figure 3-1: Schematic of the Michelson interferometer

The simplest MI is depicted in Figure 3-1. A light source illuminates a beamsplitter which divides the beam into a reference and sample arm. The light in each arm is back-reflected by a mirror after traversing distances of z_R and z_S, respectively. The back-reflected beams are recombined by the beamsplitter and detected by a photodetector. The electric fields can be written as:

$$E_R = E_{R0} e^{-i\omega t} e^{i2kz_R} \tag{3-1}$$

$$E_S = E_{S0} e^{-i\omega t} e^{i2kz_S} \tag{3-2}$$

The detected signal at the photodetector can be written as:

$$I_D = \langle |E_R + E_S|^2 \rangle \tag{3-3}$$

Where E_R and E_S are the electric fields. The photodetector acts as a square-law detector, which generates a current proportional to the intensity (squared electric field). The angled brackets indicate time averaging. In the simple case where the light source is purely monochromatic, we can remove the time-averaging, and arrive at a more simplified model:

$$I_D = |E_R + E_S|^2 \tag{3-4}$$

Here we neglect the transmission and reflection coefficients of the beamsplitter and the mirrors, as well as any phase shifts that reflective surfaces induce.

The above expression can be expanded to the following equation:

$$I(t) = I_R + I_S + 2\sqrt{I_R}\sqrt{I_S}\cos(2kz_S - 2kz_R) \tag{3-5}$$

Here I_R and I_S denote the intensity of the reference and sample arm beams, respectively; k is the optical wavenumber $k = 2\pi n/\lambda_0$; n is the refractive index; and λ_0 is the optical wavelength of the source. This equation shows two main components of the detected signal: (1) a DC term and (2) and AC term. The latter represents the interference term between the reference and sample arm beams; and therefore, this detected signal is termed an interferogram.

For illustrative purposes, the phase of the AC term can be written as:

$$\Delta\phi = 2k\Delta z = \frac{2\pi(2n\Delta z)}{\lambda_0} \tag{3-6}$$

where $\Delta z = z_S - z_R$. This equation illustrates that the phase difference is proportional to $2n\Delta z$, meaning that the AC component oscillates periodically depending on the path-length difference. The factor of 2 denotes a ‘round-trip path-length difference;’ the refractive index and path-length difference combine to form the ‘optical path-length difference.’

The phase term is the key to the powerful applications of the MI. For example, $I(t)$ can be recorded and the successive zeros of the interferogram can be determined, which correspond to $\Delta\phi$ equal to an integer multiple of π. Any of the parameters within the phase shift term can be then calculated given prior knowledge of the other terms. For example, the refractive index of a sample could be determined with careful measurement of Δz, λ_0, and $\Delta\phi$. Another application could be to measure the distance that a mirror is translated, Δz, by carefully counting the number of zero-crossings, giving knowledge of $\Delta\phi$, and prior knowledge of n and λ_0.

3.3 LOW-COHERENCE INTERFEROMETRY

Although the MI with a monochromatic light source has many uses for depth-ranging of a single mirror, it cannot distinguish between multiple reflective surfaces in the sample arm, which is required for ranging in biological tissue. In this section, we will discuss what occurs when the light-source is no longer monochromatic. We will follow closely the theory laid out by Izatt et al (74).

To represent multiple reflectors in the sample arm, we can write the reflectivity of the sample as:

$$r_S(z_S) = \sum_{n=1}^{N} r_{S_n}\delta(z_S - z_{S_n}) \tag{3-7}$$

Where r_{S_n} are the electric field reflectivities at distances z_{S_n} away from the beamsplitter.

The reference arm and sample arm electric fields can then be written as:

$$E_R = \frac{E_0}{\sqrt{2}} r_R e^{i2kz_R} \tag{3-8}$$

$$E_S = \frac{E_0}{\sqrt{2}} \sum_{n=1}^{N} r_{S_n} e^{i2kz_{S_n}} \tag{3-9}$$

where E_0 is the electric field amplitude incident on the beamsplitter from the source. Again, we can write the detected intensity as:

$$I_D(k,\omega) = \frac{\rho}{2}\langle |E_R + E_S|^2 \rangle \qquad (\ 3\text{-}10\ )$$

where ρ is the detector's sensitivity.

By inserting (3-8) and (3-9) into (3-10), it can be shown that the final detected intensity can be expanded to the following form:

$$\begin{aligned} I(k) &= \frac{\rho}{4}S(k)[R_R + R_{S1} + R_{S2} + \cdots] \\ &+ \frac{\rho}{2}\left[S(k)\sum_{n=1}^{N}\sqrt{R_R R_{S_n}}(\cos[2k(z_R - z_{S_n})])\right] \\ &+ \frac{\rho}{4}\left[S(k)\sum_{n\neq m=1}^{N}\sqrt{R_{S_n} R_{S_m}}(\cos[2k(z_{S_n} - z_{S_m})])\right] \end{aligned} \qquad (3\text{-}11)$$

Where $S(k) = \langle |s(k,\omega)|^2 \rangle$ or the power spectral density of the light source. Figure 3-2 shows a graphical derivation of the terms present in the above equation. The electric field reflectivities for the reference arm and the sample arm are crossed with one another, generating three different types groups of coefficients.

The first group of coefficients represent the DC terms. In imaging of biological samples, this term is dominated by the reference arm reflectivity. The second group of coefficients represent the cross-correlation terms, which result from interference between the sample and the reference arms. The amplitude of these terms depend on the sample arm reflectivities. Although the sample arm reflectivities themselves can be very small, the detected terms are amplified by the reference arm reflectivity, which is very high. This is referred to as optical heterodyne detection. The last group of coefficients relate to the autocorrelation terms, which are interference between reflected waves from within the sample arm. These manifest as image artifacts that reside close to the zero-delay due to their small path differences. The amplitudes are also smaller than that of the cross-correlation terms but can be present, especially when the incident light power on the sample is high.

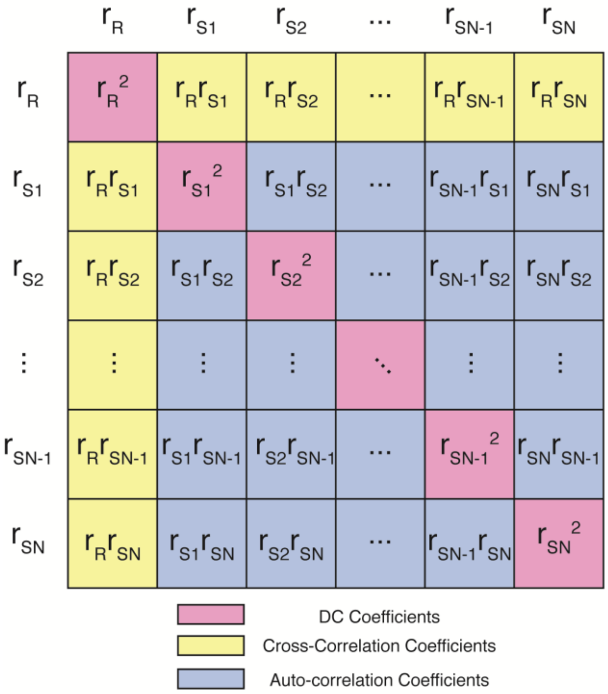

	r_R	r_{S1}	r_{S2}	…	r_{SN-1}	r_{SN}
r_R	r_R^2	$r_R r_{S1}$	$r_R r_{S2}$	…	$r_R r_{SN-1}$	$r_R r_{SN}$
r_{S1}	$r_R r_{S1}$	r_{S1}^2	$r_{S1} r_{S2}$	…	$r_{SN-1} r_{S1}$	$r_{SN} r_{S1}$
r_{S2}	$r_R r_{S2}$	$r_{S1} r_{S2}$	r_{S2}^2	…	$r_{SN-1} r_{S2}$	$r_{SN} r_{S2}$
⋮	⋮	⋮	⋮	⋱	⋮	⋮
r_{SN-1}	$r_R r_{SN-1}$	$r_{S1} r_{SN-1}$	$r_{S2} r_{SN-1}$	…	r_{SN-1}^2	$r_{SN} r_{SN-1}$
r_{SN}	$r_R r_{SN}$	$r_{S1} r_{SN}$	$r_{S2} r_{SN}$	…	$r_{SN-1} r_{SN}$	r_{SN}^2

🟪 DC Coefficients
🟨 Cross-Correlation Coefficients
🟦 Auto-correlation Coefficients

Figure 3-2: Graphical derivation of the terms of the multiple reflector model.

A Gaussian shaped spectrum is often conveniently used to model $S(k)$ due to its simple shape and Fourier transform.

$$S(k) = \frac{1}{\Delta k\sqrt{\pi}} \exp\left[-\frac{(k-k_0)}{\Delta k}\right]^2 \qquad (3\text{-}12)$$

The Fourier transform is also a Gaussian and is written with the conjugate variable to k, which is z (depth).

$$\gamma(z) = \exp[-z^2 \Delta k^2] \qquad (3\text{-}13)$$

$\gamma(z)$ is called the coherence function, and it determines the axial PSF in OCT. It can be shown that the autocorrelation function of a source is the coherence function. The Wiener-Khinchin theorem states that the autocorrelation function of a source's field is a FT pair with the source's statistical power spectral density.

The coherence length is given as the FWHM of the coherence function. For the Gaussian shaped coherence function, the coherence length can be derived as follows:

$$l_c = \frac{2\sqrt{\ln(2)}}{\Delta k} = \frac{2\sqrt{\ln(2)}}{\pi}\frac{\lambda_0^2}{\Delta\lambda} \tag{3-14}$$

3.4 TIME-DOMAIN OCT

Time-domain OCT (TD-OCT) was the first implementation of low-coherence interferometry for biological tissue imaging. However, it has largely been replaced by Fourier-domain OCT implementations due to its slow speed and low sensitivity. Nevertheless, TD-OCT can still be found in certain forms of parallel OCT imaging techniques, such as full-field OCT (130). In TD-OCT, the entire spectral interferogram from (3-11) is captured by a single photodetector; therefore, the $I(k)$ is integrated over all k.

$$\begin{aligned} I_D(z_R) &= \frac{\rho}{4}\left[S_0[R_R + R_{S1} + R_{S2} + \cdots]\right] \\ &+ \frac{\rho}{2}\left[S_0\sum_{n=1}^{N}\sqrt{R_R R_{SN}}\exp[-(z_R - z_{SN})^2\Delta k^2]\cos[2k_0(z_R - z_{SN})]\right] \end{aligned} \tag{3-15}$$

where S_0 is the integrated power spectral density over all wavenumbers.

$$S_0 = \int_0^\infty S(k)dk \tag{3-16}$$

The reference arm mirror is mechanically moved back and forth, changing z_R while detecting $I_D(z_R)$. After removal of the DC offset, the amplitude modulate of the AC term can be extracted by rectification of the signal and low-pass filtering.

3.5 FOURIER-DOMAIN OCT

In FD-OCT, the reference arm mirror is kept stationary, and the spectral interferogram is captured. In spectral-domain OCT (SD-OCT), a broad bandwidth light source is used, and a spectrometer captures the light in the detection arm. The spectrometer disperses the collected light, and a linear camera array detector detects the spectral interferogram in a single shot. In swept-source OCT, the spectral interferogram is captured sequentially by using a source which sweeps the wavenumber and using a single detector.

By collecting $I(k)$, the entire A-line can be reconstructed by performing the FT on the spectral interferogram. The FT of equation (3-11) can be shown to give the equation:

$$\begin{gathered} i_D(z) = \frac{\rho}{8}\left[\gamma(z)[R_R + R_{S1} + R_{S2} + \cdots]\right] \\ + \frac{\rho}{4}[\gamma(z) \otimes \sum_{n=1}^{N} \sqrt{R_R R_{S_n}} \delta(z \pm 2(z_R - z_{S_n}))] \\ + \frac{\rho}{8}[\gamma(z) \otimes \sum_{n \neq m=1}^{N} \sqrt{R_{S_n} R_{S_m}} \delta\left(z \pm 2(z_{S_n} - z_{S_m})\right)] \end{gathered} \tag{3-17}$$

We can see that the result consists of three terms in the z-domain. First, there is a peak at $z = 0$ which corresponds to the DC term. Second, there are delta functions symmetric about the zero-delay which correspond to the position of the reflectors in depth. These delta functions are convolved with $\gamma(z)$, as expected since $\gamma(z)$ is the axial PSF in OCT. Finally, there are auto-correlation terms close to the zero delay, which present as image artifacts in FD-OCT.

3.6 SIGNAL-TO-NOISE RATIO IN OCT

For SD-OCT, the signal-to-noise ratio (SNR) can be written as:

$$SNR_{SD} = \frac{\frac{\eta^2 e^2 P_{ref} P_{sample} \tau_i^2}{NE_V^2}}{\sigma_{r+d}^2 + \frac{\eta e^2 P_{ref} \tau_i}{NE_\nu} + \left(\frac{\eta e P_{ref} \tau_i}{NE_\nu}\right)^2 \frac{\tau_{coh}}{\tau_i}} \qquad (3\text{-}18)$$

where τ_i is the camera integration time; e is the electron charge; η is a conversion factor which converts number of incident photons to number of electrons; E_ν is the photon energy at optical frequency ν; N is the number of camera elements; and τ_{coh} is the coherence time. The numerator indicates the signal power, while the denominator includes three of the major noise sources in SD-OCT. The first term represents the readout and dark noise of the camera elements. The second term represents the shot-noise which is a Poisson distributed noise related to the number of arrivals of electrons at the photodetector. The third term is the relative-intensity noise, a noise specific to OCT which relates to uncorrelated noise between spectral components. When the shot-noise term is much greater than the RIN term the OCT system is said to be shot-noise limited.

FD-OCT possesses a significant sensitivity advantage when compared to TD-OCT. Thus, FD-OCT has been widely adopted since its inception. In the most ideal scenario, the SNR for FD-OCT can be express in terms of the SNR for time-domain OCT as:

$$SNR_{FDOCT} = \frac{SNR_{TDOCT} M}{2} \qquad (3\text{-}19)$$

where M is the number of spectral elements in the detection arm. This equation assumes a flat spectrum. In the case that the light source spectrum is Gaussian, the SNR for FD-OCT is reduced by another factor of 2.

3.7 WAVELENGTH CALIBRATION FOR SPECTROMETERS

Typical spectrometer design for SD-OCT include a collimating lens, a grating, a focusing lens, and a camera, in the Lens-Grating-Lens configuration (LGL configuration). To properly reconstruct the OCT image, the exact wavelengths distribution on the camera must be determined. Using a geometric optics derivation, it can be shown that the wavelength distribution for the j$^{\text{th}}$ camera pixel element is given by the following equation (131):

$$\lambda_j = d\bigg(\sin\theta_i + \sin(\operatorname{arcsin}\bigg(\frac{\lambda_c}{d} - \sin\theta_i\bigg) + \operatorname{atan}\bigg(\frac{w * j - x_c}{F}\bigg)\bigg)\bigg) \tag{3-20}$$

Here d is the line number of the grating; λ_c is the center wavelength; w is the width of a pixel element; F is the focal length of the imaging lens. θ_i is the incidence angle of the light on the grating.

Spectral calibration lamps are often required for the calibration procedure. Equation 3-20 can be fit to the positions of known spectral lines from neon, mercury, or argon gas lamps, for example. The equation above can also be inverted.

$$j = \frac{F\tan\left(\operatorname{asin}\left(\frac{\lambda_j}{d} - \sin\theta_i\right) - \operatorname{asin}\left(\frac{\lambda_c}{d} - \sin\theta_i\right)\right) + x_c}{w} \tag{3-21}$$

In some circumstances, wavelength calibration using the spectral calibration lamp approach, especially when the spectrometer is designed with optics that differ greatly from geometrical optics (132) (133).

3.8 ALGORITHM FOR FULL SPECTRUM OCT

A flowchart depicting the algorithm for full-spectrum OCT image reconstruction is shown in Figure 3-3. This algorithm includes some additional processing techniques, which were neglected in the more simplified derivation in section 3.5. This includes compensating for the unequal k-space mapping in the spectrometer using interpolation, numerical dispersion compensation, as well as sensitivity rolloff correction.

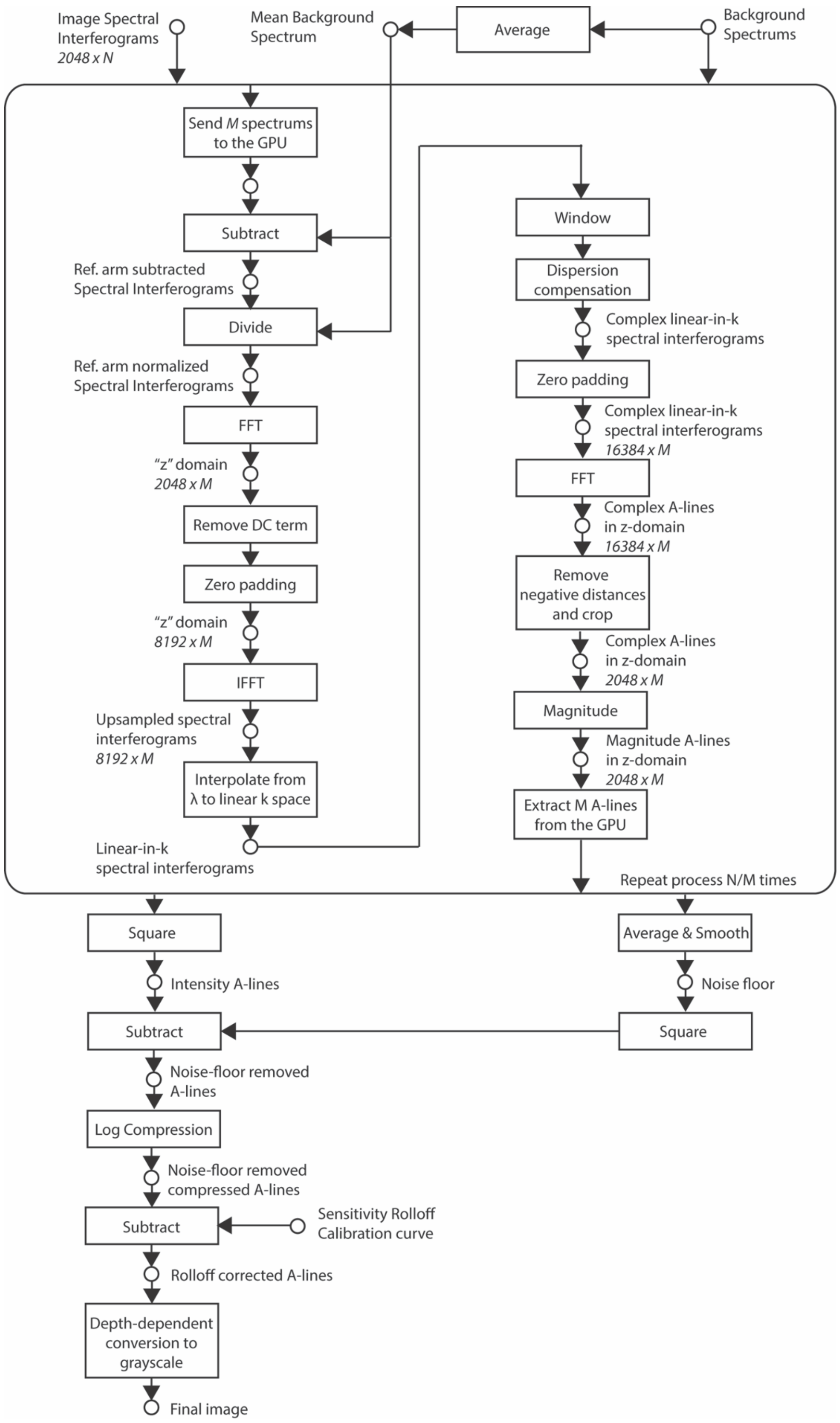
Image Spectral Interferograms
2048 x N
Mean Background Spectrum
Average
Background Spectrums
Send M spectrums to the GPU
Subtract
Ref. arm subtracted Spectral Interferograms
Divide
Ref. arm normalized Spectral Interferograms
FFT
"z" domain
2048 x M
Remove DC term
Zero padding
"z" domain
8192 x M
IFFT
Upsampled spectral interferograms
8192 x M
Interpolate from λ to linear k space
Linear-in-k spectral interferograms
Window
Dispersion compensation
Complex linear-in-k spectral interferograms
Zero padding
Complex linear-in-k spectral interferograms
16384 x M
FFT
Complex A-lines in z-domain
16384 x M
Remove negative distances and crop
Complex A-lines in z-domain
2048 x M
Magnitude
Magnitude A-lines in z-domain
2048 x M
Extract M A-lines from the GPU
Repeat process N/M times
Square
Intensity A-lines
Average & Smooth
Noise floor
Subtract
Square
Noise-floor removed A-lines
Log Compression
Noise-floor removed compressed A-lines
Subtract
Sensitivity Rolloff Calibration curve
Rolloff corrected A-lines
Depth-dependent conversion to grayscale
Final image

Figure 3-3: Algorithm for full-spectrum reconstruction of OCT images.

3.8.1 Reference arm subtraction

Reference arm subtraction is performed to remove the DC component from the raw spectral interferogram. The reference arm spectrum is given by:

$$I_{ref}(k) = \frac{\rho}{4} R_R S(k) \tag{3-22}$$

The reference arm can be estimated by two methods: (1) taking the average of all the acquired A-lines or (2) taking the average of background image file. The background image file can be acquired by blocking the sample arm and collecting the reference arm. This assumes that the light entering the spectrometer is primarily from the reference arm. Since the DC component also is composed of other terms from the sample arm, this subtraction also assumes that R_R is generally greater than R_{S1} to R_{SN}.

3.8.2 Background Normalization

The background-subtracted interferogram is then divided by the background. This process is also known as apodization and it is important for two major reasons.

First, it acts as a digital deconvolution, which can improve the width of the axial point spread function (134). Recall that the amplitude of the cross-correlation interferogram is given by:

$$I_{cross,n}(k) \propto \frac{\rho}{2}\left[S(k)\sqrt{R_R R_{S_n}}\right] \tag{3-23}$$

By dividing the measured interferogram by the reference arm, we can try to remove the source spectrum from the amplitude

$$\frac{I_{cross,n}(k)}{I_{Ref}(k)} \propto \frac{S(k)\sqrt{R_R R_{S_n}}}{R_R S(k)} = \frac{\sqrt{R_{S_n}}}{\sqrt{R_R}} \tag{3-24}$$

Equation (3-24) shows that the source spectrum can be removed from modulating the interferogram fringe. The effect is that in the spatial z-domain, the point spread function will become the FT of a rectangular window with a width equal to the length of the acquired spectrum. This usually results in a smaller FWHM of the main lobe of the PSF; however, the FT of the rectangle function is a sinc function, which has high sidelobes that can sometimes create image artifacts.

Second, reference arm normalization is an important component of spectroscopic OCT. In spectroscopic OCT, the amplitude modulation of the fringe must be isolated to effects of the sample. By equation (3-24), we can see that the new normalized spectrum is proportional to the sample reflectivities. If the reference arm spectrum is flat, then the spectrum from the sample can be recovered from the amplitude modulation of the fringes.

3.8.3 Interpolation from unequal-k to equal-k

Due to the dispersive nature of the grating used in the spectrometer, the interferogram is not sampled with equal wavenumber spacing (equal k-spacing). The Fast Fourier Transform (FFT) requires the sampling to be equal in k-space to correctly transform each of the frequency components. Although alternative FT methods allow for unequally k-space sampling, such as the non-uniform FFT (NUFFT) (135); however, here we focus on traditional methods to correct the unequal k-space sampling.

To transform the sampled interferogram from unequal k-spacing to equal k-spacing, interpolation methods are often used. By calibrating the spectrometer’s wavelength distribution, the k-spacing can be determined. Linear interpolation can be performed directly on the sampled interferogram to convert it from unequal k-spacing to equal k-spacing; however, studies have shown that this technique results in an increased noise floor with imaging depth.

An improved method to interpolate the interferograms is to first take it's FFT and add zero padding to the signal (136). Often, the signal is extended by 4 to 8 times with zeros. A second inverse FFT is performed to return the back to the k-domain. This zero-padding technique results in ideal interpolation of the interferogram and extends the number of points that the number of samples representing the interferogram. This upsampled interferogram signal can then be interpolated to the equal-k spacing. This combined technique requires more processing time compared to direct linear interpolation, but overall, it results in better noise floor performance, especially at longer depths (137).

3.8.4 Windowing

Windowing refers to multiplication of the interferogram to suppress the appearance of the sidelobes of the PSF. As discussed in 3.9.2, division by the reference arm spectrum results in a rectangular window in the k-domain, and a sinc function PSF in the z-domain. Although this may provide the highest axial resolution or the smallest FWHM of the main lobe of the PSF, the side lobes for the sinc function can be quite high. These sidelobes can be quite apparent as image artifacts, especially if the reflectivity of the sample is high. The windowing technique can be expressed as the following equation:

$$W(k)\frac{I_{cross,n}(k)}{I_{Ref}(k)} \propto W(k)\frac{\sqrt{R_{S_n}}}{\sqrt{R_R}} \tag{3-25}$$

Where $W(k)$ is the window function, and $w(z)$ is its corresponding FT. The most common windows for structural OCT imaging are a Gaussian window and the Hanning window.

3.8.5 Numerical dispersion compensation

Dispersion mismatch between the reference and sample arm is common in ophthalmic imaging. The effects of dispersion mismatch are two-fold. First, dispersion mismatch causes broadening of the axial PSF. Second, the amplitude of the PSF will also be attenuated. Therefore, dispersion mismatch must be corrected to obtain high quality OCT images.

Hardware dispersion compensation aims to balance the dispersion between the reference and sample arm by adding dispersive plates in the reference arm to compensate for optical elements in the sample arm. Sample arm elements include any imaging lenses before the eye as well as elements of the eye itself, including the cornea, lens, and vitreous, which all have different refractive indexes. Since the axial eyeball length differs between subjects, the amount of dispersion is also variable across subjects. Therefore, hardware dispersion compensation is insufficient to compensate for routine ophthalmic imaging.

Numerical dispersion compensation aims to correct the residual dispersion mismatch by multiplying the fringe by a correction factor. Dispersion introduces a phase shift $e^{i\Phi(k)}$ on the cross spectral density that causes the interferogram to be chirped. This phase term can be modeled using a Taylor expansion (138):

$$\begin{aligned}\Phi(k) = \Phi(k_0) + \left.\frac{d\Phi}{dk}\right|_{k=k_0} (k-k_0) \\ + \left.\frac{1}{2}\frac{d^2\Phi}{dk^2}\right|_{k=k_0} (k-k_0)^2 \\ + \left.\frac{1}{6}\frac{d^3\Phi}{dk^3}\right|_{k=k_0} (k-k_0)^3 + \cdots \\ + \left.\frac{1}{n!}\frac{d^n\Phi}{dk^n}\right|_{k=k_0} (k-k_0)^n\end{aligned} \tag{3-26}$$

The first two terms describe a constant offset and the group velocity, but do not cause dispersive broadening. The third order phase term is a non-linear term, which is referred to as *group velocity dispersion* (GVD). GVD causes broadening of the PSF (increasing the coherence length). The fourth term causes asymmetric distortion of the PSF shape. To perform numerical dispersion compensation, the spectral interferogram is multiplied by a complex exponential which acts to cancel the non-linear phase terms induced by the dispersion. This complex exponential can be written as:

$$\Phi_{Disp}(k) = c_1(k-k_0)^2 + c_2(k-k_0)^3 \tag{3-27}$$

for correction of the second order and third order terms. If the coefficients c_1 and c_2 can be correctly determined, then multiplying $I(k)$ by $e^{i\Phi_{Disp}(k)}$, can cancel the non-linear phase terms.

In practice, the coefficients of the phase correction term can be found using a numerical optimization procedure. Multiple cost functions can be used to determine the dispersion coefficient. These may include the sharpness of the image or the number of pixels above a specified threshold (139). Short-time fourier transform approaches have also been explored to calculate the nonlinear phase term (140).

3.8.6 Fast Fourier Transform (FFT)

Once the interferogram has been prepared, it is ready to be converted to the final OCT image using a FFT. Note that the FFT performs optimally when the length of the signal is a power of 2. A final zero-padding step is applied to the signal before the FFT to increase the final A-line length, while also avoiding improper amplitude estimation errors from spectral binning. The negative frequencies are discarded, and the positive frequencies give the axial image.

3.8.7 Compression

OCT intensity images contain a large dynamic range (96 dB if using 16 bits), which exceeds the dynamic range of the human vision (40-60 dB) (141). Therefore, compression of the dynamic range is usually performed using a logarithm operator on the OCT image. Historically, the logarithm operator was also used to compensate for the exponential attenuation of OCT amplitude in tissue (142). Nevertheless, the OCT image is displayed in decibel scale to enhance the contrast:

$$i_{Db}(z) = 20 \times Log_{10}(i(z)) \tag{3-28}$$

3.8.8 Sensitivity Rolloff Correction

The spectrometer in SD-OCT has a finite spectral resolution, which is primarily due to two factors: the finite pixel size of the spectrometer and the finite PSF of the imaging lens in the spectrometer. The spectrometer's impulse response can be represented by a function $G(k)$. Therefore, the actual measured interferogram from the spectrometer can be written as (76):

$$I_{spectrometer}(k) = G(k) \otimes I(k) \tag{3-29}$$

The result is that there is a decrease in fringe visibility for higher interferogram frequencies. This effectively translates to a rolloff of the OCT amplitude with distances away from the zero delay.

To correct for this sensitivity rolloff, we can measure the transfer function $g(z)$ by taking serial measurements of the axial PSF across the imaging depth range. Then we can perform a deconvolution step to the final OCT image to correct for the sensitivity rolloff. This can be written as:

$$i_{Db} = 20 \times Log_{10}\left(\frac{i_{spectrometer}(z)}{g(z)}\right) \tag{3-30}$$

3.8.9 Determining the depth range

The maximum imaging depth is determined by the Nyquist limit of the spectrometer's sampling rate in k-space. If the sampling rate for the spectrometer is given by $\pi/\delta k$, then the Nyquist theorem states that the maximum resolvable frequency that can reconstructed is half this sampling rate. In other words, the maximum imaging depth in air is given by:

$$z_{max} = \frac{\pi}{2\delta k} \tag{3-31}$$

If the medium has a refractive index n then the maximum imaging range is shortened by a factor of n.

3.8.10 Graphical Processing Unit Performance

Graphical processing units (GPUs) can provide parallel processing of OCT data by performing multiple FFT's in parallel, increasing the efficiency of data processing. The speed of processing; however, depends on many factors, including the number of cores and the data transfer time between the computer memory and the GPU memory. In practice, the efficiency of the GPU processing can be tested by sending different numbers of A-lines to the GPU and assessing the total processing time.

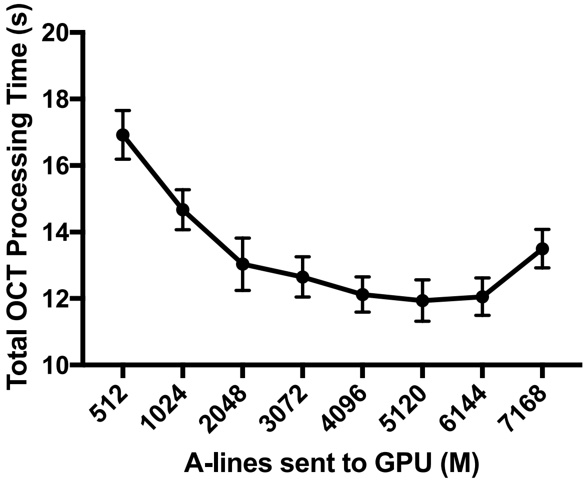

Figure 3-4 Performance of the OCT image processing algorithm on a graphics processing unit

Figure 3-4 shows an example of an experiment, where the OCT processing algorithm was implemented in MATLAB 2018 and the GPU was a Gefore GTX 1080 Ti. A ~30% increase in speed for 5120 A-lines sent to the GPU at a time was seen compared to sending M=512 A-lines at a time.

3.9 CONCLUSION

This chapter has provided the theoretical foundation of OCT starting from the Michelson interferometer. It has introduced the practical concepts of SNR and spectrometer calibration. A full OCT algorithm to reconstruct OCT images was presented. Several practical topics were discussed including windowing, numerical dispersion compensation, and sensitivity rolloff correction. The topics in this chapter serve as the foundation for the rest the signal processing found in this dissertation.

Chapter 4

Visible-light optical coherence tomography oximetry based on circumpapillary scan and graph-search segmentation

4.1 INTRODUCTION

Visible-light optical coherence tomography (vis-OCT) adds functional information to OCT, such as providing oxygenation measurements in the living retina (12, 143). Vis-OCT measures the oxygen saturation of hemoglobin (sO_2) – the percentage of oxygen-bound hemoglobin binding sites – from within individual blood vessels. Dysfunctions in oxygen supply and demand have been hypothesized as key contributors to a number of retinal diseases, including diabetic retinopathy, retinopathy of prematurity, retinal vascular occlusions, and glaucoma (27). In animal model studies of these diseases, vis-OCT can potentially help to elucidate key time-points and pathogenic mechanisms of disease (9, 144). In human studies and patient imaging (105, 145), vis-OCT may eventually identify oxygenation related biomarkers that correlate with progression of disease or a response to treatment.

Retinal oximetry with vis-OCT is based upon spectroscopic OCT (146, 147). In spectroscopic OCT, the spectral interferogram is divided into sub-bands, which are individually processed to produce a set of reduced axial-resolution images. In comparison, conventional OCT uses the entire band of the spectral interferogram to form a single, high axial-resolution image. Although the axial resolution is sacrificed in spectroscopic OCT, each image corresponds to a different wavelength band, giving the spectrum of the backscattered light that conventional OCT does not provide. The spectrum of the backscattered light can be used to calculate sO_2 by fitting it against a model of light attenuation (92).

A visible-light source is necessary for measuring sO_2 with spectroscopic OCT. Previous studies have typically used supercontinuum light sources with a spectral range between 500 nm and 650 nm. Using visible-light is more advantageous than near-infrared light for three major reasons (143). First, the shapes of the absorption spectra of oxygenated and deoxygenated hemoglobin (HbO_2 and DeHb) are more distinctive in the visible region, as there are more isosbestic points in the visible regime than in the NIR. Second, the absorption coefficient of Hb in the visible spectral range is ~2 orders of magnitude higher than that in the NIR spectral range. Third, the absorption coefficients in the visible region are around two times higher than the reduced scattering coefficients. Comparisons between visible and NIR oximetry measurements with OCT have been performed *in silico*, with Monte Carlo simulations (148), and *in* vivo, with a dual-band (visible and NIR) OCT system (149). Both studies found superior performance for oxygenation measurements in the visible regime.

Reliable estimation of the backscattered light’s true spectrum often requires averaging the OCT signal from the same depth location across multiple A-lines. Averaging is necessary for two major of reasons. First, from a hardware perspective, supercontinuum light sources suffer from increased relative intensity noise (RIN) compared to superluminescent diodes (150). Second, from an experimental perspective, breathing motion distorts the OCT volume. In human imaging, saccades and eye movement can also contribute to motion. These noise sources increase the variance of the

OCT signal, making the true estimation of the backscattered light spectrum challenging with a small sample of A-lines. Averaging schemes vary in the literature. Previously, Yi et al. and Chen et al. averaged the spectra from A-lines within the entire vessel (91, 92). Pi et al. recently also used a similar approach (8). Depending on the scanning density and the size of the vessel, this results in averages using hundreds of A-lines. A downside of this approach is that different locations within a vessel may not have the same sO_2, especially in diseased eyes. Another scanning method is to repeat B-scans at each location to obtain several A-lines for averaging. For example, Chong et al. used 100 B-scans for cerebral sO_2 measurements in rodents (151). Unfortunately, this method adds time to the experimental process and is not feasibly for clinical retinal imaging.

Here, we present a retinal oximetry algorithm using vis-OCT, which solves the averaging problem using graph-search segmentation of the vessel wall. Graph-search algorithms have been used to solve a multitude of image processing problems in OCT, including retinal layer segmentation (152-154), lumen segmentation (154), and photoreceptor segmentation (155). We show that graph-search segmentation can be used to simultaneously help with two key tasks: (1) locating the vessel wall to extract the backscattered spectrum and (2) increasing the accuracy of the OCT signal when there is axial motion. Instead of performing retinal raster scans to calculate sO_2, we focused this study on extracting sO_2 from circumpapillary scans (95). This scanning technique repeatedly scans vessels at the same location on the retina, which reduces error and bias that may arise when averaging OCT signals along the length of a vessel. After presenting an overview of our algorithm, we define each step in detail. Finally, we address the question of how much averaging is required to obtain accurate results, by taking samples of our dataset and analyzing the accuracy, precision, and bias of our measurements for different sample sizes.

4.2 MATERIALS AND METHODS

4.2.1 Animal preparation

All experimental procedures were approved by the Northwestern University IACUC and conformed to the Association for Research in Vision and Ophthalmology (ARVO) Statement on Animal Research. Our anesthesia protocol had two steps. First, we temporarily anesthetized adult Brown Norway rats (n=2) with 3% isoflurane for 3 minutes, which enabled them to be easily and safely handled. Second, we took them off isoflurane and administered an intramuscular injection of a ketamine and xylazine cocktail (ketamine: 0.37 mg/kg; xylazine: 0.07 mg/kg). The rat was then placed on a custom-made animal holder for imaging. A pulse oximeter was attached to the right rear paw to monitor peripheral arterial sO_2 and heart rate. The body temperature was maintained with a heat lamp. We applied a drop of 1% tropicamide hydrochloride ophthalmic solution to dilate the pupil. To prevent corneal dehydration, we applied commercial artificial tears after taking each image.

4.2.2 Algorithm Overview

Figure 4-1 shows a flowchart of the automatic retinal oximetry algorithm. Spectral interferograms were first processed by full-spectrum reconstruction. We flattened the retina, segmented the major layers of interest, and automatically detected the vessels. We then performed split-spectrum reconstruction for each segmented vessel. We aligned the A-lines in each vessel's B-scan using cross-correlation. To segment the boundaries of the vessel wall, we used a directional graph-search. Finally, to obtain the sO_2 in a vessel, we fit the average spectrum from the vessel wall to a previously described modified Beer's law model (92). All data processing was implemented in MATLAB (MathWorks, Inc., version 2017b)

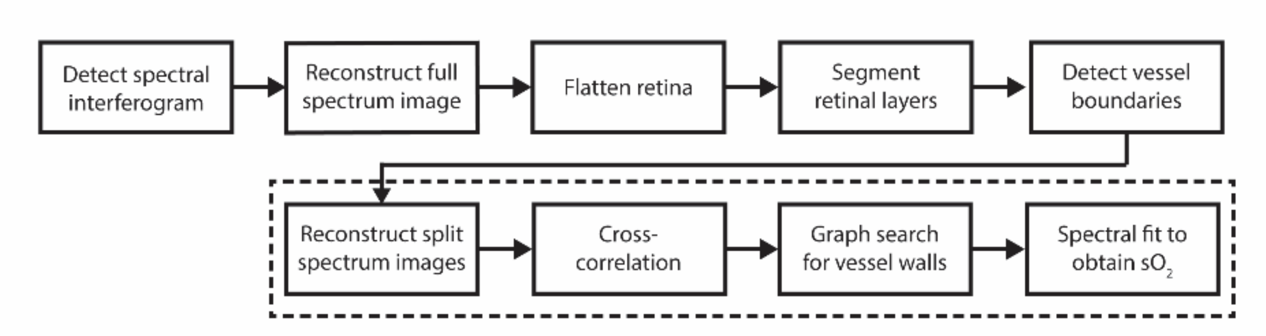

Figure 4-1: Overview of the retinal oximetry algorithm. The dashed box indicates steps of the algorithm that were performed for each vessel.

4.2.3 OCT Data Acquisition

We acquired images with a dual-band vis-OCT system, which was reported previously (149). We made two minor modifications to the system. First, we changed the 50/50 cube beam splitter to a 30/70 (sample/reference arm) cube beam splitter for increased sample arm collection efficiency. Second, to increase our field-of-view, the Keplerian telescope was modified to a 6:1 magnification (previously 5:1), using a pair of 150 mm and 25 mm achromatic lenses. In addition to the larger magnification, these lenses had a 1-inch diameter (previous 0.5 inch), enabling a larger scanning angle from the galvanometers to be used without image distortion from the lens edges. We kept all the other components, including the light source, custom-built spectrometer, and polarization controller, from the previously reported design. Illumination power at the pupil was ~1 mW.

We acquired raster scans solely for visualizing the optic nerve head and positioning the animal. We performed circumpapillary scans for our retinal oximetry measurements. Because circumpapillary scans sample the vessel at the same location, any biases or errors from sampling sO_2 at different vessel locations were reduced. Figure 4-2(A) shows the *en face* of an example raster scan. The white dashed circle indicates the clockwise circular path of the circumpapillary scan on the retina. The white numbers indicate the vessel identification number. The circumpapillary scan diameter on the retina was approximately ~1.5 mm, assuming a rat eyeball length of ~6.3 mm.

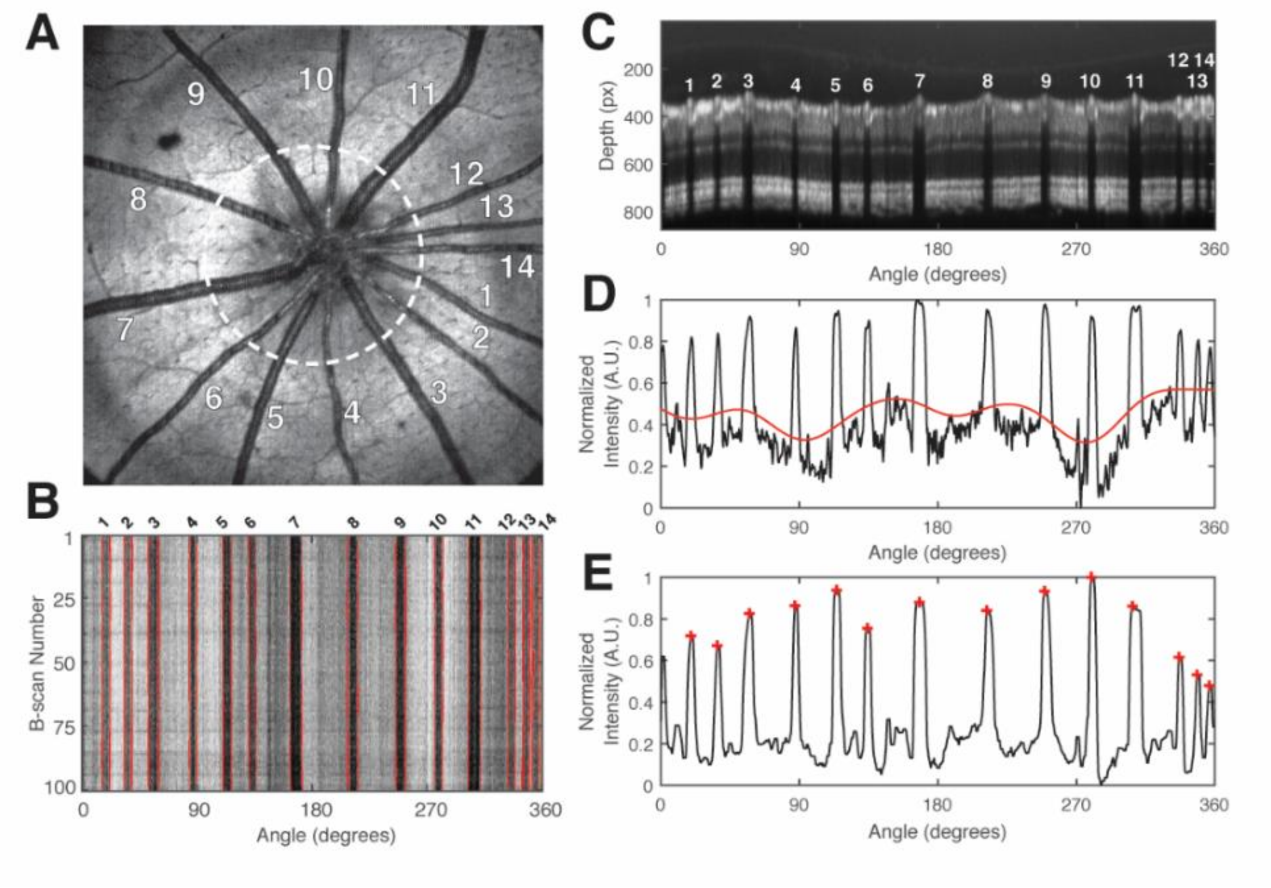

Figure 4-2: Vessel detection procedure. (A) *En face* raster scan of an adult rat retina. The white dashed circle indicates the approximate path of the circumpapillary scan on the retina. Numbers 1-14 identify the fourteen vessels; (B) *En face* of the circumpapillary scan OCT volume. Numbers 1-14 correspond to the vessels in A; (C) Average vis-OCT B-scan of the flattened circular scan volume. Numbers 1-14 correspond the numbers in A and B. Depth pixel size: 0.55 μm; (D) Black line indicates the two-dimensional shadowgram, calculated from C. Red line indicates the baseline, after low pass filtering; (E) Black line indicates the shadowgram after baseline subtraction and median filtering. Each red-cross indicates a peak corresponding to a vessel.

Raster scans consisted of 512 B-scans with 512 A-lines per B-scan, covering an area of ~4.1 mm by 4.1 mm on the retina. The spectrometer integration time per A-line was 37 µs, which corresponded to an A-line rate of 25 kHz. Total imaging time was ~10.5 seconds. Circumpapillary scans consisted of 100 B-scans with 8192 A-lines per B-scan. The spectrometer integration time per A-line was 17 µs, which corresponded to an A-line rate of 50 kHz. Total imaging time was ~16 seconds. Here, the higher A-line rate will eventually allow the calculation of blood flow using Doppler OCT in future work. Henceforth, a circumpapillary scan and B-scan may be used interchangeably, as we will only be referring to B-scans as scans from circumpapillary datasets.

4.2.4 Full spectrum reconstruction

For full-spectrum reconstruction, we performed standard OCT signal processing for a spectrometer-based OCT system, which included background subtraction, reference arm normalization, numerical dispersion compensation, and k-space resampling. Data processing was performed on a graphics processing unit (NVIDIA, GTX 980).

4.2.5 Retinal flattening

The retina in circumpapillary scans can often appear S-shaped due to the alignment of the beam not being perfectly centered at the pupil plane. To remove this artifact, we performed retinal flattening. To flatten the retina, we computed the center of mass for each A-line to obtain the approximate center location of the retina. The center of mass position was used as an upper boundary to restrict a light-to-dark graph search for the RPE layer (see section 2.6). The position of the RPE was recorded and then fitted to a 3D polynomial (7). Each A-line was then shifted to the fit to obtain a flattened volume. The flattening procedure reduced axial motion between B-scans and removed curvature from the circumpapillary scans.

4.2.6 Layer segmentation

We implemented the retinal layer segmentation algorithm outlined previously with slight modifications (152). Briefly, a two-dimensional graph was constructed, where each B-scan pixel was represented by a node. Each node had a weight, which was calculated using the weight equation reported by Chiu et al. (152). Connections between nodes were constructed in a directional pattern to save processing time (7). Each node was connected to the node directly adjacent to it on the right, and to 2 nodes above and below in the adjacent column to the right. Boundaries for the retinal layers were searched from left to right using Dijkstra's algorithm. The order of the retinal layers searched, the regional restrictions on the graph search, and the type of gradient used for the search (i.e. light-to-dark vs. dark-to-light) were modified from Srinivasan et al. for rat data (153). To further reduce processing time, we downsampled each circumpapillary B-scan from 8192 A-lines to 512 A-lines by averaging laterally 8 times. After retinal layer segmentation, we upsampled the boundaries back to the original B-scan dimensions.

4.2.7 Vessel detection

Figure 4-2 illustrates the vessel detection procedure, which determined the vessel boundaries and vessel center positions in the circumpapillary scan. The coordinates of the vessel wall were determined in a later step (see section 4.2.9). Figure 4-2(A) shows the *en face* of the raster scan. Fourteen retinal vessels were marked (white numbers). One hundred circumpapillary scans were acquired (white dashed line). Figure 4-2(B) shows an *en face* of the circumpapillary scan volume. Each of the vertical dark bars is reflectance from a retinal vessel in Figure 4-2(A).

Vessels were detected by creating a one-dimensional shadowgram from each B-scan. Figure 4-2(C) shows an average of the all the B-scans with the vessels numbered. First, A-line signals below the inner nuclear layer-outer plexiform layer (INL-OPL) boundary layer were averaged. Next, the shadowgram was then inverted and normalized (black line in Figure 4-2(D)). To remove the baseline, the shadowgram was filtered with a moving average of 100 pixels, which gave a measure of the baseline (red line in Figure 4-2(D)). Finally, a median filter was applied to reduce the noise, while preserving the shape of the peaks (black line in Figure 4-2(E)). Peaks were detected in the shadowgram signal using the 'findpeaks' method in MATLAB (red crosses in Figure 4-2(E)).

We generated shadowgrams for each B-scan and tracked the vessels using the peak-finding method. To find the boundaries of the vessel, we searched for the full-width at half-maximum to the left and right of each peak. The center of the vessel was determined by finding the center position of the full-width. The boundaries for the vessels identified in Figure 4-2(A) are delineated by the red lines in Figure 4-2(B).

4.2.8 Split-spectrum reconstruction

To perform spectroscopic OCT, we windowed the spectral interferogram in k-space and took the Fourier Transform. This procedure is often referred to as the short-time Fourier Transform, but a more appropriate name would be the short-k Fourier Transform. Here we simply refer to this procedure as spectral splitting. We applied 23 Gaussian windows with center wavelengths (λ_c) ranging from 525 nm to 591 nm, equidistantly spaced by 3 nm. The FWHM in the λ-space was 13 nm (0.25 μm^{-1} in k-space), which gave an axial resolution in air of 10.9 μm at 568 nm. These values were consistent with those used previously by Chen et al. (105).

To save on memory and computation time, we only performed spectral splitting on A-lines within the segmented vessels. After the spectral splitting procedure, each vessel was associated with a four-dimensional data set with dimensions of depth, radial position (angle), B-scan number, and λ_c. In order to reduce the dimensionality of the data and improve the signal-to-noise ratio, we compressed the dataset along the radial position dimension by averaging the 6 center A-lines of a vessel. The final spectroscopic OCT image for each vessel has three dimensions: depth, B-scan number, and λ_c.

4.2.9 Cross-correlation

Even after retinal flattening, the spectroscopic OCT images had inter-B-scan motion. In addition, graph-search segmentation techniques are more biased towards straight paths (152). Therefore, B-scans had to be aligned using a cross-correlation procedure. Unfortunately, vis-OCT images obtained with supercontinuum sources have a higher noise floor with a pink noise characteristic (105, 150). We found that this noise floor can reduce the performance of cross-correlation. To solve this problem, we estimated the noise floor by fitting the first and last 50 pixels of an averaged A-line to a 2nd-degree polynomial. We then subtracted this fitted noise floor from each B-scan before cross-correlation. The cross-correlation step was performed using a sub-pixel shift registration algorithm (156).

4.2.10 Vessel wall segmentation with graph-search

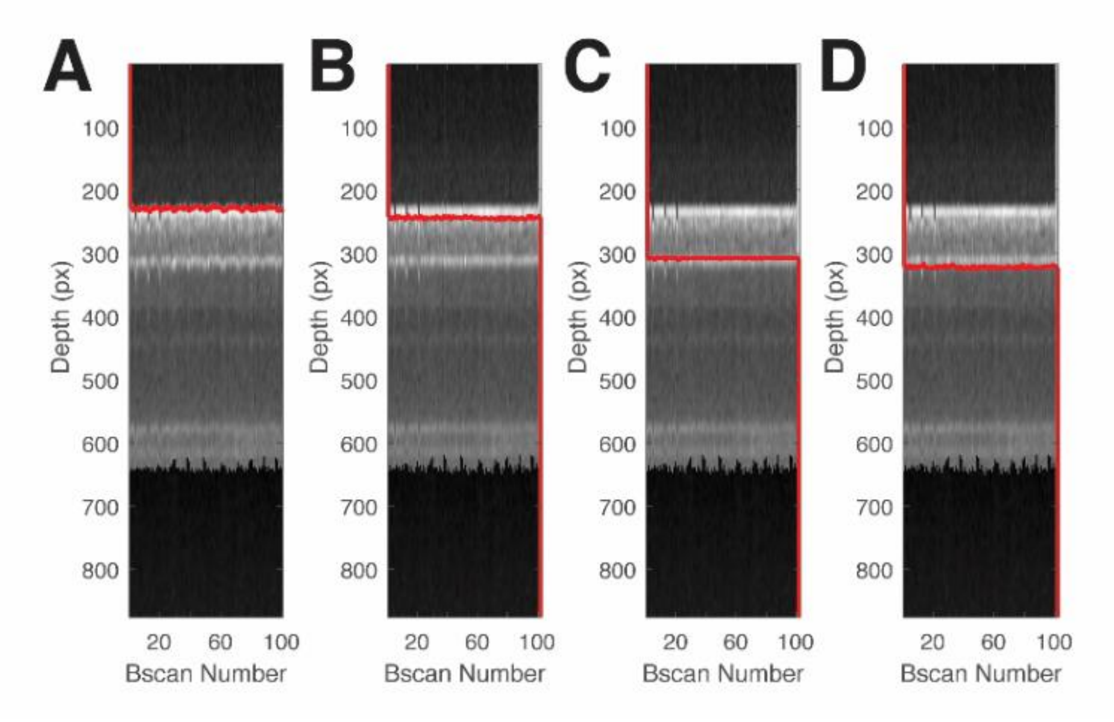

Figure 4-3: Graph-search segmentation for the anterior and posterior vessel walls. (A) Segmentation of the top of the anterior wall. (B) Segmentation of the bottom of the anterior wall. (C) Segmentation of the top of the posterior wall. (D) Segmentation of the bottom of the posterior wall. Each column shows the vessel cross-section obtained from a circular B-scan. Pixel dimension in the depth direction was approximately 0.55 μm assuming a refractive index of retinal tissue, n=1.35.

Table 4-1: Vessel wall segmentation parameters

	Upper Limit	Lower limit	Weight Type
Top of anterior wall	0 μm from ILM	2 μm from ILM	Dark to Light
Bottom of anterior wall	1 μm from top of anterior wall	11 μm from top of anterior wall	Light to Dark
Top of posterior wall	10 μm from bottom of anterior wall	80 μm from bottom of anterior wall	Dark to Light
Bottom of posterior wall	1 μm from bottom of anterior wall	11 μm from bottom of posterior wall	Light to Dark

The same graph-search design and framework from section 2.6 was applied to segment the vessel walls. Figure 4-3 shows example of graph-search based segmentation of a vessel cross-section for a selected vessel. The images shown is the final spectroscopic OCT image for the vessel, but averaged over the λ_c dimension. We searched for the vessel wall boundaries from the anterior portion of the retina towards the posterior. First, we found the top and bottom of the anterior wall (Figure 4-3(A-B)). Next, we searched for the top and bottom of the posterior wall (Figure 4-3(C-D)). Table 1 shows the search limits and weight type used for each graph cut.

4.2.11 Spectral fitting

The OCT amplitude for the posterior wall was averaged between the segmented boundaries found using graph search. The averaged OCT amplitude was then fit to the oxygenated and deoxygenated hemoglobin attenuation coefficients, using the model originally proposed by Yi et al (92). We set the W-factor to 0.2, consistent with Monte Carlo simulations performed by Chen et al. (148). Attenuation coefficients were obtained from Faber et al. (93). All twenty-three bands were used in the fitting process. For each fit, we calculated the coefficient of determination (R^2) to measure the goodness-of-fit.

4.2.12 Accuracy, bias, and precision

The 100 B-scans in each circumpapillary scan are time consuming to acquire in practice. However, our goal was to use this large number of B-scans to study how the accuracy, bias, and precision of OCT amplitude extraction and sO_2 measurements vary with the number of B-scans used. To study this, we divided the 100 B-scans into N samples of M B-scans, where M ranged from 1 to 99. B-scans were selected for each sample in sequential order. For example, to study measurements from

2 B-scans, sample #1 would have B-scans #1 and #2. Sample #2 would have B-scans #2 and #3, and so on. Given M B-scans, N was equal to M-1. This method effectively simulates acquiring an image with M B-scans and using only that data to calculate sO_2.

Accuracy is the error of measurements compared to a gold standard (GS) reference measurement. Accuracy can be quantified by the root mean square error (RMSE) of N samples (157). We chose our gold standard reference measurement to come from the best-case scenario from our data: the OCT amplitude and sO_2 measured with manual segmentation from 100 B-scans. The RMSE using M B-scans is defined as: (157)

$$RMSE_M = \left[\frac{1}{N}\sum_{n=1}^{N}\left(sO_{2;M,n} - sO_{2;GS}\right)^2\right]^{1/2}, \tag{4-1}$$

where $sO_{2;GS}$ is the sO_2 measured from 100 B-scans with manual segmentation. $sO_{2;M,n}$ is the sO_2 measured from n^th sample using M B-scans. Bias indicates whether the error is consistently negative or positive compared to the gold standard. The mean error (ME) defined in Eq. 2 gives a measure of the bias (157)

$$ME_M = \frac{1}{N}\sum_{n=1}^{N}(sO_{2;M,n} - sO_{2;GS}). \tag{4-2}$$

Precision is the spread of repeated measurements around their mean value. The standard deviation (SD) of N samples gives a measure of the precision (157).

$$SD_M = \left[\frac{1}{N}\sum_{n=1}^{N}(sO_{2;M,n} - \overline{sO_{2;M,N}})^2\right]^{1/2}, \tag{4-3}$$

where $\overline{sO_{2;M,N}}$ denotes the average value of sO_2 obtained from N samples with M B-scans per sample. Note that sO_2 is a dimensionless value between 0 and 1, and the measures of accuracy, bias, and precision defined here are in the same units as the sO_2.

4.3 RESULTS

4.3.1 Comparison of methods for OCT amplitude spectra extraction

We compared four averaging methods to extract the spectrum from the posterior wall: (1) blind averaging with manually placed straight slab, (2) cross-correlation with manually placed manual straight slab (X-Corr), (3) cross-correlation with automatic graph-search (X-Corr + GS), and (4) cross-correlation with manual segmentation (X-Corr + Manual). In blind averaging, the extracted B-scans for each vessel were displayed and a slab was manually placed near the posterior vessel wall (slab width: 11 μm). For X-Corr, a slab was placed near the posterior wall after the cross-correlation step (slab width: 11 μm). For X-Corr + G-Search, the full method was performed. For X-Corr + Manual, cross-correlation was first performed, then each A-line was plotted and the peak location of the posterior wall was selected manually (slab width: 11 μm). This method was considered the "gold standard" for our measurements. Out of the four methods, only X-Corr + G-Search method was automatic and unsupervised.

Figure 4-4 shows results from a representative blood vessel acquired in an adult rat with significant motion. Figure 4-4(A-D) show the vessel cross-sections, with the slabs indicated by the red lines. Figs. 4E-4H show the spectra from each column. Spectra from the first three methods (Figure 4-4(E-G)) were compared with the spectra from the gold standard method (Fig. 4H) on a B-scan by B-scan basis. The mean squared error between the spectral results of each method and the gold standard was computed (Figure 4-4(H-I)). Out of the three methods compared to the gold standard, the fully automatic method (X-Corr + G-Search) had the least OCT amplitude error across the spectrum (Figure 4-4I).

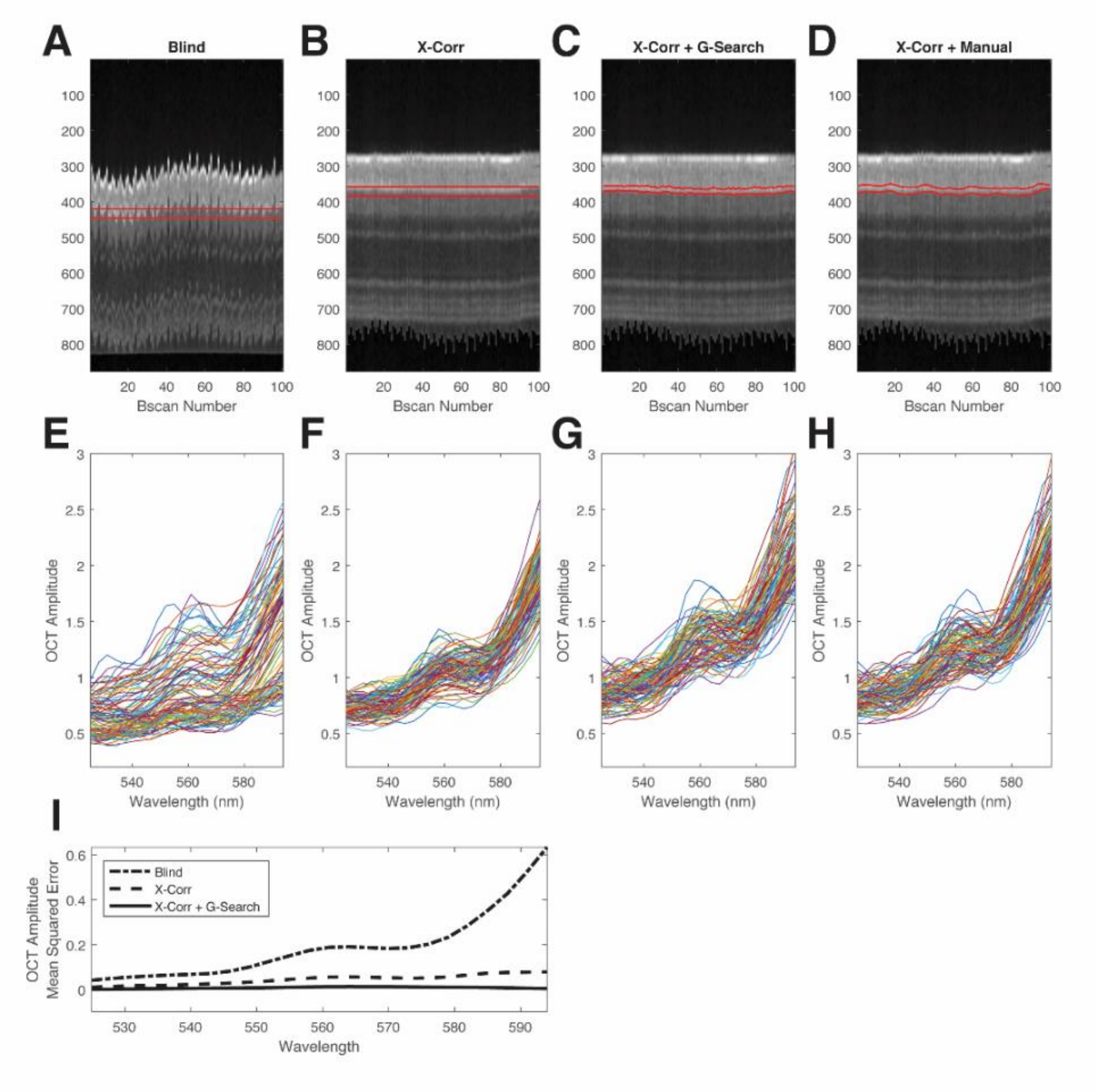

Figure 4-4: Comparison of methods to extract the average OCT amplitude from the posterior wall for a single vessel. (A) Blind manual selection of straight manual slab for blind averaging. (B) Cross-correlation with manual selection of straight slab. (C) Cross-correlation with automatic graph-search segmentation for slab selection. (D) Cross-correlation with A-line by A-line manual selection of the peak signal from the posterior wall. Red lines in (A-D) denote the region of the slabs or segmentation. (E) Measured spectra from each B-scan for blind selection. (F) Measured spectra from each B-scan for cross-correlation alone. (G) Measured spectra from each B-scan for cross-correlation with graph-search segmentation. (H) Measured spectra from each B-scan for cross-

correlation with manual selection. (I) Spectral OCT amplitude mean square error compared with the gold standard.

4.3.2 Comparison of accuracy, bias, and precision for OCT amplitude and sO2

We studied the accuracy, bias, and precision for different numbers of B-scans used to compute the average OCT amplitude and sO_2. We chose a reasonable internal gold standard as the best possible scenario in our dataset. This was the case of having 100 B-scans used for OCT amplitude averaging combined with manual peak selection of the vessel wall. Measurements of accuracy and bias used the gold standard measurement, while measurements of precision did not use the gold standard (see section 4.2.12).

Cross-correlation with graph-search segmentation was the most accurate technique for both OCT amplitude extraction and sO_2 measurements. The plots in Figure 4-5(A) and Figure 4-5(D) show the accuracy for the three methods. The gold standard (Manual) is shown as the green lines. As the number of B-scans (M) increases, the RMSE decreased for both OCT amplitude and sO_2. The X-Corr + G-Search line had the closest performance to Manual but did not completely overlap with the curve, suggesting residual error between the two methods. In addition, we also observed that the standard error of the mean (SEM) of the RMSE across vessels (see error bars in Figure 4-5(A)) were the smallest with the X-Corr + G-Search method. This suggests that the X-Corr + G-Search method had more consistent RMSE values across different vessels.

We observed a negative bias for both OCT amplitude and sO_2. We attribute this to the fact that imperfect segmentation sometimes includes non-vessel wall signals, which tend to bias the OCT amplitude in the negative direction (Figure 4-5(B)). This negative bias of the OCT amplitude further contributed towards biasing the sO_2 calculation in the negative direction (Figure 4-5(E)). Out of all the methods, X-Corr + G-Search segmentation had the least amount of bias compared to the gold standard. Again, we also observed that the SEM of the ME was smallest with the X-Corr + G-Search method (error bars in Figure 4-5(B, E)), which means the bias is more consistent across vessels.

We also investigated the precision of the methods. We observed that the precision increased (average standard deviation decreased) as the number of samples increased; however, no method improved the mean precision over another (Figure 4-5(C,F)). The blind and X-Corr methods had larger variance in their precision measurements across the vessels (see error bars in Figure 4-5(C)) compared with X-Corr + G-Search and Manual. Notably, the X-Corr + G-Search and Manual had similar precision mean values and similar variance in precision across vessels, which suggests that the X-Corr + G-Search method was close to the Manual method in terms of achieving high precision.

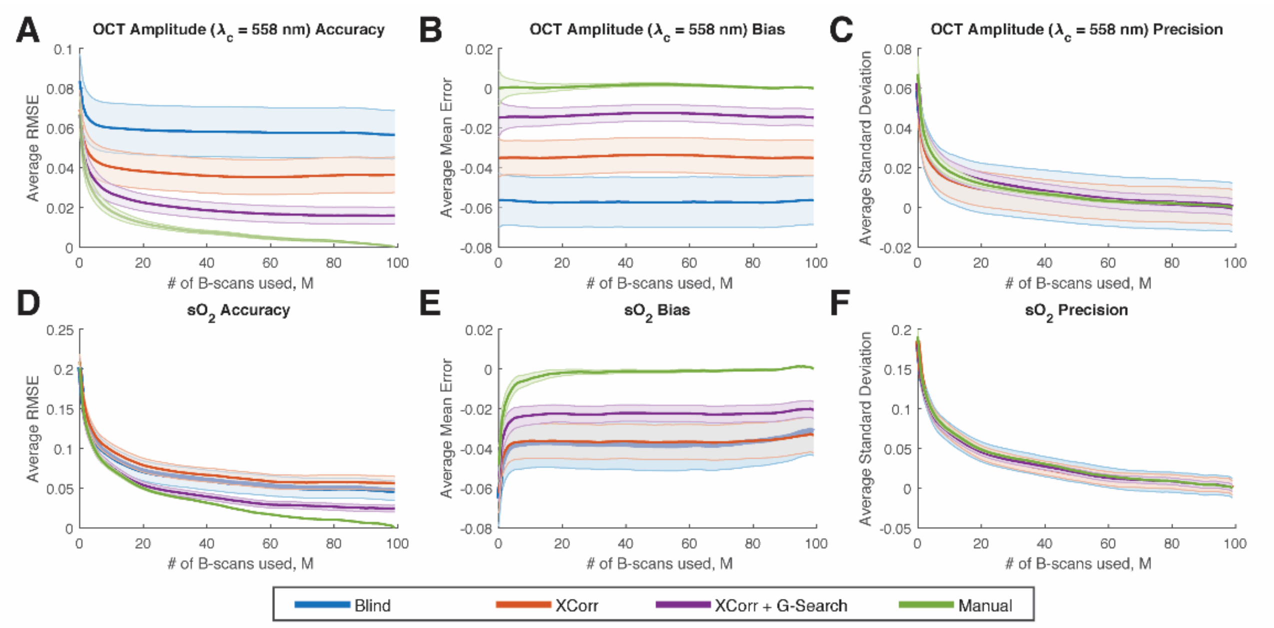

Figure 4-5: Accuracy, bias, and precision for OCT amplitude (at λ_c=558 nm) and sO_2 for different number of B-scans used for averaging. (A-C) Accuracy, bias, and precision for OCT amplitude (at λ_c=558 nm) vs. number of B-scans used per sample. (D-

F) Accuracy, bias, and precision for sO_2 vs. number of B-scans used per sample. Error bars indicate standard error of the mean across vessels.

We were also interested in the number of averaged B-scans required to achieve accurate and precise sO_2 calculation. Based on the results in Figure 4-5, we saw diminishing benefit in terms of accuracy, bias, and precision after ~20 averaging. Therefore, we believe that a reasonable number of averaged B-scans for our measurement method and imaging system would be between 20 and 40.

4.3.3 Automatic sO_2 measurements

Figure 4-6(A) and Figure 4-6(B) show representative vessel wall spectra from an artery (vessel #7 in Figure 4-2) and vein (vessel #8 in Figure 4-2), respectively (black lines). The error bars indicate the standard deviation of the OCT amplitude across the 100 B-scans used. The red dashed lines show the least-squares fits, which had good agreement to the data according to the R^2 values.

Table 4-2 shows the sO_2 values for the all the arteries and veins in Figure 4-2. An alternating pattern of high-oxygenated and medium-oxygenated vessels is observed, which is consistent with the alternating pattern of arteries and veins in the rodent eye. The average arterial and venous sO_2 values (mean ± standard error of mean) were 0.96 ± 0.01 and 0.74 ± 0.03, respectively. These measurements are also consistent with previous studies using vis-OCT (92, 158). The R^2 values were all above 0.8, with most being above 0.9, indicating that the regression predicts the measured data reasonably well.

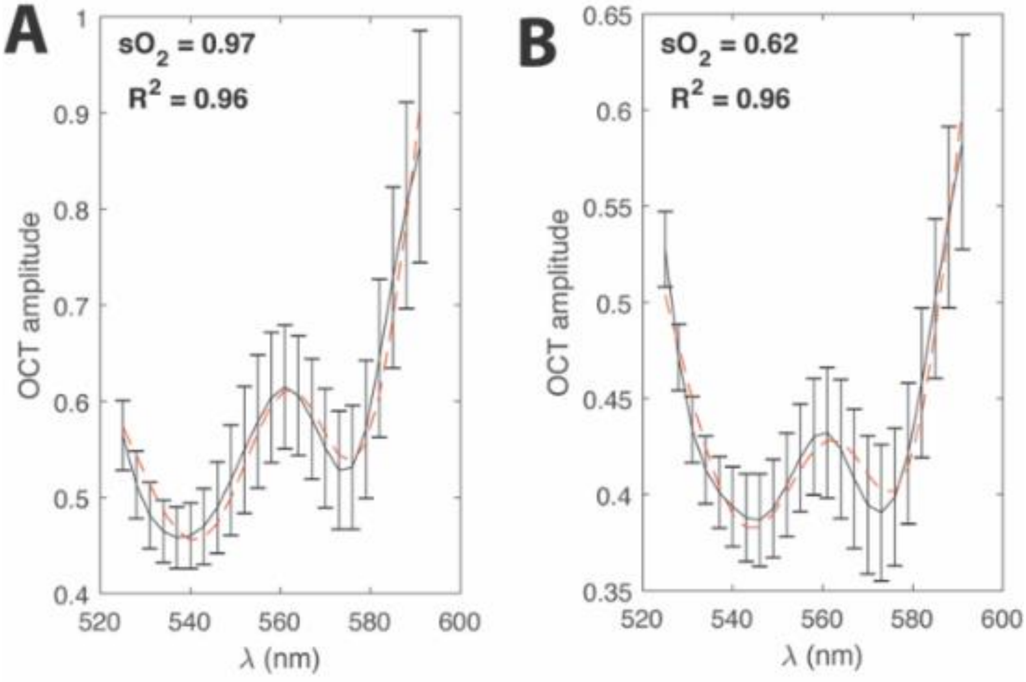

Figure 4-6: Spectral fitting. (A) Example of the least-squares spectral fit for an artery (vessel number 7 from Fig. 2). (B) Example of a least-squares spectral fit for a vein (vessel number 8 from Fig. 2). Black lines denote the measured average OCT amplitude after the graph-search algorithm. Error bars show the standard error of the mean of the OCT amplitude.

Table 4-2: Automatic sO_2 measurements obtained with graph-search segmentation.

	1	2	3	4	5	6	7	8	9	10	11	12	13	14
sO_2	0.99	0.75	0.99	0.64	0.99	0.85	0.97	0.62	0.88	0.79	0.96	0.66	0.97	0.85
R^2	0.84	0.97	0.84	0.93	0.84	0.94	0.96	0.96	0.89	0.97	0.97	0.96	0.96	0.90

4.4 DISCUSSION

We developed a method to solve the OCT amplitude extracting problem when performing vis-OCT oximetry. We combined circumpapillary scan (Figure 4-2), cross-correlation, and graph-search segmentation of the vessel walls into an automatic method to calculate sO_2 (Figure 4-3). Despite the lack of an external gold standard, we used an internal gold standard to investigate the accuracy, bias, and precision of our measurements (Figure 4-4 & Figure 4-5). This method achieves highly accurate measures of sO_2 with minimal bias compared to an internal gold standard. The variance in precision across vessels is also near-optimal. A similar analysis can be performed empirically on other vis-OCT systems, as results will vary based on the noise of the light source and performance of the spectrometer.

Our study evaluated the accuracy of X-Corr + G-Search compared with an internal gold standard. The accuracy depends mostly on the algorithm's ability to correctly segment the signal from the posterior vessel wall. In addition, the accuracy will also be affected by motion, as moving subjects add an additional noise component to the measured spectra. This motion is also especially exacerbated when performing physiological studies of hypoxia, due to an increased respiratory rate when the amount of inhaled O_2 is reduced. We found that out of all the techniques in this study, X-Corr + G-Search performed the closest to manual peak selection of the vessel wall. Unfortunately, we still observed a bias in the measurement compared with the gold standard, which we attribute to the imperfect nature of automatic segmentation. Even with the techniques in this study, some background or non-vessel wall OCT signal was inevitably selected by the automatic segmentation algorithm, which led to negative bias in the OCT amplitude. This propagated to a negative bias in the sO_2. Despite this issue, we saw that the X-Corr + G-Search method had the smallest bias out of all the methods and the smallest variance of the bias across vessels. Future techniques will improve the segmentation to further minimize the error.

We are unaware of any current method that can serve as an independent gold standard for sO_2 measurements of individual vessels of the eye. Currently, the gold standard for retinal oxygen measurements is microelectrode-based measurement of oxygen partial pressure (pO_2) in the retina

(28, 159). Unfortunately, these measurements are highly invasive, laborious to perform, and difficult to directly correlate with sO_2 measurements from within blood vessels. We note that the model used to fit the spectrum is the same as that originally proposed by Yi *et al*. (92). This model has been studied and verified *in silico* with Monte Carlo simulations and OCT reconstruction simulations (105, 148). Studies have also shown good agreement for this model *in vitro* by vis-OCT of whole blood mixed with varied oxygenation levels (91, 158). In addition, measurements of the retinal arteries *in vivo* corresponded well with the peripheral pulse oximetry measurements (158).

Our study also evaluated the precision of the amplitude and sO_2 measurements. We observed that the mean precision measures were similar between the methods. The precision includes the multiple sources of noise in OCT imaging. This includes noises from spectrometer camera, shot noise, and RIN noise. In addition, motion also adds a noise component to the OCT amplitude extraction. The variances of the precision across vessels were larger with the Blind method and X-Corr method, which signifies that some of the vessel measurements had more noise components. Since this variance decreased after adding G-Search to the X-Corr, the additional noise components likely came from motion. Future improvements in supercontinuum light sources with higher repetition rates and in spectrometers with better optical designs in the visible range, are expected to improve the precision further.

We found that averaging A-lines is important for calculating sO_2, even when manual peak segmentation was used. In this study, we found that there were diminishing benefit in OCT amplitude and sO_2 accuracy after ~20 B-scans (~120 A-lines). Results from <20 B-scans showed higher values of RMSE, ME, and SD for sO_2 measurements. Unfortunately, the exact number of averages to use cannot be directly transferred to all vis-OCT devices, since each has different light sources, camera integration times, and spectrometer designs. However, we can glean, as a general rule-of-thumb, that averaging >120 A-lines would provide accurate measurements of sO_2.

The method presented here for vessel wall segmentation is not limited to circumpapillary scans. To apply these methods to raster scans, vessel segmentation of the raster scans, akin to Fig. 2, would be required via either manual segmentation or automatic detection. Once these A-lines are collected, sections 4.2.9 to 4.2.11 could be applied. However, we caution that measuring sO_2 from along the length of a vessel combines different parts of the vessel for the measurement. Different parts of the retina receive different amounts of illumination, especially if there are cataracts or blood in the vitreous, which increases the variance of the collected spectra and biases the results. Moreover, different parts of the vessel may have different levels of oxygenation, especially in disease states (160). In this study, we sought to avoid this by using circumpapillary scans with fixed diameter, which repeatedly sampled vessels at the same retinal location.

Oxygenation measurements made with this method can be further extended to metabolic rate of oxygen measurements by combining sO_2 with retinal blood flow from Doppler OCT (144, 158). In addition, retinal oximetry measurements may be applicable to different animal models of glaucoma (161), diabetic retinopathy (9), retinopathy of prematurity (144), vein occlusions, and age-related macular degeneration (86, 162).

Our algorithm is ultimately applicable to circumpapillary scan data from human patients. Although NIR OCT is well established for human retinal imaging, vis-OCT presents a set of new challenges for OCT researchers. Concerns about visible-light laser safety have limited the power for human imaging from 150 to 226 µW on the cornea (145, 163). This limitation, coupled with the high RIN of supercontinuum light sources, can be a hurdle for achieving high signal-to-noise ratio images. In addition, due to the bright visible scanning pattern, patients' eye fixation is more challenging, resulting in more motion artifacts. Finally, for large diameter vessels, the round-trip attenuation may prevent retrieval of the vessel wall signal. Despite these challenges, future studies will likely find innovative solutions to these technical issues to enable accurate human retinal oximetry.

4.5 CONCLUSION

In conclusion, we have shown automatic measurements of sO_2 from circumpapillary scans for the first time. We have used a unique approach involving graph-search segmentation to obtain the boundaries of the anterior and posterior vessel walls. Moreover, we have provided an in-depth analysis method to study the accuracy, bias, and precision for averaging using an internal gold standard. This study lays the foundation for future investigations, where large numbers of datasets must be analyzed automatically.

Chapter 5

Simulation, calibration, and correction of spectroscopic sensitivity rolloff for spectroscopic OCT

5.1 INTRODUCTION

Spectroscopic optical coherence tomography (SOCT) provides depth-resolved spectral information from backscattered light (164, 165). SOCT can image distinct spectral features from endogenous contrasts, including cell nuclei (166), lipids in atherosclerotic plaques (167), and backscattering coefficients from different tissue types (168). In retinal imaging, SOCT serves as the foundation of visible-light OCT oximetry (6), a technique which measures the relative concentrations of oxygenated and deoxygenated hemoglobin to calculate the oxygen saturation of hemoglobin (sO_2). The contrast in OCT can also be enhanced by SOCT using exogenous contrast agents, such as gold nanorods (169-171) and gold nanocages (172).

The hardware of SOCT is the same as spectral-domain OCT (SD-OCT), but the software for analysis differs. In spectral-domain OCT (SD-OCT), a broadband light source is used, and a spectral interferogram is collected by a spectrometer. The frequency of the interferogram with respect to wavenumber encodes the depth of reflectors in the sample. Therefore, in conventional SD-OCT, a Fourier transform (FT) directly converts the interferogram into the depth-resolved image. However, the amplitude modulation of the interferogram contains the reflectivity spectrum, which is lost by direct FT. In SOCT, to resolve both depth and spectral information, a short-time FT (STFT) is performed instead of direct FT. The spectral interferogram is multiplied by short windows in k-space, and the FT is applied to each windowed spectral interferogram. The STFT procedure generates a series of depth-resolved images, where the amplitude in each image corresponds to the reflectivity spectrum.

The fundamental assumption of SOCT is that the amplitude of the interferogram purely contains the spectral information from the sample. However, the spectrometer in SD-OCT possesses a low-pass transfer function, which reduces the fringe visibility for higher frequencies of the interferogram (173). This causes reflectors at depths further from the zero-delay position to appear with a diminished OCT signal amplitude. In the OCT literature, the spectrometer's transfer function is referred to as sensitivity rolloff (SR). The SR is caused by the limited spectral resolution of the spectrometer, which is due to two main factors: (1) the finite pixel size of the camera pixel elements and (2) the finite point-spread function (PSF) width of the spectrometer's imaging system (76). SR is usually reported as OCT amplitude decrease (in dB) at 1 mm from the zero-delay.

In previous studies, the SR is usually measured for the entire k-space band of the spectrometer. However, since SOCT uses narrow bands in k-space, the SR is hypothesized to be different for each spectral band. In other words, the SR for SOCT is band-dependent, which we refer to as spectroscopic SR (SSR). If the SSR is not properly calibrated and corrected for, the spectrum information obtained by SOCT will be distorted. Moreover, placing the sample at different depths within the imaging range will yield different spectral measurements.

The main aim of this study was to investigate the effects of SSR in SOCT. We first review the theory of the SD-OCT including the effects of unequal k-space sampling and finite spectral resolution on the spectrometer's transfer function. We then discuss careful wavelength calibration for a vis-OCT spectrometer. Using this wavelength calibration information, we simulated the SSR.

We then demonstrate measurement of the SSR for a real spectrometer. Finally, we apply correction of the SSR for a practical imaging application.

5.2 THEORY

A simple SD-OCT system is shown in Fig. 1(A). The spectral interferogram between the electric fields from the reference and sample arms is captured by a grating-based spectrometer in the detection arm. Eqn. 1 represents the recorded spectral interferogram, taking into account the unequal-k space sampling and the finite spectral resolution.

$$I(q) = G\big(f_k(q)\big) * (I_{background} + I_{ref} + I_{sample} + 2\sqrt{I_{ref}}\sqrt{I_{sample}}\cos(2f_k(q)z)) \tag{5-1}$$

Here, q represents the pixel element on the line camera. $I_{background}$ refers to non-coherent light. I_{sample} and I_{ref} refer to the intensity (squared electric field) from the sample and reference arms, respectively. $f_k(q)$ refers to the non-linear mapping that gives the corresponding angular wavenumber (k) value for pixel element q. $G(k)$ is the spectrometer's transfer function.

The spectrometer has two important physical phenomena for modelling SOCT. First, the spectrometer records the spectral interferogram with unequal-k spacing. This is due to the dispersion of the grating, which is proportional to wavelength, and the aberrations from the focusing lens. Due to the Nyquist sampling theorem, the maximum frequency of the spectral interferogram before aliasing occurs is limited by the k-spacing. The maximum imaging depth can be shown to be:

$$z_{max,q} = \frac{\pi}{2\delta k_q} \tag{5-2}$$

where δk_q is the amount of k-space covered by the pixel element with index q. Note that because certain pixels of the spectrometer may have larger k-spacing, the spectral interferogram will alias at a shorter imaging depth for those pixel elements specifically.

Second, the spectrometer spectral resolution is finite, due to the fixed camera element size as well as the point spread function of the focusing lens. This is modelled in the k-domain by convolution with $G(k)$. The FT of $G(k)$ can be shown to be (76):

$$g(z) = \exp[-a^2 \left(\frac{\delta k_q}{\delta x}\right)^2 z^2] \frac{\sin(\delta k_q z)}{\delta k_q z} \tag{5-3}$$

where a is the full width at half maximum (FWHM) of the PSF, and δx is the pixel element size in the x-direction. The first exponential term represents the effects of a Gaussian distributed PSF on the camera pixel element. The second term represents a sinc shaped falloff, which comes from the finite pixel element size. Note that although the pixel elements are physically the same size, due to the unequal k-spacing, each pixel element integrates different amounts of the spectral interferogram. Therefore, SSR depends strongly on the k-spacing between spectrometer elements.

5.3 METHODS

5.3.1 Calibration of pixel-to-wavelength mapping for visible light spectrometers

Measurements with spectroscopic OCT require precise wavelength mapping for each spectrometer pixel element. The simplest way to map the wavelength distribution of the spectrometer is to use spectral calibration lamps, which contain gas mixtures with known spectral lines. The position of these spectral lines on the camera can be fit to a polynomial or to a geometric optics model of the spectrometer (174). Unfortunately, the number of spectral lines in the visible range is limited for the neon, mercury and argon lamps, making the fitting imprecise in wavelength regions without data points. Other methods have been proposed for wavelength mapping, which rely on careful measurements of the phase of the interferogram (175, 176). Assuming absent dispersion mismatch, the phase is linear in wavenumber, and can therefore be used to map it. These methods, however, require careful experiments and phase stability.

To map the spectrometer's wavelength distribution, we used a recent method by Uribe-Patarroyo et al. (133). Spectral interferograms were acquired with the sample mirror positioned every ~40 um throughout the imaging range. The Uribe-Patarroyo method finds the optimal wavelength distribution mapping that minimizes the non-linear phase of the interferograms across all depths. The advantages of this technique are that the system's dispersion does not have to be perfectly matched between the two arms, and the sample arm mirror does not have to be precisely positioned. The algorithm returns a relative wavenumber mapping, $f_{k,rel}(q)$, for each pixel element, which can be used to interpolate the fringes from unequal k-spacing to equal k-spacing. For SOCT, however, the relative wavenumber mapping must be converted to absolute wavenumber mapping such that the center locations of the STFT windows can be determined.

To map the relative wavenumber mapping to absolute wavenumber mapping, we measured spectral lines from a neon (Ne) and mercury/argon (Hg/Ar) spectral calibration lamps (Newport Optics). An example of the Ne and Hg/Ar lamp spectra is shown in Fig. 2(B). Note that there is an absence of spectral calibration points for the pixel numbers 1 to 1000, which would making fitting calibration methods inaccurate. The wavenumbers of the spectral lines (radians/mm) were fit to the following equation to find the coefficients c_1 and c_2 in (radians/mm).

$$f_{k,abs}(q) = c_1 \frac{f_{k,rel}(q)}{N-1} + c_2 \qquad (\ 5\text{-}4\ )$$

N is the number of pixel elements. $f_{k,abs}(q)$ is the final absolute wavenumber (radians/mm) mapping for each pixel q. The wavelength mapping for the spectrometer is shown in Fig. 1(C).

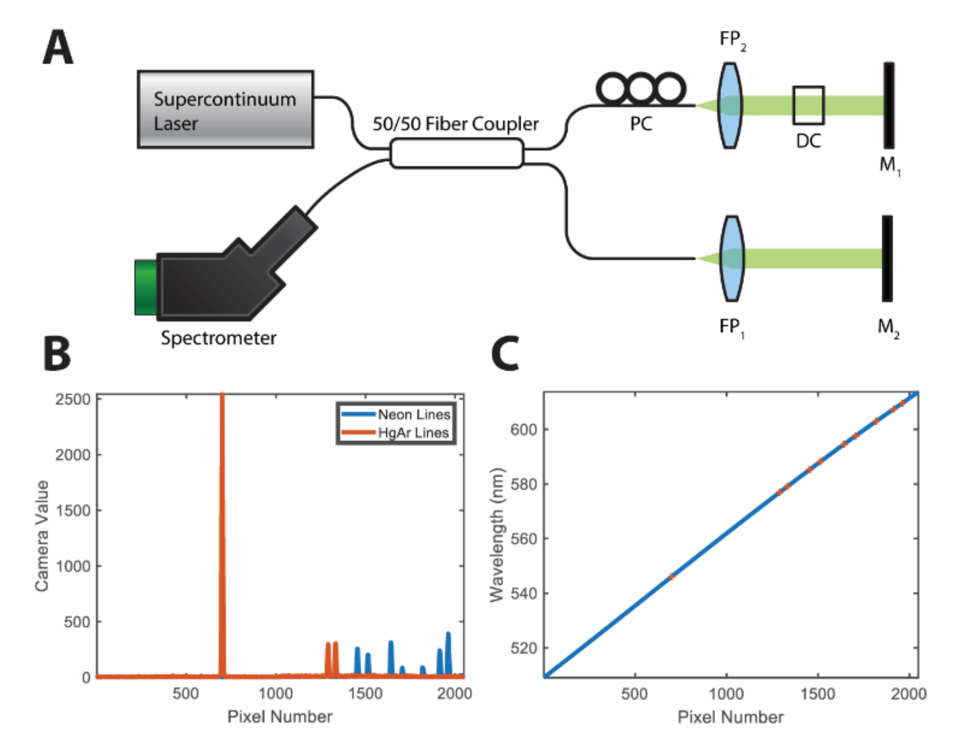

Figure 5-1: Calibration of pixel-to-wavelength mapping. (A) Setup of interferometer. (B) Calibration lamp spectral lines. (C) Final wavelength mapping after fitting the relative wavenumber mapping to the spectral lines. The red points indicate the positions of the measured spectral lines from Fig. 1(C).

5.3.2 Simulation of spectroscopic sensitivity rolloff

To simulate SSR, we generated ideal interferograms using Eq. 1. We then performed SOCT on the interferograms. The interferograms were first upsampled using zero-padding technique (ideal interpolation), by taking the FFT, zero-padding to increase the array to 4 times the length, and then taking the inverse FFT. The zero-padding method improves the noise performance of linear interpolation from unequal k-spacing to equal k-spacing (136, 137). The upsampled fringe was then interpolated from unequal k-spacing to equal k-spacing using linear interpolation. We performed the STFT, by windowing the spectral interferogram in k-space and taking the FT. We applied 23 Gaussian windows with center wavelengths (λ_n) ranging from 525 nm to 591 nm, equidistantly spaced by 3 nm. The FWHM in the λ-space was 13 nm (0.25 μm^{-1} in k-space), which corresponds to an axial resolution of ~10.9 μm at 568 nm. These values were consistent with those previously used for vis-OCT oximetry methods (105, 177). The center wavelength, band spacing, and bandwidth can be tailored to specific SOCT applications.

5.3.3 Measuring spectroscopic sensitivity rolloff

Spectral interferograms were recorded with the interferometer shown in Fig. 1(A) by moving the sample arm mirror throughout the entire imaging depth range in ~40 um steps. At each z-position, four types of spectrums were recorded. The first spectrum was the background spectrum, $I_{background}$, which was collected with both the sample and references arm blocked. This records the incoherent light from backreflections in the interferometer and noise biases of the camera. The second spectrum I_2 was with the reference arm open and sample arm closed. The third spectrum I_3 was with the reference arm closed and sample arm open. Note that $I_{ref} = I_2 - I_{background}$ and $I_{sample} = I_3 - I_{background}$. The fourth spectrum wa s with the reference arm and sample arm both open, which measures $I(q)$ from Eq. 1. For each type of spectrum, 5000 measurements were taken to obtain average measurements. Fringes were only averaged after the STFT due to potential phase noise. The SSR was measured by performing the SOCT procedure and taking the peak height at each measured depth. The peaks were fitting with splines to interpolate the rolloff for the entire depth range.

5.3.4 Numerical correction for residual dispersion mismatch

Correction for residual dispersion mismatch is paramount for obtaining accurate measures of the SSR. Dispersion mismatch results in non-linear phase terms, which cause chirping in the spectral interferogram. This leads to broadening of the axial PSF, and attenuation of the PSF amplitude. The latter leads to inaccurate SSR measurements. Numerical dispersion compensation can be applied by multiplying the fringe by a complex exponential phase term, given by the equation $\Phi_{Disp}(k) = c_1(k - k_0)^2 + c_2(k - k_0)^3$, where c_1 and c_2 are coefficients to be estimated numerically (138, 139).

Although many optimization techniques have been proposed to find c_1 and c_2, most techniques are not optimized for SOCT. We found the optimal coefficients by using the apparent position of the mirror within each of the STFT bands. In the ideal case, correction of the dispersion mismatch will result in the location of the mirror peak being at the same position in each of the STFT bands. However, if dispersion mismatch is not correctly cancelled, the mirror position will be at different apparent positions across the bands. If we denote the mirror position in band λ_n as $z_{mirror}(\lambda_n)$, then we can numerically solve the following least-squares optimization problem to find c_1 and c_2.

$$\min_{c_1,c_2} \sum_{n=1}^{M} \left(z_{mirror}(\lambda_n) - \frac{1}{M} \sum_{n=1}^{M} z_{mirror}(\lambda_n) \right)^2 \qquad (5\text{-}5)$$

5.4 RESULTS

5.4.1 Simulation of the spectroscopic sensitivity rolloff

Fig. 2(A) and Fig. 2(B) graphically illustrate the unequal k-spacing distribution on the first ten elements and last ten elements of the spectrometer's camera, respectively. Although the pixel elements are physically evenly spaced (red dots), they integrate different amounts of k-space (blue dots). The differential of the wavenumber mapping across the spectrometer, corresponding to $\delta k_q = df_k(q)/dq$ is plotted in Fig. 2(C). In our spectrometer, the elements corresponding to lower wavelengths (smaller pixel number) had larger k-spacing, while the elements corresponding to higher wavelengths (larger pixel number) had smaller k-spacing. This is likely a general phenomenon in all grating-based spectrometers because the diffraction grating disperses the incident light proportional to λ.

Fig. 2(D) shows the result of the simulated SSR for a spectrometer with a perfect focusing lens but a finite pixel element size (i.e. $a = 0$ for Eq. 3). We can clearly see that shorter wavelength bands have a faster SR than longer wavelength bands. In addition, we also see that shorter wavelength bands (525 nm to 555 nm) begin to alias at a depth shorter than the overall full spectrum imaging range, as expected by Eq. 2.

Fig. 2(D) shows the result of the simulated SSR for a spectrometer with a finite spectrometer PSF (a=4.5 microns) but a finite pixel element size. We can see a significantly different rolloff function for different spectral bands.

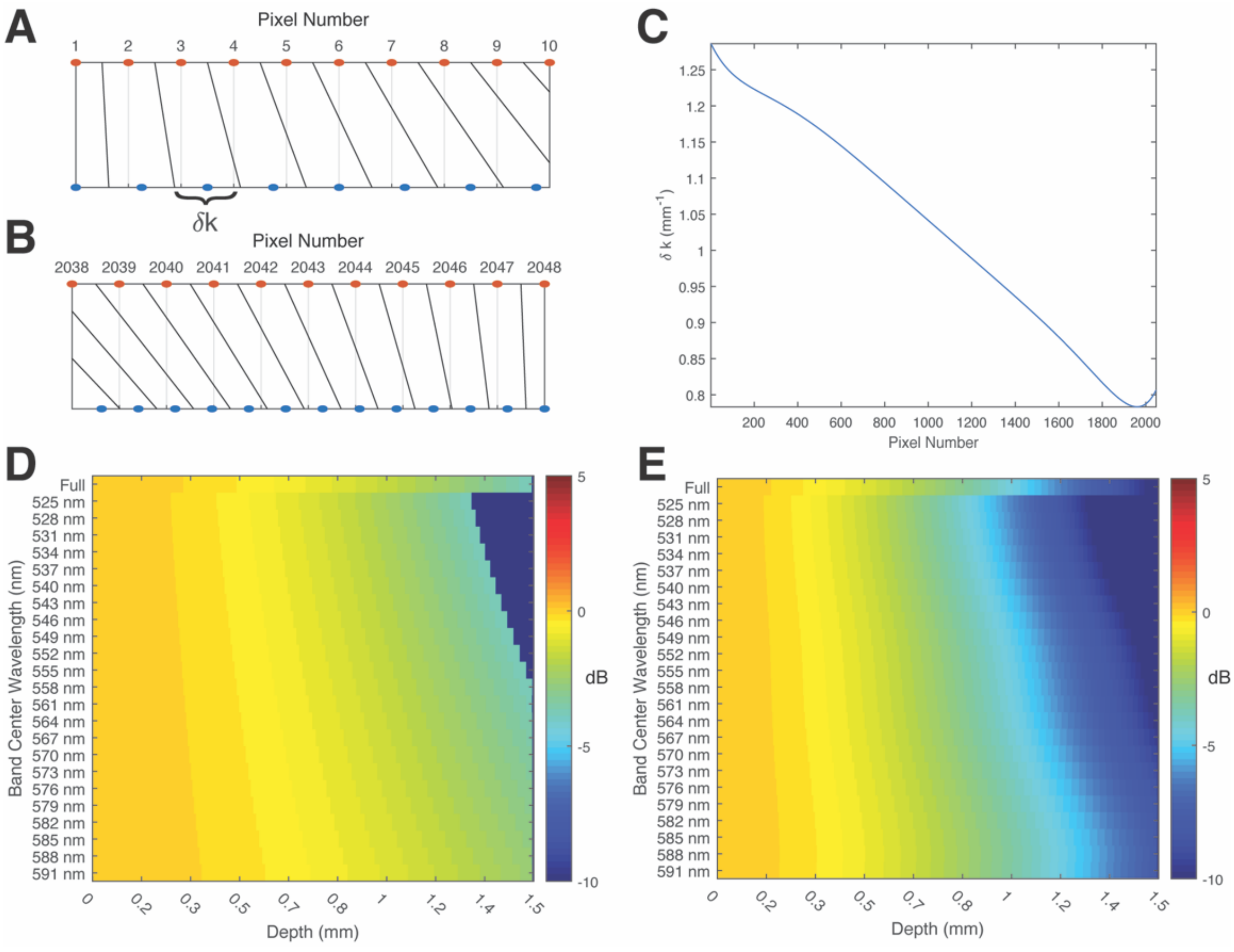

Figure 5-2: Simulation of spectroscopic sensitivity rolloff. (A) Illustration of k-spacing for pixel elements 1 to 10. (B) Illustration of k-spacing for pixel elements 2038 to 2048. (C) Plot of the k-spacing versus spectrometer pixel number. (D) Simulated SSR for a finite pixel element size (10 um) with a perfect lens PSF. (E) Simulated SSR for a finite pixel element size (10 um) with a lens PSF with a = 4.7 um.

5.4.2 Measurements of the spectroscopic sensitivity rolloff

Fig. 3(A) shows example of the four spectrum measurements acquired at z=~200 um. The reference arm (yellow curve), sample arm (red curve), and background term (green curve) are shown as averages. The DC term was computed from Eq. 1 (purple curve). Fig. 3(B) shows the fringe after subtraction of the DC term and normalization by $2\sqrt{I_{ref}}\sqrt{I_{sample}}$. Since this fringe is from a z-position close to the zero-delay, there is minimal SSR, and the fringe amplitude is flat across the spectrum.

Fig. 3(C) illustrates the SSR of the spectrometer. The Hilbert transform of the normalized, DC-subtracted fringes across all the measured depths is plotted. Close to the zero-delay, the fringe height is spectrally flat, as expected. However, as the fringe frequency increases (larger distance from zero-delay), the normalized fringe shows decreased fringe visibility as indicated by the decreasing amplitudes. However, we see that the side of the spectrometer with smaller wavelengths has a faster rolloff in amplitude than the side with longer wavelengths.

Fig. 3(D) shows the peak positions (filled circles) of the mirror after STFT processing. The solid lines show the spline fits to the measured data. This data forms the basis for the SSR calibration curve of this spectrometer.

Fig. 3(E) shows the SSR at a depth of 1 mm. There is ~2 dB difference in amplitude between the lowest band (525 nm) and the highest band (594 nm). Therefore, the highest band has a signal about 1.26 times higher than the lowest band.

Fig. 3(F) shows the SSR correction table, which can be used to correct SOCT and compensate for the SSR. Note its similar qualitative appearance to the simulated SSR found in Fig. 2(E).

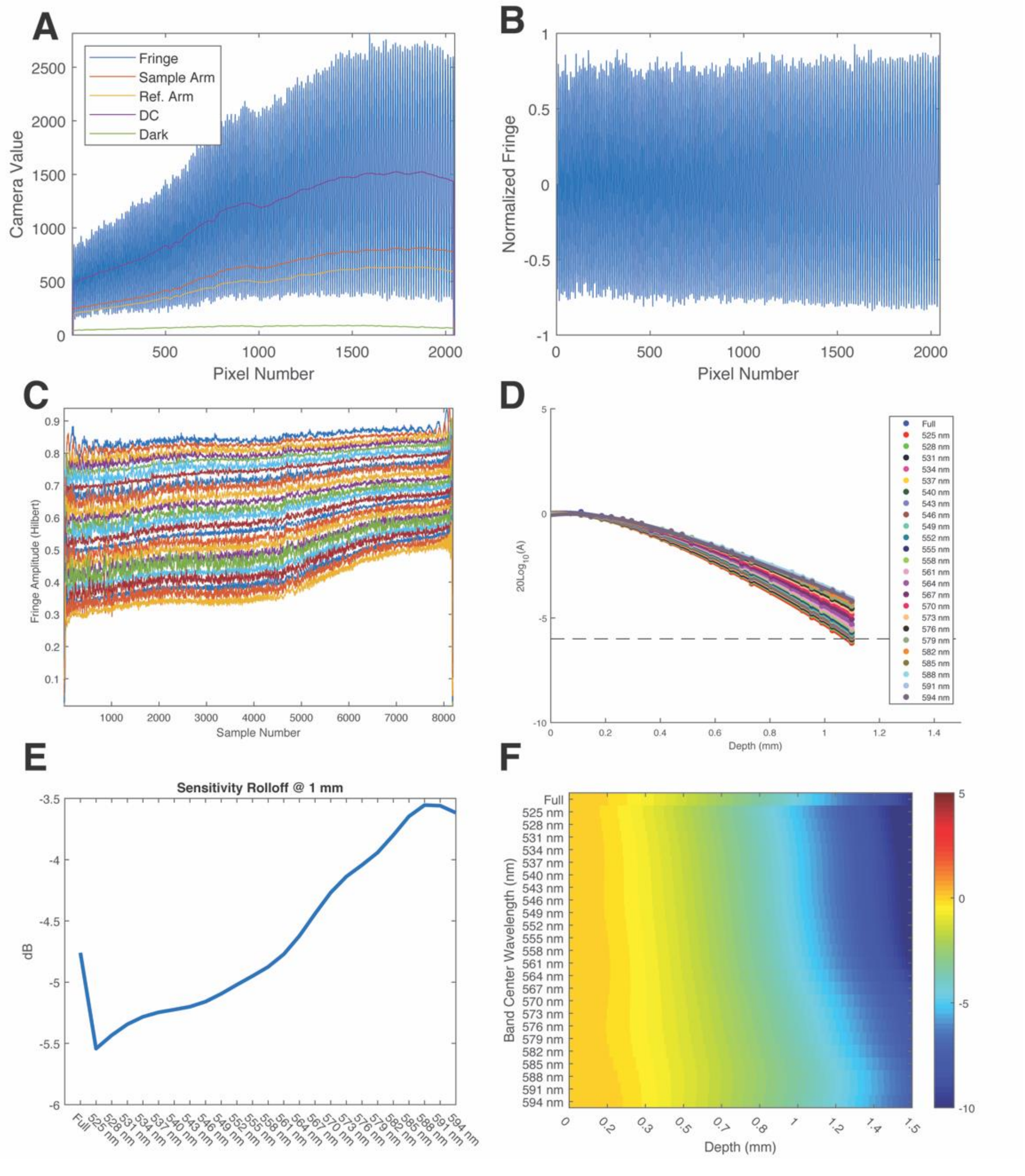

Figure 5-3: Measurement of spectroscopic sensitivity rolloff for a visible-light spectrometer. (A) Example measurements of the four types of spectrums taken at each mirror position. (B) The fringe after DC subtraction and normalization by the reference and sample arm square-root intensities. (C) Hilbert transform of the fringes over the depth range showing the SR and SSR. (D) Measured peak heights of the axial PSF versus

depth and center wavelength. (E) SSR across the spectral bands at 1 mm. (F) SSR calibration matrix for correcting SSR in SOCT.

5.5 DISCUSSION

For the first time, this article discusses and presents the phenomena of SSR for SOCT. We started from the theoretical model of the spectrometer's transfer function in SD-OCT to show where the SSR arises from. We carefully measured the k-spacing mapping for a vis-OCT spectrometer, and used it to simulate the SSR for an ideal spectrometer with a perfect imaging system as well as one with a fixed spot size. To verify our predictions, we then demonstrated the measurement of the SSR from the same vis-OCT spectrometer. From our measurements, we derived a true SSR calibration map, which can be applied to SOCT images to correct for the SSR.

In this study, we used a professionally designed vis-OCT spectrometer, which was purposefully manufactured for OCT imaging in the visible range. Due to the careful manufacturing and alignment of the spectrometer's components, the full band sensitivity rolloff at 1 mm was only ~4.75 dB. However, in our experience, custom-built laboratory spectrometers can have more severe overall rolloff. In previous studies, full band SR of 5-10 dB/mm have been reported. A larger full band SR can indicate a more severe SSR than seen in this demonstration. Therefore, it is advised that when performing SOCT that the SSR be measured and corrected for as described in this study.

From our model, it was apparent that the k-spacing mapping is an important component to the SSR. A question arises as to whether a spectrometer could be designed to avoid the SSR. Previous studies have investigated the design of spectrometers with an equal k-space mapping (178, 179), which would in theory remove some of the SSR. However, the imaging PSF of the spectrometer is still unlikely to be equal in size across the field due to aberrations in the imaging lens. Moreover, in practice, imperfect alignment of the spectrometer will also cause some SSR to exist.

When performing SOCT on tissue samples, it may be possible to place the image close to the zero delay, which avoids most of the SSR. However, there are circumstances when this is not possible especially in *in vivo* SOCT. For example, when performing human retinal oximetry with vis-OCT, patient movement is inevitable (145), and the retinal image will be found at different distances from the zero delay in different B-scans. In such circumstances, the SSR will certainly affect the measured spectra and must be accounted for.

5.6 CONCLUSION

The SSR is an important attenuation factor which affects the measured spectrum in SOCT. Not only does it attenuate the measured spectrum, but it may change the spectrum's shape, leading to erroneous measurements and conclusions. We have demonstrated the underlying theory and experimental protocol for simulating and measuring the SSR, so that it can be compensated in SOCT. This work will improve the accuracy of SOCT measurements in future studies.

Chapter 6

Inner retinal oxygen metabolism in the 50/10 oxygen-induced retinopathy model

6.1 INTRODUCTION

Retinopathy of prematurity (ROP) is a major cause of blindness in children. In the United States alone, ROP affects approximately 550,000 preterm infants born each year (~11% of births) (180), primarily premature infants with very low birth weight and gestational age (181). A biphasic hypothesis has been proposed to explain the pathogenesis of the disease. At birth, the retinas of premature infants are incompletely developed and have an avascular peripheral zone (182). In the first phase, hyperoxia occurs due to inhalation of either room air or supplemental oxygen, and suppresses hypoxia-induced vascular growth factors, leading to a delay in vascular maturation (183). As the neuronal retina matures, its rate of oxygen consumption increases and outgrows the rate of oxygen delivery provided by its limited vascular supply, leading to hypoxia. In the second phase, retinal hypoxia results in the activation of hypoxia-inducible genes, which drive retinal angiogenesis and pre-retinal neovascularization (184). Other biochemical mediators, including erythropoietin, growth hormone, and insulin-like growth factor-1, also appear to be important in mediating the neovascularization (182, 185). The newly formed, immature vessels lead to bleeding, fibrosis, and scarring. Eventually, if left unchecked, the fibrosis and scarring can evolve into retinal detachment and, ultimately, blindness (186).

Rodent oxygen-induced retinopathy (OIR) models mimic the immature vascular development, oxygen susceptibility, and neovascularization that characterize ROP, and have contributed to an enhanced understanding of ROP pathogenesis. We chose to study the rat OIR model because it more closely mimics the exposure and retinal findings of human ROP than other models (181). To induce 50/10 OIR in rats, Sprague-Dawley pups are exposed to alternating hyperoxia (50% O_2) and hypoxia (10% O_2) every 24 hours, beginning at birth and continuing until postnatal day 14 (P14).(187) Upon return to room air at P14, the peripheral rat retina shows vaso-attenuation, which by P18, evolves into areas of peripheral neovascularization.

Although oxygen is thought to be a key player in the pathogenesis of OIR, ROP, and other proliferative retinopathies (e.g. diabetic retinopathy), oxygen metabolism has not been well studied in these diseases. In part, this may be due to the absence of imaging technologies than can quantify the inner retinal metabolic rate of oxygen ($irMRO_2$) and inner retinal delivery rate of oxygen ($irDO_2$), functional markers which fully describe the tissue oxygen consumption and oxygen delivery, respectively. Other markers, such as the oxygen saturation of hemoglobin (sO_2), total retinal blood flow (F_{Total}), and oxygen extraction fraction (OEF), contribute to the $irMRO_2$ and $irDO_2$; however, studying any of these measurements in isolation warrants caution because its provides a limited picture of oxygen metabolism. To illustrate how several of the biomarkers are connected, the $irMRO_2$ equation can be written as follows:

$$irMRO_2 = \varepsilon \times C_{Hb} \times OEF \times s_aO_2 \times F_{Total} \tag{6-1}$$

where ε is the oxygen binding capacity of hemoglobin; C_{Hb} is the total hemoglobin concentration; and s_aO_2 is the arterial oxygen saturation. A commonly used marker of oxygenation is the OEF, a unit-less quantity that represents the fraction of oxygen extracted from the blood and entering the tissue. The OEF can be written as follows:

$$OEF = \frac{irMRO_2}{irDO_2} = \frac{s_aO_2 - s_vO_2}{s_aO_2} \tag{6-2}$$

Note that, although $irMRO_2$ and $irDO_2$ individually depend on F_{Total}, taking their ratio results in the cancellation of the flow terms; therefore, the OEF only depends on the oxygen saturation of hemoglobin for arteries (s_aO_2) and veins (s_vO_2). Since the OEF is a ratio, the interpretation of its value can be ambiguous. For example, an increase in the OEF can mean one of two things: either the $irMRO_2$ is increased (increased oxygen consumption) or the $irDO_2$ is decreased with the $irMRO_2$ unchanged. Therefore, when interpreting the OEF, it is best to have measurements of $irMRO_2$ and $irDO_2$ to have a complete picture of oxygen metabolism.

Over the past 20 years, optical coherence tomography (OCT) has improved the diagnosis and management of retinal diseases by providing cross-sectional, high-resolution, structural imaging of the retina (188). Recent advancements in OCT technology have steered the field towards functional imaging approaches. Using the Doppler effect, OCT can quantify retinal blood flow and perform retinal micro-angiography (94, 189-191). More recently, our group developed visible-light optical coherence tomography (vis-OCT), which can uniquely quantify sO_2 in the inner retinal vessels *in vivo* (89, 91). Combining Doppler OCT, for measuring blood flow, with vis-OCT, for measuring oxygen saturation, enables the measurement of all the parameters required for $irMRO_2$ and $irDO_2$, in a single imaging device.

In this study, our primary objective was to use vis-OCT to quantify the $irMRO_2$ and $irDO_2$ in rats with 50/10 OIR. This is the first study that quantifies the $irMRO_2$ in the 50/10 OIR model, providing important insight into retinal oxygen metabolism in proliferative retinopathies, including ROP.

6.2 METHODS

6.2.1 Animal model

All animal studies were approved by and in compliance with the Institutional Animal Care and Use Committee at Northwestern University and the Association for Research in Vision and Ophthalmology Statement for the Use of Animals in Ophthalmic and Vision Research. The 50/10 rat OIR model has been previously described (187). Within six hours after birth, Sprague-Dawley (Charles River, Wilmington MA) rat pups and their nursing moms were placed in a Plexiglas chamber with an oxygen controller (Pro-Ox 110; Biospherix, Lacona, NY). Starting on P0, the oxygen concentration was cycled between 50% and 10% every 24 hours for 14 days. After 14 days, the pups were returned to room air. Age-matched control pups were maintained in room air throughout the duration of the experiment. At P18, the OIR and control pups were imaged using vis-OCT, and following imaging were euthanized for retinal harvest.

6.2.2 Animal preparation

The anesthesia protocol used during the vis-OCT imaging session was 0.25-0.3ml ketamine/xylazine mixture (ketamine: 11.45 mg/ml; xylazine:1.7 mg/ml, in saline), injected intraperitoneally. The body temperature of the animal was maintained at 37° C using a heating pad (homeothermic blanket system, Stoelting Co.). We applied 0.5% tetracaine HCl ophthalmic solution to the eyes for local anesthesia and 1% tropicamide ophthalmic solution to dilate the pupil. Commercial artificial tears were applied to the eyes during imaging to prevent corneal dehydration. The pups were maintained on a custom-made animal holder during the imaging session.

6.2.3 Quantification of sO_2

Measurements of sO_2 were made using our vis-OCT system described previously (89). Briefly, vis-OCT utilizes the prototypical frequency-domain OCT optical design based on the Michelson interferometer. Instead of using a broadband laser source in the infrared spectrum, vis-OCT incorporates a supercontinuum source (NKT photonics, SuperK), which has a spectrum from 500 nm to 620 nm. The sO_2 was determined as follows. First, to segment the inner retinal vessels from the background, we utilized the contrast between the background and the retinal vessel shadows and applied Otsu's method to automatically determine a global threshold for vessel segmentation (192). Once the inner retinal vessels were segmented and manually selected, the vessel centerlines were determined. Since OCT system uses broadband light source, spectroscopic analysis is possible at any given location (147). Thus, short-time Fourier transforms were calculated at the centerline to extract the spectra from the bottom of the vessel wall. Based on the distinct absorption spectrum from oxygenated and deoxygenated hemoglobin, the sO_2 can be calculated by fitting the vis-OCT spectrum with the standard hemoglobin spectra (84, 89). All post-processing was performed in MATLAB (R2012b, MathWorks).

6.2.4 Quantification of retinal blood vessel diameter, blood velocity, and blood flow

Assuming the rat eye diameter is approximately 3 mm at P18 (193), the estimated inner and outer radius of the circular scans across the retina were 0.21 mm and 0.31 mm, respectively. The difference in displacement of the blood vessels between the two circular B-scans can be used to calculate the Doppler angle (θ) – the angle between the illumination beam and the flowing blood. Equations for calculating the Doppler angle with this setup can be found in the supplementary section of a previous study by Song et al. (115). To obtain valid velocity measurements, we aimed to keep the Doppler angles approximately 10 degrees away from 90 degrees (i.e. 80 or 100 degrees). The phase component of the inverse Fourier transform of the OCT interferometric signal was then used in combination with the Doppler angle to calculate the flow speed. The phase difference between adjacent A-lines after bulk-motion correction, $\Delta\phi$, is proportional to the flow speed (99). The blood flow speed can be calculated with $\Delta\phi$ and θ with the equation:

$$v = \frac{f_s \lambda_0 \Delta\phi}{4\pi n \cos\theta} \tag{6-3}$$

where f_s is the A-line scanning frequency, λ_0 is the center wavelength of the light source, and n is the refractive index of the sample (f_s was 25 kHz; λ_0 was 568 nm; and n was 1.4) (94). For each vessel, $\Delta\phi$ was averaged over 16 scans to obtain an average velocity. To correct for phase wrapping, the blood flow direction was inferred from the velocity at the vessel boundary, where flow is slow enough to not suffer from phase-wrapping. Additionally, using the sO_2 measurements obtained with vis-OCT, each vessel was labeled as an artery or a vein, which also assisted in the determination of blood flow direction (arteries flow away from the optic nerve towards the periphery and veins vice versa).

To determine the vessel diameter, D, ellipsoids were manually user-fitted in MATLAB over the hyper-reflective vessel wall seen in the OCT structural images obtained from the inner and outer circular scans. Because the depth resolution (1.07 μm) was much higher than the transverse resolution (6 μm), only the depth dimension was used to measure the vessel diameter, as depicted by the arrows in Figure 6-1. The diameter measurements were then averaged across all scans. Assuming cylindrical vessels, the cross-sectional area is given by $A = \pi D^2/4$. Assuming laminar flow within the blood vessels, the product of the cross sectional area, A, and average blood velocity, $\langle v \rangle$, yields the volumetric blood flow, F (194).

6.2.5 F_{Total}, $irDO_2$, OEF, and $irMRO_2$ quantification

F_{Total} (in ml blood/min) was calculated using the equation:

$$F_{Total} = \frac{N}{2} \frac{(\overline{F_a} + \overline{F_v})}{2}. \tag{6-4}$$

$\overline{F_a}$ and $\overline{F_v}$ are the average arterial and venous blood flows, respectively. N indicates the total number of vessels counted on the *en face* shadow image.

Inner retinal oxygen delivery, $irDO_2$, was calculated using the following equation:

$$irDO_2 = \varepsilon \times C_{Hb} \times F_{Total} \times \overline{s_a O_2}. \tag{6-5}$$

Here ε is the oxygen binding capacity of hemoglobin (1.36 ml O_2/g of Hb).(102) C_{Hb} is the total hemoglobin concentration (150 g of Hb/L of blood). OEF was calculated using the following equation:

$$OEF = \frac{\overline{s_a O_2} - \overline{s_v O_2}}{\overline{s_a O_2}} \quad . \tag{6-6}$$

where $\overline{s_a O_2}$ and $\overline{s_v O_2}$ are the average arterial and venous sO_2 percentages, respectively. $irMRO_2$ was calculated based on total blood flow and arteriovenous sO_2 differences using the equation:

$$irMRO_2 = \varepsilon \times C_{Hb} \times F_{Total} \times (\overline{s_a O_2} - \overline{s_v O_2}). \tag{6-7}$$

which is equivalent to Equation (6-1).

The units of $irDO_2$ and $irMRO_2$ were in nl min^{-1}.

6.2.6 Retinal dissection, flat mounts, and immunostaining

Rat eyes were enucleated and fixed for 24 hours in 10% neutral buffered formalin at room temperature and then transferred to 70% EtOH. The retinal eye cups were dissected as described previously (195). The retinas were washed with phosphate buffer saline (PBS) for three hours before being placed overnight in PBS with 0.5% Triton X-100 solution to help improve vascular visibility. The following day the retinas were washed in PBS for three hours and then stained overnight in 4°C with Alexa Fluor 594 isolectin GS-IB4 conjugate (1:75 dilution; Invitrogen, Carlsbad, CA) in PBS with $MgCl_2$, $CaCl_2$, and 0.3% Triton X-100 solution. Following a two hour wash in PBS with 0.025% Triton X-100 solution, the retinal cups were cut in quadrants, flat mounted, and cover slipped with ProLong Gold mounting medium (Life Technologies, Carlsbad, CA, USA).

Single-plane fluorescence images of the immunostained retinal flatmount were acquired with Nikon Eclipse 80i upright microscope (Nikon Instruments Inc, Melville, NY, USA) using a Photometrics ES CoolSnap camera (Photometrics, Tuscan, AZ, USA) and MetaMorph software (Molecular Devices, Sunnyvale, CA, USA). Five individual images of the retinal flaps were taken at 2x magnification and then merged using the stitching plugin in ImageJ software (National Institutes of Health, Bethesda MD) (196, 197). For each eye, two masked graders (A.A.F. and P.P.) independently measured the avascular area and neovascularization, and the average of their measurements was used for subsequent analysis. To measure avascular area, graders traced both avascular and total retinal areas using the "Freehand selections tool" in ImageJ. Avascularity was computed as the ratio of the avascular to the total retinal area. To score neovascularization, each retinal quadrant was divided into three equal parts (clock hour) and the total number of clock-hours with neovascularization was counted as described previously (198).

To examine the vascular density of the superficial and deep networks, we used confocal microscopy (543 nm, Zeiss LSM 510, Jena, Germany) to image the isolectin-stained retinal flatmounts. Two z-stacks per eye were obtained near the optic nerve head, halfway between the optic nerve head and periphery, and at the periphery of the retinal flaps. The dimensions of the z-stacks were 900 μm x 900 μm x 120 μm with a z-interval of 1.4 μm, resulting in approximately 85 images (depending on the retinal thickness). To avoid measurement error of the vascular density, images were captured in areas without any immunostaining artifacts. In addition, the two z-stacks were captured approximately 180 degrees apart from each other on the retina. The superficial and deep vascular networks were distinguished from one another by their z-position within the z-stack. Each z-stack was then collapsed into two maximum amplitude projections (MAP) of the superficial and deep vascular networks. The MAP's were then regionally thresholded using Otsu's method and the function *blkproc* (44 μm x 44 μm with 13 μm overlap) (192). We then skeletonized the vessels and performed spur removal. As previously described (199, 200), the vascular density was quantified as the length of skeletonized vessel divided by the image area.

6.2.7 Histological sections

Fellow eyes (non-imaged) were enucleated and fixed as described above. For paraffin section preparation, eyes were submerged in Davidson's fixative for 24 hours to help preserve retinal morphology, embedded vertically in paraffin along the corneo-scleral axis orientation, and sectioned at 7 μm intervals. Sections were then stained with hematoxylin & eosin (H&E) and imaged at 10x magnification with brightfield microscopy. Sections with the optic nerve were chosen for analysis. Two masked graders (B.T.S. and R.S.) measured retinal layer thicknesses at regions 150 to 200 μm away from the optic nerve (central) and from the peripheral retinal border (peripheral). The NFL/GCL, IPL, INL, OPL, ONL, and PR layers were individually measured using the ImageJ plug-in *distance_between_polylines.java* (201).

6.2.8 Statistical analysis

All measurements were first averaged within each animal. A final average was then computed for all animals. Quantitative data were expressed as mean ± standard error of the mean (S.E.M). The statistical test used was an unpaired Student's t-test (two-tailed with unequal variance). We considered a p-value less than 0.05 to be statistically significant. All analyses were performed using Graphpad Prism (Version 6, GraphPad Software, San Diego California USA).

6.3 RESULTS

6.3.1 Multi-parameter assessment of oxygen delivery and metabolism with vis-OCT.

Using vis-OCT and dual-circle scanning Doppler OCT (89, 94, 115), we obtained three-dimensional (3-D) anatomical images of the retina along with sO_2, vessel diameter, and blood velocity. For each rat, we collected a series of two-dimensional B-scans by raster-scanning the illumination beam over an area of 2x2 mm^2 and subsequently combined them to form a 3-D image of the retina. Because hemoglobin is highly absorbing within the visible-light spectral range, shadows were cast underneath the inner retinal blood vessels. Taking advantage of this light attenuation, we selected a 3-D slab of retina below the inner retinal vessels and performed maximum amplitude projection (MAP), along the depth dimension, to obtain an *en face* image of the inner retinal vessel shadows. An example image of the shadows from a healthy rat at P18 is shown in Figure 6-1(a). The contrast of the shadow image can be inverted and color-coded according to the measured sO_2 values. Figure 6-1(b) shows an example of an artery-vein pair from

Figure 6-1(a), carrying oxygenated (97%) and deoxygenated (71%) blood to and from the retinal periphery, respectively.

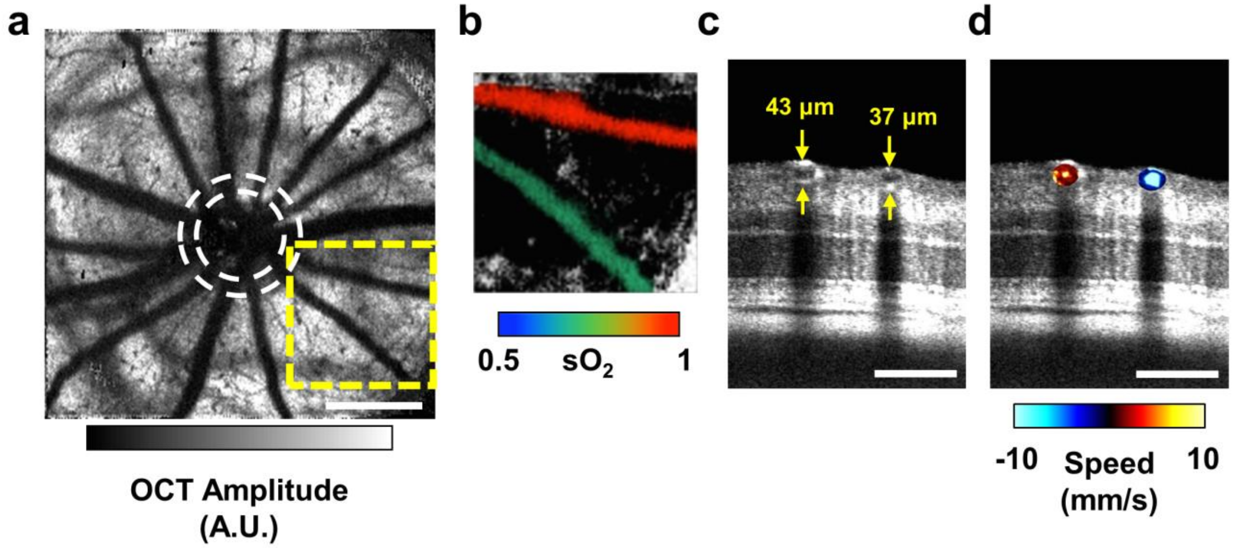

Figure 6-1: Multi-parameter assessment of oxygen delivery and metabolism with visible-OCT. (a) *En face* maximum amplitude projection of the shadows of the inner retinal vessels. White dashed circles indicate the approximate inner and outer scanning paths for dual-circle Doppler OCT. A.U.: arbitrary units. Scale bar: 500 μm. (b) An artery-vein pair from the yellow dashed box in (a) color-coded according to measured sO_2. (c) An angular section from the outer circle of the dual-circle scan, showing the artery-vein pair in (b) and their respective measured diameters. Scale bar: 100 μm (d) The same artery-vein pair color-coded according to speed measured by Doppler OCT after phase unwrapping. Scale bar: 100 μm

To measure vessel diameter and blood velocity, we implemented a dual-circle scanning protocol on the same vis-OCT system (94, 95). The dual-circle scanning method does not require an entire 3D volumetric scan. Instead, the illumination beam is rapidly scanned around the optic disk in two concentric circles such that all the major blood vessels are captured, as depicted by the dashed circles in Figure 6-1(a). Figure 6-1(c) shows an angular section from the outer circle scan, which matches the artery-vein pair shown in Figure 6-1(b). An example of blood velocity measurements for the pair is shown in Figure 6-1(d).

The accuracy of sO_2 and blood velocity measurement is supported by previous studies from our group. Using vis-OCT, Yi et al. monitored arterial sO_2 in a mouse ear in response to hyperoxia and hypoxia challenges (84). The study found high correlation between vis-OCT measurements and pulse-oximetry readings. In another study, Song et al. confirmed that a 25 kHz sampling rate and averaging measurements over multiple scans enabled accurate mean blood flow measurements in rodents using the dual-circle scanning Doppler OCT (115).

6.3.2 Inner retinal sO_2, diameter, blood velocity, and blood flow

Figure 6-2(a) shows a comparison of arterial and venous sO_2 measurements between room-air-raised rats (N; n = 6) and rats with OIR (O; n = 4) at P18. In the control animals, the average arterial sO_2 was higher when compared with the arterial sO_2 in the OIR group (0.964 ± 0.013 vs. 0.928 ± 0.006; $p < 0.05$). This finding may be explained by the physiologic differences between the two groups. In particular, rats with 50/10 OIR have poor weight gain and decreased systemic arterial oxygen (similar to values seen in infants in the neonatal ICU) when compared with their room-air-raised controls (202). A statistically significant difference was not found between the average venous sO_2 in the N and O groups (0.741 ± 0.017 vs. 0.684 ± 0.023; $p = 0.09$).

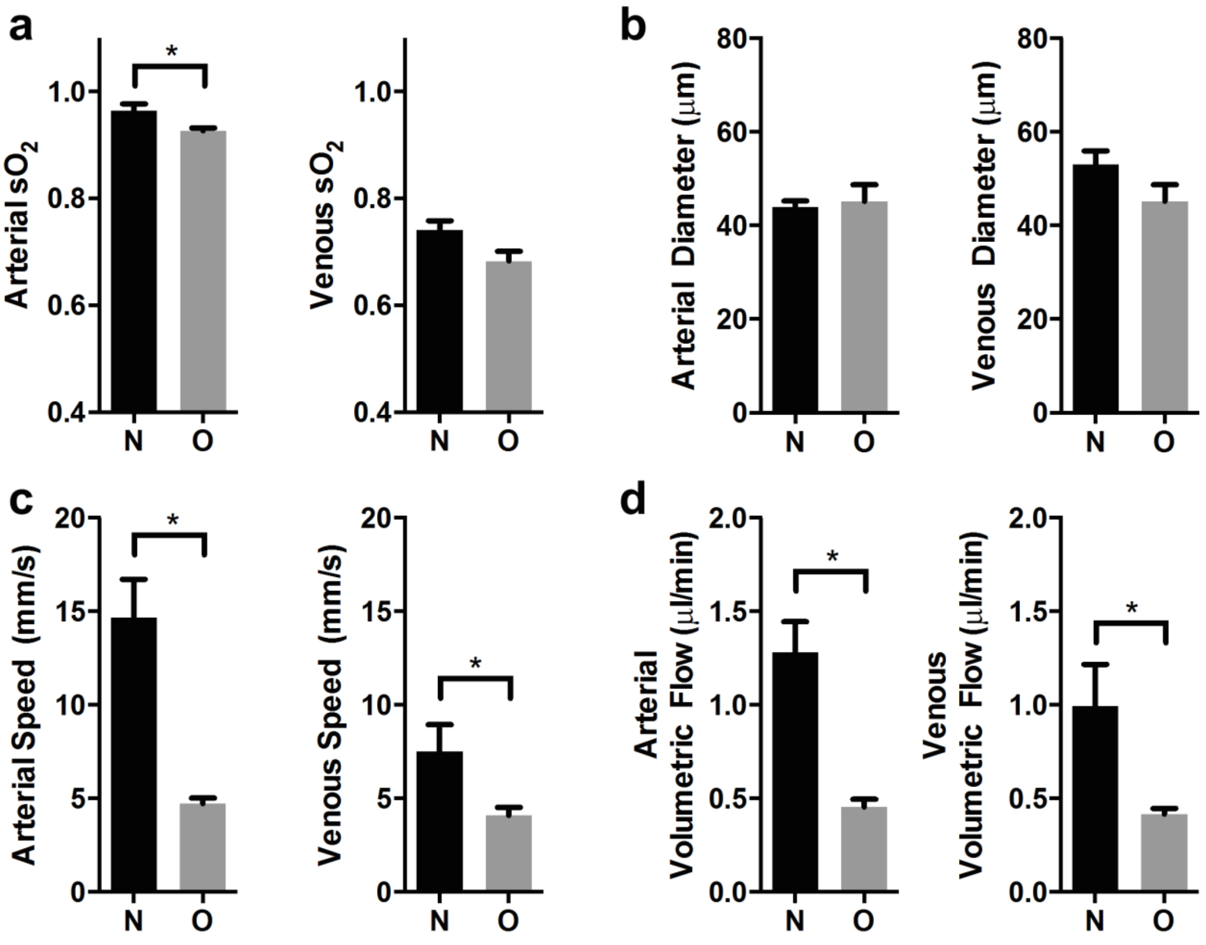

Figure 6-2: Comparison of retinal metabolic parameters between room-air-raised and oxygen induced retinopathy (OIR) rats at P18. (a) Average arterial and venous sO_2 measurements acquired with vis-OCT in room-air-raised (N; n = 6) and OIR rats (O; n = 4) (b) Arterial and venous diameter measurements acquired with from dual-circle scanning OCT (c) Arterial and venous speed measurements acquired with Doppler OCT (d) Calculated arterial and venous volumetric flow for the two groups. * $p < 0.05$

Our sO_2 results for the control rats agreed with previous investigations of the inner retina sO_2 in normal rats. Yi et al. used vis-OCT to measure inner retinal arterial and venous sO_2 in Long Evans pigmented rats and found the sO_2 to be 95% and 72%, respectively.(89) Song et al. used photoacoustic ophthalmoscopy (PAOM) to image normal adult Sprague-Dawley rat and obtained an average arterial and venous sO_2 of 93.0% and 77.3%, respectively, which match well with our measurements using vis-OCT (115). In another study, using phosphorescence lifetime measurements to measure intravascular partial pressure of oxygen (pO_2) in Long Evans pigmented rats, the authors found arterial sO_2 and venous sO_2 (after conversion from pO_2 using the hemoglobin disassociation curve) in normal conditions to be 61% and 34%, respectively. These findings were lower than those in our study; however, the authors noted that their measurements were lower than those seen in humans and that anesthesia may have induced respiratory depression, leading to systemic hypoxia (203).

Figure 6-2(b) compares the arterial and venous diameter between the N and O groups. Arterial diameter was not significantly different between controls and rats with OIR (43.9 ± 1.4 μm vs. 45.2 ± 2.9 μm; $p = 0.72$). Likewise, venous diameter was not significantly different between controls and rats with OIR (53.1 ± 2.9 μm vs. 48.1 ± 2.5 μm; $p = 0.23$). Our diameter measurements of the major arteries and veins in the OIR group were relatively similar to those reported using *ex vivo* retinal flatmounts for arteries (45.1 μm) and veins (45.7 μm) in this model.(187) Figure 2(c) shows the average arterial and venous blood flow speeds for the two groups. Arterial blood flow speed was significantly higher in controls compared to rats with OIR (14.68 ± 2.03 mm/s vs. 4.65 ± 0.37 mm/s; $p < 0.01$). Similarly, venous blood flow speed was also significantly higher in controls compared to rats with OIR (7.52 ± 1.41 mm/s vs. 3.71 ± 0.31 mm/s; $p < 0.05$). Figure 2(d) shows the average arterial and venous volumetric flows. Average arterial volumetric flow was significantly different between control and rats with OIR (1.28 ± 0.16 μl/min vs. 0.45 ± 0.05 μl/min; $p < 0.01$). Similarly, average venous volumetric flow was significantly different between control and rats with OIR (-1.00 ± 0.40 μl/min vs. 0.59 ± 0.06 μl/min; $p < 0.05$). Overall, we successfully obtained high quality flow measurements from 70% of the vessels in the control rats and 50% of the vessels in rats with OIR. There was no significant difference in the number of major inner retinal vessels between controls and rats with OIR (13 ± 0.45 vessels vs. 13 ± 1.3 vessels; $p > 0.99$). Across all measurements in the control group, the average Doppler angle was 101 ± 3 degrees. In the rats with OIR, the average Doppler angle was 102 ± 3 degrees. All measurements had Doppler angles greater than 95 degrees.

6.3.3 Total retinal blood flow, oxygen delivery, oxygen extraction fraction, and metabolic rate of oxygen

As shown in Figure 6-3(a), the average F_{Total} in rats with OIR was significantly lower than in controls (2.74 ± 0.58 µl/min vs. 7.37 ± 2.96 µl/min; $p < 0.05$). F_{Total} measurements for the controls were consistent with previously reported measurements made using *en face* Doppler OCT in adult Sprague-Dawley rats (6.48 µl/min) (204), and fluorescent microsphere imaging in adult Long Evans pigmented rats (7.9 µl/min) (205, 206). We found significant reduction in $irDO_2$ in rats with OIR versus controls as shown in Figure 6-3(b) (568.0 ± 54.99 nl min^{-1} vs. 1473 ± 231.9 nl min^{-1}; $p < 0.05$).

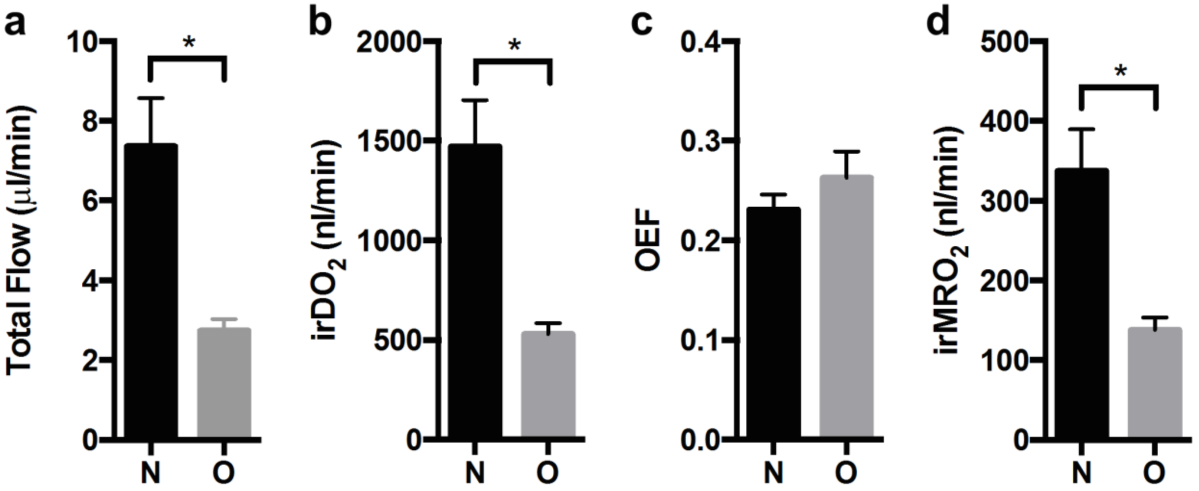

Figure 6-3: Inner retinal oxygen delivery ($irDO_2$) and metabolic rate of oxygen ($irMRO_2$) are decreased in OIR rats at P18. (a) Estimated total blood flow (F_{Total}) for

room-air-raised controls (N; n = 6) and rats with OIR (O; n = 4) (b) inner retinal oxygen delivery (irDO$_2$) measurements for N and O groups. (c) Oxygen extraction fraction (OEF) measurements for the N and O groups. (d) Inner retinal metabolic rate of oxygen (irMRO$_2$) measurements for N and O groups. * $p < 0.05$

Because the OEF calculation does not require blood flow measurements, the OEF is sometimes used to characterize the oxygen metabolism in tissue. OEF is described only by sO$_2$ values (see Equation (6-2); therefore, it only serves as a static measure of oxygen metabolism. As shown in Figure 6-3(c), there was no significant difference in the OEF between the two groups (0.231 ± 0.037 vs. 0.262 ± 0.054; p = 0.36). In comparison, Figure 6-3(d) shows that irMRO$_2$ was significantly lower in rats with OIR versus controls (138 ± 16 nl min^{-1} vs. 338 ± 52 nl min^{-1}; $p < 0.05$). As we discussed in the introduction, the OEF is a unit-less ratio, which can sometimes be difficult to interpret. Case in point, we found that the OEF was not significantly different when normal rats to rats with OIR. This can be explained by the fact that the irMRO$_2$ and the irDO$_2$ were proportionately decreased. We could only determine the latter because we measured both F_{Total} and sO$_2$. Our study, therefore, cautions scientists to avoid drawing conclusions based on OEF measurements alone, without considering blood flow and metabolic rate of oxygen.

Our irMRO$_2$ measurements in normal rats agree with those obtained using a combination of PAOM and Doppler OCT in adult Sprague Dawley rats (297.86 nl O$_2$/min) (207). However, using phosphorescence lifetime imaging to measure pO$_2$ and fluorescent microsphere imaging to measure F_{Total}, in two separate studies, Wanek et al. measured the irMRO$_2$ to be ~500 nl O$_2$/min in normal adult Long Evans pigmented rats, which is higher than what we obtained in our current study (205, 206). These differences in the normal irMRO$_2$ could be attributed to species and age differences between the animals in the respective studies. Notably, differences in the anesthesia protocol are known to affect F_{Total}, which could account for differences in the calculated irMRO$_2$.

In particular, due to its vasodilating action, isofluorane anesthesia may result in higher flow speeds than ketamine/xylazine used in our study (189).

6.3.4 Retinal avascularity, clock hours with neovascularization, and retinal vascular density

To investigate the reason for decreased irDO$_2$, we performed fluorescence microscopy on isolectin-stained flatmounts of the retinal vasculature. Figure 6-4(a) and Figure 6-4(b) show representative flatmounts from controls and rats with OIR. The rats with OIR (n = 4) had 4.25 ± 2.25 clock hours with neovascularization. Rats with OIR had on average 10.92 ± 3.50 % peripheral retinal avascular areas. By definition, normal rat eyes had completely vascularized peripheral retina and zero clock hours of neovascularization. In this study, the number of clock hours with neovascularization was similar to that reported at P19 (~3.5 clock hours)(193), but was less than that originally reported by Penn et al. at P18 (8 clock hours) (187). Our measurements of peripheral avascularity measured in this model were less than those reported by Akula et al. (~20%) and Penn et al. (25.2% peripherally and 4.2% centrally) (187, 193).

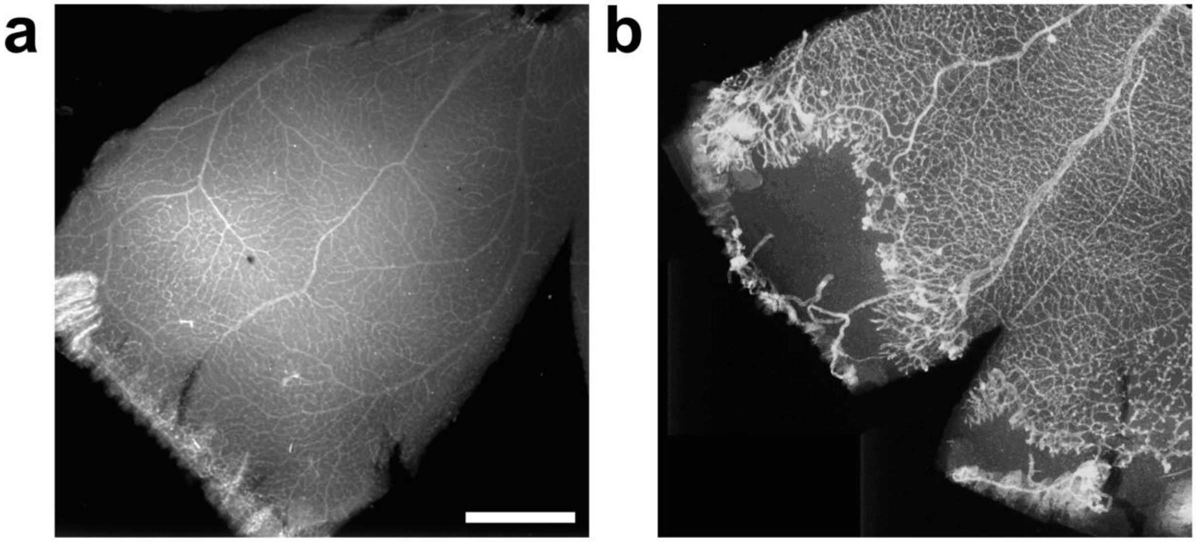

Figure 6-4: Immuno-stained retinal flatmounts show peripheral avascular retina and neovascular tufts in OIR rats at P18. (a) Room-air-raised control (b) Rat with oxygen-induced retinopathy OIR. Scale bar: 1 mm.

To study the vascular density in the superficial and deep capillary plexi, we used confocal microscopy to optically section the isolectin-stained flatmounts. We imaged the retinal flatmounts at three locations: near the optic nerve head (ONH), halfway between the ONH and the periphery (middle), and near the periphery. At those three locations, we measured the vascular density in room-air-raised rats (N; $n = 4$) and rats with OIR (O; $n = 4$). Figure 6-5(a) shows a representative image of the vasculature near the ONH in room-air-raised rats. The image was color-coded according to depth; therefore, the superficial vascular network was colored red, while the deep capillary network was colored blue. Figure 6-5(b) shows a representative image of the vasculature near the ONH in a rat with 50/10 OIR. Here the deep capillary network is colored yellow-green because the retina was thinner in this group (see next section), and thus, the deep capillary network was closer to the superficial vessels. Figure 6-5(c) compares the measured vascular density for the N and O groups. We found that superficial vascular density in the O group was significantly decreased near the ONH compared to the N group (14.5 ± 1.0 mm^{-1} vs. 19.0 ± 0.7 mm^{-1}; $p < 0.05$), but differences in deep vascular density were not statistically significant (30.7 ± 0.4 mm^{-1} vs. 28.1 ± 1.2 mm^{-1}; $p = 0.14$).

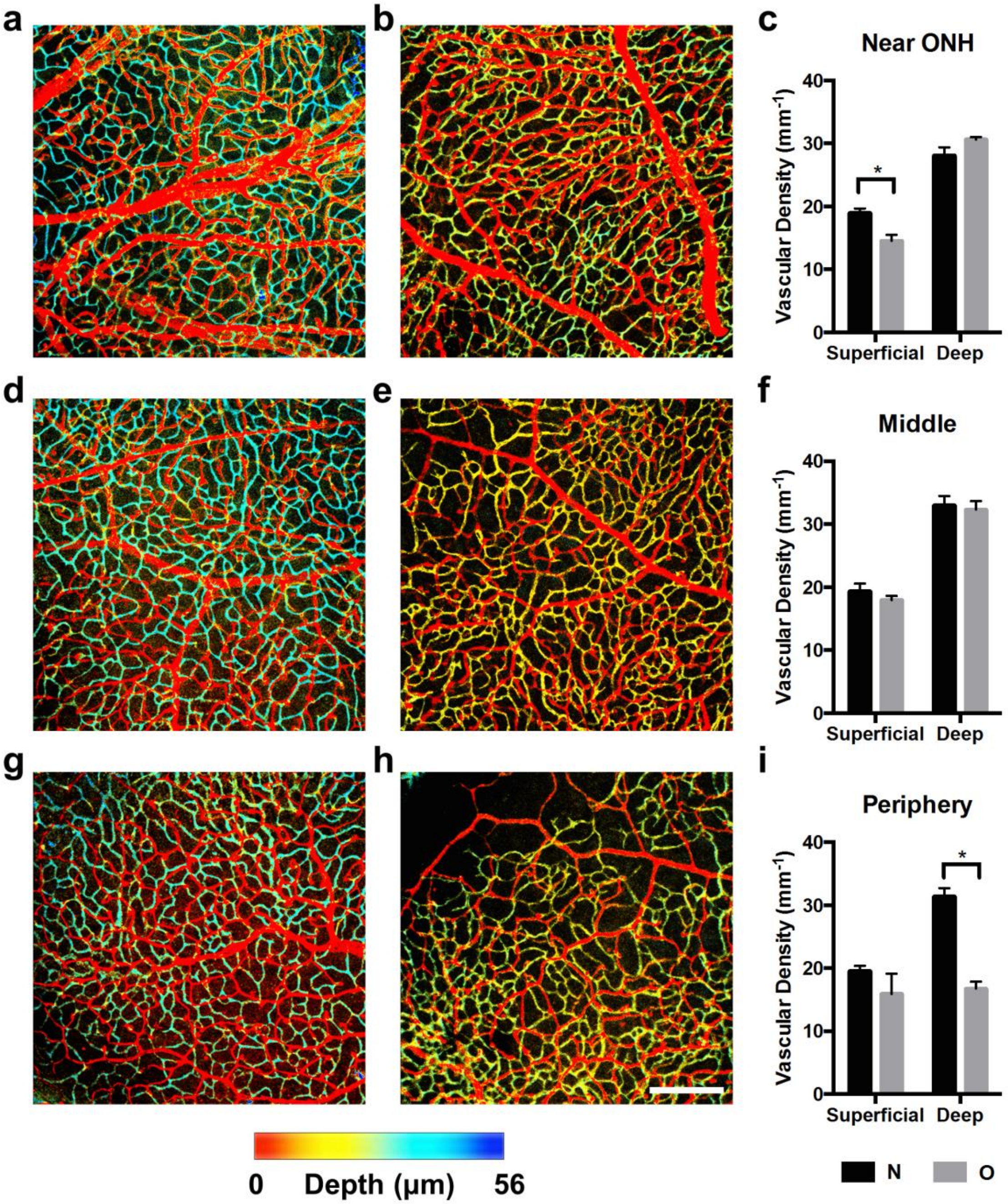

Figure 6-5: Retinal vascular density of the superficial and deep vascular networks is decreased in the OIR rats. (a) En face maximum amplitude projection of the vasculature near the optic nerve hear (ONH) acquired with confocal microscopy in a healthy rat at P18, which has been color-coded according to depth. (b) Vasculature near the ONH in a rat with OIR. (c) Vascular density measurements near the ONH. (d) Vasculature at halfway between the ONH and the periphery (middle) in a room-air-raised

control. (e) Vasculature at halfway between the ONH and the periphery and in a rat with OIR. (f) Vascular density measurements in the middle. (g) Vasculature at the periphery in a room-air-raised control. (h) Vasculature at the periphery in a rat with OIR. Scale bar: 200 μm. (i) Peripheral vascular density measurements. * $p < 0.05$.

Figure 6-5(d) and Figure 6-5(e) show representative images of the vasculature taken halfway between the ONH and the periphery, and Figure 6-5(f) shows the corresponding vascular density measurements. We found no statistically significant differences in superficial or deep vascular density between the N and O groups at this location (superficial: 19.3 ± 1.2 mm^{-1} vs. 18.0 ± 0.6 mm^{-1}; $p = 0.37$; deep: 33.0 ± 1.5 mm^{-1} vs. 32.3 ± 1.4 mm^{-1}; $p = 0.74$). Figure 5(g) and Figure 5(h) show representative images of the vasculature at the periphery, and Figure 5(i) shows the corresponding vascular density measurements. We found no statistically significant difference in the superficial vascular density (19.5 ± 0.8 mm^{-1} vs. 15.9 ± 3.2 mm^{-1}; $p = 0.35$); however, the O group showed a statistically significant decrease in deep capillary density (31.4 ± 1.3 mm^{-1} vs. 16.7 ± 1.1 mm^{-1}; $p < 0.001$). These results reflect observations that the superficial vascular network develops before the deep capillary network in rats (208).

In a previous study, Wang et al. found that vascular density in the superficial and deep networks was decreased in 50/10 OIR rats compared with room-air-raised controls (209). Using wide-field fluorescence microscopy, the authors measured a single vascular density for the entire retina. In this study, we measured the density in distinct locations across the retina using confocal microscopy. Our results suggest that differences were located in the superficial network near the ONH, while the effects on the deep vascular network were more prominent in the retinal periphery.

6.3.5 Retinal layer thickness

To investigate the reason for decreased oxygen consumption in rats with OIR, we performed histologic cross-sections to measure retinal sublayer thicknesses. Representative histological sections of the central retina for a normal rat and rats with OIR are shown in Figure 6-6(a) and Figure 6-6(b) respectively. As shown in Figure 6-6(c), we found that all retinal layers in the central retina were significantly thinner in rats with OIR (O; n=4) than controls (N; n = 4) ($p < 0.05$). Figure 6-6(d) and Figure 6-6(e) show representative peripheral retinal sections for a healthy rat and a rat with OIR respectively. We found that the OIR peripheral retina had statistically significant thinning of the inner plexiform (IPL), outer plexiform (OPL), outer nuclear (ONL), and photoreceptor layer (PR). These measurements were highly correlated between the two masked graders (Pearson's correlation coefficient > 0.85 for all layers except OPL which had a low coefficient of correlation= 0.53.

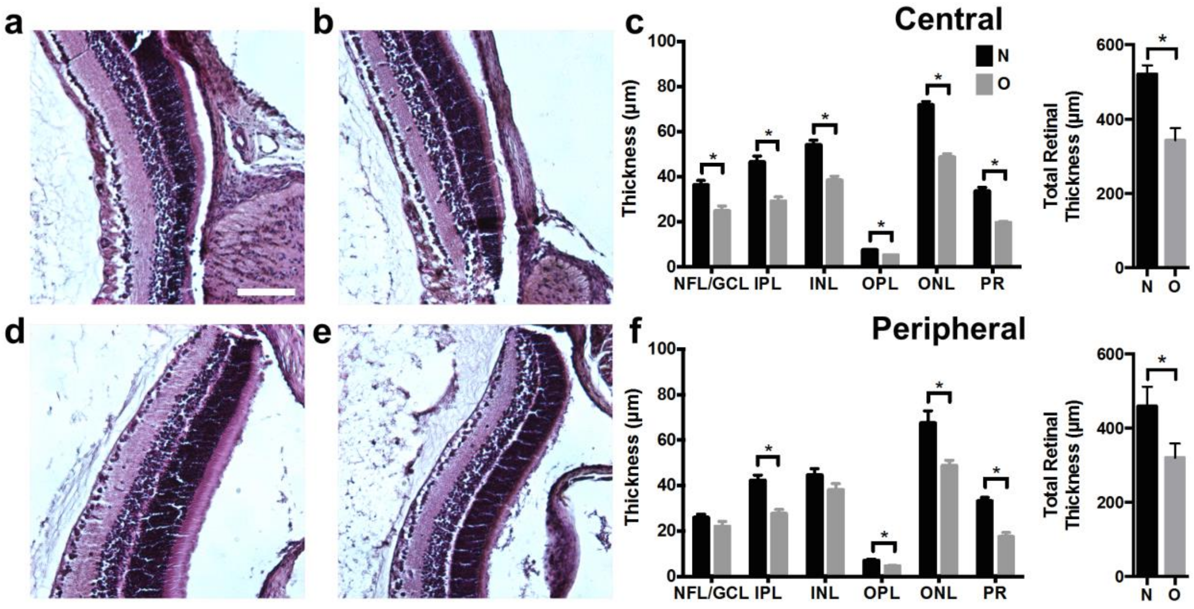

Figure 6-6: Retinal sublayer thinning in rats with OIR at P18. (a) Example central histological section from a room-air-raised control. Scale bar: 100 µm. (b) Example central histological section from a rat with OIR. (c) Central retinal sublayer thickness and total central retinal thickness measurements from room-air-raised controls (N; n = 4) and rats with OIR (O; n = 4). (d) Example peripheral histological section from a room-air-raised control. (e) Example peripheral histological section from a rat with OIR. (f) Peripheral retinal sublayer thickness and total peripheral retinal thickness measurements. * $p < 0.05$. Layer name abbreviations: Nerve fiber layer and ganglion cell layer (NFL/GCL), inner plexiform layer (IPL), inner nuclear layer (INL), outer plexiform layer (OPL), outer nuclear layer, (ONL), photoreceptor layer (PR).

Our total retinal thickness measurements in room-air-raised rats (central: 242 µm; peripheral 160 µm) were similar to those made by Akula et al. at P19 (central: 225 µm; peripheral: 205 µm).(193) In addition, our total thickness measurements in 50/10 OIR (central: 213.5; peripheral 149.0 µm) were also similar to thickness measurements in rats with 50/10 OIR at P19 (central: 185 µm; peripheral: 164 µm). In their study, Akula et al estimated approximately a 40% decrease in retinal volume in the rats with OIR. Similar to our results, these authors also concluded that the post-receptor layers were significantly thinner in rats with 50/10 OIR than in controls.

6.4 DISCUSSION

We found a significant reduction in inner retinal oxygen delivery in rats with OIR compared to controls at P18 (Figure 6-3(b)). Decreased F_{Total} contributed the most to the reduced oxygen delivery (Figure 6-3(a)); however, the reason for the reduced F_{Total} was not readily apparent. The Hagen-Poiseuille law relates volumetric flow, Q, and pressure drop, ΔP, across a single cylindrical pipe, given by the following equation:

$$\Delta \mathrm{P} = \frac{8\mu \mathrm{L}}{\pi \mathrm{r}^4} \mathrm{Q} \tag{6-8}$$

where μ is the blood viscosity, L is the length of the tube, and r is the vessel radius.(210) According to this law, reductions in the radii of the major retinal vessels could significantly affect the flow magnitude. However, we found that diameter measurements obtained *in vivo* in major arteries and veins were not significantly different between controls and rats with OIR (Figure 6-2(b)). Therefore, the difference in F_{Total} between the two experimental groups does not arise from changes in the vessel caliber at the pre-capillary or post-capillary level in the inner retinal vascular network.

Alternatively, the magnitude of ΔP could significantly affect F_{Total}. The pressure drop across an inner retinal vessel depends on the systemic arterial and venous pressures as well as the intermediate resistance of the capillary bed. The former is less likely to be different in rats with OIR compared to controls; therefore, we hypothesized that increased capillary bed resistance in rats with OIR was leading to decreased blood velocity in rats with OIR, as shown in Figure 6-2(c), and thereby, decreased F_{Total}. Similar findings have been observed in patients with hypertension and reduced retinal blood velocity (211).

A number of possibilities potentially explain why the capillary bed may have high resistance. Presumably, the peripheral neovascular lesions could contribute to increased vascular resistance, especially considering how this is one of the more striking vascular findings at P18; however, this is unlikely because we found that the tufts lay only in the periphery and occupied a small percentage of the retinal area (4 clock hours). Instead, we hypothesized that the overall retinal capillary bed was abnormal in rats with OIR at P18. Plausible structural abnormalities, which could significantly increase resistance, included either increased dynamic capillary closure or an overall decrease in the vascular density. To investigate the latter possibility, we measured vascular density in isolectin-stained retinal flat mounts imaged with high-resolution confocal microscopy (Figure 6-5). In rats with OIR at P18, we observed decreased capillary density in the superficial capillary bed near the ONH and in the deep capillary bed in the periphery. These findings suggest that oxygen delivery is reduced at P18 in rats with OIR because of these differences in the construction of the vascular tree; however, they do not exclude the possibility that there is potential dynamic capillary closure in addition to the changes in the overall vascular density. Future *in-vivo* studies using micro-angiography techniques may be able to assess whether capillary closure is a contributing factor.

The findings of decreased oxygen delivery appear to be consistent with functional magnetic resonance imaging (MRI) measurements of functional oxygenation, revealed by measurement of the change in pO_2 (ΔpO_2) in response to an oxygenation challenge in rats with 50/10 OIR. Berkowitz et al. found a lower ΔpO_2 in response to a 2-minute carbogen breathing challenge in OIR, when compared to controls at P12 (before the appearance of neovascularization) (212). A similar significant lowering of the ΔpO_2 at P20 (after neovascularization) was also found (213). The authors cited poor retinal perfusion, which would limit oxygen delivery, as one potential explanation for the decreased ΔpO_2; however, blood flow measurements were not conducted to verify this possibility. The decreased oxygen delivery and decreased vascular density found in our study could explain the abnormal ΔpO_2 in these studies. In addition, the decreased oxygen delivery would also serve as an explanation why Saito et al. found that supplemental oxygen did not reduce concentrations of conjugated retinal pimonidazole, a marker of retinal hypoxia, at P18 (214). Supplemental oxygen would likely not be able to overcome the significant decrease in total retinal blood flow and vascular density.

Given the decreased oxygen delivery found at P18, we expected the OEF to be elevated in rats with OIR. In states of ischemia (i.e. decreased oxygen delivery), the metabolic oxygen consumption of the tissue is usually elevated relative to the oxygen delivered, and thus a greater percentage of hemoglobin-bound oxygen diffuses through the capillary wall to compensate, resulting in an increased OEF measurement. This type of pathophysiology – termed "misery perfusion" in the field of neurology – is commonly seen in the setting of acute ischemic stroke (215). Surprisingly, however, we found only a modest elevation in OEF (Figure 6-3(c)). The minimal increase in OEF at P18 in the OIR rats suggested that although there was diminished oxygen delivery, the oxygen consumption of the retina was also reduced. Indeed, irMRO$_2$, which reflects the oxygen consumption of the retina per unit time, was reduced, proportionate to the decrease in oxygen delivery (Figure 6-3(d)). To explain this unexpected decrease in irMRO$_2$, we hypothesized that there was an overall decrease in the number of cells and synapses and, therefore, a lower inner retinal oxygen demand in OIR rats. To investigate this hypothesis, we compared retinal sublayer thicknesses in control and OIR eyes (Figure 6-6(a,b,d,e)), and confirmed that the retinal layers were significantly thinner in rats with OIR (Figure 6-6(c,f)). Previous electroretinography studies further support our observation (216); receptor sensitivity, postreceptor sensitivity, and oscillatory potentials were reduced at P20 in OIR rats when compared with normal controls (217, 218). In summary, irMRO$_2$ at P18 in OIR rats is markedly reduced, likely owing to decreased retinal thickness and decreased oxygen demand throughout the retinal layers.

The OEF and irMRO$_2$ findings at P18 potentially explain some of the peculiar characteristics of the retinopathy in rats with OIR. Interestingly, isolectin-stained flatmounts at P30 in rats with 50/10 OIR show a fully vascularized retina with no signs of neovascularization (193). In other words, at some point between P18 and P30, the neovascularization regresses and the retinal periphery becomes completely vascularized. How can we extrapolate from our results to explain this phenomenon? After exiting the oxygen chamber at P14, the oxygen consumption of the retina most likely exceeds the oxygen delivery, resulting in a state of hypoxia and, presumably, high

OEF. Supporting this statement, several studies have observed that VEGF levels appear to be the highest when returning to room air at P14 in the 50/10 model (219-221). Through VEGF, hypoxia at P14 likely drives the neovascularization, which is maximally observed at P18. Further exacerbating this hypoxia, vaso-attenuation of the peripheral vasculature also may progress between P14 and P18 as one study found (193); however, another study on rats with OIR found the contrary (220), so it is currently unclear if this plays a significant role. Around this same time period in normal neonatal rat eye development (from P10 to P25), the photoreceptors and retinal neurons undergo physiologic culling, whereby an initial excess of photoreceptors undergo apoptosis to reach levels for adult life. Hypoxia has been shown to substantially exacerbate this process, especially from P15 to P22 in rats (222, 223). Therefore, at P14 in OIR, the simultaneous occurrence of hypoxia and physiologic culling likely causes a dramatic increase in neuronal apoptosis, which in turn decreases the overall oxygen demand of the retina. Our retinal thickness, OEF, and $irMRO_2$ results suggest that by P18 in OIR, the oxygen demand has sufficiently decreased to almost match the pathologically decreased oxygen delivery. Beyond P18, the neuronal culling continues, and oxygen delivery and consumption become progressively balanced, decreasing the stimulus for angiogenesis. Eventually, the neovascularization subsides, and the physiologic retinal vascular development proceeds. Further studies are necessary to confirm this hypothesis, but our study is the first to suggest this as a likely possibility.

We note several limitations to this study. First, the equation used to calculate $irMRO_2$ in this study is only an approximation to the true $irMRO_2$ equation. To model oxygen delivery physically, the $irMRO_2$ equation should include individual feeding and draining vessels as separate terms instead of using averaged quantities for flow and oxygen saturation (224). This latter equation has not been demonstrated in the retina as of yet likely because it requires measurement of all feeding and draining vessels and highly accurate flow speeds to ensure that feeding and draining volumetric flows are closely conserved. In this study, a combination of hyaloid vasculature, vitreous hemorrhage, and cataract formation, which were more common in rats with OIR, limited our ability to obtain high quality flow speeds and sO_2 measurements for all the retinal vessels, and precluded the use of a more specific $irMRO_2$ equation. To ensure accurate flow measurement, we selected vessels with high signal-to-noise ratio and made averages over 16 scans to improve imaging quality. Second, our $irMRO_2$ equation does not take into account pO_2. However, owing to low solubility of oxygen in blood, intravascular pO_2 only makes up a small percentage (< 2%) of the oxygen carried in the blood, and thus it is reasonable to disregard pO_2 (225). Third, other factors may contribute to the decreased F_{Total} besides capillary bed resistance and vessel diameter. These factors include the cardiac output, total circulating blood volume, ocular pressure, and weight gain of the subjects, which were not measured in this study. Finally, vessel diameters were measured by fitting an ellipsoid over the hyper-reflective vessel walls, which is likely to be greater than the true inner diameter of the vessel; therefore, our diameter measurements may overestimate the F_{Total}, However, since such an overestimation was systematic, comparisons between groups should not be affected because diameters were measured consistently.

Future studies for longitudinal measurement of the $irMRO_2$ with vis-OCT would further elucidate the pathophysiology of the OIR model; however, several challenges remain. First, this OIR model relies upon the tightly regulated oxygen control within the animal chamber from P0 to P14; therefore, prolonged exposure to room air for imaging experiments before P14 would significantly disrupt the animal model. Second, imaging experiments at P14 may prove difficult given the significant persistence of the hyaloidal vasculature and developmental eyelid closure, which opens around P14-15 in the rat. Finally, at P18 and beyond, cataract and vitreous opacity in the OIR model may also hinder satisfactory image quality.

In summary, we capitalized on the unique capability of vis-OCT to simultaneously measure sO_2, vessel diameter, and blood flow, and quantified the retinal MRO_2 in healthy neonatal rats and OIR rats, for the first time. In addition, we combined this new technology with immunostaining and histological analysis to gain an improved understanding of the biological implications of these metabolic measurements. The findings in this study help explain the pathophysiology of consumption and delivery in rats with OIR, which can be extrapolated to retinal diseases involving inner retinal hypoxia and retinal angiogenesis in humans, including diabetic retinopathy. Our findings lay the foundation for future studies to explore retinal oxygen metabolism at various time-points in the progression of retinopathy in this animal model, as well as human studies of ROP and diabetic retinopathy at various stages of their development. We envision that future technological improvements to vis-OCT, with enhanced speed and scan range, will permit volumetric structural measurements of the entire retina (ora-to-ora), and improved segmentation of the retinal sublayers, which would allow more detailed correlation between structural alterations and retinal oxygen consumption.

Chapter 7

Optical coherence tomography angiography of retinal vascular occlusions produced by imaging-guided laser photocoagulation

7.1 INTRODUCTION

Retinal vascular occlusive diseases represent the most common cause of visual disability in the elderly population (14). Two important vascular occlusive diseases are retinal vein occlusions (RVO), and retinal artery occlusions (RAO), with each having different etiologies, pathogenesis, and visual outcomes. Generally speaking, these diseases present with painless, sudden vision loss or blurring in a patient greater than 50 years of age. A unifying feature of these diseases is reduced blood flow, which occurs either in a retinal vein (RVO), or in a retinal artery (RAO). Causes for the ischemia include vessel blockage by either thrombi or emboli, among many others. For RVO, the central vein or a branch thereof can be affected, which are termed central RVO (CRVO) and branch RVO (BRVO), respectively. Similarly, RAO can also be classified into central RAO (CRAO) and branch RAO (BRAO). Importantly, BRVO is the second most common retinal vascular disease after diabetic retinopathy, affecting approximately 16.4 million people worldwide (226).

Two major techniques have been developed to create rodent models of retinal vascular occlusions. In the first technique, the fundus is visualized with a modified slit-lamp biomicroscope using a high-power laser delivery system (~100-200 mW) (227-229). A skilled operator then manually delivers high energy laser shots to a target retinal vessel until vascular occlusion appears to have occurred. The high-power laser shots may damage the retina, leading to interstitial edema. In turn, the edema eventually compresses the target vessel, resulting in vascular occlusion. In the case of RVO’s, the retina appears swollen and pale, and retinal vessels may appear tortuous and white. In the second technique, a photoreactive dye, such as fluorescein or Rose Bengal (RB), is injected intravenously (60-63). Similar to the first technique, high-power laser shots are delivered to a target vessel. When exposed to high-power light, the intravascular RB (or fluorescein) releases singlet oxygen, which in turn, react with proteins and fatty acids on the blood vessel wall. This oxidation process results in the recruitment of platelets and activation of the coagulation cascade, which altogether lead to the formation of an intravascular thrombus at the targeted site. Compared to the first technique, the second technique creates occlusions which better resemble the pathophysiology of human retinal vascular occlusions; therefore, in this paper, we sought to improve upon the second technique.

Unfortunately, using a slit-lamp biomicroscope to observe and initiate occlusion has several drawbacks. First, extensive training and expertise are required to maneuver the slit-lamp and deliver the laser shots (230), especially when dealing with the small dimensions of the mouse eye and the fast clearance of RB from the circulation (~5 minutes). This steep learning curve also introduces variations among different operators. Second, the spot size of the high-power laser on the retina is difficult to control visually; therefore, a large area around the vessel may be illuminated with high-power, resulting in unwanted tissue damage. Finally, the retinal vascular occlusion is not monitored using the direct evidence from examining the blood flow within the vessel. Instead, vascular occlusion is inferred when the retinal vessel, or the surrounding area, appears pale.

Here we developed a multimodal imaging system for producing laser-induced vascular occlusions with RB. Multimodal imaging systems are capable of both producing, imaging, and monitoring an animal model. These systems may include combinations of fundus photography (231), scanning laser ophthalmoscopy (SLO) (46, 55, 232, 233), autofluorescence imaging (234), or photoacoustic ophthalmoscopy (32), with optical coherence tomography (OCT). Certain systems, especially in neuroscience (235, 236), include directed laser delivery, which enables researchers to consistently reproduce animal models with reduced training time. Recently, such approaches have been developed for ophthalmology research. For example, laser-induced choroidal neovascularization (CNV) in rodents, which is a model of wet age-related macular degeneration, can sometimes be difficult to produce due to inconsistent laser burns administered by a slit-lamp protocol. As a potential solution, a recent multimodal device was able to consistently produce this animal model (230). In this paper, we have created a system for producing animal models of retinal vascular occlusive diseases.

The aims of our system were four-fold: (1) to visualize the three-dimensional (3D) retinal structure before and after vascular occlusion; (2) to visualize the retinal microvasculature before and after vascular occlusion; (3) to precisely direct actinic laser light to a specific vessel location with minimal laser power; and (4) to visualize vascular occlusions in real-time. To achieve these goals, we developed an integrated optical coherence tomography (OCT) and fluorescent scanning laser ophthalmoscope (SLO) system. The OCT sub-system performed high-resolution cross-sectional imaging of the retina and granted us the ability to perform OCT angiography, which can obtain high-contrast images of the microvasculature. The SLO sub-system enabled us to perform

RB angiograms, ensuring RB within the retinal vasculature. Subsequently, the SLO also enabled us to direct actinic light precisely to a selected vessel location, while also visualizing the occlusion process in real-time. Ultimately, with our multimodal imaging system, we demonstrate BRVO, CRVO, and BRAO patterns in the murine retina.

7.2 MATERIALS AND METHODS

7.2.1 System setup

In this section, we describe the combined OCT and SLO system as shown in Figure 7-1. The light source in the spectral-domain OCT (SD-OCT) sub-system was a superluminescent light emitting diode (SLED) (IPSDW0825C-0314, InPhenix) with a center wavelength of 840 nm and a bandwidth of 95 nm (full width at half maximum). A 50/50 fiber coupler (FUSED-22-850, OZ Optics) collected the light from the SLED and split it into sample and reference arms. The beam at each arm was collimated by an aspheric fiberport (FP_1 and FP_2; PAF-X-11-PC-B, Thorlabs). The sample arm beam was combined with the SLO illumination beam by a short pass dichroic mirror (DC_1; FF746, Semrock). The x-y scanning galvanometer mirrors (QS-7, Nutfield Technology) deflected the combined beam for raster scanning. A 5/1 Keplerian telescope consisting of two achromatic lenses (L_1 and L_2; VIS-NIR coated, 75 mm and 15 mm focal lengths, Edmund Optics) created a point conjugate to the scanning mirrors, which was aligned at the pupil plane of the mouse eye. The reference arm beam was reflected back by a silver mirror (M_1) after passing through several BK7 glass plates, which were used for dispersion compensation. The back-reflected sample beam recombined and interfered with the backscattered light from the sample. A homemade spectrometer detected and digitized the interference signals.

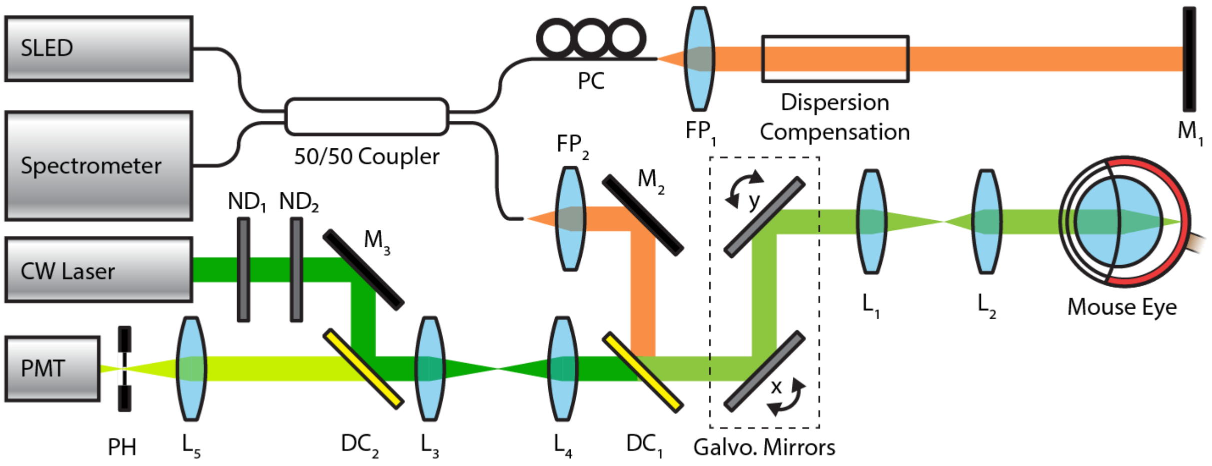

Figure 7-1: Schematic of the combined OCT and SLO system. CW Laser: continuous wave laser. DC: dichroic mirror. FP: fiber port collimator. M: mirror. ND: neutral density filter wheel. PC: polarization controller. SLED: superluminescent light emitting diode. Focal lengths of lenses L_1, L_2, L_3, L_4, L_5 were 75 mm, 15 mm, 40 mm, 50 mm, and 30 mm, respectively.

The SLO and laser occlusion sub-system used a continuous wave (CW) diode-pumped solid-state laser (532 nm, 100 mW). For coarse control of the laser power, the SLO illumination beam passed through a manual neutral density filter wheel (ND_1; Thorlabs, FW1AND). For fine control of the laser power, the SLO illumination also passed through a continuous neutral density filter wheel (ND_2; Thorlabs, NDC-50C-2M-A). A long pass dichroic mirror (DC_2; FF560, Semrock) served to reflect the illumination beam and pass RB fluorescence (peak emission: 571 nm). A Keplerian telescope (L_3 and L_4) resized the illumination beam and passed it to the dichroic mirror (DC_1) shared with the OCT sub-system. The SLO and OCT illumination beams were coaxially aligned, such that they shared the same relay optics and scanning mirrors to reach the subject's pupil plane. After passing through the long pass dichroic mirror (DC_2), the RB fluorescence was focused by a lens (L_5) and spatially filtered by a pinhole (PH; 50 microns, Thorlabs). A photomultiplier tube (PMT; Hamamatsu) captured the fluorescence signal, which was subsequently converted from current to voltage and digitally acquired.

7.2.2 Scanning protocols for OCT and SLO imaging

Both OCT and SLO used raster scanning to acquire images. The galvanometer mirrors deflected the illumination beams, which changed the angle of the illumination beam at the pupil plane, to achieve raster scanning of the retina. OCT detected backscattered photons by low-coherence interferometry, while SLO collected RB fluorescence in retinal blood flow. We used custom Labview software (2015 SP1, 64 bit, National Instruments) to control the imaging systems.

7.2.3 OCT imaging protocols

We designed two OCT imaging protocols: a *preview* OCT protocol and a *high-density* OCT/OCTA protocol. For both protocols, the A-line acquisition rate was 70 kHz; the scanning area was 2.5 mm x 2.5 mm; and the illumination at the pupil plane was 1 mW. The *preview* OCT protocol allowed us to quickly position the eye and preview the image quality. The image contained 64 B-scans with 128 A-lines in each B-scan. To preview the volumetric OCT image in real-time, we composed a CUDA C program and ran the CUDA-accelerated parallel functions on a graphics card (GeForce GTX 750Ti, NVIDIA Corporation). The real-time preview has a frame rate of 5.9 frames per second (FPS), which was limited by the galvanometer mirrors. We generated *en face* images by calculating the maximum amplitude projection (MAP) along the axial direction of the 3D volume data. Alongside the MAP, a selected B-scan from the 3D volume was displayed, helping the operators to better position the eye.

Once the initial alignment is completed, we captured images using the *high-density* OCT/OCTA protocol, where 400 x 512 A-lines were recorded per image. Additionally, at each of the 512 B-scan position, we sequentially acquired additional five co-localized B-scans for OCTA, making the total acquired B-scans equal to 2560. The total acquisition time for this protocol was 20.5 seconds. In this protocol, the data was processed offline with a custom MATLAB program. Due to limited field of view in each acquisition, we repeated the *high-density* protocol at different fundus locations and montaged those images later.

OCT images from the high-density protocol were constructed from an average of the five repeated B-scans. The OCT angiogram was constructed from the five repeated B-scans using an amplitude-based OCTA algorithm (80). B-scans were correlated and shifted to adjust for global and lateral phase fluctuations (237). For visualization, the 3D OCTA volumes were converted to depth color coded MAP, as described previously (85). When possible, OCTA images were automatically montaged together using i2k Retina software (DualAlign LLC, Clifton Park, NY). If the automatic montaging failed, images were manually montaged in Adobe Photoshop (Creative Cloud, Adobe Systems Incorporated, San Jose, CA).

7.2.4 SLO imaging

The SLO sub-system also had two imaging protocols: an *angiography* protocol and an *actinic protocol.* The purpose of the *angiography protocol* was to obtain RB fluorescence angiograms of the retinal vessels. The scanning area was 2.5 mm by 2.5 mm (same as OCT) with a scanning density of 128×128 pixels; the illumination power at the pupil was 400 μW; and acquisition rate was 1.9 FPS. The purpose of the *actinic* protocol was to deliver high-power actinic light to a target vessel. Here, by manipulating the deflection angle of the x-y scanning galvanometers, the scanning area was reduced and shifted to cover only the diameter of the target vessel. The scanning density was 64×64 pixels; the illumination power at the pupil was 25 mW to 35 mW; and the acquisition rate was 5.9 FPS.

7.2.5 Retinal Vascular Occlusion Protocol

Wildtype C57BL/6 mice were anesthetized with an intraperitoneal injection (10 ml/kg body weight) of a ketamine/xylazine cocktail (ketamine: 11.45 mg/ml; xylazine:1.7 mg/ml, in saline). A drop of 0.5% tetracaine hydrochloride ophthalmic solution (Bausch & Lomb, Rochester, NY) was administered on the cornea for topical anesthesia. For pupil dilation, a drop of 1% tropicamide ophthalmic solution (Akorn, Lake Forest, IL) was also administered. The mice were placed on a custom-made animal holder, which allowed for translation and rotation. In between image acquisitions, we administered artificial tears (Henry Schein, Melville, NY, USA) to prevent corneal dessication. We followed the guidelines established by the ARVO Statement for the Use of Animals in Ophthalmic and Visual Research as well as those set by the Northwestern University Institutional Animal Care and Use Committee.

Figure 7-2 illustrates the major steps of the retinal vascular occlusion protocol. After centering the optic nerve head on the OCT *en face* image using the preview protocol, we acquired baseline OCT/OCTA volumes using high-density protocol. Using the *en face* preview, we also selected either an artery or vein for vascular occlusion. Arteries could be distinguished from veins on *en face* OCT by their smaller diameter and more frequent branch points in the nerve fiber layer (229). Next, RB (Sigma Aldrich, Milwaukee, WI) was prepared in physiological saline (5 mg/ml of saline), and 0.2 ml was injected into one of the lateral tail veins**.** RB was preferred over fluorescein because of its higher quantum yield (~25x) for producing reactive single oxygen (238)**.** Immediately after successful tail injection, we started RB angiography using the SLO angiography imaging protocol, enabling real-time visualization of RB in the retinal vasculature. We then selected a location along the target vessel for occlusion. Previous studies of BRVO in mice have noted that the distance from the optic nerve head (ONH) appeared to correlate with severity of the vascular occlusion. Specifically, vein occlusions close to the ONH tend to result in a CRVO pattern, while vein occlusions farther away from the ONH result in a BRVO pattern (62).

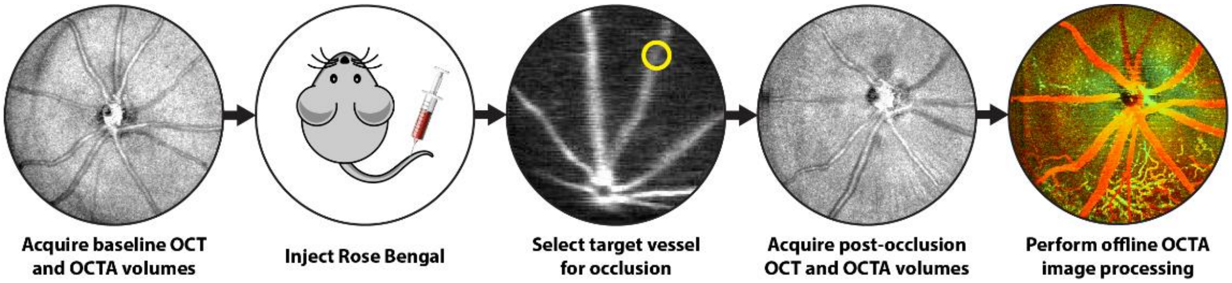

Figure 7-2: Key steps of the retinal vascular occlusion protocol.

Once the occlusion site was determined, we initiated the SLO *actinic* protocol. We reduced the scanning area to span the vessel diameter and increased the laser power to 25 mW by adjusting the controllable ND filters. We then monitored the occlusion process using SLO. If the occlusion was successful, the intravascular fluorescence signal dramatically fell within several seconds. If the vessel appeared to be only partially occluded, we increased the laser power up to a maximum of 35 mW to finish the occlusion process. Previous techniques to produce vascular occlusions used laser powers of 100-200 mW. Using OCT, we found that these powers often led to vessel hemorrhage, rupture of Bruch’s membrane, or severe edema immediately following laser delivery. Therefore, we opted to reduce the power to 25-35 mW to minimize these effects.

After completing the vascular occlusion, we reduced the SLO illumination power back to 400 μW and obtained a post-occlusion RB angiogram (SLO angiography protocol). We also collected post-occlusion OCT/OCTA volumes for comparison with baseline images (high-density OCT imaging protocol). After imaging, we placed the mice in a recovery area with a heat lamp. OCTA images were then processed offline.

7.3 RESULTS

To demonstrate our technique for producing retinal vascular occlusions in the mouse retina, we created a BRVO pattern at the 10 o’ clock vein in a healthy mouse eye (Figure 7-3). To increase the probability of creating a BRVO pattern, we targeted a vessel location greater than four ONH diameters away from the ONH. To aid this process, we aligned the mouse eye, using the *preview* OCT protocol for guidance, such that the ONH was at the bottom right corner of the FOV. This alignment step placed a longer length of the vein within the FOV, thus enabling us to select an appropriate target location away from the ONH. Next, we acquired a pre-occlusion baseline OCTA image, showing the vein of interest, v, in Figure 7-3(A). We administered RB via tail injection and immediately acquired a co-localized pre-occlusion RB angiogram (Figure 7-3(A)) using the SLO *angiography* protocol. RB was seen flowing with the retinal arteries and veins. We selected a specific location on the vein for occlusion, indicated by the red box in Figure 7-3(A).

To begin the occlusion procedure (*actinic* protocol), the SLO FOV was decreased until the target vein spanned the FOV. Continuous SLO scanning at high laser power (25 mW) was then initiated. From the collected SLO images, we calculated the mean RB fluorescence signal versus time, as shown in Figure 7-3(B). In this experiment, the occlusion procedure lasted 12 seconds. Four selected frames of the vessel are shown as insets in Figure 7-3(B, 1-4). Frame 1 shows the first acquired SLO image, where the vessel spans most of the FOV. At 2 s (frame 2), diminished SLO signal near the vessel wall was observed (yellow arrow), which represents the nidus for platelet aggregation (239, 240). By 6 s (frame 3), RB fluorescence within the FOV was diminishing, which implied decreasing intravascular blood flow. At 9 s (frame 4), the RB SLO signal diminished abruptly, which indicated that blood flow was completely stopped at the target site. To ensure stable thrombus formation, we waited for an additional 3 seconds after observing diminished intravascular RB SLO signal, before we shut off the high-power scanning.

Afterwards, we returned to the SLO *angiography* protocol (Fig. 3(C)), which revealed vessel discontinuity at the target location and absence of RB fluorescence upstream of the occlusion site, indicating a successful occlusion. Moreover, co-localized post-occlusion OCTA showed diminished OCTA signal within the target vein (Figure 7-3(D)), which also indicates reduced blood flow. Comparing the SLO image with OCTA image, OCTA showed higher contrast and more details of the deeper capillary network. The most striking difference between the pre-occlusion and post-occlusion OCTA images is an area of capillary non-perfusion in a sector surrounding the occluded vein (white dashed region in Figure 7-3(E)). Pre-occlusion cross-sectional OCT revealed intact retinal layers and a vessel shadow corresponding to the target vessel (Figure 7-3(F)). After the occlusion, the vessel shadow disappeared indicating less absorption by hemoglobin from the reduced blood flow (Figure 7-3(G)). The Bruch's membrane and RPE were intact. There was no evidence of retinal edema or swelling, and retinal layers were intact even in the areas with capillary non-perfusion on OCTA.

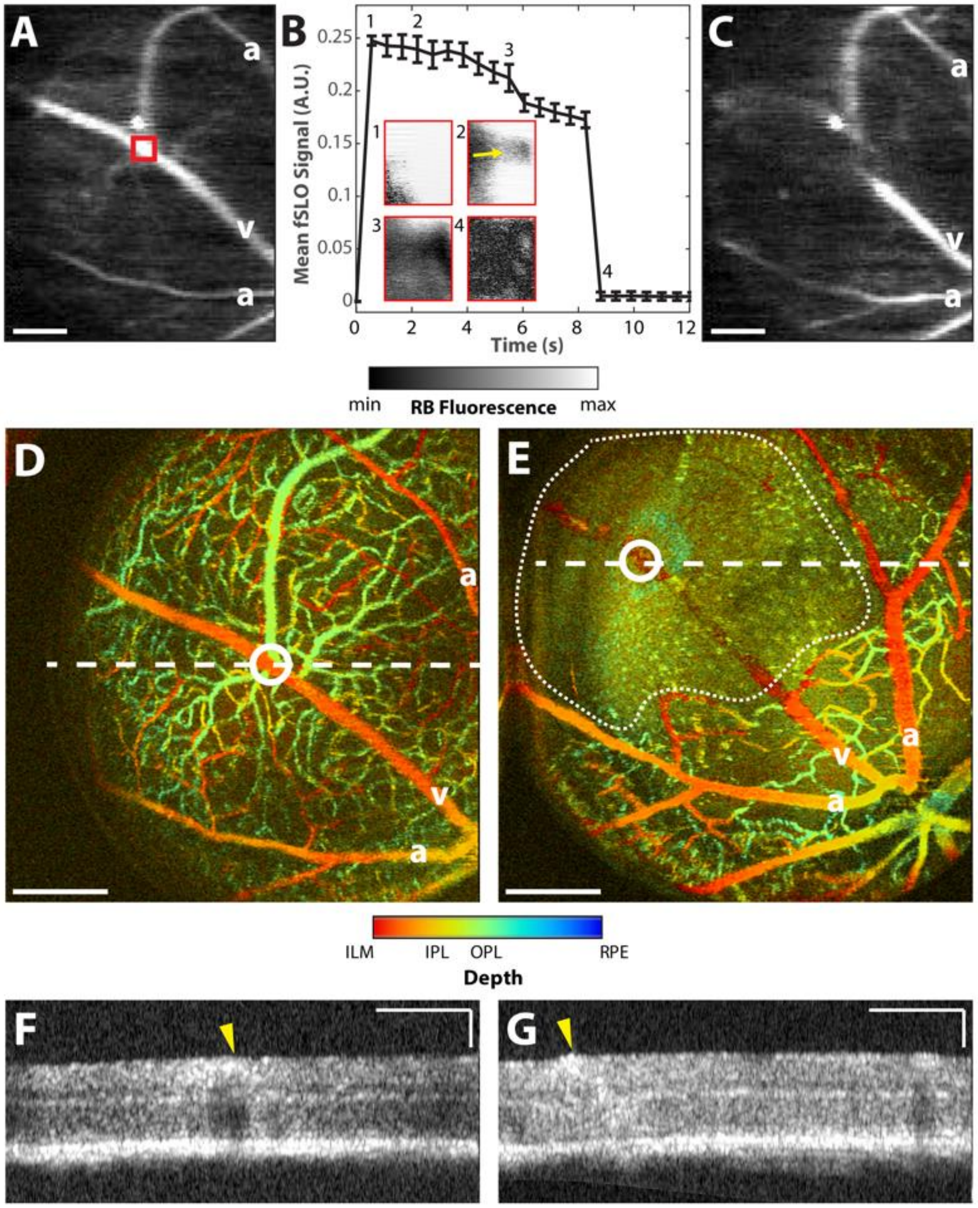

Figure 7-3: Producing a branched retinal vein occlusion. (A) Pre-occlusion RB angiogram. Red box indicates scanning area for occlusion. (B) Mean RB fluorescence signal during occlusion corresponding to red box in A. Insets 1 to 4 show frames at points 1 to 4 on the curve. Laser power was 25 mW at the pupil. (C) Post-occlusion RB angiogram. (D) Pre-occlusion OCTA of a retinal vein. (E) Post-occlusion OCTA. White solid circles in D and E indicate the site of occlusion. White dashed region indicates area of capillary non-perfusion. (F) Pre-occlusion OCT B-scan at the white dashed line in D. (G) Post-occlusion OCT B-scan at the white dashed line in E. Yellow arrows in F and G indicate vessel location. Horizontal scale bars are 500 µm. Vertical scale bars are 100 µm. a: artery; v: vein.

We performed another BRVO experiment where we longitudinally monitored the retinal microvasculature before and after the occlusion. A BRVO was created at the 9 o’ clock position, indicated by the yellow circles on the pre-occlusion and post-occlusion RB angiograms (Figure 7-4(A) & Figure 7-4(B)). The post-occlusion RB angiogram showed increased dilation and tortuosity before reaching the occlusion site (yellow arrow). Additionally, we also observed leakage of the RB dye in the peripheral area (magenta arrow). Pre-occlusion (Figure 7-4(C), post-occlusion (Figure 7-4(D)) and day 1 (Figure 7-4(E)) OCTA montages were performed. The montages consisted of nine images and covered a larger FOV of approximately 3.5 mm^2. In the pre-occlusion depth-colored OCTA (Figure 7-4(C)), three healthy vascular networks can be seen: one near the inner limiting membrane (ILM) in red, a second near the inner plexiform layer (IPL) in orange-yellow, and a third near the outer plexiform layer (OPL) in green (229). Labeled arteries, a, and veins, v, alternate in the typical mouse retinal pattern. The BRVO location is denoted by the white solid circle at the 9 o’ clock position.

The white dashed region in Figure 7-4(D) shows the sectorial area of capillary non-perfusion associated with the vein occlusion. At day 1, the area of capillary non-perfusion enlarged but stopped at the nearest adjacent veins (white dashed region in Fig. 4(E)). This progression of capillary non-perfusion has been observed in both monkey and rat models of RVO (241, 242). Slow blood flow may predispose to increased clot formation in the capillary bed, and the interstitial edema may create enough interstitial pressure to close capillaries (242).

Previous investigations of BRVO mouse models have observed interstitial edema and increased retinal thickness by day 3 post-occlusion (62, 63). We observed similar results in our animal model. A pre-occlusion OCT B-scan through the ONH showed normal intact retinal layers

(Figure 7-4(F)). On the post-occlusion B-scan (Figure 7-4(G)), the retinal layers were still distinguishable on both the sides of the ONH. On day 1, the OCT B-scan showed evident increase in retinal thickness on the side of the retina with the occlusion (Figure 7-4(H)). On the side with occlusion, we observed increased scattering in the GCL, IPL, and INL layers, and the retinal layer boundaries became hard to distinguish. The retinal layers on the side without occlusion appeared intact. Retinal thickness measurements on the side of the occlusion were 265 µm, 273 µm, and 389 µm pre-occlusion, post-occlusion, and day 1 post-occlusion, respectively. On the opposing side, retinal thickness measurements were 257 µm, 250 µm, and 266 µm pre-occlusion, post-occlusion, and day 1 post-occlusion, respectively. Measurements were performed at a radial distance of 800 µm from the ONH.

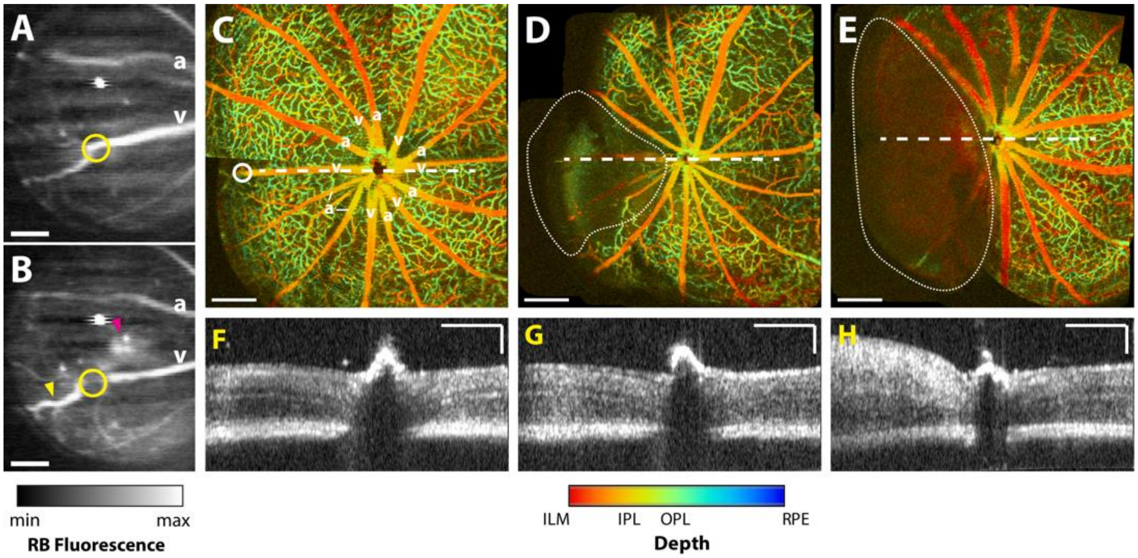

Figure 7-4: Longitudinal OCTA of branched vein occlusion. (A) Pre-occlusion RB angiogram. (B) Post-occlusion RB angiogram. Yellow arrow indicates dilated, tortuous vein. Magenta arrow indicates vascular leakage. Yellow circles in A and B indicates site targeted for occlusion. (C) Montage of 9 OCTA images before vein occlusion. a and v denote arteries and veins respectively. White circle denotes the targeted site of occlusion on the 9 o' clock vein. (D) Montage after vein occlusion. (E) Montage on day 1 after the vein occlusion. White dotted regions in B and C denote areas of capillary non-perfusion.

(F,G,H) OCT B-scans at the ONH before, after, and at day 1 for a vein occlusion. White dashed lines in C,D, and E denote the B-scan position for F,G, and H. Horizontal scale bars are 500 µm. Vertical scale bars are 100 µm.

To demonstrate that our technique could also produce CRVO patterns of occlusion, we targeted a 12 o' clock retinal vein at a location approximately 4 ONH diameters away from the ONH. As reported previously, CRVO patterns are more likely when the target location along the vessel is positioned more proximal to the ONH (62). Figure 7-5(A) shows the pre-occlusion RB angiogram with the target location indicated by the yellow circle. Figure 7-5(B) and Figure 7-5(C) show the post-occlusion RB angiograms. RB flow was only observed past the occlusion site. The baseline OCTA image shows a healthy adult vascular network (Figure 7-5(D)). However, unlike the BRVO-like post-occlusion OCTA montages, the CRVO-like post-occlusion OCTA showed widespread capillary non-perfusion extending beyond the adjacent retinal veins (Figure 7-5(E)). On day 1, the capillary networks are markedly absent on OCTA, as shown in Figure 7-5(F). The corresponding OCT B-scans pre-occlusion for each point in time are shown in Figure 7-5(G,H,I). The pre-occlusion and post-occlusion OCT B-scans showed intact retinal layers on both sides of the ONH. On day 1 post-occlusion, however, the retinal layer boundaries were obscured and there was increased scattering throughout the inner retinal layers. Diffuse swelling of the retina was observed on day 1 (Figure 7-5(I)), which differed from the BRVO pattern in Fig. 4. The pre-occlusion retinal thickness measurements were 257 µm nasally and 246 µm temporally. The post-occlusion retinal thickness measurements were 273 µm nasally and 250 µm temporally. The retinal thickness measurements on day 1 were 524 µm nasally and 514 µm temporally.

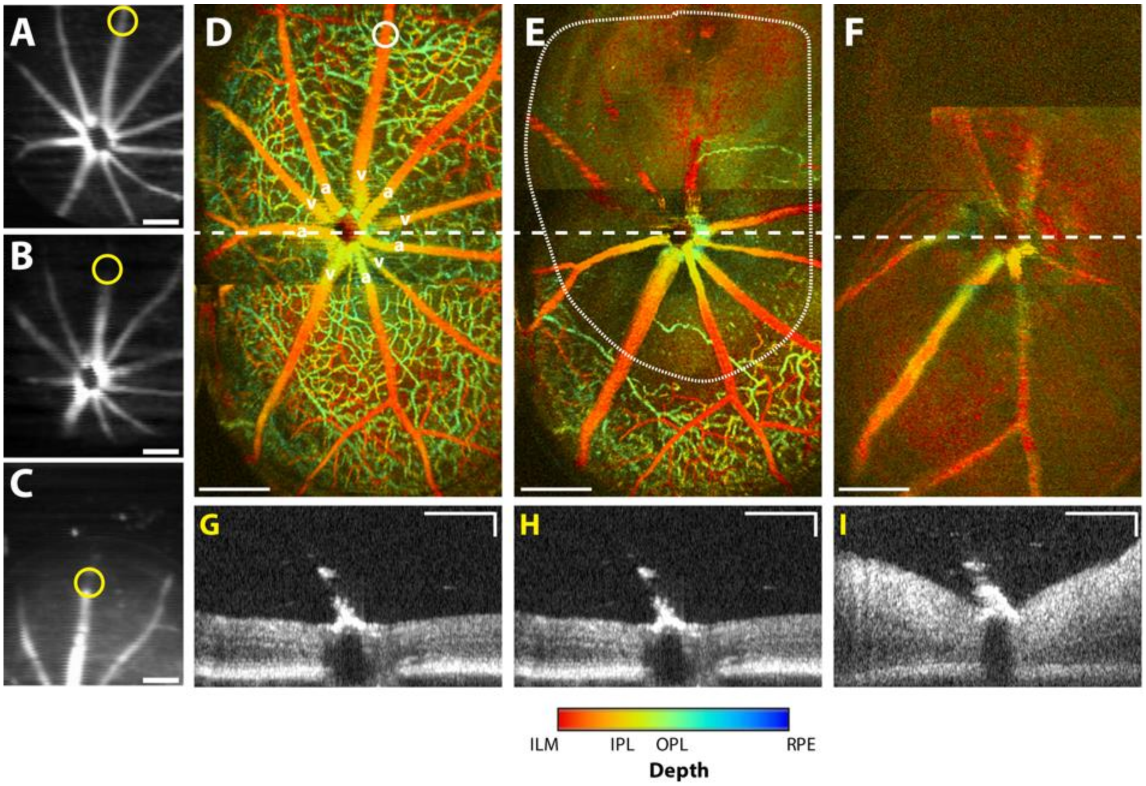

Figure 7-5: Longitudinal OCTA of central vein occlusion. (A) Pre-occlusion RB angiogram. Yellow circle indicates site of occlusion. (B) Post-occlusion RB angiogram. (C) Post-occlusion RB angiogram positioned away from ONH. (D) Montage of 3 OCTA images pre-occlusion. “a” and “v” label the arteries and veins, respectively. White solid circle shows the target site for vessel occlusion. (E) Montage of 3 OCTA images post-occlusion. White dotted region denotes area of capillary non-perfusion. (F) Montage of 3 OCTA images at day 1. (G,H,I) OCT B-scans at the white dashed lines in D,E,F, respectively. Horizontal scale bars are 500 µm. Vertical scale bars are 100 µm.

Figure 7-6 demonstrates that our imaging-guided vascular occlusion technique could also produce animal models of artery occlusive disease. Figure 7-6(A) shows the pre-occlusion RB angiogram with the target location marked by the yellow circle. The white arrow indicates a branch point of the arterial tree. Figure 7-6(B) shows the post-occlusion RB angiogram. There was limited flow past the occlusion site. In pre-occlusion OCTA, shown in Figure 7-6(C), the white solid circle indicates the target site of occlusion on an artery at the 12 o’ clock position. In the post-occlusion OCTA, shown in Figure 7-6(D), we observed a sector of non-perfusion, similar to the vein occlusions shown previously. The white arrows on Figure 7-6(A-D) highlight a bifurcation of the retinal artery. Since the artery occlusion was positioned past the bifurcation, one of the branches had diminished OCTA signal, while the other branch continued to have OCTA signal, post-occlusion, which is expected for arterial blood flow. On day 1, the OCTA montage showed that region of non-perfusion increased in size, extending to the next adjacent artery (Figure 7-6(C)).

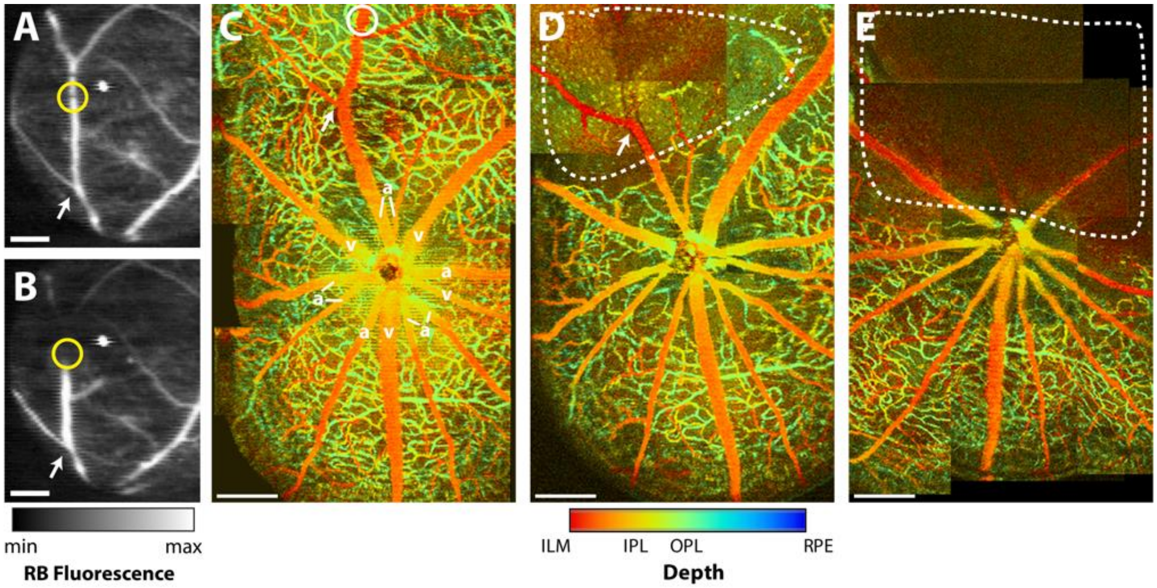

Figure 7-6: Longitudinal OCTA of branched artery occlusion (A) Pre-occlusion RB angiogram. Yellow circle indicates site of occlusion. (B) Post-occlusion RB angiogram. (C) Montage of 3 pre-occlusion OCTA images. White solid circle denotes the site of occlusion. White solid arrow indicates an arterial branch point. a: artery; v: vein; (D) Montage of 3 post-occlusion OCTA images. White dashed region denotes area of capillary non-perfusion. White solid arrow indicates an arterial branch point (E) Montage of 3 OCTA images on day 1. White dashed region denotes area of capillary non-perfusion. Scale bars: 500 µm.

7.4 DISCUSSION

We successfully developed an imaging system and experimental protocol for producing precise retinal occlusions in the murine inner retina (Figure 7-1 & Figure 7-2). To the best of our knowledge, this is the first demonstration of SLO guidance to produce retinal vascular occlusions for animal studies. To target a vessel for occlusion, we used SLO to ensure that RB fluorescence was observable within the retinal vasculature. After precisely choosing a target vessel location, we used the same SLO system at a higher laser power to deliver actinic light to the intravascular RB (Figure 7-3). Using this imaging system and occlusion protocol, we demonstrated the production of BRVO (Figure 7-4), CRVO (Figure 7-5), and BRAO (Figure 7-6) patterns in the mouse retina.

Our system has permitted the characterization of retinal occlusions with OCT and OCTA Acquired OCT volumes allowed us to observe the retinal edema associated with vascular occlusion. Whereas previous studies have used fluorescein angiography (FA) to study retinal vascular occlusions (61, 62), we used OCTA to monitor the longitudinal changes in the retinal microvasculature, pre-occlusion, immediately post-occlusion, and on day 1 post-occlusion. Unlike FA, OCTA provides 3D images of the vascular network, enabling us to use a depth color map on our *en face* OCTA montages. Additionally, no contrast agent was required to obtain the angiograms with OCTA, which was extremely desirable for longitudinal monitoring. Moreover, FA has difficulty visualizing the complete deep vascular network compared to OCTA (243). With OCTA, we were able to monitor the changes in capillary non-perfusion cases of BRVO, CRVO, and BRAO.

Creating retinal occlusions has depended primarily upon the slit-lamp biomicroscope (60-63, 227-229). Our multimodal imaging system for producing retinal occlusions in animal models has several advantages over using a slit-lamp biomicroscope. First, the system is easy to use and requires little training to perform the procedure, other than learning how to perform tail injections. Second, the SLO enables the verification of RB within the retinal vessels of the eye. Since RB has a short half-life in the bloodstream of approximately 5 minutes (244), it is important to verify that

RB is within the target retinal vessel. Third, instead of relying on non-specific signs of occlusion (e.g. whitening of the vein) to determine when vascular occlusion occurs, SLO enables monitoring of the thrombus formation in real time. The real-time monitoring allows the operator to remove the high-power illumination after the occlusion is observed, which prevents excess laser dosage to the animal eye. On the other hand, real-time monitoring with SLO also enables the operator to tell if the occlusion is partially formed. At that point, the operator can choose to increase the illuminating laser power to ensure the full formation of the occlusion. Finally, compared with the slit-lamp biomicroscope, the spot size on the retina is better controlled in SLO because the same spot size used for imaging is also used to perform the occlusion. This makes the actinic laser delivery much more precise and minimizes damage to the surrounding retina.

There are some limitations to this work. First, producing retinal vascular occlusions using RB, although similar to producing a thrombus, is similar, but not equivalent, to the pathogenesis of human retinal occlusive diseases. For example, the pathogenesis of the disease for BRVO's in humans is believed to result from arterial compression of venules by stiffened arteries at arterio-venous crossings (14). Additionally, thrombus formations usually cause CRVO's, but emboli usually account for BRAOs (14, 245). Nevertheless, the RB method provides a reliable method to produce an animal model with similarities to human retinal vascular occlusions, such as the inner retinal edema. Another limitation of this study is that it is unknown why occlusions performed close to the ONH cause a CRVO pattern while occlusions further from the ONH result in a BRVO pattern. This phenomenon has also been observed by other researchers (62). Explanations of this phenomenon remain to be explored in detail by future investigations, but they may include that the thrombus formed by RB travels further down towards the central vein, thereby affecting more branches. Alternatively, the retinal circulation in mice may be interconnected such that capillary closure close to the ONH affects a larger radius than closure farther away from the ONH.

Other limitations relate to the angiographic methods used in this study. We noticed that there was some discrepancy between OCTA and RB angiography in showing the flow in the major vessels, especially in areas near the occlusion site. In some cases, RB still showed flow, while OCTA did not. This could be because the OCTA takes some time to acquire after the occlusion, when the flow patterns are adjusting to the intervention. Another possible reason could be that the OCTA only detects blood movement, while RB angiography detects both moving and static dye. This could be modified in future studies by changing the time between successive B-scans (246). Finally, another limitation is that RB angiography was unable to observe retinal capillaries in the deep retinal network, which is likely due to the low fluorescence quantum yield of RB (0.05 in ethanol) (247). For comparison, fluorescein has a quantum yield of 0.79 (248). Future work may incorporate other fluorescing dyes with higher quantum yields for better visualization of the deep capillary network.

In conclusion, we have outlined the development of an OCT and SLO based retinal vascular occlusion system. We have detailed the retinal vascular occlusion protocol when using this system. In addition, we have showed real-time monitoring of retinal vascular occlusions with RB and performed OCT and OCTA monitoring of the occlusions. Finally, we have discussed the benefits and limitations of the system as compared with traditional approaches. The demonstrated ability to precisely and consistently create vascular occlusions in the rodent retina will be an important step for animal studies of retinal vascular occlusive disease.

Chapter 8

Visible-light Optical Coherence Tomography Angiography for Monitoring Laser-induced Choroidal Neovascularization in Mice

8.1 INTRODUCTION

Age-related macular degeneration (AMD) is a leading cause of blindness in people 50 years of age or older in the United States (249-251). There are two major subtypes of advanced AMD: dry, also known as atrophic, and wet, also known as neovascular. In the dry AMD subtype, atrophy of the macular retinal pigment epithelium (RPE) leads to the formation of yellow crystalline deposits, or drusen. In the wet AMD subtype, the hallmark is choroidal neovascularization (CNV),(252-254) which can cause exudative leakage, hemorrhage, and fibrosis, leading to photoreceptor damage and, ultimately, irreversible vision loss (250, 252). Although geographic atrophy is a more prevalent cause of vision loss than neovascular AMD, with the use of anti-angiogenic therapy, the latter remains the only AMD subtype which is pharmacologically treatable.

Imaging technologies, such as fluorescein angiography (FA), indocyanine green angiography (ICG), and spectral-domain optical coherence tomography (SD-OCT), guide the clinical diagnosis and management of AMD.(251, 255) Of the three, SD-OCT is by far the least invasive. SD-OCT does not require intravenous contrast agents and is also unique in that, by capturing high-resolution depth information, it is inherently cross-sectional, providing three-dimensional (3-D) imaging. By contrast, FA and ICG can only provide two-dimensional (2-D) images. With these unique advantages, SD-OCT has enabled the study of the intricate, 3-D relationship between AMD lesions and the overall structure of the retina (251, 255). One disadvantage of SD-OCT, for the specific purposes of diagnosing neovascular AMD, is that the pathological vessels of CNV cannot be directly visualized. Because of this limitation, among others, the diagnosis of CNV cannot rely solely on SD-OCT findings (254); instead, current clinical guidelines require that the structural findings from SD-OCT be interpreted in conjunction with leakage seen on FA in order to conclusively diagnose CNV in AMD (256).

The laser-induced CNV model in mice, which is one of the most widely used models in neovascular AMD research (257, 258), is an accepted, reliable animal model for neovascular AMD (258-262). Neovascularization in human AMD arises from an aging-related, multifactorial, complex disease state; however, neovascularization in the murine model arises from experimental laser injury. The RPE, with its many darkly colored granules of melanin and other chromophores, absorbs the laser energy, which results in a localized, thermal rupture of Bruch's membrane, followed by a cascade of inflammatory factors and a self-limited, pro-angiogenic process (263, 264). Historically, experimental CNV has been studied *in vivo*, with FA, or *ex vivo*, with choroid flatmount preparation (259). SD-OCT has also been used to visualize CNV formation(259, 265) ; however, as discussed previously, this method does not allow direct visualization of the vessels in the neovascular complex (266).

Recent improvements in both hardware and software have led to the development of OCT angiography (OCTA) (266, 267). Unlike SD-OCT, OCTA is sensitive to motion contrast, enabling 3-D visualization of blood flowing within vascular networks. Moreover, OCTA allows 3-D visualization of pathological CNV in AMD without the administration of intravenous contrast agents (266, 268, 269). OCTA volumes can be segmented according to the different layers of the retina and choroid, such that vasculature can be measured in each separate layer, visualized in cross section, or volumetrically reconstructed.(266) This 3-D visualization enables the discrimination of abnormal neovascular tissue from the surrounding tissues allowing a more precise localization of CNV (55, 266). Historically, near-infrared (NIR) light has been utilized in OCT technology; however, our group has recently developed visible-light OCT (vis-OCT), which uses a broad-spectrum light source that is centered in the visible wavelength (270). Because of the shorter wavelengths, a visible-light source provides higher axial and lateral resolution for OCT than NIR light source. In addition to improved imaging resolution, visible light spectrum makes it feasible to examine oxygen saturation within the living retina, providing functional information (89). Recently, we extended the applications of vis-OCT to angiography (vis-OCTA), to examine the retinal vasculature *in vivo* (89, 106, 271).

In this study, for the first time, we used vis-OCTA to image laser-induced CNV in mice. To best visualize the lesions, we developed an image processing protocol, which removes imaging artifacts and enhances the contrast of the lesion using color-coding. By monitoring laser-induced CNV lesions at different points in time and comparing vis-OCTA with *ex vivo* stained flatmounts, we were able to determine the earliest time point at which vis-OCTA can detect CNV.

8.2 METHODS

8.2.1 Animals

All animal studies followed the guidelines established by the ARVO Statement for the Use of Animals in Ophthalmic and Visual Research as well as those set by the Northwestern University Institutional Animal Care and Use Committee. Twenty-five adult mice aged 4-8 weeks of mixed background were used for this study. Over the course of the experiment, mice were sacrificed at pre-determined time points based on the data set that was to be examined (day 2 post laser, day 3 post laser, etc.). For laser injury procedures, anesthesia was achieved via intraperitoneal injection of 2,2,2-tribromoethanol (Avertin; 20mg/kg; Sigma-Aldrich, St. Louis, MO) to minimize cataract formation (272).

During imaging procedures, mice were placed on a custom-made mouse holder allowing fine manipulation of their position in three dimensions. Anesthesia during imaging and during the perfusion staining procedure performed immediately after imaging was achieved via an intraperitoneal injection of a xylazine (10 mg/kg) and ketamine (87 mg/kg) cocktail. Pupils were dilated with 1% tropicamide solution and kept hydrated with artificial tears (Alcon Laboratories, Ft. Worth, TX, USA).

8.2.2 Laser-induced CNV

We performed laser photocoagulation using an argon 532 nm laser (IRIDEX Oculight GLx, Mountain View, CA, USA) attached to a slit lamp delivery system (Carl Zeiss 30SL-M, Jena, Germany). To flatten the cornea and allow visualization of the retina, a glass coverslip with a drop of artificial tear solution was gently placed on the surface of the mouse eye (273). Laser spots (75 μm spot size, 100 millisecond duration, 100 mW power) were delivered at 3, 6, 9, and 12 o'clock positions around the optic nerve of both eyes of each animal. Lesions that resulted in "bubble" formation, indicating rupture Bruch's membrane, were deemed successful. Lesions that did not meet this criterion, or resulted in hemorrhage, were excluded from further analysis.

8.2.3 Visible-light optical coherence tomography angiography

Our custom-built vis-OCT imaging system is similar to most other SD-OCT imaging systems, except for the light source, which used a supercontinuum laser (SuperK EXTREME EXW-6, NKT

Photonics) with a spectrum from 500 nm to 620 nm (89, 271). A detailed description of the imaging system can be found in a study by Yi et al. (89). Our system has a fast scanning axis and a slow scanning axis. For the fast scanning axis, A-lines were acquired at 50 kHz. Using our custom-built vis-OCT system, we obtained 3-D structural images, covering a 0.92 x 0.92 mm^2 area on the mouse retina. The lateral and axial resolution for this system is approximately 15 μm and 1.7 μm, respectively. A set of glass plates in the reference arm compensated for dispersion introduced by the optical components of the system. Dispersion introduced by the eye was compensated for in post-acquisition data processing.

To better visualize the CNV lesion, we employed vis-OCTA, which uses the same imaging system as vis-OCT, but requires a modified scanning pattern and additional post-processing of the imaging data. Our vis-OCTA scanning pattern requires that five B-scans be acquired at each position along the slow scanning axis (271). After image acquisition, the five B-scans are post-processed using a phase-sensitive decorrelation algorithm to produce a 3-D angiography volume, whose signal represents motion contrast from flowing blood (80). Angiograms were also motion-corrected for bulk image shift, axial global phase fluctuations, and lateral global phase fluctuations (237). The relationship between the OCTA decorrelation signal and velocity is non-linear, and may be affected by the pulsatile nature of blood flow in living subjects. Therefore, OCTA images can help visualize moving blood, but does not provide quantitative measurements of the velocity of blood. Further details of the angiography and signal processing algorithms can be found in a study by Chen et al. (271).

8.2.4 Image processing for visualizing CNV

Building upon our experience with structural and functional applications of vis-OCT (89, 106, 267, 271, 274, 275), we developed an imaging and data processing protocol for vis-OCTA of laser-induced CNV. The image processing protocol for visualizing CNV consists of three major steps: flattening the vis-OCTA volume to a reference surface, performing a maximum amplitude projection (MAP), and color-coding the MAP based on depth.

Due to the natural curvature of the retina, the signals within vis-OCT and vis-OCTA volumes are not flat, making it difficult to isolate the CNV lesion for the purposes of visualization. Therefore, to flatten the vis-OCTA volumes, we first generated a reference surface from the structural vis-OCT volumes. For each A-line in the vis-OCT volume, we determined the z-positions of the first maximum signal (i.e. the ILM) and the last maximum signal (i.e. the Bruch membrane). We then averaged these z-positions to obtain an approximate reference surface, representing the middle of the retina. Some areas of the image had low signal-to-noise ratio, making surface detection difficult; therefore, we performed 3-D interpolation to fill these areas. Finally, to achieve a flattened vis-OCTA volume, we shifted each A-line in the volume by the z-positions of the reference surface.

Maximum amplitude projections enable the visualization of 3-D volumes in a 2-D format. If we denote a 3-D volume (whether it be a vis-OCT or vis-OCTA volume), then we can mathematically define its MAP along the depth direction as the following:

$$M(x, y) = \max_{z} I(x, y, z) \tag{8-1}$$

where the max function returns the maximum value along the z-axis at each (x, y) position. With the vis-OCTA volume flattened, we generated three MAPs for three separate ranges in the z-dimension. The first MAP, which we term the “entire retina” *en face* angiogram, spanned from the ILM to the choroid. The second MAP, which we term the “inner retina” angiogram, spanned from the ILM to the OPL-ONL junction. The third MAP, which we term the “outer retina” angiogram, spanned from the OPL-ONL junction to the choroid (approximately 100 μm in thickness). To eliminate mirror image artifacts from superficial vessels from the outer retina angiogram, we subtract the inner retina angiogram from the outer retina angiogram, turning bright areas, where artifacts are present, to dark areas. This method appears to be similar to the one employed by Jia et al. (269).

When the MAPs were performed, we also saved the z-position of the location of the maximum amplitude. Using the same notation for a 3-D volume as above, the depth information can be extracted using the following equation:

$$D(x,y) = \underset{z}{argmax}\, I(x,y,z) \tag{8-2}$$

From this information, we were able to color code each pixel based on depth. This process provided an improved contrast to the vessels of the CNV, which aided our graders in determining the CNV area from vis-OCTA. CNV lies above the plane of the choroid; therefore, the CNV was colored red or yellow, while the deeper choroidal structures were colored blue and green.

8.2.5 Choroidal flatmount preparation and isolectin staining of CNV lesions

After vis-OCTA imaging at each of the six time-points, CNV lesions were evaluated post-mortem using isolectin stained choroidal flatmounts. Two isolectin stains were used: one that highlights only perfused blood vessels and one that highlights both perfused and non-perfused blood vessels. In order to highlight *perfused* blood vessels, mice were anesthetized and underwent cardiac perfusion with isolectin GS-IB$_4$ conjugated with Alexa Fluor 488 (Life Technologies, Carlsbad, CA, USA), as reported previously (276, 277). Here we injected 50μL of isolectin GS-IB_4 conjugated with Alexa Fluor 488 (0.33 mg/mL) into the left ventricle. A flash of blood followed by a visible flow of blood into the syringe indicated successful puncture of the left ventricle and, therefore, success of the cardiac perfusion procedure (277). Five minutes after the cardiac perfusion, the animals were sacrificed, and eyes were enucleated and fixed in 4% PFA for 30 minutes at room temperature.

In order to highlight both *perfused* and *non-perfused* vessels, we subsequently performed post-mortem counterstaining with conjugated with Alexa Fluor 594 (IB_4 594, 1:100, Life Technologies, Carlsbad, CA, USA), which binds to all endothelial cells to label all the vasculature. In addition, this stain also highlights microglia and macrophages. The procedure for this staining is described as follows. After the enucleated eyes have been fixed in 4% PFA for 30 minutes at room temperature, they were transferred to PBS at 4^{o}C. The anterior segment and the lens were removed, and the neurosensory retina was carefully separated from the underlying RPE.(278, 279) The remaining RPE-choroid-sclera complex was washed with PBS, blocked with 10% NDS in PBS with 0.5% Triton X-100, and then stained with isolectin GS-IB_4 594 (280). Four relaxing radial incisions were made on the RPE-choroid-sclera complex, which was then flatmounted with Prolongold anti-fade reagent (Life Technologies, Eugene, OR, USA) and cover-slipped.

8.2.6 CNV area quantification

To calculate the area of the CNV lesions in the vis-OCTA images, two masked independent graders (R.S. & B.T.S.) independently delineated the outlines of the CNV lesions, using the lasso tool in ImageJ (National Institutes of Health, Bethesda, MD, USA). Then, using ImageJ's area calculation tool, the area was of the CNV lesion was determined and converted from pixel number to physical dimensions (μm^2). The results of the two graders were compared and the correlation coefficients were calculated. Additionally, we constructed a Bland-Altman plot to check for inter-grader agreement and to ensure that there was no systematic pattern of bias.

Choroidal flatmounts were evaluated using confocal microscopy (Zeiss LSM Meta 510, Jena, Germany). The only landmarks to judge the extent of the lesion in the z-direction were the top of the CNV lesion and the RPE. Therefore, we acquired an image stack where the first image visualized the top of the CNV lesion and the last image visualized the RPE (281, 282). The resulting stack thickness was approximately 20 to 25 μm. For each of the CNV lesions, we simultaneously acquired images at the two isolectin B4 wavelengths. The MAP of the confocal microscopy z-stack was performed using ImageJ . The excellent contrast of the obtained stained images allowed the use of an automatic segmentation program to quantify the areas of the lesions. The MAPs were imported into a custom-built, supervised, automated, threshold and area-calculating program in MATLAB 2015 (Mathworks, Natick, MA, USA). This program used a simple thresholding algorithm to obtain a binary mask and subsequently calculate the area of immunofluorescent area. Lesions that could not be adequately visualized due to poor staining with either the perfused IB_4 488 or the whole-mount IB_4 594, and lesions that were damaged during tissue handling were excluded from analysis.

8.2.7 Statistical analysis

The results are expressed as mean ± standard error of the mean, except where noted otherwise. Comparisons were made using a two-tailed paired t-test. A value of $p < 0.05$ was considered significant. All analyses were performed using Graphpad Prism (Version 6, GraphPad Software, San Diego California USA).

8.3 RESULTS

8.3.1 Vis-OCTA image processing

Figure 8-1 illustrates the differences between images acquired using vis-OCT, vis-OCTA, and vis-OCTA with post-acquisition image processing. An example *en-face* vis-OCT MAP, which captured the area surrounding a CNV lesion on post injury day 7, is shown in Figure 8-1(A). Because vis-OCT images do not reflect motion contrast, only large retinal vessels are visible in the vis-OCT MAP, and no CNV is visible. The vis-OCTA volume can be collapsed into an *en face* 2-D MAP, in the same manner as the vis-OCT volume in Figure 8-1 (A). Figure 8-1 (B) shows an example vis-OCTA MAP for the same CNV lesion corresponding to the same area shown in Figure 8-1(A). The vis-OCTA MAP has been color-coded by depth, with red denoting vessels near the inner limiting membrane (ILM) and blue denoting vessels near the choroid. Here we see that there is a large CNV lesion (yellow-green) lying above the choroid.

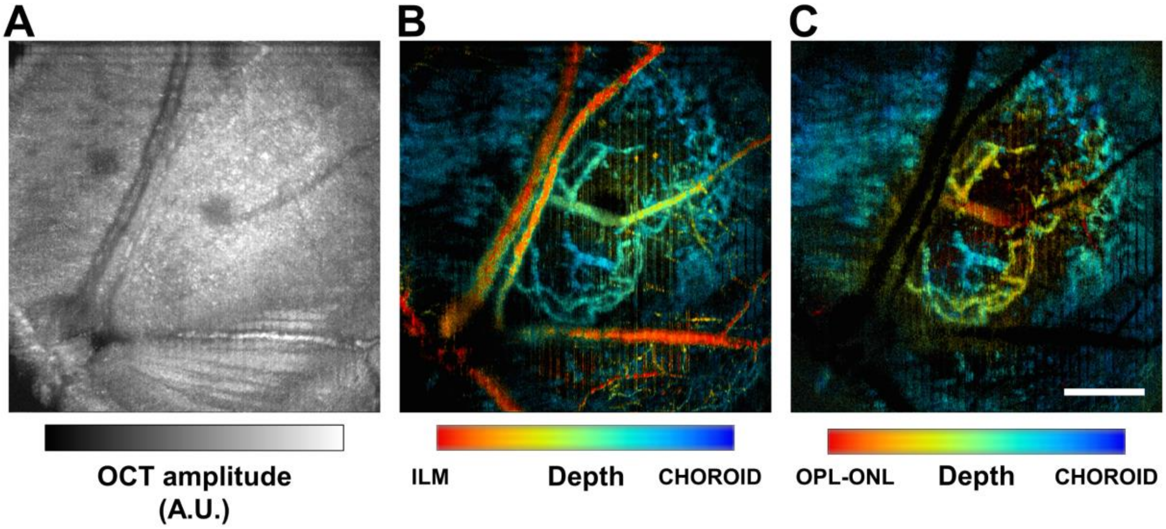

Figure 8-1: Overview of the visible-light OCT angiography protocol and post-acquisition image processing. **A.** *En face* maximum amplitude projection (MAP) of a typical structural vis-OCT volume. The CNV lesion is not visible. (A.U.: arbitrary units). **B.** *En face* MAP vis-OCT angiography of the same area, revealing the CNV lesion. Image color coded by depth. (ILM: Inner limiting membrane) **C.** Final post-processed outer retina

en-face angiogram, color-coded by depth. (OPL-ONL: junction between outer plexiform layer and outer nuclear layer). Scale bar: 200 µm.

We performed additional post-acquisition image processing to enhance the visibility of the CNV lesion. First, instead of performing the MAP along the depth dimension for the entire OCTA volume as in Figure 8-1(B), we performed the MAP on a smaller volume extending from the junction of the outer plexiform layer and outer nuclear layer (OPL-ONL), to the choroid, and modified our depth-color-coding accordingly. Second, we removed OCTA artifacts, which have also been observed by other groups using different angiography techniques (269, 283, 284). Vessels in the superficial layers of the retina (e.g. nerve fiber layer) cause a projection artifact onto deeper layers of the retina (e.g. photoreceptor outer segments). Because of these artifacts, it may appear that vasculature is present in deeper layers of the OCTA volume, when there are, in fact, no vessels physically present. Therefore, the interpretation of OCTA images requires caution, especially if no post-processing has been performed to remove or diminish these artifacts. We removed these artifacts using a simple subtraction method, detailed in the methods section. Finally, our post-processing yields a color-coded MAP of a CNV lesion alone. An example, corresponding to the lesion shown in Figure 8-1(B) (pre-processed), is shown in Figure 8-1(C) (post-processed).

8.3.2 Time course of laser-induced CNV using vis-OCTA compared with choroidal flatmounts

In a series of experiments at different points in time after laser injury, we correlated vis-OCTA images of laser-induced CNV choroidal flatmounts stained with endothelial cell marker isolectin B_4. As described in the methods section, two different forms of isolectin staining were used: an intracardiac perfusion method and a total tissue endothelial staining method. The intracardiac perfusion method used green isolectin B_4 488 to highlight *perfused* blood vessels. The total tissue endothelial staining method used red isolectin B_4 594 to highlight *all* of the blood vessels (both perfused and non-perfused) as well as supporting microglia and macrophages, in the lesion area.

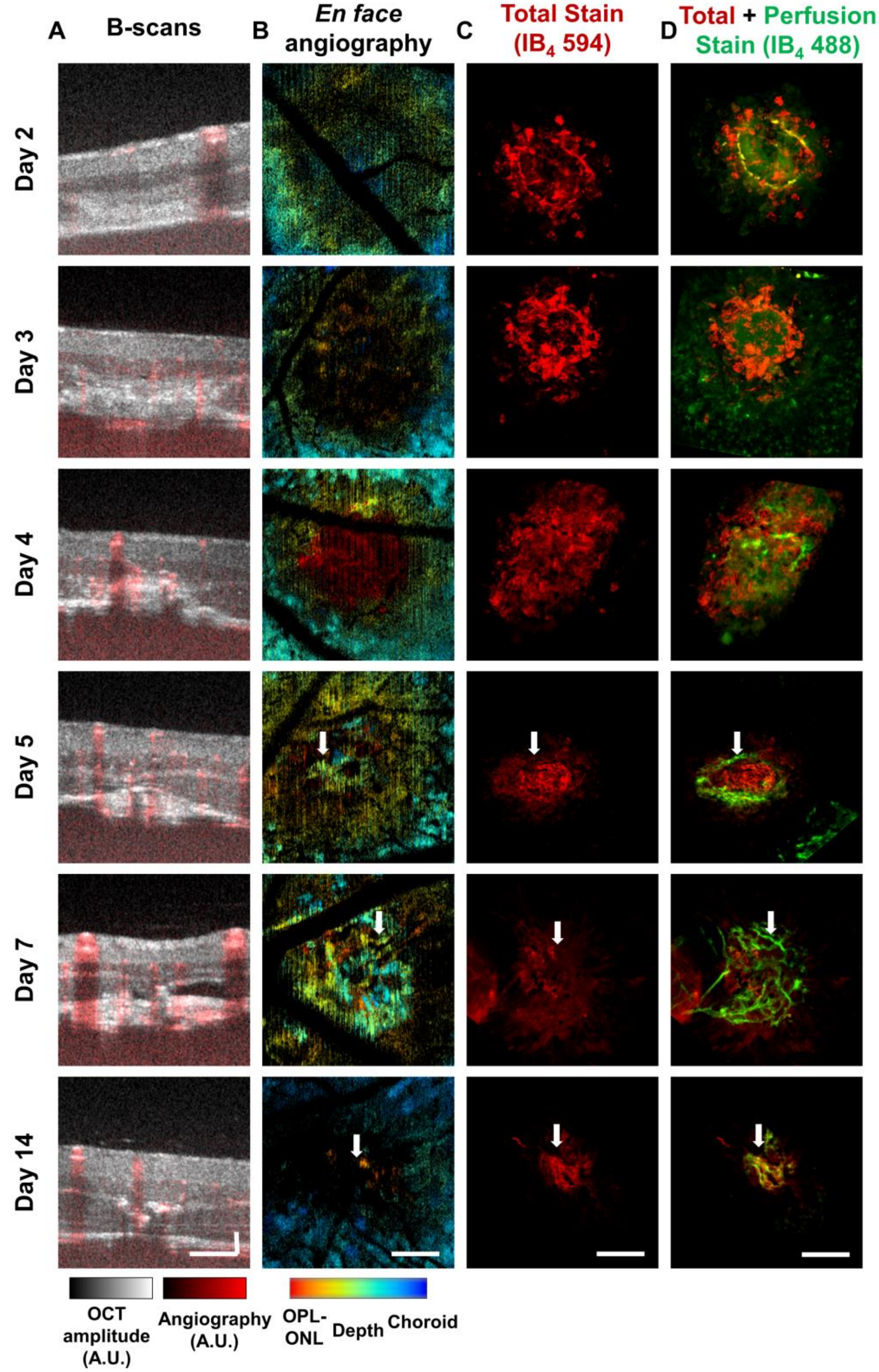

Figure 8-2: Comparison between *in vivo* vis-OCT angiography (vis-OCTA) of choroidal neovascular (CNV) lesions and the corresponding *ex-vivo* isolectin B$_4$

stained flatmounts over time. Each row represents a different animal, which was observed at days 2, 3, 4, 5, 7, and 14 after laser injury, respectively. Each column represents a different technique to visualize the CNV lesions. Column A: Vis-OCT structural B-scans, taken through the center of the CNV lesions, with vis-OCTA B-scans overlaid in red. The horizontal dimension matches the other columns, while the vertical dimension does not (because OCT is anisotropic). (A.U.: arbitrary units). Column B: Vis-OCTA of CNV lesions after post-processing. Color-coded by depth from the OPL-ONL to the choroid. (OPL-ONL: junction between outer plexiform layer and outer nuclear layer). The images were cropped from their original size for better comparison with columns C and D. Column C: CNV lesions stained after incubation with the endothelial cell marker, isolectin B_4 594 (red). Isolectin B_4-stained areas show presence of all vasculature in CNV lesion (as well as accessory macrophages and microglia). Column D: CNV lesions stained after cardiac perfusion with isolectin B_4 488 (green). Isolectin stained areas (green) show only perfused vasculature in CNV lesion. Images show combined images of total staining (IB_4 594, red) and perfusion staining (IB_4 488, green). Arrows show corresponding vessels in OCTA and immunostained images. All scale bars: 100 μm.

Using vis-OCTA, we imaged CNV lesions on days 2, 3, 4, 5, 7, and 14 post laser injury. Example images for each of the six points in time are shown in Figure 8-2(A) and Figure 8-2(B). Figure 8-2(A) shows cross-sectional structural B-scans through the center of the CNV lesion for each point in time. The vis-OCTA cross-sectional B-scans, shown as red overlays in Figures 2(A) give a general sense of the CNV blood flow, but can be difficult to interpret due to projection artifacts from superficial vessels in the inner retina. The best visualization, then, appears to be the post-processed *en face* view of the CNV lesion, as shown in Figure 8-2(B). For easier visual comparison between the vis-OCTA *en face* views and the stained flatmounts, we cropped the vis-OCTA images to display all images in Figure 8-2 with the same physical dimensions (except for the depth dimension of the B-scans). Figure 8-2(C) shows corresponding confocal microscopy images of the total tissue endothelial cell staining (red), while Figure 8-2(D) show co-registered, merged confocal microscopy images of both the intracardiac perfusion (green) and the total tissue endothelial cell stain (red).

8.3.3 Comparison of CNV area between vis-OCTA and isolectin-stained flatmounts

CNV lesions area measurements from vis-OCTA images were compared with area measurements from choroidal flatmounts. The area measurements from the two masked independent graders are plotted against each other in Figure 8-3(A). There is good correlation of the area measurements between the graders, which indicates that our vis-OCTA post-processing protocol provides excellent contrast for robust, easy visualization of the vessels. The measured r-value for this data was 0.98, and the R^2 was 0.96, again, indicating excellent correlation. Second, a Bland-Altman plot of the area gradings was created, with the difference in grader measurements on the y-axis and the average of grader measurements on the x-axis (Figure 8-3(B)). No particular trend was found in this plot, suggesting that there is no systematic bias (285, 286). Moreover, the bias (calculated as the mean of the differences) was small: 3.6e-4 with a standard deviation of 6.4e-3. The dashed lines on Figure 8-3(B) indicate the 95% confidence interval for the difference in measurements (also known as the 95% limits of agreement), which was -0.012 to 0.013. Given the lack of apparent bias and good agreement between graders, we considered the average of our grader's measurements for the remainder of our analysis.

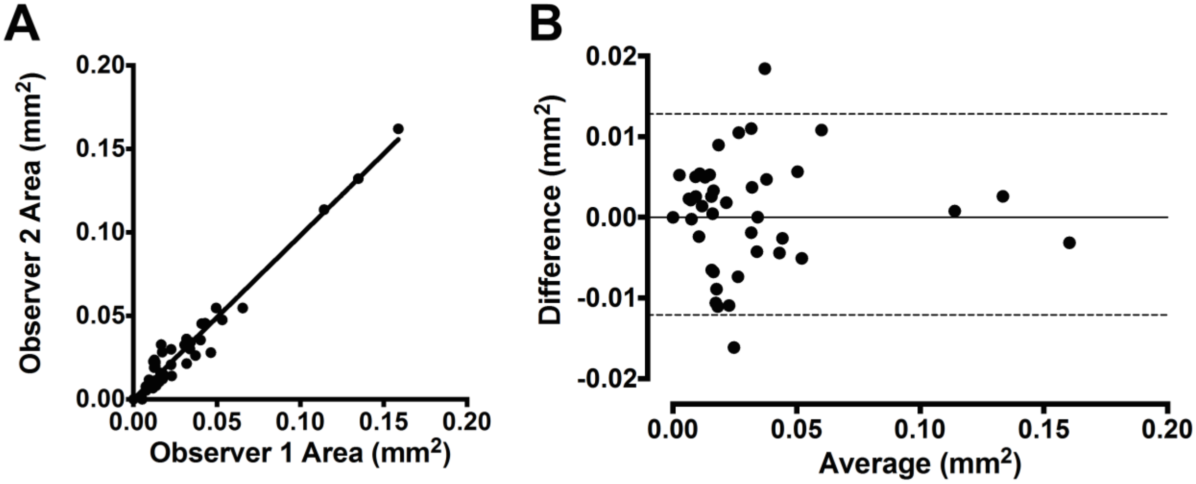

Figure 8-3: Inter-grader reliability for grading of CNV areas in vis-OCTA images. **A.** Inter-grader correlation of measurements. r value was 0.98, and R^2 was 0.96. **B.** Bland-Altman plot show the agreement of the measurements between the two graders. Dash lines indicate the 95% limits of agreement confidence interval. In several lesions, the graders observed no CNV lesion. In these instances, the graders designated the measured area as 0 mm^2. Therefore, for these data points, the difference between the areas was also 0 mm^2.

A comparison between the flatmount and the vis-OCTA CNV area measurements is shown in Figure 8-4(A). We used areas from the total isolectin IB_4-stained flatmounts (red) for comparison with our vis-OCTA areas, because this method is more reflective of the entirety of neovascularization present in the area, and specifically, can detect the immature, non-perfused vascular buds sooner than perfusion staining (280). The disadvantage of the perfused immunostaining method is that, like the OCTA, it only can provide the area of vessels that are patent enough to have detectable flow. However, total staining can highlight both nascent areas that are below this flow threshold as well as the mature vessels. Since this metric is a better reflection of the true area of the endothelial growth, the OCTA area was compared to only the total staining. Manual measurements on vis-OCTA show an overall progressive increase of CNV lesion area over time, from day 2 through day 7, with CNV area peaking at day 7 after laser injury. The average lesion area decreased between days 7 and 14. Flatmount CNV area calculations showed a similar trend: CNV lesion areas increased during the initial phases from days 2 through 7, with maximum area at day 7, and then subsequently decreased up to day 14.

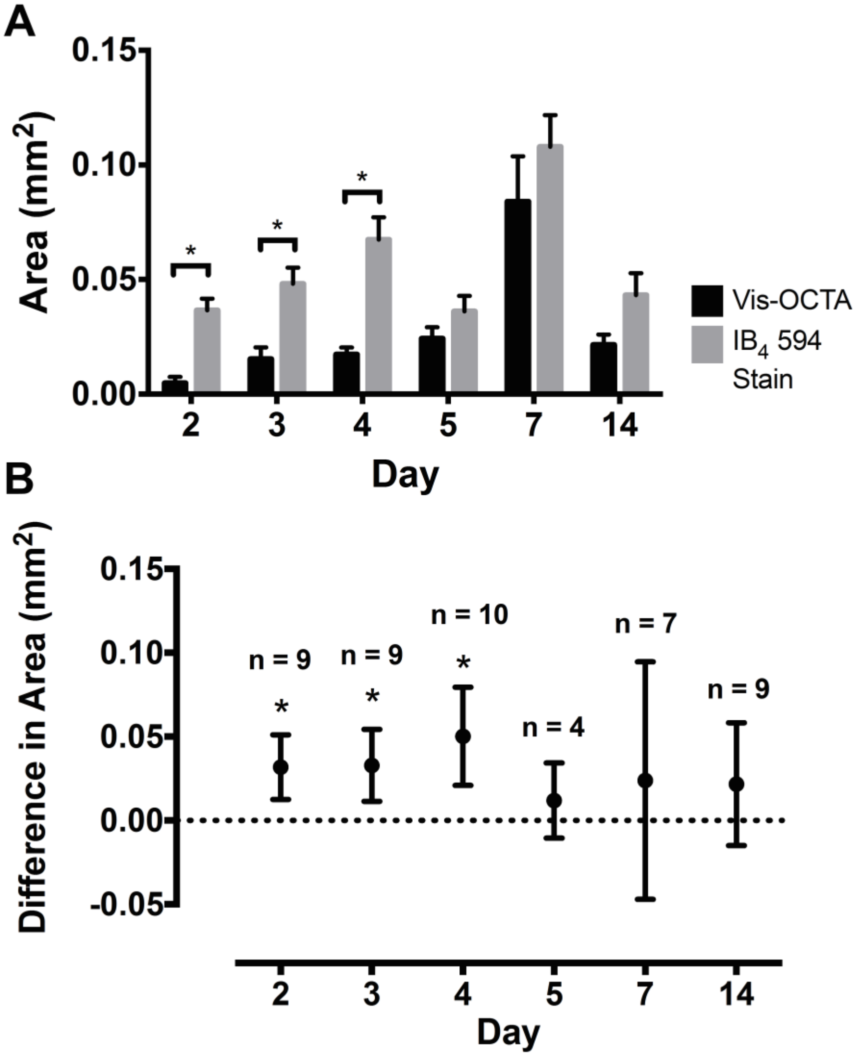

Figure 8-4: Comparison of CNV area on vis-OCTA with areas measured from isolectin-stained flatmounts. A. Average CNV areas for vis-OCTA images and isolectin stained flatmount images. Mean ± S.E.M. **B.** Average differences in vis-OCTA areas and flatmount areas over time. Mean ± S.D. Two-tailed paired t-test with 0.05 significance level cut-off (*). n = number of lesions analyzed, followed by (number of eyes) for each group was as follows: Day 2: n = 9 (5), Day 3: n = 9 (3), Day 4: n = 10 (5), Day 5: n = 4 (3), Day 7: n = 7 (6), Day 14: n = 9 (7).

In order to determine the time points at which vis-OCTA and the isolectin staining had maximum correlation, the average difference between corresponding vis-OCTA and flatmount CNV areas over time was plotted, as shown in Figure 8-4(B). Statistical analysis showed significant area differences for days 2, 3, and 4, but no significant differences at days 5, 7, and 14, with total IB_4 measuring larger areas than the vis-OCTA angiograms at all points. The earliest time point vis-OCTA was able to detect CNV without significant difference from the isolectin-stained flatmounts was day 5 post laser injury.

8.4 DISCUSSION

To our knowledge, this is the first time that OCTA has been used to longitudinally monitor laser-induced CNV in mice. While previous studies have examined the structural components of CNV lesions with SD-OCT and fluorescein angiography (259, 265), and compared them to H&E, immunofluorescence staining, and choroidal flatmounts, these imaging techniques were incapable of OCT angiography. Therefore, these studies could not detect the earliest stages of perfusion of the CNV lesions in the living animal non-invasively with OCTA, and, hence, they were not directly comparable to the stained vascular labeling. As shown in Figure 8-1, we were able to successfully acquire and post-process vis-OCTA images to reveal laser-induced CNV lesions, with high contrast and free of artifacts. Indeed, vis-OCTA enabled us, for the first time, to visualize the perfusion of CNV lesions at different points in time post laser injury *in vivo* (Figure 2).

Using vis-OCTA, we explored the earliest time point at which this imaging modality was able to detect CNV. We imaged at various time intervals over a two-week period to track the overall progress of CNV development, which could be separated into three phases, as previously described (259, 263, 287). At Day 5 post laser injury the vis-OCTA system was able to detect the first signs of a perfused lesion, a time point that coincided with findings of perfusion staining of CNV, which confirms vis-OCTA is detecting flow through the CNV lesion (Figure 8-2(B)). In the following paragraphs, we compare our vis-OCTA results with the isolectin stained flatmount data and to other studies in the literature, and discuss findings of vis-OCTA at each of the experimental time points. In a temporal fashion, we consider the “early” stage as days 2 and 3 post laser injury, the “intermediate” stage as days 4 and 5, and the “final” stage as days 7 and 14.

During the early stage of CNV development (days 2 and 3 post laser injury), the *en face* angiograms cannot detect the presence of blood flow within lesion’s vessels (Figure 8-2(B)). This stage represents an early angiogenesis growth phase (287), when the CNV lesion is still in its post injury inflammatory stages. Pro-angiogenic factors, triggered by the post injury inflammatory cascade, cause the release of matrix metalloproteinases, which degrade the basement membrane of vessels in the choroid (288, 289). Next, certain endothelial cells are selected to become tip cells, which lead the formation of the new vessels into the outer retina. In order to prevent unorganized growth, cells lateral to the tip cell are muted and, instead, become stalk cells, which make up the tube of the nascent vessels (288, 289). Accessory microglial cells and recruited macrophages are also present to aid the organization and expansion of the new vessels (290-292). Altogether, the CNV at this early stage has not developed many vessels with fully formed lumens (280, 288, 293). Therefore, we hypothesized that at this early stage there would be little to no detectable flow on OCTA within the area of the CNV lesion. Indeed, the vis-OCTA *en face* angiograms of the CNV lesions (Figure 8-2(B)) reveal a dark circular area at the location of the laser injury, distinct from the surrounding normal retinal and choroidal vasculature. No vessels are visible within this dark area, meaning that CNV could not be detected with vis-OCTA at this stage. In addition, the structural OCT B-scans demonstrate the butterfly-shaped lesion of laser injury, but the overlaid angiography signals showing no evidence of flow in the lesion (Figure 8-2(A)). Furthermore, Figure 8-4(B) shows a large average difference in measured area between vis-OCTA and total isolectin staining, which further illustrates the undetectable nature of CNV at this early stage.

Corresponding retinal flatmounts stained with red IB_4 594 (Figure 8-2(C)) show areas of dense hyperfluorescent circular areas without noticeable lumens, representing budding, naïve blood vessels, immature sprouting stubs of endothelial cells, and associated support microglia (288). Isolectin B_4 specifically targets a-D-galactosyl residues, which are present on many cells involved in the early angiogenic process, including endothelial cells, microglia, and macrophages (291, 292, 294, 295). Therefore, the presence of staining at this stage is not surprising, given that these cells are known to play a part in early vessel formation and inflammation. Also important to note is that due to multiplicity of cells stained by isolectin B_4, the isolectin stained CNV lesion may be artificially larger, giving the appearance of a more robust lesion than detected by the vis-OCTA system. The green intracardiac injection staining with IB_4 488 reflects perfused blood vessels. Interestingly, the Day 2 lesion shows co-localization of both red total tissue isolectin staining and green perfusion staining in a ring-like structure around the laser crater. According to previous studies, this ring-like structure does not indicate formed vessels, but rather represents an auto-fluorescent myofibroblasic scaffold that forms after laser injury (280, 293). Since the blood vessels are still in their naïve non-patent and non-perfused forms at this early time point, it is not surprising that no definite staining of vessel-like structures is observable. Moreover, the green perfusion staining that is observable in the area of the lesion could represent leakage of dye from these newly formed immature vessels into the lesion. The Day 3 lesion is very similar to the Day 2 lesion in character, except has an increased area of staining correlating with an increase in CNV complex area.

During the intermediate stage of CNV development (days 4 and 5 post laser injury), the *en face* angiograms can detect the presence of blood flow within lesion vessels (Figure 8-2(B)). On the OCTA angiogram, the previous dark circular area of the CNV lesion from the early stage has been replaced by small areas of bright signal scattered throughout; however, an organized vascular network is not evident. Moreover, the flow signal overlaid onto cross-sectional B-scans reveals vascular flow in the area of laser injury, demonstrated by the small red patches of angiography signal near the laser-induced disruption (Figure 8-2(A)). Furthermore, area analysis shown in Figure 8-4(A) and Figure 8-4(B) for these time points shows a close matching of area between vis-OCTA and isolectin staining, especially at Day 5, when the differences in areas no longer become statistically significant between the two measurements. Corresponding total tissue (red) flatmounts show further development of blood vessels past the initial budding seen in the previous time points, including some with tubular structure, without evidence of a completely formed network, in accordance with the vis-OCTA observations (Figure 8-2(C)). Intracardiac perfusion staining (green) showed a greater degree of overlap between total tissue and perfusion staining compared to the early phase lesions, suggesting maturation of tubular vasculature; however, the majority of vessels still do not appear to be fully interconnected as a mature network (Figure 8-2(D)). At the cellular level, by this point the tip cells have extended outwards and the stalk cells have established lumen in the new vessels and perfusion has begun (288, 289). The vascular network will continue to grow until it reaches a peak size and creates an interconnected web of vessels, which, in our study, occurred seven days after laser injury. In our study we were able to visualize CNV with the vis-OCTA system at the same time point at which perfusion isolectin staining demonstrated tubular formed vasculature: five days post laser injury. We concluded that this time point was when the two modalities overlapped because of the lack of statistically significant difference in their area measurements and qualitatively, this is when the image produced by vis-OCTA CNV visualization began to definitively resemble the one obtained from isolectin flatmounts. Although perfusion of the lesion began at the Day 4 time point, a finding agreeing with previous experiments that detected flow via fluorescein isothiocyanate (FITC) dextran perfusion (280), we believe that the Day 5 time point is when the vis-OCTA system definitively detected the lesion.

At the final stage of CNV development (days 7 and 14 post laser injury), the vis-OCTA system is able to detect a fully formed, perfused vascular lesion (Figure 2(B)). The imaged area shows brightly detectable flow signal, with clearly visualized mature network of inter-connected vessels. The angiography overlay B-scan (Figure 8-2(A)) supports this, as this B-scan has the greatest concentration of flow signals compared to other time points. Flatmount analysis of the lesion also demonstrates a fully formed network (Figure 8-2(C)). Intracardiac perfusion (green) staining shows clear overlap between mature vessels with OCTA flow and flatmounted vessels (Figure 8-2(D)). This indicates that the flatmount IB_4 staining of *all* endothelial cells in the laser lesion is consistent with the staining highlighted by the perfused IB_4 of blood vessels, which have flow. By Day 14, however, substantial lesion regression has occurred, as shown by the reduced area from Day 7 in Figure 8-4(A). By inspection, since Figure 8-2(C) and Figure 8-2(D) are arranged with the same physical dimensions, we see that the red immunostained flatmount shows a smaller sized lesion than Day 7. Although evidence of perfusion is still present (Figure 8-2(D)), decreased lesion size and vascular character resembles those of the intermediate stage. Lesion regression is thought to be primarily driven by reactive RPE that envelops the CNV lesion and absorbs the accumulated subretinal fluid from the leaky, aberrant vessels. (296) Furthermore, the RPE may initiate a wound healing response (e.g. platelet derived growth factor, epidermal growth factor, hepatocyte growth factor) to control the size of the CNV lesion. (263, 293, 296-299) Another possible mechanism is that the RPE cells could envelope the abnormal vessels in the lesion; a histopathologic study has shown that intact RPE cells proliferate in a papillary pattern around the periphery of the CNV lesion, from areas of healthy, undamaged RPE cells, and slowly grow toward the center of the lesion, enveloping the abnormal vessels. (296) Moreover, using fluorescein angiography, the investigators were able to demonstrate the disappearance of leakage from the CNV site. (296)

Although vis-OCTA and near-infrared (NIR) OCTA were not explicitly compared in this study, we will briefly discuss some of the potential theoretical advantages and disadvantages of the two modalities. The two major advantages of using a vis-OCT system are greater imaging resolution and functional measurement of oxygen saturation of hemoglobin. With its shorter wavelength, visible light-OCT enables greater axial resolution and lateral resolution of the retina compared to NIR based OCT, allowing more detailed images of specific retinal structures, or in this case, angiograms of choroidal neovascularization (271). Although not performed in this study, the additional benefit of functional imaging with vis-OCT remains to be demonstrated for laser-induced CNV, as it is currently unknown whether oxygen levels play a role in this disease. Interestingly, vis-OCT has recently been demonstrated to measure relative choroidal oxygen saturation values in rodents, which suggests that future studies with vis-OCT could explore this potential area (271). One major drawback of vis-OCTA versus NIR-OCTA is that, due to higher light absorption in the visible spectral range, the depth of penetration is lower than that of NIR-OCTA. However, based on a preliminary study characterizing the vis-OCTA system in human subjects, our group has imaged the deeper retinal layers and choroid, suggesting neovascular CNV in AMD patients could possibly be visualized. Overall, these comparisons will be important future experiments to explore whether vis-OCTA can provide additional clinically useful information over its NIR counterpart.

There were some limitations to the imaging performed in this study. The OCTA signal can be blocked by hemorrhage or opacities in the eye (300). In addition, all angiography techniques have a minimum detectable flow threshold, primarily determined by the signal-to-noise ratio of the system. If the flow signals at Days 2 and 3 were below this minimum detection threshold, then no flow would be detectable on Days 2 and 3 post-laser. Further studies are required to investigate the minimum detectable flow for OCTA. Another limitation is that large overlying retinal vessels can cause projected artifacts, which we removed with image processing but may, at the same time, remove truly detected flow signals from the deeper layers (269, 300). This shadowing artifact may also lead to a smaller detected CNV from the OCTA lesion compared to its immunostained counterpart, which has had the retina peeled away and is thus not subject to shadowing.

For the first time, our study has performed longitudinal monitoring of laser-induced CNV lesions in mice using OCTA. Our structural findings agreed well, in both character and course, with previous findings using NIR-based SD-OCT. The major advantage of this study is that, with the addition of OCTA, we were able to acquire information about the perfusion of CNV lesions, which has heretofore only been characterized either by *ex vivo* histology or by *in vivo* contrast-based imaging methods (e.g. FA or ICG). Since vis-OCTA successfully detected flow in the CNV vessels at the same time point as the histological data, it validates the ability of this technology to accurately reflect changes *in vivo*. Further supporting this statement, a recent study compared vis-OCTA and FA for the evaluation of murine laser-induced CNV (55). The study found that vis-OCTA is better than FA at resolving retinal capillaries in healthy rodent eyes, and successfully detects CNV lesions, which were missed by FA (55). This study, along with ours, demonstrates the potential of vis-OCTA as an emerging technology, which can successfully characterize, both in structure and perfusion, the formation and regression of CNV lesions in the laser-induced CNV model. We envision that vis-OCTA will be a promising tool in characterizing the pathophysiology of CNV in rodents, and ultimately, once the technology matures (275), it will hopefully provide an additional new tool to study and monitor therapies for neovascular AMD in humans.

Chapter 9

Conclusions and future perspectives

This dissertation has provided advances in functional OCT. With respect to vis-OCT, an improved vis-OCT oximetry method was established using a combination of circumpapillary scanning and graph-search segmentation (Chapter 4). This method will enable more accurate sO_2 measurements to be performed in animal studies. In addition, it has been adapted for use in ongoing human sO_2 measurements in retinal diseases. In Chapter 5, this dissertation established the theory and experimental validation of the SSR – an additional attenuation factor which affects the shape of acquired spectrums in SOCT. Future studies utilizing SOCT including those involving vis-OCT oximetry are expected to involved corrections of SSR to obtain more accurate spectra from tissue samples. Chapter 6 established the measurement of the $irMRO_2$ in an animal model of ROP. Previous methods to assess oxygen in the OIR model either had limited spatial resolution or only single measurements of either retinal blood flow or oxygen saturation. This dissertation provided the first measurements in the OIR model with complete functional information involving both sO_2 and blood flow.

Future work in vis-OCT technology is expected to fall in three domains: hardware, algorithms, and human studies. Hardware advances for vis-OCT will come from better light source technology. Currently, vis-OCT light sources rely on costly supercontinuum sources, which have high RIN noise. Future broadband vis-OCT light sources will hopefully be derived from light emitting diode (LED) or superluminescent LED technology. In addition, a swept source in the visible range has yet to be demonstrated, but would undoubtedly bring certain advantages to vis-OCT, such as faster imaging speeds and better sensitivity rolloff, and fringe washout performance.

There also remain significant problems to be solved in vis-OCT oximetry software and algorithms. Vis-OCT suffers from low signal-to-noise ratio (SNR), especially in human blood vessels when the diameter of the blood vessel is large, and there is a long round-trip length of attenuation in blood. In addition, the blood vessels have high flow speeds, which causes fringe washout and further deteriorates thee SNR. Algorithms which can account and compensate for these low SNR scenarios would be particularly helpful for moving vis-OCT oximetry to the clinic. In addition, vis-OCT oximetry depends on SOCT to collect the spectral information from hemoglobin in the blood. Improved models of how the hemoglobin absorption and scattering passes through the OCT signal processing chain will be instrumental in improving the accuracy of the technique.

Although human imaging has been demonstrated with vis-OCT (105, 145), large scale studies examining a patient cohort have not been demonstrated. The central hypothesis of vis-OCT technology is that it may provide oxygen biomarkers, which are useful in evaluating patients with retinal diseases, such as diabetic retinopathy. These cohort studies will be essential to proving that vis-OCT can be helpful in clinical care.

This dissertation has also presented two advances in OCTA technology. In Chapter 7, a novel method of producing retinal vascular occlusions in rodents was presented. The technique involved a multimodal device, combining SLO with OCTA. This work will likely contribute to novel ways of investigating retinal vascular occlusions and lead to further studies into the effects of various drugs and treatments on the diseases. In Chapter 8, OCTA was used to investigate the longitudinal changes in an animal model of wet AMD. This provided evidence that OCTA could detect the early phases of CNV growth and development. This work will strengthen the use of OCTA in the evaluation and treatment of wet AMD.

OCTA is undoubtedly at a later stage of development than vis-OCT, as it has been more than a decade since the first report of OCTA in the living eye (301). Nevertheless, there are still several important future improvements for OCTA to come. The OCTA processing algorithm currently does not provide quantitative blood flow velocity. In other words, the perceived brightness of an OCTA voxel cannot be directly translated to flow speed. Moreover, the relationship between the OCTA signal and flow speed depends on many factors, including the inter-scan time of repeated B-scans, the blood vessel diameter, and the blood flow velocity (302, 303). Novel OCTA methods, which rely on swept-source technology, such as the VISTA method, will likely add quantitative information about blood flow velocity and, therefore, may be useful in quantifying flow changes in diabetic retinopathy (304). New light sources, such as swept-source OCT, may further improve imaging speed. This, in turn, would facilitate OCTA scans with larger fields of view (305).

Over the next decade, vis-OCT and OCTA are likely to have an enormous impact on the evaluation of patients with retinal diseases. Based on the history of OCT, we can safely say that it takes approximately a decade for a major advance in the lab to reach the clinical space. For example, OCTA was introduced in 2006 in a research paper. The first commercial device was released in 2014. Currently in 2018, OCTA is being tested to see if it holds clinical significance for treating wet AMD and DR, with promising early results. Vis-OCT is at its early stage of development, having been introduced in 2013. It will likely take several more years of engineering development to reach a satisfactory pre-clinical product. Ultimately, however, the detection of sO_2 in the living eye is expected to be an important success for OCT technology.

References

1. Huang D, Swanson EA, Lin CP, Schuman JS, Stinson WG, Chang W, et al. Optical coherence tomography. Science. 1991;254(5035):1178-81.
2. Klein T, Wieser W, Eigenwillig CM, Biedermann BR, Huber R. Megahertz OCT for ultrawide-field retinal imaging with a 1050nm Fourier domain mode-locked laser. Optics express. 2011;19(4):3044-62.
3. Grulkowski I, Liu JJ, Potsaid B, Jayaraman V, Lu CD, Jiang J, et al. Retinal, anterior segment and full eye imaging using ultrahigh speed swept source OCT with vertical-cavity surface emitting lasers. Biomedical optics express. 2012;3(11):2733-51.
4. Grulkowski I, Manzanera S, Cwiklinski L, Sobczuk F, Karnowski K, Artal P. Swept source optical coherence tomography and tunable lens technology for comprehensive imaging and biometry of the whole eye. Optica. 2018;5(1):52-9.
5. Linsenmeier RA, Zhang HF. Retinal oxygen: from animals to humans. Prog Retin Eye Res. 2017;58:115-51.
6. Yi J, Wei Q, Liu W, Backman V, Zhang HF. Visible-light optical coherence tomography for retinal oximetry. Opt Lett. 2013;38(11):1796-8.
7. Yi J, Liu W, Chen S, Backman V, Sheibani N, Sorenson CM, et al. Visible light optical coherence tomography measures retinal oxygen metabolic response to systemic oxygenation. Light: Science &Amp; Applications. 2015;4:e334.
8. Pi S, Camino A, Cepurna W, Wei X, Zhang M, Huang D, et al. Automated spectroscopic retinal oximetry with visible-light optical coherence tomography. Biomedical Optics Express. 2018;9(5):2056-67.
9. Liu W, Wang S, Soetikno B, Yi J, Zhang K, Chen S, et al. Increased Retinal Oxygen Metabolism Precedes Microvascular Alterations in Type 1 Diabetic Mice. Investigative Ophthalmology & Visual Science. 2017;58(2):981-9.
10. Hellström A, Smith LE, Dammann O. Retinopathy of prematurity. The lancet. 2013;382(9902):1445-57.

11. Penn JS, Tolman BL, Henry MM. Oxygen-induced retinopathy in the rat: relationship of retinal nonperfusion to subsequent neovascularization. Investigative ophthalmology & visual science. 1994;35(9):3429-35.
12. Nesper PL, Soetikno BT, Zhang HF, Fawzi AA. OCT angiography and visible-light OCT in diabetic retinopathy. Vision Research. 2017;139:191-203.
13. Gao SS, Jia Y, Zhang M, Su JP, Liu G, Hwang TS, et al. Optical Coherence Tomography Angiography. Investigative Ophthalmology & Visual Science. 2016;57(9):OCT27-OCT36.
14. Hayreh SS. Ocular vascular occlusive disorders: natural history of visual outcome. Prog Retin Eye Res. 2014;41:1-25.
15. Khayat M, Lois N, Williams M, Stitt AW. Animal Models of Retinal Vein Occlusion. Invest Ophthalmol Vis Sci. 2017;58(14):6175-92.
16. Jager RD, Mieler WF, Miller JW. Age-related macular degeneration. New England Journal of Medicine. 2008;358(24):2606-17.
17. Lambert V, Lecomte J, Hansen S, Blacher S, Gonzalez M-LA, Struman I, et al. Laser-induced choroidal neovascularization model to study age-related macular degeneration in mice. Nature Protocols. 2013;8:2197.
18. Jackman W, Webster J. On photographing the retina of the living human eye. Philadelphia photographer. 1886;23(275):275-6.
19. London A, Benhar I, Schwartz M. The retina as a window to the brain—from eye research to CNS disorders. Nature Reviews Neurology. 2012;9:44.
20. Levkovitch-Verbin H. Animal models of optic nerve diseases. Eye. 2004;18:1066.
21. Geng Y, Dubra A, Yin L, Merigan WH, Sharma R, Libby RT, et al. Adaptive optics retinal imaging in the living mouse eye. Biomed Opt Express. 2012;3(4):715-34.
22. Veleri S, Lazar CH, Chang B, Sieving PA, Banin E, Swaroop A. Biology and therapy of inherited retinal degenerative disease: insights from mouse models. Disease Models & Mechanisms. 2015;8(2):109-29.
23. Remtulla S, Hallett PE. A schematic eye for the mouse, and comparisons with the rat. Vision Research. 1985;25(1):21-31.

24. Geng Y, Schery LA, Sharma R, Dubra A, Ahmad K, Libby RT, et al. Optical properties of the mouse eye. Biomed Opt Express. 2011;2(4):717-38.

25. Strauss O. The retinal pigment epithelium in visual function. Physiological reviews. 2005;85(3):845-81.

26. Wassle H. Parallel processing in the mammalian retina. Nature reviews Neuroscience. 2004;5(10):747-57.

27. Wangsa-Wirawan ND, Linsenmeier RA. Retinal oxygen: Fundamental and clinical aspects. Archives of Ophthalmology. 2003;121(4):547-57.

28. Linsenmeier RA, Zhang HF. Retinal oxygen: from animals to humans. Progress in Retinal and Eye Research. 2017;58:115-51.

29. Kornfield TE, Newman EA. Regulation of Blood Flow in the Retinal Trilaminar Vascular Network. The Journal of Neuroscience. 2014;34(34):11504-13.

30. Kur J, Newman EA, Chan-Ling T. Cellular and physiological mechanisms underlying blood flow regulation in the retina choroid in health disease. Progress in retinal and eye research. 2012;31(5):377-406.

31. Liu T, Li H, Song W, Jiao S, Zhang HF. Fundus camera guided photoacoustic ophthalmoscopy. Curr Eye Res. 2013;38(12):1229-34.

32. Song W, Wei Q, Liu T, Kuai D, Burke JM, Jiao S, et al. Integrating photoacoustic ophthalmoscopy with scanning laser ophthalmoscopy, optical coherence tomography, and fluorescein angiography for a multimodal retinal imaging platform. J Biomed Opt. 2012;17(6):061206.

33. Li H, Liu W, Dong B, Kaluzny JV, Fawzi AA, Zhang HF. Snapshot hyperspectral retinal imaging using compact spectral resolving detector array. J Biophotonics. 2017;10(6-7):830-9.

34. Hardarson SH, Harris A, Karlsson RA, Halldorsson GH, Kagemann L, Rechtman E, et al. Automatic retinal oximetry. Invest Ophthalmol Vis Sci. 2006;47(11):5011-6.

35. Gullstrand A. Neue methoden der reflexlosen ophthalmoskopie. Berichte Deutsche Ophthalmologische Gesellschaft. 1910;36(8):326.

36. Link D, Strohmaier C, Seifert BU, Riemer T, Reitsamer HA, Haueisen J, et al. Novel non-contact retina camera for the rat and its application to dynamic retinal vessel analysis. Biomedical Optics Express. 2011;2(11):3094-108.
37. Chaudhuri A, Hallett PE, Parker JA. Aspheric curvatures, refractive indices and chromatic aberration for the rat eye. Vision Res. 1983;23(12):1351-63.
38. Bedford RE, Wyszecki G. Axial chromatic aberration of the human eye. J Opt Soc Am. 1957;47(6):564-5.
39. Li H, Liu W, Zhang HF. Investigating the influence of chromatic aberration and optical illumination bandwidth on fundus imaging in rats. J Biomed Opt. 2015;20(10):106010.
40. Paques M, Guyomard JL, Simonutti M, Roux MJ, Picaud S, Legargasson JF, et al. Panretinal, high-resolution color photography of the mouse fundus. Invest Ophthalmol Vis Sci. 2007;48(6):2769-74.
41. Hawes NL, Smith RS, Chang B, Davisson M, Heckenlively JR, John SW. Mouse fundus photography and angiography: a catalogue of normal and mutant phenotypes. Molecular vision. 1999;5:22.
42. Cohan BE, Pearch AC, Jokelainen PT, Bohr DF. Optic disc imaging in conscious rats and mice. Invest Ophthalmol Vis Sci. 2003;44(1):160-3.
43. Haddock LJ, Kim DY, Mukai S. Simple, inexpensive technique for high-quality smartphone fundus photography in human and animal eyes. Journal of ophthalmology. 2013;2013:518479.
44. Webb RH, Hughes GW, Pomerantzeff O. Flying spot TV ophthalmoscope. Appl Opt. 1980;19(17):2991-7.
45. Webb RH, Hughes GW, Delori FC. Confocal scanning laser ophthalmoscope. Appl Opt. 1987;26(8):1492-9.
46. Zhang P, Zam A, Jian Y, Wang X, Li Y, Lam KS, et al. In vivo wide-field multispectral scanning laser ophthalmoscopy-optical coherence tomography mouse retinal imager: longitudinal imaging of ganglion cells, microglia, and Muller glia, and mapping of the mouse retinal and choroidal vasculature. J Biomed Opt. 2015;20(12):126005.

47. Soetikno BT, Shu X, Liu Q, Liu W, Chen S, Beckmann L, et al. Optical coherence tomography angiography of retinal vascular occlusions produced by imaging-guided laser photocoagulation. Biomed Opt Express. 2017;8(8):3571-82.
48. LaRocca F, Dhalla AH, Kelly MP, Farsiu S, Izatt JA. Optimization of confocal scanning laser ophthalmoscope design. J Biomed Opt. 2013;18(7):076015.
49. Remtulla S, Hallett PE. A schematic eye for the mouse, and comparisons with the rat. Vision Res. 1985;25(1):21-31.
50. Hughes A. A schematic eye for the rat. Vision Res. 1979;19(5):569-88.
51. Roorda A. Applications of adaptive optics scanning laser ophthalmoscopy. Optom Vis Sci. 2010;87(4):260-8.
52. Zhang P, Goswami M, Zam A, Pugh EN, Zawadzki RJ. Effect of scanning beam size on the lateral resolution of mouse retinal imaging with SLO. Optics letters. 2015;40(24):5830-3.
53. Park JS, Choi CK, Kihm KD. Optically sliced micro-PIV using confocal laser scanning microscopy (CLSM). Experiments in Fluids. 2004;37(1):105-19.
54. Wilhelm S, Grobler B, Gluch M, Heinz H. Confocal Laser Scanning Microscopy. Principles. Microscopy from Carl Zeiss, microspecial. 2003.
55. Liu W, Li H, Shah RS, Shu X, Linsenmeier RA, Fawzi AA, et al. Simultaneous optical coherence tomography angiography and fluorescein angiography in rodents with normal retina and laser-induced choroidal neovascularization. Opt Lett. 2015;40(24):5782-5.
56. Roorda A, Duncan JL. Adaptive optics ophthalmoscopy. Annual review of vision science. 2015;1:19-50.
57. Zhang L, Capilla A, Song W, Mostoslavsky G, Yi J. Oblique scanning laser microscopy for simultaneously volumetric structural and molecular imaging using only one raster scan. Sci Rep. 2017;7(1):8591.
58. Zhang L, Song W, Shao D, Zhang S, Desai M, Ness S, et al. Volumetric fluorescence retinal imaging in vivo over a 30-degree field of view by oblique scanning laser ophthalmoscopy (oSLO). Biomedical Optics Express. 2018;9(1):25-40.

59. Paques M, Simonutti M, Roux MJ, Picaud S, Levavasseur E, Bellman C, et al. High resolution fundus imaging by confocal scanning laser ophthalmoscopy in the mouse. Vision Res. 2006;46(8-9):1336-45.

60. Zhang Y, Cho CH, Atchaneeyasakul LO, McFarland T, Appukuttan B, Stout JT. Activation of the mitochondrial apoptotic pathway in a rat model of central retinal artery occlusion. Invest Ophthalmol Vis Sci. 2005;46(6):2133-9.

61. Zhang Y, Fortune B, Atchaneeyasakul LO, McFarland T, Mose K, Wallace P, et al. Natural history and histology in a rat model of laser-induced photothrombotic retinal vein occlusion. Curr Eye Res. 2008;33(4):365-76.

62. Ebneter A, Agca C, Dysli C, Zinkernagel MS. Investigation of retinal morphology alterations using spectral domain optical coherence tomography in a mouse model of retinal branch and central retinal vein occlusion. PLoS One. 2015;10(3):e0119046.

63. Dominguez E, Raoul W, Calippe B, Sahel JA, Guillonneau X, Paques M, et al. Experimental Branch Retinal Vein Occlusion Induces Upstream Pericyte Loss and Vascular Destabilization. PLoS One. 2015;10(7):e0132644.

64. Cahoon JM, Olson PR, Nielson S, Miya TR, Bankhead P, McGeown JG, et al. Acridine orange leukocyte fluorography in mice. Exp Eye Res. 2014;120:15-9.

65. Nishiwaki H, Ogura Y, Kimura H, Kiryu J, Miyamoto K, Matsuda N. Visualization and quantitative analysis of leukocyte dynamics in retinal microcirculation of rats. Invest Ophthalmol Vis Sci. 1996;37(7):1341-7.

66. Miyahara S, Kiryu J, Miyamoto K, Katsuta H, Hirose F, Tamura H, et al. In vivo three-dimensional evaluation of leukocyte behavior in retinal microcirculation of mice. Invest Ophthalmol Vis Sci. 2004;45(11):4197-201.

67. Miyamoto K, Khosrof S, Bursell SE, Moromizato Y, Aiello LP, Ogura Y, et al. Vascular endothelial growth factor (VEGF)-induced retinal vascular permeability is mediated by intercellular adhesion molecule-1 (ICAM-1). The American journal of pathology. 2000;156(5):1733-9.

68. Miyamoto K, Khosrof S, Bursell SE, Rohan R, Murata T, Clermont AC, et al. Prevention of leukostasis and vascular leakage in streptozotocin-induced diabetic retinopathy via

intercellular adhesion molecule-1 inhibition. Proceedings of the National Academy of Sciences of the United States of America. 1999;96(19):10836-41.

69. Huang D, Swanson EA, Lin CP, Schuman JS, Stinson WG, Chang W, et al. Optical coherence tomography. Science. 1991;254(5035):1178-81.

70. Fujimoto J, Swanson E. The Development, Commercialization, and Impact of Optical Coherence Tomography. Invest Ophthalmol Vis Sci. 2016;57(9):OCT1-OCT13.

71. de Boer JF, Leitgeb R, Wojtkowski M. Twenty-five years of optical coherence tomography: the paradigm shift in sensitivity and speed provided by Fourier domain OCT [Invited]. Biomedical Optics Express. 2017;8(7):3248-80.

72. Fercher AF. Optical coherence tomography – development, principles, applications. Zeitschrift für Medizinische Physik. 2010;20(4):251-76.

73. Fercher AF, Drexler W, Hitzenberger CK, Lasser T. Optical coherence tomography-principles and applications. Reports on progress in physics. 2003;66(2):239.

74. Izatt JA, Choma MA, Dhalla A-H. Theory of optical coherence tomography. Optical Coherence Tomography: Technology and Applications. 2015:65-94.

75. Kalkman J. Fourier-Domain Optical Coherence Tomography Signal Analysis and Numerical Modeling. International Journal of Optics. 2017;2017:16.

76. Hu Z, Pan Y, Rollins AM. Analytical model of spectrometer-based two-beam spectral interferometry. Appl Opt. 2007;46(35):8499-505.

77. Chen C-L, Wang RK. Optical coherence tomography based angiography [Invited]. Biomedical Optics Express. 2017;8(2):1056-82.

78. Makita S, Hong Y, Yamanari M, Yatagai T, Yasuno Y. Optical coherence angiography. Opt Express. 2006;14(17):7821-40.

79. Gorczynska I, Migacz JV, Zawadzki RJ, Capps AG, Werner JS. Comparison of amplitude-decorrelation, speckle-variance and phase-variance OCT angiography methods for imaging the human retina and choroid. Biomed Opt Express. 2016;7(3):911-42.

80. Jia Y, Tan O, Tokayer J, Potsaid B, Wang Y, Liu JJ, et al. Split-spectrum amplitude-decorrelation angiography with optical coherence tomography. Opt Express. 2012;20(4):4710-25.

81. Gao SS, Liu G, Huang D, Jia Y. Optimization of the split-spectrum amplitude-decorrelation angiography algorithm on a spectral optical coherence tomography system. Optics letters. 2015;40(10):2305-8.
82. An L, Wang RK. In vivo volumetric imaging of vascular perfusion within human retina and choroids with optical micro-angiography. Opt Express. 2008;16(15):11438-52.
83. Zhi Z, Qin W, Wang J, Wei W, Wang RK. 4D optical coherence tomography-based micro-angiography achieved by 1.6-MHz FDML swept source. Optics letters. 2015;40(8):1779-82.
84. Yi J, Chen S, Backman V, Zhang HF. In vivo functional microangiography by visible-light optical coherence tomography. Biomed Opt Express. 2014;5(10):3603.
85. Shah RS, Soetikno BT, Yi J, Liu W, Skondra D, Zhang HF, et al. Visible-Light Optical Coherence Tomography Angiography for Monitoring Laser-Induced Choroidal Neovascularization in Mice. Invest Ophthalmol Vis Sci. 2016;57(9):OCT86-95.
86. Shah RS, Soetikno BT, Lajko M, Fawzi AA. A Mouse Model for Laser-induced Choroidal Neovascularization. J Vis Exp. 2015(106):e53502.
87. Park JR, Choi W, Hong HK, Kim Y, Jun Park S, Hwang Y, et al. Imaging Laser-Induced Choroidal Neovascularization in the Rodent Retina Using Optical Coherence Tomography Angiography. Invest Ophthalmol Vis Sci. 2016;57(9):OCT331-40.
88. Pi S, Camino A, Zhang M, Cepurna W, Liu G, Huang D, et al. Angiographic and structural imaging using high axial resolution fiber-based visible-light OCT. Biomed Opt Express. 2017;8(10):4595-608.
89. Yi J, Wei Q, Liu W, Backman V, Zhang HF. Visible-light optical coherence tomography for retinal oximetry. Opt Lett. 2013;38(11):1796-8.
90. Nesper PL, Soetikno BT, Zhang HF, Fawzi AA. OCT angiography and visible-light OCT in diabetic retinopathy. Vision Res. 2017;139:191-203.
91. Chen S, Yi J, Zhang HF. Measuring oxygen saturation in retinal and choroidal circulations in rats using visible light optical coherence tomography angiography. Biomedical Optics Express. 2015;6(8):2840-53.
92. Yi J, Wei Q, Liu W, Backman V, Zhang HF. Visible-light optical coherence tomography for retinal oximetry. Optics Letters. 2013;38(11):1796-8.

93. Faber DJ, Aalders MC, Mik EG, Hooper BA, van Gemert MJ, van Leeuwen TG. Oxygen saturation-dependent absorption and scattering of blood. Phys Rev Lett. 2004;93(2):028102.

94. Wang Y, Bower BA, Izatt JA, Tan O, Huang D. In vivo total retinal blood flow measurement by Fourier domain Doppler optical coherence tomography. J Biomed Opt. 2007;12(4):041215.

95. Yimin Wang, Bradley A. Bower, Joseph A. Izatt, Ou Tan, David Huang. Retinal blood flow measurement by circumpapillary Fourier domain Doppler optical coherence tomography. Journal of Biomedical Optics. 2008;13(6):064003.

96. Nam AS, Chico-Calero I, Vakoc BJ. Complex differential variance algorithm for optical coherence tomography angiography. Biomed Opt Express. 2014;5(11):3822-32.

97. Uttam S, Liu Y. Fourier phase in Fourier-domain optical coherence tomography. J Opt Soc Am A Opt Image Sci Vis. 2015;32(12):2286-306.

98. Szkulmowska A, Szkulmowski M, Kowalczyk A, Wojtkowski M. Phase-resolved Doppler optical coherence tomography--limitations and improvements. Optics letters. 2008;33(13):1425-7.

99. White BR, Pierce MC, Nassif N, Cense B, Park BH, Tearney GJ, et al. In vivo dynamic human retinal blood flow imaging using ultra-high-speed spectral domain optical Doppler tomography. Opt Express. 2003;11(25):3490-7.

100. Liu W, Yi J, Chen S, Jiao S, Zhang HF. Measuring retinal blood flow in rats using Doppler optical coherence tomography without knowing eyeball axial length. Med Phys. 2015;42(9):5356-62.

101. Hendargo HC, McNabb RP, Dhalla A-H, Shepherd N, Izatt JA. Doppler velocity detection limitations in spectrometer-based versus swept-source optical coherence tomography. Biomedical Optics Express. 2011;2(8):2175-88.

102. Hall JE, Guyton AC. Textbook of Medical Physiology: Saunders; 2011.

103. Chen S, Yi J, Liu W, Backman V, Zhang H. Monte Carlo Investigation of Optical Coherence Tomography Retinal Oximetry. IEEE transactions on bio-medical engineering. 2015.

104. Sorenson CM, Wang S, Gendron R, Paradis H, Sheibani N. Thrombospondin-1 Deficiency Exacerbates the Pathogenesis of Diabetic Retinopathy. Journal of diabetes & metabolism. 2013;Suppl 12:10.4172/2155-6156.S12-005.

105. Chen S, Shu X, Nesper PL, Liu W, Fawzi AA, Zhang HF. Retinal oximetry in humans using visible-light optical coherence tomography [Invited]. Biomedical Optics Express. 2017;8(3):1415-29.

106. Soetikno BT, Yi J, Shah R, Liu W, Purta P, Zhang HF, et al. Inner retinal oxygen metabolism in the 50/10 oxygen-induced retinopathy model. Sci Rep. 2015;5:16752.

107. de la Zerda A, Paulus YM, Teed R, Bodapati S, Dollberg Y, Khuri-Yakub BT, et al. Photoacoustic ocular imaging. Opt Lett. 2010;35(3):270-2.

108. Jiao S, Jiang M, Hu J, Fawzi A, Zhou Q, Shung KK, et al. Photoacoustic ophthalmoscopy for in vivo retinal imaging. Opt Express. 2010;18(4):3967-72.

109. Hu S, Rao B, Maslov K, Wang LV. Label-free photoacoustic ophthalmic angiography. Opt Lett. 2010;35(1):1-3.

110. Hu S, Maslov K, Wang LV. Second-generation optical-resolution photoacoustic microscopy with improved sensitivity and speed. Optics letters. 2011;36(7):1134-6.

111. Yeh C, Soetikno B, Hu S, Maslov KI, Wang LV. Microvascular quantification based on contour-scanning photoacoustic microscopy. J Biomed Opt. 2014;19(9):96011.

112. Yeh C, Soetikno B, Hu S, Maslov KI, Wang LV. Three-dimensional arbitrary trajectory scanning photoacoustic microscopy. J Biophotonics. 2015;8(4):303-8.

113. Zhang HF, Maslov K, Stoica G, Wang LV. Functional photoacoustic microscopy for high-resolution and noninvasive in vivo imaging. Nat Biotechnol. 2006;24(7):848-51.

114. Wang LV, Hu S. Photoacoustic tomography: in vivo imaging from organelles to organs. Science. 2012;335(6075):1458-62.

115. Song W, Wei Q, Liu W, Liu T, Yi J, Sheibani N, et al. A combined method to quantify the retinal metabolic rate of oxygen using photoacoustic ophthalmoscopy and optical coherence tomography. Sci Rep. 2014;4:6525.

116. Liu W, Schultz KM, Zhang K, Sasman A, Gao F, Kume T, et al. In vivo corneal neovascularization imaging by optical-resolution photoacoustic microscopy. Photoacoustics. 2014;2(2):81-6.

117. Shu X, Li H, Dong B, Sun C, Zhang HF. Quantifying melanin concentration in retinal pigment epithelium using broadband photoacoustic microscopy. Biomed Opt Express. 2017;8(6):2851-65.

118. Shu X, Liu W, Zhang HF. Monte Carlo investigation on quantifying the retinal pigment epithelium melanin concentration by photoacoustic ophthalmoscopy. Journal of Biomedical Optics. 2015;20(10):106005.

119. Dong B, Chen S, Zhang Z, Sun C, Zhang HF. Photoacoustic probe using a microring resonator ultrasonic sensor for endoscopic applications. Optics letters. 2014;39(15):4372-5.

120. Li H, Dong B, Zhang Z, Zhang HF, Sun C. A transparent broadband ultrasonic detector based on an optical micro-ring resonator for photoacoustic microscopy. Scientific Reports. 2014;4:4496.

121. Dong B, Sun C, Zhang HF. Optical Detection of Ultrasound in Photoacoustic Imaging. IEEE Transactions on Biomedical Engineering. 2017;64(1):4-15.

122. Shu X, Bondu M, Dong B, Podoleanu A, Leick L, Zhang HF. Single all-fiber-based nanosecond-pulsed supercontinuum source for multispectral photoacoustic microscopy and optical coherence tomography. Opt Lett. 2016;41(12):2743-6.

123. Lombardo M, Serrao S, Devaney N, Parravano M, Lombardo G. Adaptive Optics Technology for High-Resolution Retinal Imaging. Sensors (Basel, Switzerland). 2013;13(1):334-66.

124. Roorda A, Duncan JL. Adaptive Optics Ophthalmoscopy. Annual Review of Vision Science. 2015;1(1):19-50.

125. Jian Y, Zawadzki RJ, Sarunic MV. Adaptive optics optical coherence tomography for in vivo mouse retinal imaging. Journal of Biomedical Optics. 2013;18(5):056007.

126. Silverman RH. High-resolution ultrasound imaging of the eye–a review. Clinical & experimental ophthalmology. 2009;37(1):54-67.

127. de Boer JF, Hitzenberger CK, Yasuno Y. Polarization sensitive optical coherence tomography – a review [Invited]. Biomedical Optics Express. 2017;8(3):1838-73.

128. Michelson AA, Morley EW. On the Relative Motion of the Earth and of the Luminiferous Ether. Sidereal Messenger, vol 6, pp 306-310. 1887;6:306-10.

129. Abbott BP, Abbott R, Abbott T, Abernathy M, Acernese F, Ackley K, et al. Observation of gravitational waves from a binary black hole merger. Physical review letters. 2016;116(6):061102.

130. Dubois A, Boccara AC. Full-Field Optical Coherence Tomography. In: Drexler W, Fujimoto JG, editors. Optical Coherence Tomography: Technology and Applications. Berlin, Heidelberg: Springer Berlin Heidelberg; 2008. p. 565-91.

131. Park B, Pierce MC, Cense B, Yun SH, Mujat M, Tearney G, et al. Real-time fiber-based multi-functional spectral-domain optical coherence tomography at 1.3 microm. Opt Express. 2005;13(11):3931-44.

132. Szkulmowski M, Tamborski S, Wojtkowski M. Spectrometer calibration for spectroscopic Fourier domain optical coherence tomography. Biomed Opt Express. 2016;7(12):5042-54.

133. Uribe-Patarroyo N, Kassani SH, Villiger M, Bouma BE. Robust wavenumber and dispersion calibration for Fourier-domain optical coherence tomography. Opt Express. 2018;26(7):9081-94.

134. Marks DL, Carney PS, Boppart SA. Adaptive spectral apodization for sidelobe reduction in optical coherence tomography images. Journal of biomedical optics. 2004;9(6):1281-8.

135. Chan KK, Tang S. High-speed spectral domain optical coherence tomography using non-uniform fast Fourier transform. Biomedical optics express. 2010;1(5):1309-19.

136. Desjardins AE, Vakoc BJ, Suter MJ, Yun S-H, Tearney GJ, Bouma BE. Real-Time FPGA Processing for High-Speed Optical Frequency Domain Imaging. IEEE transactions on medical imaging. 2009;28(9):1468-72.

137. Dorrer C, Belabas N, Likforman J-P, Joffre M. Spectral resolution and sampling issues in Fourier-transform spectral interferometry. JOSA B. 2000;17(10):1795-802.

138. Cense B, Nassif N, Chen T, Pierce M, Yun SH, Park B, et al. Ultrahigh-resolution high-speed retinal imaging using spectral-domain optical coherence tomography. Opt Express. 2004;12(11):2435-47.

139. Wojtkowski M, Srinivasan V, Ko T, Fujimoto J, Kowalczyk A, Duker J. Ultrahigh-resolution, high-speed, Fourier domain optical coherence tomography and methods for dispersion compensation. Opt Express. 2004;12(11):2404-22.

140. Hillmann D, Bonin T, Lührs C, Franke G, Hagen-Eggert M, Koch P, et al. Common approach for compensation of axial motion artifacts in swept-source OCT and dispersion in Fourier-domain OCT. Optics express. 2012;20(6):6761-76.
141. Ali M, Parlapalli R. Algorithms for Optical Coherence Tomography on TMS320C64x. 2010.
142. Hee MR. Optical coherence tomography of the eye: Massachusetts Institute of Technology; 1997.
143. Shu X, Beckmann L, Zhang H. Visible-light optical coherence tomography: a review. Journal of Biomedical Optics. 2017;22(12):1-14.
144. Soetikno BT, Yi J, Shah R, Liu W, Purta P, Zhang HF, et al. Inner retinal oxygen metabolism in the 50/10 oxygen-induced retinopathy model. Scientific Reports. 2015;5:16752.
145. Yi J, Chen S, Shu X, Fawzi AA, Zhang HF. Human retinal imaging using visible-light optical coherence tomography guided by scanning laser ophthalmoscopy. Biomed Opt Express. 2015;6(10):3701-13.
146. Morgner U, Drexler W, Kärtner FX, Li XD, Pitris C, Ippen EP, et al. Spectroscopic optical coherence tomography. Optics Letters. 2000;25(2):111-3.
147. Oldenburg AL, Xu C, Boppart SA. Spectroscopic Optical Coherence Tomography and Microscopy. IEEE J Sel Top Quant. 2007;13(6):1629-40.
148. Chen S, Yi J, Liu W, Backman V, Zhang HF. Monte Carlo Investigation of Optical Coherence Tomography Retinal Oximetry. IEEE transactions on bio-medical engineering. 2015;62(9):2308-15.
149. Chen S, Shu X, Yi J, Fawzi A, Zhang HF. Dual-band optical coherence tomography using a single supercontinuum laser source. Journal of Biomedical Optics. 2016;21(6):66013.
150. Brown WJ, Kim S, Wax A. Noise Characterization of Supercontinuum Sources for Low Coherence Interferometry Applications. Journal of the Optical Society of America A, Optics, image science, and vision. 2014;31(12):2703-10.
151. Chong SP, Merkle CW, Leahy C, Srinivasan VJ. Cerebral metabolic rate of oxygen (CMRO2) assessed by combined Doppler and spectroscopic OCT. Biomed Opt Express. 2015;6(10):3941-51.

152. Chiu SJ, Li XT, Nicholas P, Toth CA, Izatt JA, Farsiu S. Automatic segmentation of seven retinal layers in SDOCT images congruent with expert manual segmentation. Optics Express. 2010;18(18):19413-28.

153. Srinivasan PP, Heflin SJ, Izatt JA, Arshavsky VY, Farsiu S. Automatic segmentation of up to ten layer boundaries in SD-OCT images of the mouse retina with and without missing layers due to pathology. Biomed Opt Express. 2014;5(2):348-65.

154. Kang L, Xiaodong W, Chen DZ, Sonka M. Optimal Surface Segmentation in Volumetric Images-A Graph-Theoretic Approach. IEEE Transactions on Pattern Analysis and Machine Intelligence. 2006;28(1):119-34.

155. Chiu SJ, Lokhnygina Y, Dubis AM, Dubra A, Carroll J, Izatt JA, et al. Automatic cone photoreceptor segmentation using graph theory and dynamic programming. Biomed Opt Express. 2013;4(6):924-37.

156. Guizar-Sicairos M, Thurman ST, Fienup JR. Efficient subpixel image registration algorithms. Optics Letters. 2008;33(2):156-8.

157. Walther BA, Moore JL. The concepts of bias, precision and accuracy, and their use in testing the performance of species richness estimators, with a literature review of estimator performance. Ecography. 2005;28(6):815-29.

158. Yi J, Liu W, Chen S, Backman V, Sheibani N, Sorenson CM, et al. Visible light optical coherence tomography measures retinal oxygen metabolic response to systemic oxygenation. Light: Science & Applications. 2015;4(9).

159. Lau JCM, Linsenmeier RA. Oxygen consumption and distribution in the Long-Evans rat retina. Experimental Eye Research. 2012;102:50-8.

160. Yeh C, Liang J, Zhou Y, Hu S, Sohn RE, Arbeit JM, et al. Photoacoustic microscopy of arteriovenous shunts and blood diffusion in early-stage tumors. Journal of Biomedical Optics. 2016;21(2):020501.

161. Feng L, Chen H, Yi J, Troy JB, Zhang HF, Liu X. Long-Term Protection of Retinal Ganglion Cells and Visual Function by Brain-Derived Neurotrophic Factor in Mice With Ocular Hypertension. Investigative Ophthalmology & Visual Science. 2016;57(8):3793-802.

162. Shah RS, Soetikno BT, Yi J, Liu W, Skondra D, Zhang HF, et al. Visible-Light Optical Coherence Tomography Angiography for Monitoring Laser-Induced Choroidal Neovascularization in Mice. Investigative Ophthalmology & Visual Science. 2016;57(9):OCT86-95.
163. Chong SP, Bernucci M, Radhakrishnan H, Srinivasan VJ. Structural and functional human retinal imaging with a fiber-based visible light OCT ophthalmoscope. Biomed Opt Express. 2017;8(1):323-37.
164. Zhou Y, Zhao Y, Kim S, Wax AJOME. Spectroscopic OCT: towards an effective tool for distinguishing authentic and artificial Chinese freshwater pearls. 2018;8(3):622-8.
165. Oldenburg AL, Xu C, Boppart SAJIJoSTiQE. Spectroscopic optical coherence tomography and microscopy. 2007;13(6):1629-40.
166. Xu C, Vinegoni C, Ralston TS, Luo W, Tan W, Boppart SA. Spectroscopic spectral-domain optical coherence microscopy. Opt Lett. 2006;31(8):1079-81.
167. Tanaka M, Hirano M, Murashima K, Obi H, Yamaguchi R, Hasegawa T. 1.7-μm spectroscopic spectral-domain optical coherence tomography for imaging lipid distribution within blood vessel. Opt Express. 2015;23(5):6645-55.
168. Yi J, Backman V. Imaging a full set of optical scattering properties of biological tissue by inverse spectroscopic optical coherence tomography. Opt Lett. 2012;37(21):4443-5.
169. Liba O, SoRelle ED, Sen D, de la Zerda A. Contrast-enhanced optical coherence tomography with picomolar sensitivity for functional in vivo imaging. Scientific Reports. 2016;6:23337.
170. Oldenburg AL, Hansen MN, Ralston TS, Wei A, Boppart SA. Imaging gold nanorods in excised human breast carcinoma by spectroscopic optical coherence tomography. J Mater Chem. 2009;19:6407.
171. Chhetri RK, Blackmon RL, Wu W-C, Hill DB, Button B, Casbas-Hernandez P, et al. Probing biological nanotopology via diffusion of weakly constrained plasmonic nanorods with optical coherence tomography. Proceedings of the National Academy of Sciences. 2014;111(41):E4289.
172. Cang H, Sun T, Li Z-Y, Chen J, Wiley BJ, Xia Y, et al. Gold nanocages as contrast agents for spectroscopic optical coherence tomography. Opt Lett. 2005;30(22):3048-50.

173. Izatt JA, Choma MA. Theory of Optical Coherence Tomography. In: Drexler W, Fujimoto JG, editors. Optical Coherence Tomography: Technology and Applications. Berlin, Heidelberg: Springer Berlin Heidelberg; 2008. p. 47-72.

174. Hyle Park B, Pierce MC, Cense B, Yun S-H, Mujat M, Tearney GJ, et al. Real-time fiber-based multi-functional spectral-domain optical coherence tomography at 1.3 µm. Opt Express. 2005;13(11):3931-44.

175. Chong SP, Merkle CW, Leahy C, Radhakrishnan H, Srinivasan VJ. Quantitative microvascular hemoglobin mapping using visible light spectroscopic Optical Coherence Tomography. Biomed Opt Express. 2015;6(4):1429-50.

176. Szkulmowski M, Tamborski S, Wojtkowski M. Spectrometer calibration for spectroscopic Fourier domain optical coherence tomography. Biomed Opt Express. 2016;7(12):5042-54.

177. Soetikno BT, Beckmann L, Zhang X, Fawzi AA, Zhang HF. Visible-light optical coherence tomography oximetry based on circumpapillary scan and graph-search segmentation. Biomed Opt Express. 2018;9(8):3640-52.

178. Lan G, Li G. Design of a k-space spectrometer for ultra-broad waveband spectral domain optical coherence tomography. Scientific Reports. 2017;7:42353.

179. Hu Z, Rollins AM. Fourier domain optical coherence tomography with a linear-in-wavenumber spectrometer. Opt Lett. 2007;32(24):3525-7.

180. Hamilton BE, Hoyert DL, Martin JA, Strobino DM, Guyer B. Annual summary of vital statistics: 2010-2011. Pediatrics. 2013;131(3):548-58.

181. Hartnett ME, Penn JS. Mechanisms and management of retinopathy of prematurity. N Engl J Med. 2012;367(26):2515-26.

182. Chen J, Smith LE. Retinopathy of prematurity. Angiogenesis. 2007;10(2):133-40.

183. Smith LE. Through the eyes of a child: understanding retinopathy through ROP the Friedenwald lecture. Invest Ophthalmol Vis Sci. 2008;49(12):5177-82.

184. Hellström A, Smith LEH, Dammann O. Retinopathy of prematurity. The Lancet. 2013;382(9902):1445-57.

185. Hartnett ME. Pathophysiology and mechanisms of severe retinopathy of prematurity. Ophthalmology. 2015;122(1):200-10.

186. Gilbert C, Foster A. Childhood blindness in the context of VISION 2020 — The Right to Sight. Bull World Health Organ. 2001;79(3):227-32.

187. Penn JS, Henry MM, Tolman BL. Exposure to alternating hypoxia and hyperoxia causes severe proliferative retinopathy in the newborn rat. Pediatr Res. 1994;36(6):724-31.

188. Gabriele ML, Wollstein G, Ishikawa H, Kagemann L, Xu J, Folio LS, et al. Optical Coherence Tomography: History, Current Status, and Laboratory Work. Invest Ophthalmol Vis Sci. 2011;52(5):2425-36.

189. Choi W, Baumann B, Liu JJ, Clermont AC, Feener EP, Duker JS, et al. Measurement of pulsatile total blood flow in the human and rat retina with ultrahigh speed spectral/Fourier domain OCT. Biomed Opt Express. 2012;3(5):1047-61.

190. Leitgeb R, Schmetterer L, Drexler W, Fercher A, Zawadzki R, Bajraszewski T. Real-time assessment of retinal blood flow with ultrafast acquisition by color Doppler Fourier domain optical coherence tomography. Opt Express. 2003;11(23):3116.

191. Lee JC, Wong BJ, Tan O, Srinivas S, Sadda SR, Huang D, et al. Pilot study of Doppler optical coherence tomography of retinal blood flow following laser photocoagulation in poorly controlled diabetic patients. Invest Ophthalmol Vis Sci. 2013;54(9):6104-11.

192. Otsu N. A Threshold Selection Method from Gray-Level Histograms. IEEE Trans Syst Man Cybern. 1979;9(1):62-6.

193. Akula JD, Favazza TL, Mocko JA, Benador IY, Asturias AL, Kleinman MS, et al. The anatomy of the rat eye with oxygen-induced retinopathy. Doc Ophthalmol. 2010;120(1):41-50.

194. Shih AY, Friedman B, Drew PJ, Tsai PS, Lyden PD, Kleinfeld D. Active dilation of penetrating arterioles restores red blood cell flux to penumbral neocortex after focal stroke. J Cereb Blood Flow Metab. 2009;29(4):738-51.

195. Chou JC, Rollins SD, Fawzi AA. Trypsin digest protocol to analyze the retinal vasculature of a mouse model. J Vis Exp. 2013(76):e50489.

196. Preibisch S, Saalfeld S, Tomancak P. Globally optimal stitching of tiled 3D microscopic image acquisitions. Bioinformatics. 2009;25(11):1463-5.

197. Schindelin J, Arganda-Carreras I, Frise E, Kaynig V, Longair M, Pietzsch T, et al. Fiji: an open-source platform for biological-image analysis. Nat Methods. 2012;9(7):676-82.

198. Zhang S, Leske DA, Holmes JM. Neovascularization Grading Methods in a Rat Model of Retinopathy of Prematurity. Invest Ophthalmol Vis Sci. 2000;41(3):887-91.

199. Tam J, Martin JA, Roorda A. Noninvasive visualization and analysis of parafoveal capillaries in humans. Invest Ophthalmol Vis Sci. 2010;51(3):1691-8.

200. Pinhas A, Razeen M, Dubow M, Gan A, Chui TY, Shah N, et al. Assessment of perfused foveal microvascular density and identification of nonperfused capillaries in healthy and vasculopathic eyes. Invest Ophthalmol Vis Sci. 2014;55(12):8056-66.

201. Olaisen B. Distance between lines, a plugin for ImageJ. NIH ImageJ Archives 2006 [Available from: http://imagej.1557.x6.nabble.com/Distance-Between-Lines-a-plugin-for-ImageJ-td3701802.html.

202. Penn JS, Tolman BL, Henry MM. Oxygen-Induced Retinopathy in the Rat: Relationship of Retinal Nonperfusion to Subsequent Neovascularization. Invest Ophthalmol Vis Sci. 1994;35(9):34-293435.

203. Blair NP, Wanek JM, Mori M, Shahidi M. Abnormal retinal vascular oxygen tension response to light flicker in diabetic rats. Invest Ophthalmol Vis Sci. 2009;50(11):5444-8.

204. Srinivasan VJ, Radhakrishnan H. Total average blood flow and angiography in the rat retina. J Biomed Opt. 2013;18(7):76025.

205. Wanek J, Teng PY, Blair NP, Shahidi M. Inner retinal oxygen delivery and metabolism under normoxia and hypoxia in rat. Invest Ophthalmol Vis Sci. 2013;54(7):5012-9.

206. Wanek J, Teng PY, Blair NP, Shahidi M. Inner retinal oxygen delivery and metabolism in streptozotocin diabetic rats. Invest Ophthalmol Vis Sci. 2014;55(3):1588-93.

207. Song W, Wei Q, Jiao S, Zhang HF. Integrated photoacoustic ophthalmoscopy and spectral-domain optical coherence tomography. J Vis Exp. 2013(71):e4390.

208. Cairns J. Normal development of the hyaloid and retinal vessels in the rat. The British journal of ophthalmology. 1959;43(7):385.

209. Wang H, Yang Z, Jiang Y, Flannery J, Hammond S, Kafri T, et al. Quantitative analyses of retinal vascular area and density after different methods to reduce VEGF in a rat model of retinopathy of prematurity. Invest Ophthalmol Vis Sci. 2014;55(2):737-44.

210. Ganesan P, He S, Xu H. Analysis of retinal circulation using an image-based network model of retinal vasculature. Microvasc Res. 2010;80(1):99-109.

211. Wolf S, Arend O, Schulte K, Ittel TH, Reim M. Quantification of retinal capillary density and flow velocity in patients with essential hypertension. Hypertension. 1994;23(4):464-7.

212. Berkowitz BA, Penn JS. Abnormal panretinal response pattern to carbogen inhalation in experimental retinopathy of prematurity. Invest Ophthalmol Vis Sci. 1998;39(5):840-5.

213. Berkowitz BA, Zhang W. Significant Reduction of the Panretinal Oxygenation Response after 28% Supplemental Oxygen Recovery in Experimental ROP. Invest Ophthalmol Vis Sci. 2000;41(7):1925-31.

214. Saito Y, Uppal A, Byfield G, Budd S, Hartnett ME. Activated NAD(P)H oxidase from supplemental oxygen induces neovascularization independent of VEGF in retinopathy of prematurity model. Invest Ophthalmol Vis Sci. 2008;49(4):1591-8.

215. Yamauchi H, Fukuyama H, Nagahama Y, Nabatame H, Nakamura K, Yamamoto Y, et al. Evidence of misery perfusion and risk for recurrent stroke in major cerebral arterial occlusive diseases from PET. J Neurol Neurosurg Psychiatry. 1996;61(1):18-25.

216. Fulton AB, Hansen RM, Moskowitz A, Akula JD. The neurovascular retina in retinopathy of prematurity. Prog Retin Eye Res. 2009;28(6):452-82.

217. Akula JD, Hansen RM, Martinez-Perez ME, Fulton AB. Rod photoreceptor function predicts blood vessel abnormality in retinopathy of prematurity. Invest Ophthalmol Vis Sci. 2007;48(9):4351-9.

218. Akula JD, Mocko JA, Moskowitz A, Hansen RM, Fulton AB. The oscillatory potentials of the dark-adapted electroretinogram in retinopathy of prematurity. Invest Ophthalmol Vis Sci. 2007;48(12):5788-97.

219. Werdich XQ, McCollum GW, Rajaratnam VS, Penn JS. Variable oxygen and retinal VEGF levels: correlation with incidence and severity of pathology in a rat model of oxygen-induced retinopathy. Experimental eye research. 2004;79(5):623-30.

220. McColm JR, Geisen P, Hartnett ME. VEGF isoforms and their expression after a single episode of hypoxia or repeated fluctuations between hyperoxia and hypoxia: relevance to clinical ROP. Mol Vis. 2004;10:512-20.

221. Geisen P, Peterson LJ, Martiniuk D, Uppal A, Saito Y, Hartnett ME. Neutralizing antibody to VEGF reduces intravitreous neovascularization and may not interfere with ongoing

intraretinal vascularization in a rat model of retinopathy of prematurity. Mol Vis. 2008;14:345-57.

222. Stone J, Maslim J, Valter-Kocsi K, Mervin K, Bowers F, Chu Y, et al. Mechanisms of photoreceptor death and survival in mammalian retina. Prog Retin Eye Res. 1999;18(6):689-735.

223. Maslim J, Valter K, Egensperger R, Hollander H, Stone J. Tissue oxygen during a critical developmental period controls the death and survival of photoreceptors. Invest Ophthalmol Vis Sci. 1997;38(9):1667-77.

224. Yao J, Maslov KI, Zhang Y, Xia Y, Wang LV. Label-free oxygen-metabolic photoacoustic microscopy in vivo. J Biomed Opt. 2011;16(7):076003.

225. Boron WF, Boulpaep EL. Medical Physiology, 2e Updated Edition: with STUDENT CONSULT Online Access: Elsevier Health Sciences; 2012.

226. Rogers S, McIntosh RL, Cheung N, Lim L, Wang JJ, Mitchell P, et al. The prevalence of retinal vein occlusion: pooled data from population studies from the United States, Europe, Asia, and Australia. Ophthalmology. 2010;117(2):313-9 e1.

227. Sun C, Li XX, He XJ, Zhang Q, Tao Y. Neuroprotective effect of minocycline in a rat model of branch retinal vein occlusion. Exp Eye Res. 2013;113:105-16.

228. Rehak M, Hollborn M, Iandiev I, Pannicke T, Karl A, Wurm A, et al. Retinal gene expression and Muller cell responses after branch retinal vein occlusion in the rat. Invest Ophthalmol Vis Sci. 2009;50(5):2359-67.

229. Paques M, Tadayoni R, Sercombe R, Laurent P, Genevois O, Gaudric A, et al. Structural and hemodynamic analysis of the mouse retinal microcirculation. Invest Ophthalmol Vis Sci. 2003;44(11):4960-7.

230. Gong Y, Li J, Sun Y, Fu Z, Liu CH, Evans L, et al. Optimization of an Image-Guided Laser-Induced Choroidal Neovascularization Model in Mice. PLoS One. 2015;10(7):e0132643.

231. Kocaoglu OP, Uhlhorn SR, Hernandez E, Juarez RA, Will R, Parel JM, et al. Simultaneous fundus imaging and optical coherence tomography of the mouse retina. Invest Ophthalmol Vis Sci. 2007;48(3):1283-9.

232. Rosen RB, Hathaway M, Rogers J, Pedro J, Garcia P, Dobre GM, et al. Simultaneous OCT/SLO/ICG imaging. Invest Ophthalmol Vis Sci. 2009;50(2):851-60.

233. Zawadzki RJ, Jones SM, Pilli S, Balderas-Mata S, Kim DY, Olivier SS, et al. Integrated adaptive optics optical coherence tomography and adaptive optics scanning laser ophthalmoscope system for simultaneous cellular resolution in vivo retinal imaging. Biomed Opt Express. 2011;2(6):1674-86.

234. Komar K, Stremplewski P, Motoczynska M, Szkulmowski M, Wojtkowski M. Multimodal instrument for high-sensitivity autofluorescence and spectral optical coherence tomography of the human eye fundus. Biomed Opt Express. 2013;4(11):2683-95.

235. Shih AY, Nishimura N, Nguyen J, Friedman B, Lyden PD, Schaffer CB, et al. Optically induced occlusion of single blood vessels in rodent neocortex. Cold Spring Harb Protoc. 2013;2013(12):1153-60.

236. Kleinfeld D, Friedman B, Lyden PD, Shih AY. Targeted occlusion to surface and deep vessels in neocortex via linear and nonlinear optical absorption. Animal models of acute neurological injuries. 2009:169-85.

237. Lee J, Srinivasan V, Radhakrishnan H, Boas DA. Motion correction for phase-resolved dynamic optical coherence tomography imaging of rodent cerebral cortex. Opt Express. 2011;19(22):21258-70.

238. DeRosa MC, Crutchley RJ. Photosensitized singlet oxygen and its applications. Coordin Chem Rev. 2002;233:351-71.

239. Nanda SK, Hatchell DL, Tiedeman JS, Dutton JJ, Hatchell MC, McAdoo T. A new method for vascular occlusion. Photochemical initiation of thrombosis. Arch Ophthalmol. 1987;105(8):1121-4.

240. Royster AJ, Nanda SK, Hatchell DL, Tiedeman JS, Dutton JJ, Hatchell MC. Photochemical initiation of thrombosis. Fluorescein angiographic, histologic, and ultrastructural alterations in the choroid, retinal pigment epithelium, and retina. Arch Ophthalmol. 1988;106(11):1608-14.

241. Genevois O, Paques M, Simonutti M, Sercombe R, Seylaz J, Gaudric A, et al. Microvascular remodeling after occlusion-recanalization of a branch retinal vein in rats. Invest Ophthalmol Vis Sci. 2004;45(2):594-600.

242. Hamilton AM, Kohner EM, Rosen D, Bird AC, Dollery CT. Experimental retinal branch vein occlusion in rhesus monkeys. I. Clinical appearances. Br J Ophthalmol. 1979;63(6):377-87.

243. Giannakaki-Zimmermann H, Kokona D, Wolf S, Ebneter A, Zinkernagel MS. Optical Coherence Tomography Angiography in Mice: Comparison with Confocal Scanning Laser Microscopy and Fluorescein Angiography. Transl Vis Sci Technol. 2016;5(4):11.

244. Zhang S, Murphy TH. Imaging the impact of cortical microcirculation on synaptic structure and sensory-evoked hemodynamic responses in vivo. PLoS Biol. 2007;5(5):e119.

245. Hayreh SS. Prevalent misconceptions about acute retinal vascular occlusive disorders. Prog Retin Eye Res. 2005;24(4):493-519.

246. Choi W, Moult EM, Waheed NK, Adhi M, Lee B, Lu CD, et al. Ultrahigh-Speed, Swept-Source Optical Coherence Tomography Angiography in Nonexudative Age-Related Macular Degeneration with Geographic Atrophy. Ophthalmology. 2015;122(12):2532-44.

247. Linden SM, Neckers DC. Type I and type II sensitizers based on Rose Bengal onium salts. Photochem Photobiol. 1988;47(4):543-50.

248. Kellogg RE, Bennett RG. Radiationless Intermolecular Energy Transfer. III. Determination of Phosphorescence Efficiencies. J Chem Phys. 1964;41(10):3042-5.

249. Bressler NM, Bressler SB, Fine SL. Age-related macular degeneration. Surv Ophthalmol. 1988;32(6):375-413.

250. Congdon N, O'Colmain B, Klaver CC, Klein R, Munoz B, Friedman DS, et al. Causes and prevalence of visual impairment among adults in the United States. Arch Ophthalmol. 2004;122(4):477-85.

251. Jager RD, Mieler WF, Miller JW. Age-related macular degeneration. N Engl J Med. 2008;358(24):2606-17.

252. Campochiaro PA, Soloway P, Ryan SJ, Miller JW. The pathogenesis of choroidal neovascularization in patients with age-related macular degeneration. Mol Vis. 1999;5:34.

253. Lim LS, Mitchell P, Seddon JM, Holz FG, Wong TY. Age-related macular degeneration. Lancet. 2012;379(9827):1728-38.

254. Mowatt G, Hernandez R, Castillo M, Lois N, Elders A, Fraser C, et al. Optical coherence tomography for the diagnosis, monitoring and guiding of treatment for neovascular age-

related macular degeneration: a systematic review and economic evaluation. Health Technol Assess. 2014;18(69):1-254.

255. Regatieri CV, Branchini L, Duker JS. The role of spectral-domain OCT in the diagnosis and management of neovascular age-related macular degeneration. Ophthalmic Surg Lasers Imaging. 2011;42 Suppl:S56-66.

256. de Carlo TE, Bonini Filho MA, Chin AT, Adhi M, Ferrara D, Baumal CR, et al. Spectral-domain optical coherence tomography angiography of choroidal neovascularization. Ophthalmology. 2015;122(6):1228-38.

257. Grossniklaus HE, Kang SJ, Berglin L. Animal models of choroidal and retinal neovascularization. Prog Retin Eye Res. 2010;29(6):500-19.

258. Pennesi ME, Neuringer M, Courtney RJ. Animal models of age related macular degeneration. Mol Aspects Med. 2012;33(4):487-509.

259. Giani A, Thanos A, Roh MI, Connolly E, Trichonas G, Kim I, et al. In vivo evaluation of laser-induced choroidal neovascularization using spectral-domain optical coherence tomography. Invest Ophthalmol Vis Sci. 2011;52(6):3880-7.

260. Tobe T, Ortega S, Luna JD, Ozaki H, Okamoto N, Derevjanik NL, et al. Targeted disruption of the FGF2 gene does not prevent choroidal neovascularization in a murine model. Am J Pathol. 1998;153(5):1641-6.

261. Ryan SJ. The development of an experimental model of subretinal neovascularization in disciform macular degeneration. Trans Am Ophthalmol Soc. 1979;77:707-45.

262. Montezuma SR, Vavvas D, Miller JW. Review of the ocular angiogenesis animal models. Semin Ophthalmol. 2009;24(2):52-61.

263. Miller H, Miller B, Ishibashi T, Ryan SJ. Pathogenesis of laser-induced choroidal subretinal neovascularization. Invest Ophthalmol Vis Sci. 1990;31(5):899-908.

264. Kwak N, Okamoto N, Wood JM, Campochiaro PA. VEGF is major stimulator in model of choroidal neovascularization. Invest Ophthalmol Vis Sci. 2000;41(10):3158-64.

265. Hoerster R, Muether PS, Vierkotten S, Schroder S, Kirchhof B, Fauser S. In-vivo and ex-vivo characterization of laser-induced choroidal neovascularization variability in mice. Graefes Arch Clin Exp Ophthalmol. 2012;250(11):1579-86.

266. Jia Y, Bailey ST, Wilson DJ, Tan O, Klein ML, Flaxel CJ, et al. Quantitative optical coherence tomography angiography of choroidal neovascularization in age-related macular degeneration. Ophthalmology. 2014;121(7):1435-44.

267. Yi J, Chen S, Backman V, Zhang HF. In vivo functional microangiography by visible-light optical coherence tomography. Biomed Opt Express. 2014;5(10):3603-12.

268. Srinivasan VJ, Jiang JY, Yaseen MA, Radhakrishnan H, Wu W, Barry S, et al. Rapid volumetric angiography of cortical microvasculature with optical coherence tomography. Opt Lett. 2010;35(1):43-5.

269. Jia Y, Bailey ST, Hwang TS, McClintic SM, Gao SS, Pennesi ME, et al. Quantitative optical coherence tomography angiography of vascular abnormalities in the living human eye. Proc Natl Acad Sci U S A. 2015;112(18):E2395-402.

270. Yi J, Li X. Estimation of oxygen saturation from erythrocytes by high-resolution spectroscopic optical coherence tomography. Opt Lett. 2010;35(12):2094-6.

271. Chen S, Yi J, Zhang HF. Measuring oxygen saturation in retinal and choroidal circulations in rats using visible light optical coherence tomography angiography. Biomed Opt Express. 2015;6(8):2840-53.

272. Lambert V, Lecomte J, Hansen S, Blacher S, Gonzalez ML, Struman I, et al. Laser-induced choroidal neovascularization model to study age-related macular degeneration in mice. Nat Protoc. 2013;8(11):2197-211.

273. Shah RS, Soetikno BT, Lajko M, Fawzi AA. A Mouse Model for Laser-induced Choroidal Neovascularization. J Vis Exp. 2015(106):e53502.

274. Chen S, Yi J, Inayat S, Liu W, Cang J, Zhang HF. Measuring absolute microvascular blood flow in cortex using visible-light optical coherence tomography. Conf Proc IEEE Eng Med Biol Soc. 2014;2014:3881-4.

275. Yi J, Chen S, Shu X, Fawzi AA, Zhang HF. Human retinal imaging using visible-light optical coherence tomography guided by scanning laser ophthalmoscopy. Biomed Opt Express. 2015;6(10):3701-13.

276. Rattner A, Yu H, Williams J, Smallwood PM, Nathans J. Endothelin-2 signaling in the neural retina promotes the endothelial tip cell state and inhibits angiogenesis. Proc Natl Acad Sci U S A. 2013;110(40):E3830-9.

277. Campbell JP, Merkel AR, Masood-Campbell SK, Elefteriou F, Sterling JA. Models of bone metastasis. J Vis Exp. 2012(67):e4260.

278. McMenamin PG. Optimal methods for preparation and immunostaining of iris, ciliary body, and choroidal wholemounts. Invest Ophthalmol Vis Sci. 2000;41(10):3043-8.

279. Claybon A, Bishop AJ. Dissection of a mouse eye for a whole mount of the retinal pigment epithelium. J Vis Exp. 2011(48).

280. Campos M, Amaral J, Becerra SP, Fariss RN. A novel imaging technique for experimental choroidal neovascularization. Invest Ophthalmol Vis Sci. 2006;47(12):5163-70.

281. Sakurai E, Anand A, Ambati BK, van Rooijen N, Ambati J. Macrophage depletion inhibits experimental choroidal neovascularization. Invest Ophthalmol Vis Sci. 2003;44(8):3578-85.

282. Jawad S, Liu B, Li Z, Katamay R, Campos M, Wei L, et al. The role of macrophage class a scavenger receptors in a laser-induced murine choroidal neovascularization model. Invest Ophthalmol Vis Sci. 2013;54(9):5959-70.

283. Kim DY, Fingler J, Zawadzki RJ, Park SS, Morse LS, Schwartz DM, et al. Optical imaging of the chorioretinal vasculature in the living human eye. Proc Natl Acad Sci U S A. 2013;110(35):14354-9.

284. Jia Y, Morrison JC, Tokayer J, Tan O, Lombardi L, Baumann B, et al. Quantitative OCT angiography of optic nerve head blood flow. Biomed Opt Express. 2012;3(12):3127-37.

285. Hanneman SK. Design, analysis, and interpretation of method-comparison studies. AACN Adv Crit Care. 2008;19(2):223-34.

286. Giavarina D. Understanding Bland Altman analysis. Biochem Med (Zagreb). 2015;25(2):141-51.

287. Campa C, Costagliola C, Incorvaia C, Sheridan C, Semeraro F, De Nadai K, et al. Inflammatory mediators and angiogenic factors in choroidal neovascularization: pathogenetic interactions and therapeutic implications. Mediators Inflamm. 2010;2010.

288. Carmeliet P. Mechanisms of angiogenesis and arteriogenesis. Nat Med. 2000;6(4):389-95.

289. Potente M, Gerhardt H, Carmeliet P. Basic and therapeutic aspects of angiogenesis. Cell. 2011;146(6):873-87.

290. Caicedo A, Espinosa-Heidmann DG, Pina Y, Hernandez EP, Cousins SW. Blood-derived macrophages infiltrate the retina and activate Muller glial cells under experimental choroidal neovascularization. Exp Eye Res. 2005;81(1):38-47.

291. Checchin D, Sennlaub F, Levavasseur E, Leduc M, Chemtob S. Potential role of microglia in retinal blood vessel formation. Invest Ophthalmol Vis Sci. 2006;47(8):3595-602.

292. Rymo SF, Gerhardt H, Wolfhagen Sand F, Lang R, Uv A, Betsholtz C. A two-way communication between microglial cells and angiogenic sprouts regulates angiogenesis in aortic ring cultures. PLoS One. 2011;6(1):e15846.

293. He L, Marneros AG. Macrophages are essential for the early wound healing response and the formation of a fibrovascular scar. Am J Pathol. 2013;182(6):2407-17.

294. Benton RL, Maddie MA, Minnillo DR, Hagg T, Whittemore SR. Griffonia simplicifolia isolectin B4 identifies a specific subpopulation of angiogenic blood vessels following contusive spinal cord injury in the adult mouse. J Comp Neurol. 2008;507(1):1031-52.

295. Laitinen L. Griffonia simplicifolia lectins bind specifically to endothelial cells and some epithelial cells in mouse tissues. Histochem J. 1987;19(4):225-34.

296. Miller H, Miller B, Ryan SJ. The role of retinal pigment epithelium in the involution of subretinal neovascularization. Invest Ophthalmol Vis Sci. 1986;27(11):1644-52.

297. Sugino IK, Wang H, Zarbin MA. Age-related macular degeneration and retinal pigment epithelium wound healing. Mol Neurobiol. 2003;28(2):177-94.

298. Harada C, Mitamura Y, Harada T. The role of cytokines and trophic factors in epiretinal membranes: involvement of signal transduction in glial cells. Prog Retin Eye Res. 2006;25(2):149-64.

299. Xu KP, Yu FS. Cross talk between c-Met and epidermal growth factor receptor during retinal pigment epithelial wound healing. Invest Ophthalmol Vis Sci. 2007;48(5):2242-8.

300. de Carlo TE, Romano A, Waheed NK, Duker JS. A review of optical coherence tomography angiography (OCTA). Int J Retina Vitreous. 2015;1:5.

301. Makita S, Hong Y, Yamanari M, Yatagai T, Yasuno Y. Optical coherence angiography. Optics Express. 2006;14(17):7821-40.

302. Tokayer J, Jia Y, Dhalla A-H, Huang D. Blood flow velocity quantification using split-spectrum amplitude-decorrelation angiography with optical coherence tomography. Biomedical optics express. 2013;4(10):1909-24.

303. Su JP, Chandwani R, Gao SS, Pechauer AD, Zhang M, Wang J, et al. Calibration of optical coherence tomography angiography with a microfluidic chip. Journal of Biomedical Optics. 2016;21(8):086015-.

304. Choi W, Moult EM, Waheed NK, Adhi M, Lee B, Lu CD, et al. Ultrahigh-speed, swept-source optical coherence tomography angiography in nonexudative age-related macular degeneration with geographic atrophy. Ophthalmology. 2015;122(12):2532-44.

305. Choi W, Mohler KJ, Potsaid B, Lu CD, Liu JJ, Jayaraman V, et al. Choriocapillaris and choroidal microvasculature imaging with ultrahigh speed OCT angiography. PloS one. 2013;8(12):e81499.

Vita

Brian Soetikno received his B.S. Biomedical Engineering from Washington University in St. Louis, MO, U.S.A. in 2013. In the summer of 2013, he matriculated into the Medical Scientist (M.D./Ph.D.) Training Program at the Northwestern University Feinberg School of Medicine. He started his Ph.D. in the Department of Biomedical Engineering, Northwestern University, Evanston, IL, U.S.A. in the fall of 2015. His research interests include photoacoustic imaging, optical coherence tomography, optical coherence tomography angiography, and ophthalmology. He has authored 20 peer-reviewed publications, 1 review article, 1 book chapter, and 1 patent. He has presented at multiple conferences including the ARVO Annual Meeting, SPIE Photonics West, and the OCTA Summit. His notable awards include the Outstanding Poster Award (OCTA Summit 2017, Portland, OR), the 2017 BME Research Day Imaging and Biophotonics Research Progress Award, the 2016 Illinois Society for the Prevention of Blindness Grant, the 2016 SPIE Optics and Photonics Education Scholarship, and the 2015 ARVO Travel Award (National Eye Institute). He is the principal investigator of a NIH F30 Ruth L. Kirschstein National Research Service Award (National Eye Institute). He expects to receive his Ph.D. and M.D. degrees in the winter of 2018 and summer of 2020, respectively.